Doctoral theses at NTNU, 2016:221

Belma Talic

Metallic Interconnects for Solid Oxide Fuel Cells

High Temperature Corrosion and Protective Spinel Coatings

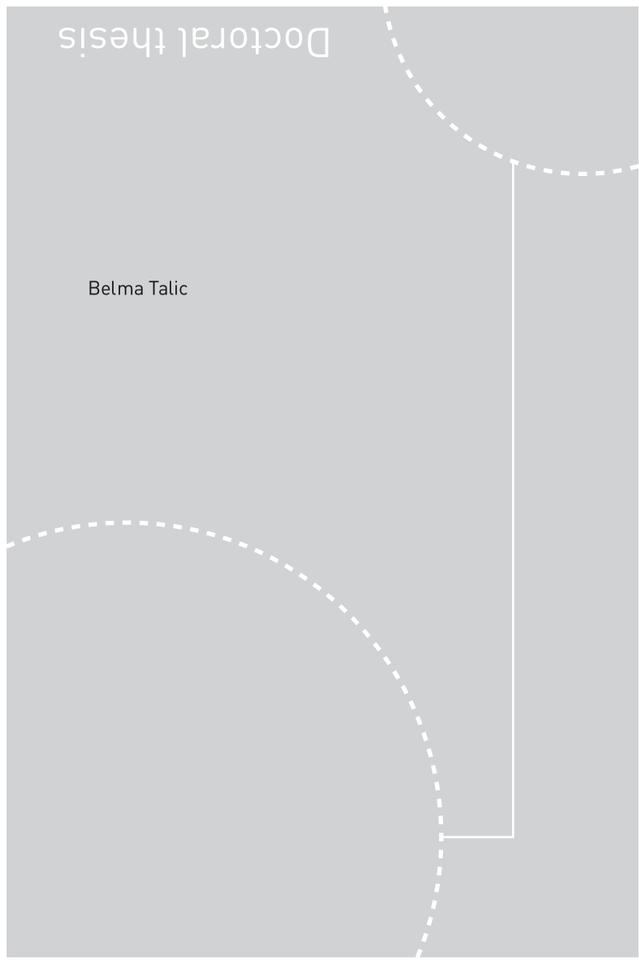

ISBN 978-82-326-1780-7 (printed ver.)
ISBN 978-82-326-1781-4 (electronic ver.)
ISSN 1503-8181

NTNU
Norwegian University of
Science and Technology

NTNU
Norwegian University of
Science and Technology
Thesis for the Degree of
Philosophiae Doctor
Faculty of Natural Sciences and Technology
Department of Materials Science and
Engineering

Doctoral theses at NTNU, 2016:221

NTNU

Belma Talic

Metallic Interconnects for Solid Oxide Fuel Cells

High Temperature Corrosion and Protective Spinel Coatings

Thesis for the Degree of Philosophiae Doctor

Trondheim, July 2016

Norwegian University of Science and Technology
Faculty of Natural Sciences and Technology
Department of Materials Science and Engineering

NTNU
Norwegian University of
Science and Technology

NTNU
Norwegian University of Science and Technology

Thesis for the Degree of Philosophiae Doctor

Faculty of Natural Sciences and Technology
Department of Materials Science and Engineering

ISBN 978-82-326-1780-7 (printed ver.)
ISBN 978-82-326-1781-4 (electronic ver.)
ISSN 1503-8181

IMT-report 2016:230

Doctoral theses at NTNU, 2016:221

Printed by NTNU Grafisk senter

This thesis has been submitted to

Department of Materials Science and Engineering
Norwegian University of Science and Technology

in partial fulfillment of the requirements for
the academic degree

Philosophiae Doctor

July 2016

Acknowledgments

First and foremost I would like to thank my main supervisor Hilde Lea Lein for granting me the opportunity to work with this interesting topic for three years. I greatly appreciate the freedom you gave me to shape the contents of this project along the way based on what I found the most interesting. Your encouragement, support and positive attitude the past three years have been invaluable. Thanks are also due to my co-supervisor Kjell Wiik for valued input on various topics throughout this project, particularly during the first year spend on materials synthesis and characterization.

I am grateful towards my co-supervisor Peter Vang Hendriksen, for generously welcoming me to stay with his group at the Department of Energy Conversion and Storage (DTU) for nearly two whole years as a guest PhD student. Your vast knowledge and numerous ideas have been of great value to this work. I don't remember ever leaving your office without at least three new things on my to-do list.

Sebastian Molin and Vinothini Venkatachalam worked as postdocs within the same topic at DTU and have contributed significantly to shape the contents of this work. Vinothini is thanked for help with troubleshooting and finally making the EPD process work, and Sebastian for sharing his overall knowledge on high temperature corrosion and electrical measurements, and for giving me feedback on article drafts. Both of your comments and our many mutual discussions have helped me towards becoming a better researcher.

At DTU I would additionally like to thank Nikos Bonanos for teaching me about electrical conductivity measurements; Karsten Agersted and Carsten Gynter Sørensen for assistance with thermal analysis and for fixing the TG just in time for me to collect data for this thesis; Michela Della Negra for help with zeta potential measurements; and Åsa Helen Persson for organizing the high temperature corrosion group meetings. All the technical staff at the Department of Energy Conversion and Storage deserve great thanks for their help with various practical tasks in the laboratory. Pernille Hedmark and Ebtisam Abdellahi are especially acknowledged for preparing a seemingly endless number of SEM samples.

At NTNU I would like to thank Pei Na Kui for assistance with operation of the spray pyrolysis furnace; Sverre Magnus Selbach and Katherine Inzani for running some of my samples in the dilatometer; and Julian Tolchard and Kristin Høydalsvik Wells for assistance with XRD. Sophie Weber (now at Cerpotech) deserves

great thanks for providing me with constructive feedback on writing and some much needed pep-talks along the way.

I would also like to thank Hannes Falk-Windisch (Chalmers University) for help with measuring the Cr-evaporation of my samples for his contagious enthusiasm for the topic of SOFC interconnects.

Siri Marie Skaftun, Mariia Stepanova and Ingrid Roten Mattson did a great job of keeping me updated about life in KII while I was away. Your company and our long coffee breaks have been missed the last two years.

I am grateful to have been raised in a supportive and loving family who have taught me both to work hard and to take breaks to enjoy life. Hvala za sve, mama i tata!

Finally, I would like to thank Sivert for coping with my ups and downs the past couple of months and for doing his best to keep me sane.

Preface

This thesis is based on work carried out from August 2013 to July 2016. The experiments were carried out at the Department of Materials Science and Engineering, Norwegian University of Science and Technology (NTNU) and at the Department of Energy Conversion and Storage, Technical University of Denmark (DTU). The main supervisor has been Associate Professor Hilde Lea Lein (NTNU), with Professor Kjell Wiik (NTNU) and Professor Peter Vang Hendriksen (DTU) as co-supervisors.

I have preformed all the experimental work presented in this thesis, with the following exceptions: a major part of the Cr-evaporation measurements were carried out by Hannes Falk-Windisch (Chalmers University, Sweden), thermogravimetrical analysis was performed with assistance from Carsten Gynther Sørensen (DTU), and Pei Na Kui (NTNU) assisted in operation of the spray pyrolysis furnace.

Copenhagen, 1 July, 2016
Belma Talic

Summary

Solid oxide fuel cells (SOFC) offer an environmentally friendly way of converting hydrogen to electrical energy with a high electrical conversion efficiency. The commercialization of this technology is however inhibited by high costs and a limited lifetime. These issues are in part related to degradation of the ferritic stainless steel (FSS) interconnect material. The two most important challenges with the use of FSS are the increase in electrical resistance due to growth of modestly conductive oxide scales, and the vaporization of Cr(VI) species leading to poisoning of the SOFC cathode. This thesis investigates the use of $MnCo_2O_4$-based spinel coatings as a way of mitigating these issues.

The first part of this work was devoted to exploring whether the long term stability of the spinel coating could be improved by partially substituting some of the Co in $MnCo_2O_4$ with Cu or Fe. The crystal structure, thermal expansion and electrical conductivity of $MnCo_{2-x}M_xO_4$ (M = Fe, Cu; x=0, 0.1, 0.3, 0.5) were characterized using X-ray diffraction, dilatometry, and 4-point conductivity measurements. All materials could be successfully synthesized by aqueous based spray pyrolysis, and crystallized in the cubic spinel structure, although several observations pointed towards poor high-temperature stability of the Cu-substituted materials. The thermal expansion coefficient (TEC) of all materials was observed to increase above ca. 400 °C. The extra expansion was proposed to be due to a low-spin to high-spin transition of trivalent Co on the octahedral sites. Substitution with Fe resulted in a more linear thermal expansion behavior and a decrease of the TEC to a value better matching other typically used SOFC materials. The electrical conductivity was increased by Cu-substitution and decreased by Fe-substitution. Nevertheless, all materials were found to be sufficiently conductive (> 30 S/cm at 800 °C) for the application as interconnect coating materials.

Three compositions, $MnCo_2O_4$ (MC), $MnCo_{1.7}Fe_{0.3}O_4$ (MCFe) and $MnCo_{1.7}Cu_{0.3}O_4$ (MCCu), were chosen for further investigations as protective coatings on Crofer 22 APU. The oxidation kinetics were studied in simulated SOFC cathode side environment of air between 700 and 900 °C for up to 4000 h. At 800 and 900 °C, the parabolic oxidation rate was lowered by all of the spinel coatings, while none of the coatings provided any apparent improvement of the oxidation resistance at 700 °C. The area specific resistance (ASR) of spinel coated and bare Crofer 22 APU was measured in contact with $La_{0.85}Sr_{0.1}Mn_{1.1}O_3$ at 800 °C in air, to simulate the interaction with the cathode in a SOFC stack. After ca. 4300 h, the ASR of bare Crofer 22 APU had already exceeded the acceptable maximum for an interconnect

material (> 100 $\mathrm{m\Omega\,cm^2}$ with 0.5 $\mathrm{A/cm^2}$). The lowest ASR was measured for MC coated Crofer 22 APU (29 $\mathrm{m\Omega\,cm^2}$ after ca. 4300 h), however, the ASR of MCFe and MCCu coated samples was only marginally higher (31 $\mathrm{m\Omega\,cm^2}$). During oxidation, a several $\mu\mathrm{m}$ thick, Cr-rich $(\mathrm{Mn,Co,Fe,Cr})_3\mathrm{O}_4$ reaction layer formed at the coating/alloy interface. It was argued that the low ASR and improved oxidation resistance of spinel coated Crofer 22 APU can be attributed to the formation of this reaction layer by consumption of the thermally grown oxide scale on the alloy.

To obtain a better understanding of the formation and growth of the Cr-rich reaction layer, the interaction between chromia and MC, MCFe, and MCCu spinel oxides was studied at 900 °C in air using diffusion couples. During annealing, a reaction product rich in chromium and cobalt formed at the diffusion couple interface. By using Pt-particles to mark the original interface, it was revealed that this reaction product grew by diffusion of $\mathrm{Co^{2+}}$ from the spinel oxide to the chromia/reaction product interface. The growth of the reaction product followed parabolic kinetics, however, the parabolic rate constants (10^{-5}-10^{-4} $\mu\mathrm{m^2/s}$) indicated a considerably faster growth rate than observed with spinel coated Crofer 22 APU. It was suggested that the presence of Mn in the alloy, which diffuses outward into the coating during oxidation, was largely responsible for the discrepancy.

The second part of this thesis was devoted to a topic highly relevant for the commercial potential of the spinel coating. For maximum density, $(\mathrm{Mn,Co})_3\mathrm{O}_4$ coatings have typically been sintered in a two-step process, involving heat treatment first in reducing and then in oxidizing atmospheres. To reduce production costs, it would be beneficial if the coating instead could be sintered *in-situ* during warm-up of the SOFC stack. However, omitting the reduction step results in a highly porous coating. To examine the implications of this, oxidation and Cr-evaporation behavior was studied on MCFe coated Crofer 22 APU, heat treated to produce different levels of porosity in the coating. A highly dense MCFe coating, produced by the two-step sintering process, reduced the Cr-evaporation rate of Crofer 22 APU by 97 % in air-3%$\mathrm{H_2O}$ at 800 °C. In comparison, a 88 % reduction in the Cr-evaporation rate was achieved by a highly porous coating, produced by sintering in air at 900 °C for 2 h. Based on evaluation of the long term (5000 h) oxidation behavior in air at 800 °C it was concluded that both the highly dense and porous coatings reduced the oxidation rate of Crofer 22 APU sufficiently to meet SOFC lifetime requirements. Oxidation studies of uncoated Crofer 22 APU revealed that part of the improved oxidation resistance observed for spinel coated samples should be attributed to an effect of alloy pre-oxidation.

Contents

Abbreviations

ASR	Area specific resistance
BSE	Backscatter electron
Cu1	$MnCo_{1.9}Cu_{0.1}O_4$
Cu3/MCCu	$MnCo_{1.7}Cu_{0.3}O_4$
Cu5	$MnCo_{1.5}Cu_{0.5}O_4$
DIL	Dilatometry
E_A	Activation energy
EDX	Energy dispersive X-ray spectroscopy
Fe1	$MnCo_{1.9}Fe_{0.1}O_4$
Fe3/MCFe	$MnCo_{1.7}Fe_{0.3}O_4$
Fe5	$MnCo_{1.5}Fe_{0.5}O_4$
FSS	Ferritic stainless steel
HCR	Heating and cooling rate
HS	High spin
k_P	Parabolic rate constant
LS	Low spin
LSM	$La_{0.85}Sr_{0.1}Mn_{1.1}O_3$
MC	$MnCo_2O_4$
pO_2	Oxygen partial pressure
ρ	Material density
σ	Conductivity
SEM	Scanning electron microscope
SOFC	Solid oxide fuel cell
TEC	Thermal expansion coefficient
TGA	Thermogravimetric analysis
TPB	Triple phase boundary
XRD	X-ray diffraction
YSZ	Yttrium Stabilized Zirconia

1. Introduction

1.1 Background

The human impact on global warming is well established and has raised increasing concern the last decades [1]. One of the main reasons for the rising global average temperature is an increased concentration of green house gasses such as CO_2 in the atmosphere. In Europe, it has been estimated that 32 % of the green house gas emissions in 2013 were due to production of heat and electricity [2]. The European Union has set a long term goal that by 2050, green house gas emissions should be reduced by 80-95% relative to 1990 levels [3]. In order to reach this goal, a larger part of the energy demand needs to be covered by renewable sources with low carbon emissions such as sun and wind power. The challenge with sun and wind power is however the large fluctuation in energy production as the weather changes over the course of a day. This makes the ability to convert and store the produced energy critical [4]. A promising solution to this challenge is using hydrogen as an energy carrier. During periods of the day when the energy production is higher than the demand, excess power can be used to produce hydrogen by electrolysis of water, while in the opposite situation, the produced hydrogen can be converted back to electrical energy using a fuel cell.

The principle of a fuel cell was first described by Schonebein [5] in 1839 and demonstrated experimentally by Grove [6] the same year. Several types of fuel cells have been developed since then, the most common today being the proton exchange membrane fuel cell (PEM-FC), alkaline fuel cell (AFC), phosphoric acid fuel cell (PAFC), molten carbonate fuel cell (MCFC) and solid oxide fuel cell (SOFC). The main difference between these are their range of operating temperatures and the type of materials employed as the electrolyte. The focus of this work will be the SOFC, which has an operating temperature of 650–1000 °C and, as the name suggests, employs a solid oxide as the electrolyte material. Some of the advantages of the SOFC include a high electrical conversion efficiency (up to 60 % has been demonstrated experimentally [7]) and the possibility to be operated in the reverse mode to produce hydrogen by electrolysis of water [8]. Unlike many of the other fuel cells, SOFCs can utilize a variety of different fuels such as methanol [9] and diesel [10] in addition to hydrogen. This opens up a market for the technology also before establishment of a "hydrogen society". However, despite its many advantages, there are still several challenges that need to be resolved before SOFCs will become commercially attractive on a large scale.

A single SOFC unit consists of two porous electrodes separated by a dense solid oxide electrolyte and has an open circuit potential of ca. 1 V [11]. To obtain a usable power output, several cells are connected together in series to form a stack. Interconnects are then used between the individual cells to provide the electrical contact, and separate and distribute the fuel and oxidant gasses. One of the factors limiting the lifetime and performance of SOFC stacks today is degradation of the ferritic stainless steel (FSS) used as the interconnect material. Under SOFC operating conditions the steel is oxidized, forming a several μm thick Cr_2O_3 and $(Mn, Cr)_3O_4$ scale on the surface [12]. Because of the modest electrical conductivity of these oxides, the resistance across the stack increases with time as the scale thickens, consequently leading to a decrease in the power output [13]. Furthermore, Cr_2O_3 and $(Mn, Cr)_3O_4$ are prone to form volatile Cr(VI)-species, that have been shown to degrade the SOFC cathode performance [14, 15]. A possible way to mitigate these challenges is to coat the FSS interconnect with a protective material. $(Mn, Co)_3O_4$ spinels are considered promising coating materials for the cathode (oxidant) side of the interconnect. In previous studies it has been demonstrated that these spinel coatings may reduce the oxidation rate of FSS [16], limit Cr-vaporization [17] and ensure a lower contact resistance against the cathode material [18–20]. There is however a lack of knowledge on why the $(Mn, Co)_3O_4$ coatings are effective and some concerns about whether they are protective *enough* to enable 40 000 h service of FSS interconnects [21, 22]. There have also been some contradictory reports about how the spinel coatings interact with the FSS interconnect. Some studies have reported on formation of several μm thick, Cr-rich reaction layers at the coating/alloy interface [23, 24], while others have claimed no reaction or incorporation of Cr in the coating [25, 26]. The Cr-rich reaction layers are generally unwanted due to their poor electrical conductivity and mismatch in thermal expansion with the alloy and coating.

1.2 Aim of work

The principal aim of this work is to contribute to a better understanding of the degradation processes of spinel coated ferritic stainless steel in the typical SOFC cathode atmosphere. The interactions between spinel coatings and the thermally grown oxide scale on an interconnect alloy will be in focus. More knowledge about the interaction mechanism is important both for a more reliable prediction of the service lifetime of spinel coated interconnects, and to facilitate further improvement of the alloy/coating system.

The thesis has been written as a collection of manuscripts, that will be submitted for publication in relevant journals. Chapter 2 provides first a general introduction

to the theory related to the present work, along with a review of relevant literature. The manuscripts reporting the results of the experimental work are presented in Chapter 3. The first three manuscripts focus on investigating iron and copper substitutions in $MnCo_2O_4$ as a way of improving the protective properties of the spinel coating. Iron and copper were chosen as substitutional elements based on a review of available literature on spinel oxides. An investigation of several binary spinels by Petric and Ling [27] indicated that copper containing spinels exhibit appreciable electrical conductivities, while ferrite spinels typically have thermal expansion coefficients matching that of other commonly used SOFC materials. Diffusion couple experiments have furthermore indicated that both Cu and Fe substitution may be beneficial for reducing the formation of poorly conductive Cr-rich reaction layers at the spinel coating/oxide scale interface [28, 29]. A thorough characterization of the electrical and thermal properties of $MnCo_{2-x}M_xO_4$ (M = Fe, Cu; x=0, 0.1, 0.3, 0.5) is reported in Manuscript I. Manuscripts II deals with the ability of these materials to reduce the oxidation rate and area specific resistance of Crofer 22 APU. In Manuscript III, diffusion couples of chromia, and Fe and Cu doped $MnCo_2O_4$ were used as a model system to obtain more information about the interaction between these coatings and FSS during oxidation.

The focus in Manuscript IV is shifted to processing of the spinel coatings. Powder-based coating deposition methods such as slurry spraying, screen printing and electrophoretic deposition are attractive from a commercial point of view due to their low costs and opportunity for high production through-put. The disadvantage with these methods is however the requirement to sinter the coating after deposition. To ensure maximum density while avoiding excessive oxidation of the alloy substrate, spinel coatings have typically been sintered in a two step reduction and re-oxidation procedure. Omitting the reduction step and instead sintering the spinel coating *in-situ* during warm-up of the SOFC stack would be beneficial for further reducing production costs. The objective in Manuscript IV was to investigate how different heat treatments, resulting in different coating densities, influence the oxidation and chromium evaporation behavior of spinel coated Crofer 22 APU. While working with this topic, little information could be found in literature about how these heat treatments might have modified the oxidation resistance of the alloy substrate. This inspired an investigation of the effect of pre-oxidation on the oxidation resistance of uncoated Crofer 22 APU, which is reported in Manuscript V. A summary and some concluding remarks for the five manuscripts, and recommendations for further work are presented in Chapters 4 and 5, respectively.

2. Theory

2.1 Solid oxide fuel cells

A solid oxide fuel cell is an electrochemical device that converts chemical energy stored in fuels, for example hydrogen gas, to electrical energy. The following section will provide an overview of the basics of SOFC technology and some of the commonly used materials.

2.1.1 Operating principle

The basic components and operating principle of a solid oxide fuel cell (SOFC) are illustrated in Figure 2.1. At the cathode electrode, oxygen gas reacts with electrons to form oxide ions according to:

$$\tfrac{1}{2}\mathrm{O_2(g)} + 2\mathrm{e^-} \rightarrow \mathrm{O^{2-}} \tag{2.1}$$

The oxide ions migrate through the electrolyte to combine with the fuel (H_2) at the anode electrode:

$$\mathrm{H_2(g)} + \mathrm{O^{2-}} \rightarrow \mathrm{H_2O} + 2\mathrm{e^-} \tag{2.2}$$

The electrons liberated in the reaction between the fuel and oxide ions flow through the external circuit to the cathode and can be utilize to produce electricity. According to the reactions above and the example shown in Figure 2.1, the fuel is hydrogen and the only by-product is water. SOFCs can however also utilize hydrocarbons such as methane or CO as the fuel, in which case CO_2 will form as an additional by-product. Using SOFC to convert hydrocarbons to electrical energy is more environmentally friendly than using a conventional combustion engine, since the SOFC is not limited by the Carnot cycle and therefore can reach a higher conversion efficiency [30].

The open circuit potential over a single SOFC unit like that illustrated in Figure 2.1 is approximately 1 V. However, by stacking several cells together in series, a more usable power output is easily achievable [30]. Interconnects are then used between the cathode and anode of adjacent cells to provide a current path and separate the anode and cathode gasses.

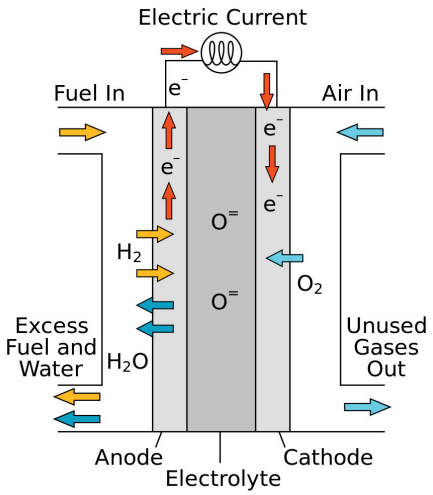

Figure 2.1: Illustration of solid oxide fuel cell components and basic operating principle. Figure from [31].

2.1.2 Electrolyte and electrode materials

Electrolytes

The main purpose of the electrolyte material is to transport oxide ions from the cathode to the anode, i.e. the electrolyte material should be a good ionic conductor. Other important requirements are chemical stability in the oxygen partial pressure gradient between the anode and cathode, minimal electronic conductivity at the cell operating temperature and good sinterability to enable a fully dense structure to be fabricated. The majority of research has focused on three main classes of materials, for which the ionic conductivities as a function of temperature are plotted in Figure 2.2. Yttria-stabilized zirconia (YSZ) was first discovered by Nernst [32] in 1899 and is still considered the most suitable electrolyte material at the current operating temperatures of SOFC ($> 650\,^{\circ}\mathrm{C}$). The addition of yttrium stabilizes the cubic fluorite structure of ZrO_2, which otherwise has a monoclinic $\rightarrow$ tetrahedral $\rightarrow$ cubic phase transition with increasing temperature [33]. Yttrium doping up to 8 mol.% also increases the ionic conductivity by introducing oxygen vacancies [34].

The perovskite $(La, Sr)(Mg, Ga)O_3$ (LSMG) and related compositions have higher ionic conductivites than YSZ and are potentially more compatible with a wider range of cathode materials [35]. The main drawbacks of LSMG are the high reactivity with the commonly used Ni-YSZ anode and the uncertain cost of Ga-

sources [30, 36]. Doped ceria based oxides such as $Ce_{1-x}Gd_xO_2$ are considered the most promising electrolyte materials for intermediate-temperature (< 600 °C) SOFC due to their high ionic conductivity at low temperatures [37]. At higher operating temperatures, these materials suffer from high electrical conductivities under reducing conditions [38].

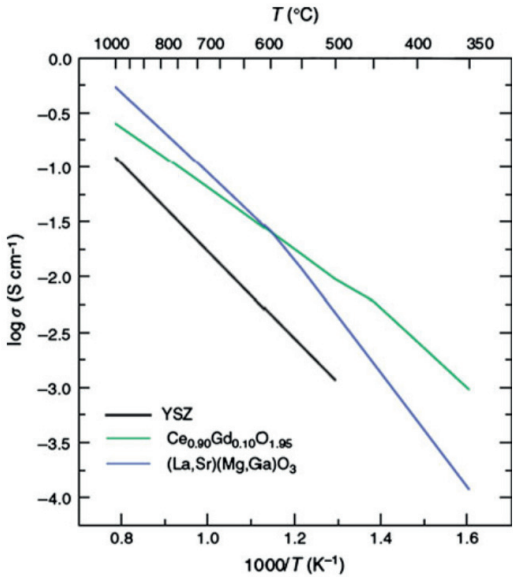

Figure 2.2: Ionic conductivity as a function of temperature in air for the three most common SOFC electrolyte materials. Figure from [30].

Anodes

The SOFC anode material should have catalytic activity towards electrochemical oxidation of the fuel, a high electrical conductivity and high stability in the reducing environment. In addition, if the electrode is to be used in a fuel cell running on hydrocarbon fuels, the anode should display catalytic activity towards the water shift and reforming reactions and a tolerance for sulfur as well. Nickel is a relatively cheap metal that has a very high catalytic activity towards the oxidation of H_2 [39]. However, nickel cannot be used on it own due to a high thermal expansion coefficient and problems with Ni-grain growth leading to microstructural coarsening [30]. The solution has been to make a porous ceramic–metal composite (cermet) of Ni and YSZ. The role of the YSZ, in addition to lowering the thermal expansion coefficient and hindering Ni-coarsening, is to extend the triple-phase boundary (TPB) area at which the anode reaction can take place, as illustrated in

2.3 [40]. The biggest drawbacks with Ni-YSZ electrodes are poor red-ox stability, low tolerance for sulfur and carbon deposition in carbon containing fuels [11, 41]. Several alternative anode materials have been suggested, for example $Cu-CeO_2$ composites [9] and $La_xSr_{1-x}TiO_3$ [42]. Nevertheless, Ni-YSZ remains the most commonly used anode material today.

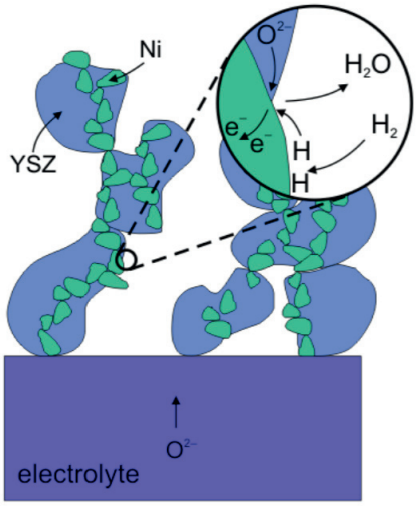

Figure 2.3: Illustration of oxidation reaction on the tripple phase boundary of a Ni-YSZ cermet anode. Figure from [43].

Cathodes

The cathode material in a SOFC should have high catalytic activity towards oxygen dissociation and reduction, high electrical conductivity and be chemically stable in the oxidizing environment. Most economically viable candidate materials belong to the perovskite family, with lanthanum strontium manganite (LSM) being the most popular choice to date. By doping $LaMnO_3$ with Sr, a thermal expansion coefficient closely matching YSZ and an appreciable electrical conductivity can be achieved [44]. The electrocatalytic activity of LSM is modest but may be significantly improved by infiltration or impregnation with catalytic nanoparticles [45]. Because LSM is nearly a pure electronic conductor, it is often mixed with YSZ in order to increase the TPB area at which the oxygen reduction reaction can take place [46, 47]. Cathode materials with mixed ionic and electronic conductivity would be preferable since the electrochemically active region then would be extended from the cathode-electrolyte interface to the whole cathode surface. A promising material in this respect is $(La, Sr)(Co, Fe)O_3$ (LSCF). A challenge with

LSCF it that it reacts with YSZ to form insulating $SrZrO_3$ [48], however, this can be prevented by using doped ceria as the electrolyte material or as a buffer layer between the cathode and YSZ electrolyte [49, 50].

A major challenge for all of the conventional cathode materials is sensitivity towards chromium poisoning [51–53]. Volatile Cr(VI) species released from the metallic interconnect (see section 2.2.1) have been found to deposit both specifically on the elctrochemically active TPB sites [54], and randomly along the cathode/electrolyte interface [55, 56]. Although the exact deposition and poisoning mechanisms are under debate, it is clear that the cell voltage degrades faster than usual in the presence of volatile Cr-species [15, 57]. There is however a large difference in how sensitive the different cathode materials are towards Cr poisoning and new cathode materials with reportedly higher Cr-tolerance are under development [53, 58]

2.1.3 SOFC design and stacks

The active components of the SOFC (anode, electrolyte and cathode) can be arranged in a variety of geometric configurations. The two most common designs, the tubular and planar, are illustrated in Figure 2.4. Tubular cells can be fabricated by extruding the first layer and subsequently depositing the others by e.g. electrochemical vapor deposition or atmospheric plasma spraying. This design has the advantage of not requiring high-temperature seals to isolate the air and fuel and tubular cells typically display excellent long term stability [30]. However, the power density is limited to about 0.2 $\mathrm{W/cm^2}$ and the manufacturing costs are high. The planar design requires on the other hand less complicated processing and can achieve higher power densities. In early designs planar cells were mechanically supported by a relatively thick (150 $\mu\mathrm{m}$) YSZ electrolyte, and needed to operate at high temperatures (> 900 °C) to achieve sufficiently high ionic transport through the electrolyte [30]. Advances in ceramic processing lead to the development of anode supported cells and a reduction of the electrolyte thickness to 10–20 $\mu\mathrm{m}$. This resulted in lower ohmic losses across the electrolyte and consequently allowed for the operating temperature with the LSM/YSZ/Ni-YSZ combination of materials to be reduced to around 800 °C [59]. The latest delevelopment in SOFC design is aiming towards even lower operating temperatures (~600 °C) with metal supported cells [60]. Metal supported cells are expected to decrease the price and increase the robustness of SOFC considerably, however, so far their performance and stability is far inferior to the anode supported design.

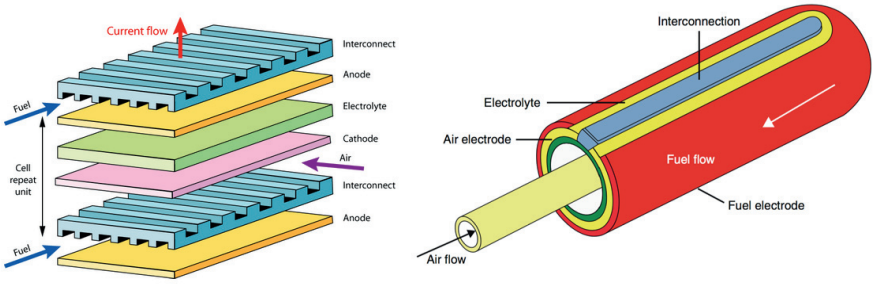

Figure 2.4: Illustration of a planar (left) and tubular (right) solid oxide fuel cell design. Figures from [61] and [30].

2.1.4 Interconnects

Requirements for the interconnect material

The main function of the interconnect is to ensure electrical contact between the cathode and anode of adjacent cells while physically separating the air on one side from the fuel gas on the other. For planar SOFC, the interconnect should preferably also provide some mechanical support to the otherwise thin ceramic components. The requirements for the choice of a suitable interconnect material are listed below [59, 62, 63]:

1. High electronic conductivity to transport the current between adjacent cells and to the outer circuit without significant losses.
2. Thermal expansion coefficient matching the other SOFC materials (typically $10\text{–}11 \cdot 10^{-6}\ \mathrm{K}^{-1}$).
3. Chemical stability in the oxidizing cathode and reducing anode environments and to the large oxygen partial pressure gradient between the cathode and anode side.
4. Chemical compatibility with the anode and cathode materials.
5. High density and low oxygen and hydrogen permeability to prevent the direct combination of fuel and air.
6. Sufficient thermal conductivity ($> 5\ \mathrm{W/m\,K}$) to allow the heat generated at the cathode to be conducted to the anode.
7. Cost effective in terms of raw materials and manufacturability, especially for planar SOFC where the interconnect is the bulkiest component.

Shift from ceramic to metallic interconnects

Very few ceramic oxides meet all the material requirements for SOFC interconnects listed above and until recently lanthanum chromite ($LaCrO_3$) was practically the only choice [59, 64]. This perovskite is commonly doped with Sr or Ca to improve its electrical conductivity and thermal expansion behavior. Doped lanthanum chromates can achieve reasonably high electronic conductivities (typically up to 50 $\mathrm{S/cm}$ at 800 °C in air), suitable thermal expansion coefficients (typically 10–11 $\cdot 10^{-6}$ K^{-1}) and are stable over a pO_2 range of 1–10 $\cdot 10^{-18}$ atm at 900 °C [59]. However, lanthanum chromates have the major disadvantage of being extremely difficult to sinter to full density [65]. This requires special care to be taken during processing, resulting in high costs.

With the development of anode supported cells that could operate at lower temperatures (see section 2.1.3), metallic interconnects came into consideration [66, 67]. Metallic interconnects offer several advantages compared to doped lanthanum chromites, such as lower costs, easier processing, and higher electrical and thermal conductivities. Kofstad and Bredesen [66] made an early comparison of possible metal and alloy candidates and suggested chromium based alloys and ferritic stainless steels (FSS) would be most suitable for the application. Silver was also mentioned as an option for operating temperatures below 800 °C, but this has not been pursued to any great extent [68]. Although alumina or silica forming alloys typically possess greater oxidation resistance than chromia formers, the low conductivity of Al_2O_3 and SiO_2 exclude the use of these alloys. Methods to work around this issue have however been suggested, for example using an Al_2O_3 forming alloy as the base and a Cr_2O_3 forming alloy at the electrical contact areas [69]. Nevertheless, FSS are today by far the most popular choice as the interconnect material for planar cells [63, 68].

FSS developed for application as interconnect

In 2003, a review of several FSS commercially available at the time was made by Quadakkers et al. [62], who concluded that the specific combination of properties required of a SOFC interconnect necessitated the development of new, more specialized alloys. After systematic investigations of several model steels [70], Crofer 22 APU was introduced to the market [71]. The composition of Crofer 22 APU and other alloys developed for the application as SOFC interconnect materials are given in Table 2.1.

Some common features of these alloys are: (i) a high content of Cr to ensure a sufficiently large "Cr-reservoir" for long-term stability; (ii) addition of Mn to promote the formation of an outer $MnCr_2O_4$ scale and thereby reduce Cr-volatility [72, 73] and (iii) addition of rare earth elements (e.g. La or Zr) for improved scale

adherence and oxidation resistance [74, 75]. Some of the alloys also have small additions of Ti, that form fine internal TiO_2 precipitates during oxidation, which are believed to aid in strengthening the near-surface region of the alloy [62, 76]. Two different strategies have been adopted by the manufacturers to prevent the formation of a continuous, electrically insulating SiO_2 layer. Crofer 22 APU and ZMG232 are fabricated by a vacuum induction melting process by which the Si content in the steel can be reduced down to a minimum. The costs of vacuum induction melting are however high. For this reason Crofer 22 H and Sanergy HT instead rely on additions of Nb and Mo or W to bind up the Si in the alloy by formation of Laves-phases. The formation of such Laves phases has the additional benefit of improving the creep and hot tensile strength of the alloy [77].

Table 2.1: Composition (in wt.%) of some ferritic stainless steels developed for the application as SOFC interconnects as specified by manufactures.

Alloy	Fe	Cr	Mn	Si	Al	La	C	Other
Crofer 22 APU [78]	bal.	20–24	0.3–0.8	<0.5	<0.5	0.04	<0.03	<0.2 Ti
ZMG232L [79]	bal.	21–23	1.0	<0.1	<0.5	0.03–0.1	<0.1	0.1–0.4 Zr
Sanergy HT [80]	bal.	22	<0.5	<0.3			<0.05	1.0 Mo; 0.75 Nb
Crofer 22 H [81]	bal.	20–24	0.8	0.1–0.6	<0.1	0.04–0.2	<0.03	0.2–1.0 Nb; 1.0–3.0 W; <0.2 Ti

2.2 High temperature oxidation

2.2.1 Oxidation theory

Unless otherwise noted, the theory in this section is taken from the textbook *High temperature corrosion* by Per Kofstad [82].

Thermodynamics

Most metals are thermodynamically unstable under ambient conditions and will react with gases present in the atmosphere [82, 83]. The general reaction between a metal, M, and oxygen can be expressed as:

$$\mathrm{aM(s)} + \mathrm{(b/2)O_2(g)} \rightarrow \mathrm{M_aO_b(s)} \tag{2.3}$$

Whether or not the oxide will form is determined by Gibbs energy (G) for the reaction, which at constant temperature and pressure is given by:

$$\Delta G = \Delta H - T\Delta S \tag{2.4}$$

where ΔH is the enthalpy change and ΔS is the entropy change of the reaction. When $\Delta \mathrm{G} < 0$ the reaction will be spontaneous. The change in Gibbs energy for

reaction (2.3) may be written as:

$$\Delta G = \Delta G^0 + RT \ln \left(\frac{a_{M_a O_b}}{a_M^a \times a_{O_2}^{(b/2)}} \right) \tag{2.5}$$

where ΔG^0 is the change in free energy when all species are in their standard state, R is the universal gas constant, T is the temperature and a represents the activity of each component. For pure solids the activity can be set equal to unity [1], while for gasses it can be expressed in terms of the partial pressure of the gas, *p*. This simplifies equation (2.5) to:

$$\Delta G = \Delta G^0 + \left(\frac{b}{2}\right) RT \ln(p_{O_2}) \tag{2.6}$$

When the system is at equilibrium ($\Delta G = 0$), equation (2.6) can be reduced and rearranged to:

$$p_{O_2(\Delta G=0)} = \exp(\Delta G^0 / bRT) \tag{2.7}$$

$\mathrm{p_{O_2(\Delta G=0)}}$ is known as the dissociation pressure of the oxide in equilibrium with the metal and is the minimum partial pressure of oxygen required thermodynamically for the metal be be oxidized.

The Ellingham-Richardson diagram, illustrated in Figure 2.5, provides a convenient way of summarising the standard Gibbs energy and dissociation pressure as a function of temperature. Assuming the entropy and enthalpy of oxide formation are independent of temperature in the range of ΔT considered results in a straight line for $\Delta \mathrm{G}^0$ as a function of temperature [82]. The oxides towards the bottom of the diagram have larger negative values of $\Delta \mathrm{G}^0$ and are therefore thermodynamically more stable. The minimum oxygen partial pressure necessary to oxidize the various metals at different temperatures can also be read out of the diagram. For example, oxidation of Cr to Cr_2O_3 at 800 °C requires a minimum oxygen partial pressure of approximately 10^{-20} atm. As seen from Figure 2.5, all oxides become thermodynamically less stable with increasing temperature.

[1] a = 1 is only valid for pure metals, while the activity of the metal in an alloy will be determined by the concentration

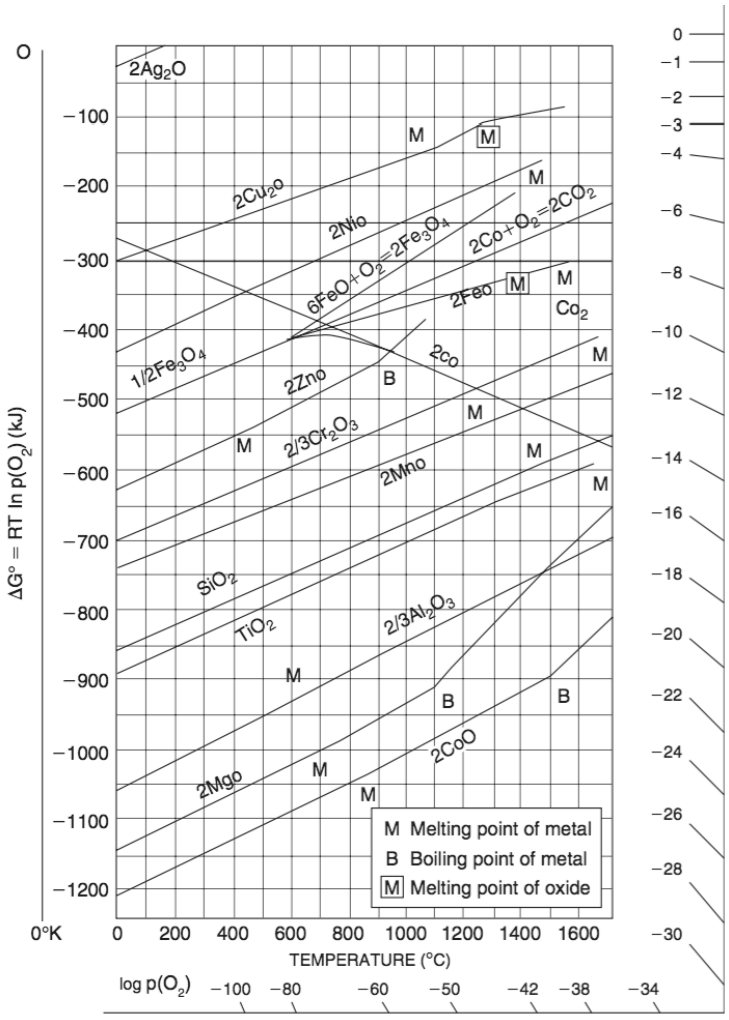

Figure 2.5: The Ellingham-Richardson diagram for a selection of oxides showing the standard Gibbs energy of oxide formation as a function of temperature. Figure from [84].

Kinetics

Although thermodynamics provide an explanation for the driving force for oxidation, they do not predict how fast different metals and alloys will be oxidized. To be able to predict component lifetimes, knowledge about the oxidation kinetics is important. The simple reaction presented in equation (2.3) consists in reality of several step, illustrated in Figure 2.6. The first two steps, oxygen adsorption and oxide nucleation and growth, are typically rapid at high temperatures. The longer term oxidation rate will depend on whether the formed oxide scale is dense and protective, or porous [83].

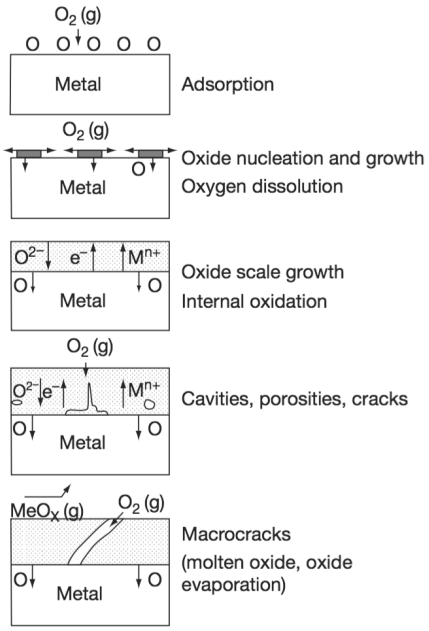

Figure 2.6: Schematic illustration of the various steps of oxide scale formation. Figure from [83].

In case of a porous, non-protective oxide scale, scale growth increases with time in a linear fashion and can be described by:

$$\frac{dx}{dt} = k_l \quad \rightarrow \quad x = k_l \cdot t + C \tag{2.8}$$

where x is the oxide scale thickness, t is the time, k_l is the linear oxidation rate constant and C is an integration constant. The oxidation rate in the linear regime is limited by chemical reactions at the gas-oxide or metal-oxide interface [83].

Parabolic scale growth is often observed when dense, protective oxide scales are formed, and can be described by:

$$\frac{dx}{dt} = \frac{k_p}{x} \quad \rightarrow \quad x^2 = 2k_p' t + C \tag{2.9}$$

where k_p is the parabolic rate constant. In the parabolic regime, rate is limited by solid state diffusion through the oxide scale and the rate decreases with time due to the continuously increasing oxide scale thickness creating a longer diffusion path for the migrating species. A perquisite for rate controlled by parabolic kinetics is that the metal surface already is covered by a continuous oxide scale, i.e. the very initial stages of metal or alloy oxidation cannot be parabolic [82].

The first theoretical treatment of parabolic oxidation kinetics was made by Carl Wagner in 1933 [85] on the basis of rate being controlled by lattice transport of ions or electrons across the oxide scale, illustrated in Figure 2.7. Wagner's model assumes that the oxide scale is dense, continuous and well-adherent, that reactions at the phase boundaries are rapid and that thermodynamic equilibrium is established both at the oxide-gas and oxide-metal interfaces, and locally within the oxide [82]. The flux of charged species across the scale will be driven by the gradient in chemical potential arising from the $\mathrm{p_{O_2}}$ difference between the oxide surface and the oxide-metal interface. For an oxide scale with higher electrical than ionic conductivity, it can be shown that the parabolic rate constant, $\mathrm{k_p'}$ $[\mathrm{cm^2/s}]$ is given by [82]:

$$k_p' = \tfrac{1}{2} \int_{p_{O_2}^0}^{p_{O_2}^i} \left(\tfrac{z_M}{|z_A|} D_M + D_O \right) \mathrm{d} \ln p_{O_2} \tag{2.10}$$

where $p_{O_2}^0$ and $p_{O_2}^i$ are the partial pressures of oxygen at the oxide surface and oxide-metal interface, z_M and z_A are the charges on the metal cation and oxide anion, and D_M and D_O are the self diffusion coefficients of the metal and oxide ions in $\mathrm{M_aO_b}$, respectively. Since lattice transport is strongly dependent on the defect structure, doping of the oxide scale may have a significant influence on the parabolic rate [86, 87]. Despite the many assumptions required in the derivation of Wagner's oxidation model, it has been found remarkably accurate in describing the scale growth kinetics of many metals and alloys, also under non-ideal conditions [82].

At constant partial pressure of oxygen the activation energy for oxidation can be determined from the Arrhenius equation [82]:

$$k = k_0 \exp(Q/RT) \tag{2.11}$$

where k is the rate constant, k_0 is a pre-exponential constant, Q is the activation energy and R is the gas constant. For parabolic oxidation kinetics the activation

energy may be related to the diffusion constant of the migrating species, in accordance with Wagner's theory [82]. For oxidation dominated by the other kinetic rate laws a physical interpretation of the activation energy is more difficult.

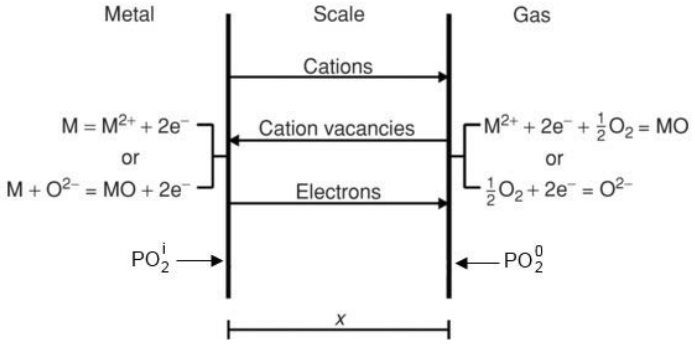

Figure 2.7: Simplified model for diffusion controlled oxidation kinetics according to Wagner's theory. Figure from [88].

The kinetics of high temperature oxidation can be determined experimentally by measuring the scale thickness as a function of time. However, for practical reasons it is more common to measure the mass change as a function of time. The parabolic oxidation rate in terms of oxide scale thickness, $k_{p,t}$ [cm^2/s], can be converted to the parabolic rate in terms of mass change, $k_{p,m}$ [$\mathrm{g}^2/\mathrm{cm}^4\,\mathrm{s}$], using the following equation [89]:

$$k_{p,m} = \left(\frac{M_{M_aO_b}}{b \cdot M_O \cdot \rho_{M_aO_b}}\right)^2 \cdot k_{p,t} \tag{2.12}$$

where $M_{M_aO_b}$ is the molar mass of the oxide, M_O is the molar mass of oxygen and $\rho_{M_aO_b}$ is the oxide density.

The growth of an oxide scale is usually quite complex, and other kinetics laws beside the two limiting cases already described can be encountered, e.g. oxidation following cubic $\left((\Delta m/A)^3 = k_c t\right)$ or logarithmic $((\Delta m/A) = A + B\ln t)$ kinetics. The rate determining mechanisms may also in certain cases change with time, for example due to depletion of one of the alloying elements. The least noble element will typically be oxidized first during the oxidation of an alloy. For example, in the case of stainless steels, an outer Cr_2O_3 scale is formed. If the Cr-supply to the surface is not sustained, less noble alloying elements will start to oxidize. This typically leads to an acceleration of the oxidation rate characterized as break-away [82]. In the case of stainless steels, break-away can be recognized as the formation of non-protective iron-rich oxides.

Cr-evaporation

The scale growth of some metals and alloys may be affected by volatilization of the scaling elements. This is particularly important during the oxidation of Cr and Cr-containing alloys. In dry oxygen or air the dominant volatilization reaction is [89]:

$$^1/_2\mathrm{Cr_2O_3(s)} + {}^3/_4\mathrm{O_2(g)} = \mathrm{CrO_3(g)} \tag{2.13}$$

In the presence of water vapor the dominant reaction becomes [90, 91]:

$$^1/_2\mathrm{Cr_2O_3(s)} + \mathrm{H_2O(g)} + {}^3/_4\mathrm{O_2(g)} = \mathrm{CrO_2(OH)_2(g)} \tag{2.14}$$

Very low amounts of water vapor are required in air below 1000 °C before $CrO_2(OH)_2$ (g) becomes by far the most dominant species and reaction (2.14) is the most relevant under conditions experienced by the SOFC interconnect [14].

The scale thickness with time will be determined by a combination of the parabolic rate constant for scale growth, k_p, and the linear rate constant for reactive evaporation of Cr, k_s [92]:

$$\frac{dx}{dt} = \frac{k_p}{2x} - k_s \tag{2.15}$$

During initial stages of exposure, the increase in scale thickness will be faster than the vaporization process, and close to parabolic oxidation behavior will be observed. However, as the growth rate drops with increasing scale thickness, vaporization will become increasingly important. After a certain period of time, the two processes will become balanced by each other, resulting in a constant oxide scale thickness. This so called limiting oxide scale thickness, x_l, is given by [92]:

$$x_l = \frac{k_p}{2k_s} \tag{2.16}$$

The rate of Cr-volatilization has been found to increase with increasing gas flow rate, oxygen partial pressure and water vapor content in the gas [93, 94].

2.2.2 Oxidation of interconnect alloys

The corrosion resistance of ferritic stainless steels (FSS) relies on the selective oxidation of Cr to form an outer Cr_2O_3 scale. Before reviewing the literature on oxidation of FSS, the oxidation of pure Cr will be briefly considered.

When pure Cr is oxidized in near-atmospheric oxygen partial pressure above 700 °C, a Cr_2O_3 scale usually grows in accordance with parabolic oxidation kinetics. However, depending on sample preparation and surface finish, the parabolic rate constant reported in literature varies by more than four orders of magnitude [95–97].

Historically, there has been great disagreement about the rate controlling transport mechanism. Outward volume diffusion of Cr through the Cr_2O_3 scale has been suggested by several authors [95, 98], while others have argued that oxide ion inward transport must contribute significantly to the oxidation process [99–101]. The lattice diffusion coefficients of both Cr and O are however very small [102, 103], and it has been increasingly acknowledged that fast diffusion paths such as grain boundaries, pores and micro-cracks likely dominate the growth rate of Cr_2O_3 on pure Cr [103, 104].

The formation of a single phase chromia scale on FSS requires a chromium content of 16–20 %, depending on exposure conditions, surface treatment and the presence of other alloying elements and impurities [105]. FSS intended for application as SOFC interconnect materials are in most cases reported to obey parabolic oxidation kinetics with $\mathrm{k_p}$ in the range of 10^{-14}-10^{-13} $\mathrm{g^2/cm^4\,s}$ when oxidized in air at 800 °C [106–109]. The chromia scale is believed to grow mainly by outward diffusion of chromium [101]. Minor alloying elements may have a significant influence on the oxidation rate. Huczkowski et al. reported that Si and Al in the alloy are internally oxidized and that the volume increase accompanying this internal oxidation leads to metal protrusion into the oxide scale, which increases the oxidation rate [12]. The addition of small quantities of rare earth reactive elements such as Y, La and Nd is on the other hand reported to have a beneficial effect on the oxidation resistance of Cr_2O_3 forming alloys, both in terms of reducing the growth rate of Cr_2O_3 and improving the scale adhesion [74, 75]. The exact mechanism behind the so-called reactive element effect has not been established, although several suggestions have been put forth [110–112].

The oxidation rate of some FSS has been reported to increase with decreasing specimen thickness [113–115]. The effect is mostly pronounced > 850 °C, but could also be of practical significance at 800 °C during long term operation. Huczkowski et al. suggested that the higher oxidation rate of thinner components is due to faster depletion of minor alloying elements and micro-cracking of the scale occurring during thermal cycling [114]. It was later proposed that although these factors may contribute, the effect is primarily a result of compressive growth stresses leading to plastic deformation of the thin specimens [113]. Accordingly, the oxidation rate of Laves-phase strengthened Crofer 22 H shows a markedly reduced dependence on thickness compared to Crofer 22 APU [105].

When Cr-evaporation contributes significantly to the mass change during oxidation, the oxidation kinetics of FSS can shift from parabolic to para-linear [116]. At 800 °C the typical Cr-evaporation rate reported for FSS is in the range of 2–$8 \cdot 10^{-10}$ $\mathrm{kg/m^2\,s}$ [72]. A correlation has been found between the Cr-evaporation rate and Mn content in the alloys: alloys with higher contents of Mn usually

have lower evaporation rates due to the formation of an outer $MnCr_2O_4$ spinel layer [72, 73, 117]. The activation energy for Cr-evaporation is lower than the typical activation energy for oxidation of FSS, meaning that the relative importance of Cr-evaporation becomes greater at lower operating temperatures [118].

Oxidation in the anode atmosphere and under dual atmosphere

The thermodynamic driving force for oxidation in the anode atmosphere is generally lower than in air, due to the lower oxygen partial pressure. However, as seen in Figure 2.5, the minimum p_{O_2} to oxidize Cr to Cr_2O_3 at 800 °C is only 10^{-20} atm, thus most FSS are observed to form an outer Cr_2O_3 scale also in the anodic atmopshere [119]. The reports on whether the oxidation rates in anodic atmopsheres are lower [107, 120], higher [121] or the same [108, 122] as in air are conflicting. Niewolak et al. [123] suggested that the disagreement in literature could be related to different Mn contents in the steels. They reported a lower long term oxidation rate in simulated anode atmosphere than in air when the Mn content was sufficient to form a continuous Cr-Mn spinel layer on the surface. The potentially greatest threat for the stability of metallic interconnects on the anode side is the observed diffusion of Ni from the anode into the FSS leading to austenite formation [124]. In addition to having different mechanical and diffusion properties, the austenite phase has a higher thermal expansion coefficient than ferrite, which can be detrimental for long-term mechanical stability during thermal cycling.

Most oxidation characterizations of metallic interconnects are performed either in air or reducing atmospheres, separately investigating the behavior in the cathode and anode environments, respectively. A number of investigations have shown that dual atmospheric conditions, i.e. simultaneous exposure to the two atmospheres on each side of the alloy, can significantly affect the oxidation behavior on the air side [125–129]. The oxide scale formed under dual atmosphere conditions is reported to contain more Fe than the scale formed when oxidized in air only, and Fe-rich nodules or hematite are typically observed in the top layers of the scale. The so-called dual atmosphere effect is believed to be caused by hydrogen diffusion through the steel, although there is no agreement about the exact mechanisms for how permeated hydrogen affects air side oxidation behavior [127, 128, 130, 131]. There is also some disagreement in literature about the severity of this effect. For the same alloy which Yang et al. [126] found a considerable difference in the oxidation behavior in dual atmosphere compared to single atmosphere, Rufner et al. [132] reported only moderate effects, while Kurokawa et al. [133] observed no effect at all. Differences in alloy specimen thickness in the three experiments has been suggested as a possible explanation for the discrepancy [134]. Local formation of Fe-rich oxides on the air side has also been observed on a metallic

interconnect after two years operation in a full SOFC stack at 700 °C, however, the observation in this case was attributed to inhomogeneities in the alloy rather than the dual atmospheric conditions [135].

Lifetime of metallic interconnects

There are at least two ways in which the lifetime of a metallic interconnect may be defined:

1. The time before the oxide scale thickness reaches a critical thickness at which spallation takes place. Due to the slight thermal expansion mismatch between FSS and the thermally grown chromia scale, the risk of spallation is highest during thermal cycling [136]. Liu et al. [21] estimated that the critical oxide scale thickness for Crofer 22 APU is 11.4 µm, predicting a lifetime of approximately 4750 h at 800 °C. This approach for predicting the lifetime has however a high degree of uncertainty since the oxide scale formed on FSS usually is non-uniform across the surface [121]

2. The time to deplete the alloy of Cr below the level at which break-away oxidation takes place. This can be calculated from the oxidation rate and initial and critical content of Cr in the alloy, as will be shown below.

Quadakkers et al. [137] derived an expression for the time to break-away for alumina forming steel, which Huczkowski et al. [114] later showed was applicable for chromia forming alloys as well. Cr diffusion in the steel bulk is assumed to be much faster than the oxidation rate, i.e. the Cr-depletion profile beneath the oxide scale is flat. This is in most cases found to be valid for ferritic stainless steels oxidized at 800–900 °C [105, 114]. For a thin plate of infinite width and length, the amount of Cr locked up in the oxide scale can be found by converting the measured mass gain due to oxygen uptake to equivalent amount of Cr in Cr_2O_3 from:

$$\Delta m(Cr)[g] = \frac{2M_{Cr}}{3M_O} \cdot (k_p \cdot t)^{\left(\frac{1}{2}\right)} \cdot A \tag{2.17}$$

where M_{Cr} and M_O are the molar mass for Cr and O, respectively, k_p is the parabolic rate constant, t is the time, and A is the sample area. The amount of Cr depleted from the alloy is given by:

$$\Delta m(Cr)[g] = \frac{C_0 - C_t}{100} \cdot \rho_{alloy} \cdot \tfrac{1}{2} \cdot A \cdot d \tag{2.18}$$

where C_0 and C_t are the initial and critical concentrations of Cr in the alloy, ρ_{alloy} is the alloy density and d is the component thickness. A simple mass balance then results in an equation giving the time before break-away:

$$t_B = \left[(C_0 - C_B) \cdot \rho_{alloy} \cdot d \cdot 2.3 \cdot 10^{-3}\right]^2 \cdot \tfrac{1}{k_p} \tag{2.19}$$

For Crofer 22 APU oxidized in air the critical Cr-content before break-away has been reported to be 16 wt.% [114]. Huczkowski et al. [114] estimated that to avoid break-away over a service lifetime of 40 000 h, a metallic interconnect made of Crofer 22 APU needs to be > 0.25 mm thick for an operating temperature of 800 °C and > 1 mm thick for an operating temperature of 900 °C. Break-away oxidation can however occur on the corners and edges of the specimen long before the bulk concentration of the protective scale element has reached the critical value [115, 116, 138]. This has been explained on the basis of the higher surface-to-volume ratio of the surface and edges leading to faster depletion of Cr and is aggravated by high rates of Cr-evaporation.

Electrical resistance of oxide scales

Given that one of the main purposes of the interconnect material is to provide electrical contact between the anode and cathode of adjacent cells, the electrical conductivity of the interconnect is of great importance. This is usually characterized in terms of contact or area specific resistance (ASR), which can be expressed as [13]:

$$ASR = \tau_s l_s + 2\tau_o l_o \tag{2.20}$$

where τ_s and l_s are the resistivity and thickness of the steel substrate, respectively, and τ_o and l_o are the resistivity and thickness of the oxide layer on each side of the substrate, respectively. The generally accepted ASR limit for the interconnect during its service lifetime is 100 $\mathrm{m\Omega\,cm^2}$ [13]. The electrical resistivity of steel is several orders of magnitude smaller than the resistivity of the oxide scale, such that the first term in equation (2.20) may be omitted. Since the ASR of a metallic interconnect primarily will be determined by the thickness and resistivity of the oxide scale, it should ideally show the same time dependence as the growth rate of the oxide scale. In practice however, this is rarely the case, for reasons explained in the following.

The oxide scale formed on most interconnect alloys consists of Cr_2O_3 and possibly $(Mn, Cr)_3O_4$. The electrical conductivity of $(Mn, Cr)_3O_4$ is generally slightly higher than that of Cr_2O_3 and will be treated in greater detail in section 2.4.2. The electrical conductivity of Cr_2O_3 can be divided into two temperature regimes:

1. At high temperatures (>1000 °C), Cr_2O_3 displays n-type intrinsic conductivity, independent of the oxygen partial pressure [139].

2. At lower temperatures (< 1000 °C), pure Cr_2O_3 is a p-type extrinsic conductor showing some dependence on the oxygen partial pressure [140]. The electrical conductivity at 800 °C is typically reported to be in the range of 1–$8 \cdot 10^{-2}$ $\mathrm{S/cm}$ [140–142], however the value can vary even more with the pres-

ence of unintentional impurities or intentional dopants. For example, doping Cr_2O_3 with Y_2O_3 or La_2O_3 has been found to increase the electrical conductivity [142]. One reason for the complex ASR behavior is thus a change in impurity level and defect chemistry of the thermally grown chromia scale. Another factor, as pointed out by Linder et al. [143], it that the typical morphology of a thermally grown chromia scale favors a non-homogeneous current distribution, in which large parts of the current flow across thinner regions of the scale. There have also been some reports that the current applied during ASR measurements influences the growth rate of the chromia scale [144, 145].

An illustration of the general four-point experimental set-up for measuring ASR is shown in Figure 2.8. The contact material can be either a nobel metal like gold, silver or platinum or a ceramic oxide like LSM ($La_{1-x}Sr_xMnO_3$) or LSC ($La_{1-x}Sr_xCoO_3$). The measured ASR will depend on the choice of contact material, with noble metals typically resulting in lower values and different development over time than the ceramic oxides [146–148]. The oxides used for contacting are similar to the cathode materials used in SOFC and should therefore give a better estimation of the contact resistance in a real fuel cell stack. The disadvantage with these materials is however their tendency to sinter and react with the oxide scale on the interconnect. This results in an initially decreasing ASR that may mask the resistance increase due to growth of the chromia scale [149]. Noble metals should on the other hand in theory not react with the alloy or oxide scale and therefore provide a theoretical estimation of solely the interconnect's contribution to ASR. In practice, it has been shown that prolonged contact with Pt can lead to accelerated oxidation [150]. In summary, noble metals could be a suitable choice for short-term measurements and for comparison of different alloys and coatings, while ceramic oxides can provide valuable information about how the contact resistance will develop in an actual SOFC stack during long-term operation. Due to the different ASR values obtained with different contacting materials, it is challenging to compare the ASR reported by different sources directly against each other.

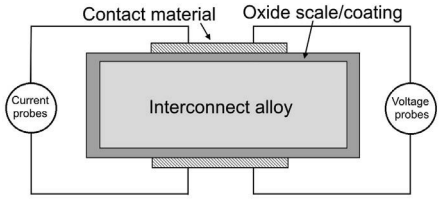

Figure 2.8: Illustration of the general four-point set-up for measuring area specific resistance of interconnect materials.

2.3 Protective coatings for metallic interconnects

The challenges of high Cr-evaporation and oxidation rates make it unrealistic to use bare FSS as the interconnect material in SOFC, despite the advancements made in developing new alloys specifically targeted towards this application [72, 114]. For example, stack tests at Research Center Juelich with one of the most promising new alloys, Crofer 22 APU, as the interconnect showed voltage degradation of 21%/1000 h, which was mainly attributed to Cr-poisoning of the LSM cathode [151]. Today it is generally acknowledged that the metallic interconnect will need to be coated in order to survive the expected service lifetime of 40 000 h [63, 152]. The requirements for a suitable interconnect coating material are much the same as for the interconnect itself in terms of thermal expansion, electrical conductivity, cost and ease of manufacturing. In addition, since the purpose of the coating is to improve oxidation resistance and reduce Cr-evaporation from the FSS, the coating material should possess low chromium and oxide ion diffusion coefficients. The majority of suggested coating materials can be divided into three categories, and will be briefly reviewed in the following.

2.3.1 Reactive elements

As already mentioned in section 2.2.2, the addition of reactive elements (RE) such as La, Ce and Y to ferritic stainless steels may improve scale adhesion and oxidation resistance. RE are usually added as an alloying element to the steel, however, they have also been explored as surface coatings with several reports of reduced oxidation rates and ASR [74, 75, 109, 153]. Nevertheless, the long-term benefits appear to be limited: Fontana et al. [154] measured the ASR of La_2O_3 and Y_2O_3 coated Crofer 22 APU and found that after 23 000 h of oxidation at 800 °C both coatings had exceeded the 100 $\mathrm{m\Omega\,cm^2}$ maximum set as a limit for the interconnect. An even greater shortcoming of RE coatings is that they have negligible effect on the Cr-evaporation rate [155, 156].

2.3.2 Perovskites

Lanthanum based perovskite oxides are used as cathodes in SOFC (see section 2.1.2) and were early on identified as possible protective coatings for metallic interconnects [157]. The most widely investigated compositions are accordingly similar to common cathode materials, for example $La_{1-x}Sr_xMnO_3$ (LSM) [17], $La_{1-x}Sr_xCoO_3$ (LSC) [108] and $La_{1-x}Sr_xFeO_3$ (LSF) [158]. These perovskites

offer the benefits of having high electrical conductivities, suitable TEC coefficients and good compatability with other SOFC components. Several studies have demonstrated that perovskite coatings can reduce the Cr-evaporation rate of stainless steel by several orders of magnitude [17, 159] and decrease the FSS oxidation rate [160]. There are however also examples of studies reporting none or only modest benefits on Cr-retention [151, 161] and corrosion resistance [158]. The discrepancies can be explained by differences in powder properties and deposition methods in the mentioned references leading to differences in coating density. Difficulties with processing the pervoskite coatings, particularly with obtaining dense structures at sufficiently low temperatures, is considered one of their major drawbacks [152].

2.3.3 Spinel oxides

$(Mn, Co)_3O_4$ spinel oxide was first proposed as a possible coating material by Larring and Norby [18]. Most of the work has been done on $MnCo_2O_4$ [162–165] and $Mn_{1.5}Co_{1.5}O_4$ [16, 20, 166, 167], although Cu-Mn [168, 169], Cu-Fe [170, 171] and pure Co [172, 173] spinels have also received some attention[2]. The physical properties of these materials will be reviewed in section 2.4.

Contrary to perovskites, spinel coatings may be sintered to sufficient density at temperatures that do not damage the alloy substrate significantly, thus they may be deposited by relatively cheap powder-based methods such as spray coating [16, 174], screen printing [175] and electrophoretic deposition (EPD) [176, 177]. Densification of the coatings is usually realized by a two-step procedure involving heat treatment first in reducing and then in oxidizing atmospheres. During the first step $MnCo_2O_4$ is reduced according to [178]:

$$\mathrm{MnCo_2O_4} \rightarrow \mathrm{MnO} + 2\mathrm{Co} + \tfrac{3}{2}\mathrm{O_2} \tag{2.21}$$

When the coating subsequently is heat treated in air, the spinel phase is reformed and densification is believed to be promoted by a reaction-sintering type mechanism [179, 180].

$(Mn, Co)_3O_4$ coatings have been demonstrated to be very effective in limiting Cr-evaporation from FSS [17, 181]. Several studies have shown that $(Mn, Co)_3O_4$ coatings also have a positive effect on the oxidation resistance and ASR [16,19,20].

[2]Note that several of these coating materials are deposited as a metallic layer, e.g. as Co metal. During exposure to air at elevated temperatures, these metals are quickly oxidized to spinel-type oxides. The listed coatings may thus be regarded as a form of spinel oxide coatings.

There has however been some concern about the long-term stability of these coatings. The lifetime of $Mn_{1.5}Co_{1.5}O_4$ coated Crofer 22 APU was investigated by Liu et al. [21] and Akanda et al. [22] based on mechanical modeling and experimental measurements of the interfacial shear stress vs. strength, and the interfacial fracture energy, respectively. The lifetime was estimated based on the time before spallation with 4.2 μm determined to be the critical Cr_2O_3 scale thickness in both studies. Liu et al. [21] predicted a lifetime of 15 500 h at 800 °C, while Akanda et al. [22] predicted a lifetime of 34 700 h at 750 °C.

2.4 Structure and properties of $(Mn,Co,M)_3O_4$ (M=Fe, Cu, Cr) spinels

The spinel structure is named after the mineral spinel, $MgAl_2O_4$ and is adopted by a wide range of different oxides and calcogenides [182]. The widespread occurrence of the structure can be attributed to its flexibility of accommodating cations of varying size and valency. This opens up the possibility for several interesting physical properties in spinel oxides, such as magnetism, superconductivity and transparency in connection with electrical conductivity [183–185]. In the following, a brief review will be given on the $(Mn,Co,M)_3O_4$ (M=Fe, Cu, Cr) group of spinels and some of their properties that are relevant for SOFC interconnects.

2.4.1 The spinel structure

The spinel structure can be described as a nearly cubic close packed arrangement of 32 anions. In this arrangement there are 64 tetrahedral cation sites, of which 8 are occupied, and 32 octahedral cation sites, of which 16 are occupied. A single unit cell, consisting of 8 AB_2O_4 formula units, is illustrated in Figure 2.9. Most spinel compounds belong to the $Fd\bar{3}m$ space group (no. 227), but the symmetry is sometimes lowered due to Jahn-Teller effects [186]. This is typically the case when $Mn^{3+}(d^4)$ or $Cu^{2+}(d^9)$ are present at the B-sites or when $Ti^{3+}(d^1)$ or $Fe^{2+}(d^6)$ are present at the A-sites [187]. However, a minimum fraction of so-called Jahn-Teller active cations is required to cause a cooperative bulk distortion of the structure.

The exact position of anions in the spinel structure is determined by the relative size of cations in the octahedral and tetrahedral sites and can be calculated from [189]:

$$u = \frac{R^2/4 - 2/3 + (11R^2/48 - 1/18)^{1/2}}{2R^2 - 2} \tag{2.22}$$

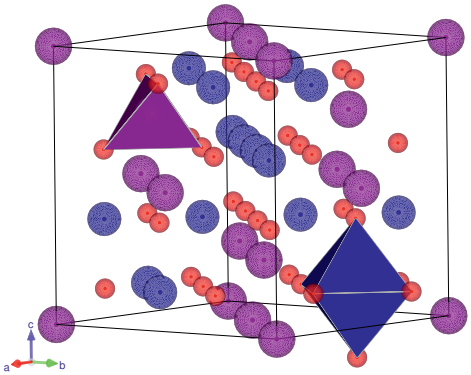

Figure 2.9: Unit cell of the spinel structure with origin at point symmetry $\bar{4}3m$. Illustration made using VESTA [188].

where u is the anion or oxygen parameter and R is the ratio of the octahedral to tetrahedral cation-anion bond lengths. The cation to anion bond lengths are given by:

$$R_{tet} = a\sqrt{3(u - 1/8)} \tag{2.23}$$

$$R_{oct} = a(3u^2 - 2u + 3/8)^{1/2} \tag{2.24}$$

In an ideal cubic packing, $u = 0.375$ and the octahedral bond is 1.155 times longer than the tetrahedral bond [3]. Ideal cubic packing is however rarely achieved and most spinels fall within the range of $0.375 < u < 0.500$ [189], which involves an expansion of the tetrahedron and a compression of the octahedron.

The phase diagram for the Mn_3O_4-Co_3O_4 system, with the $MnCo_2O_4$ composition highlighted, is shown in Figure 2.10. Although not explicitly shown in this diagram, $MnCo_2O_4$ has been confirmed to be a single phase cubic spinel down to room temperature [190]. For $x \geq 1.3$, $Mn_xCo_{3-x}O_4$ is a two-phase mixture of the cubic ($Fd\bar{3}m$) $MnCo_2O_4$ and tetragonal ($I4_1/amd$) Mn_2CoO_4 spinel-type phases, due to the large number of Jahn-Teller active Mn^{3+} ions on the octahedral sites [190,191]. The minimum fraction of Mn^{3+} to cause a cooperative Jahn-Teller effect increases with increasing temperature and accordingly, the $Mn_{1.5}Co_{1.5}O_4$

[3] $u = 0.375$ is expressed in terms of $\bar{4}3m$ point symmetry. The spinel structure is sometimes described using the $\bar{3}m$ point symmetry, for which the ideal $u = 0.25$.

composition is observed to transform from the two phase mixture to a single phase cubic spinel at approximately 400 °C [192].

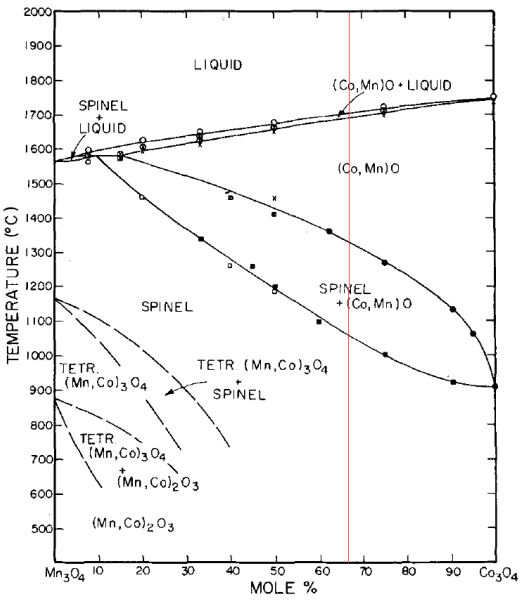

Figure 2.10: Phase diagram for the Mn_3O_4-Co_3O_4 system as reported by [193]. The $MnCo_2O_4$ composition is marked with a red line.

Cation distribution

The general cation distribution in the spinel structure can be written as $(A_{1-x}B_x)[A_{x/2}B_{1-(x/2)}]_2X_4$, where square brackets [] designate cations in octahedral positions, round brackets () designate cations in tetrahedral positions and x is the degree of inversion. When x=0 the structure is said to be normal, while when x=1 the structure is said to be inverse [194]. All intermediate distributions are in principle also possible.

Over the last 70 years, several theoretical models for predicting the cation distribution in spinels have been suggested [186, 195–200]. When transition metal cations are involved, the principles of crystal field stabilization energy (CFSE) have proved particularly useful [197–199]. The d-orbitals of a transition metal cation surrounded by anions will be split into degenerate energy levels separated by an energy difference Δ. The CFSE is the relative energy difference of the electron configurations in the ligand and isotropic fields and is given by $\Delta_{\mathrm{oct}}(4\mathrm{m} - 6\mathrm{n})/10$ in the case of an octahedral lignad field and $\Delta_{\mathrm{tetr}}(6\mathrm{p} - 4\mathrm{q})/10$ in the case of a tetrahed-

ral ligand field. The Octahedral Site Preference Energy (OSPE) is defined as the CFSE difference between the octahedral and tetrahedral configurations. Cations with the highest OSPE are predicted to have the strongest preference for the octahedral position in the spinel structure. An overview of empirical and theoretical site preference energies for selected divalent and trivalent cations arranged in order of increasing OSPE are shown in Figure 2.11. According to a recent review, the concept of CFSE succesfully predicts the cation distribution in approximately 50 % of transition metal spinels [182]. With the increased accessibility of cheap computer power, most theoretical predictions of spinel cation distributions today make use of first-principle and Density Functional Theory (DFT) calculations [200,201]. However, although such calculations have a higher success rate, they require significant knowledge of various material parameters, limiting the applicability.

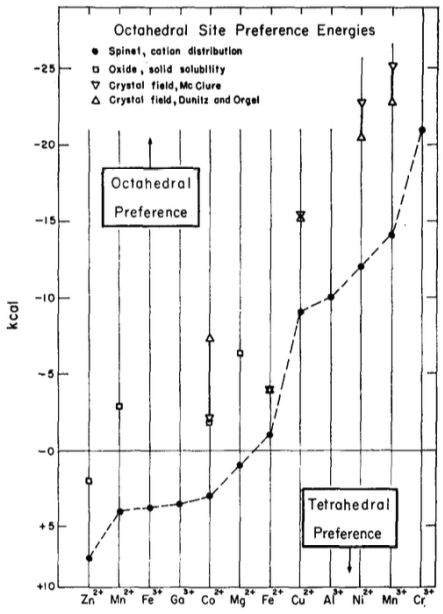

Figure 2.11: Empirical site preference energies for selected ions in the spinel structrue reported by [202].

Some of the suggested cation distributions for $MnCo_2O_4$ are listed in Table 2.2. Most of these agree that tetrahedral sites primarily are occupied by Co^{2+}, while there is more disagreement about the valences of cations on the octahedral sites. It should be pointed out that X-ray diffraction results cannot be considered trustworthy due to the similar scattering factors of manganese and cobalt. However, as seen in Table 2.2, results from neutron diffraction are not consistent either. It has

been known for a while that the cation distribution in spinels can vary with temperature and pressure of preparation [203,204]. Thus, the different cation distributions could be due to differences in thermal history of the investigated samples.

Table 2.2: Suggested room temperature cation distributions in the $MnCo_2O_4$ spinel. Co^{III}designates the low spin state.

Cation distribution	Characterization method	Ref.
$(Co^{2+})[Co^{3+}Mn^{3+}]O_4^{2-}$	XRD, magnetism	[205]
$(Mn^{2+}_{0.04}Co^{2+}_{0.96})[Co^{2+}_{0.04}Co^{3+}Mn^{3+}_{0.96}]O_4^{2-}$	XRD, TG, conductivity	[206]
$(Co^{2+})[Co^{3+}Mn^{3+}]O_4^{2-}$	Neutron diffraction, magnetism	[207]
$(Mn_{0.25}Co_{0.75})[Mn_{0.75}Co_{1.25}]$	Neutron diffraction	[204]
$(Co^{2+})[Co^{III}Mn^{3+}_{0.45}Mn^{4+}_{0.55}]O_4^{2-}$	XRD, magnetism, conductivity	[208]
$(Co^{2+}_{0.97}Mn^{2+}_{0.04})[Co^{2+}_{0.4}Co^{III}{}_{0.6}Mn^{3+}_{0.6}Mn^{4+}_{0.4}]O_4^{2-}$	Neutron diffraction	[209]

For $(Mn, Co)_3O_4$ spinels containing chromium it is generally agreeed that monovalent Cr^{3+} ions selectively occupy the octahedral positions [210–212], which is in accordance with the CFSE theory predicting Cr^{3+} to have the strongest octahedral site preference among the transition metal cations (see Figure 2.11).

Defect chemistry

Study of defect chemistry in spinels is complicated by the presence of two cation sub-lattices and, when transition metal cations are involved, the possibility of several stable valence states. The concentration of oxygen vacancies in spinel oxides is generally believed to be low ($<10^{16}$ cm^{-3}) due to a large defect formation energy [213, 214]. There have however been several reports of $MnCo_2O_4$ displaying oxygen excess, or rather cation deficiency, when prepared by low-temperature wet-chemical methods or in the form of a thin film [215–218]. Nevertheless, the defect related properties of spinels are believed to be primarily dominated by self-doping or so-called anti-site defects [214, 219] such as intersite exchange between octahedral and tetrahedral positions [220]:

$$M^{2+}_{tet} + M^{3+}_{oct} = M^{2+}_{oct} + M^{3+}_{tet} \tag{2.25}$$

$$M1^{2+}_{tet} + M2^{3+}_{oct} = M1^{2+}_{oct} + M2^{3+}_{tet} \tag{2.26}$$

where tet and oct refer to tetrahedral and octahedral positions, respectively and M1 and M2 are different cations. The thermodynamics of equations (2.25) and (2.26) have been reviewed by O'Neill and Navrotsky for a number of transition metal

spinel oxides [220–222]. The intersite Fe^{2+}/Fe^{3+} exchange was found to be particularly favorable, which explains the interesting magnetic and electrical temperature dependence displayed by Fe_3O_4. The Co^{2+}/Co^{3+} and Mn^{2+}/Mn^{3+} exchanges were on the other hand regarded as unfavorable due to the strong octahedral site preference of Co^{3+} and Mn^{3+}. The dominating defect equation for compounds containing these ions was instead proposed to involve disproportionation on the octahedral sites [220]:

$$2M_{oct}^{3+} = M_{oct}^{2+} + M_{oct}^{4+} \tag{2.27}$$

2.4.2 Electrical conductivity

The $(Mn,Co,M)_3O_4$ (M=Fe, Cu, Cr) group of spinel oxides are all semiconductors for which the electrical conductivity has been found to follow the small polaron hopping model [187]. A polaron is the quantification of the lattice polarization arising from strong interactions between charge carriers (electrons or holes) and the ionic lattice. The charge carriers can be imagined as trapped in potential wells around certain lattice sites. In order for them to move from one such potential well to another a sufficient amount of energy is required. This implies that charge transfer in the small polaron hopping model is a thermally activated process, i.e. the charge carrier mobility increases with increasing temperature [223, 224]. The electrical conductivity due to small polaron hopping is given by [225]:

$$\sigma = ne\mu = \frac{ne^2a^2}{k_BT\tau_0}exp\left(\frac{-E_a}{k_BT}\right) \tag{2.28}$$

where n is the charge carrier density, e is the electronic charge, μ is the charge carrier mobility, a is the jump distance, k_B is Boltzmann's constant, T is the absolute temperature, τ_0 is the hopping attempt frequency and E_a is the activation energy for hopping. In oxides with the spinel structure charge hopping is believed to be primarily between octahedral sites due to the shorter cation-cation distance [183]. Hopping can only take place between equivalent sites, which means that electrical conductivity will be higher in spinels where the octahedral sites are occupied by cations of mixed valency [187]. The electrical conductivity of $MnCo_2O_4$ has typically been ascribed to hopping between Mn^{3+}/Mn^{4+} pairs on the octahedral sites, although some recent studies have argued that the $Co^{2+}/Co^{III/3+}$ octahedral site pairs must contribute as well [212,226]. Most spinel oxides are p-type conductors, meaning that the charge carriers are electron holes [227].

The reported electrical conductivity of several $(Mn,Co,M)_3O_4$ (M=Fe,Cu,Cr) spinels is summarized in Table 2.3. There is considerable scatter in the reported values for

$(Mn,Co)_3O_4$. Given the strong link between the electrical conductivity and cation distribution in these materials, part of the discrepancy is possibly due to differences in thermal history between the different samples (see section 2.4.1). The phase purity of the some of the investigated samples is however also questionable, seeing as a majority of them have been sintered at temperatures above the spinel stability limit of ca. 1050 °C (according to the phase diagram in Figure 2.10). This has previously been pointed out by Liu et al. [228] who showed that the electrical conductivity of $MnCo_2O_4$ sintered at 1200 °C could be increased from 51 to 87 S/cm by annealing the same sample at 1000 °C. The lower electrical conductivity value was attributed to the presence of MnO and CoO secondary phases, that were completely dissolved back into the spinel with annealing [228]. Despite the scatter in reported values, there is a clear trend of decreasing electrical conductivity with increasing amount of Cr in the material. The only possible oxidation state for chromium in the spinel structure is Cr^{3+}, which as seen in Figure 2.11, has a very strong preference for the octahedral sites [202, 212]. The decreasing electrical conductivity can therefore be explained by the reduced number of available hopping sites when the chromium content increases. Consequently, although the formation of a Cr-rich spinel is beneficial for reducing Cr-evaporation and oxidation rate of FSS (see section 2.3.3), these phases are highly undesirable from an electrical conductivity point of view. The addition of copper to the spinel oxides appears to increase the electrical conductivity, while addition of iron appears to decrease it (see Table 2.3). However, with the wide range of reported values for the base compositions ($MnCo_2O_4$ and $Mn_{1.5}Co_{1.5}O_4$), it is also possible to argue for the opposite trends.

2.4.3 Thermal expansion

When experiencing a change in temperature, all materials tend to undergo a change in volume. For the vast majority of materials, the volume increases with increasing temperature, although there are also examples of the opposite behavior exhibited by some materials under limited temperature intervals [237]. The origin of the positive volume change is commonly explained by considering the asymmetric variation of interatomic potential with interatomic separation distance, illustrated in Figure 2.12. Increase in temperature leads to increase in kinetic energy, which again increases the vibrational amplitude. Due to the asymmetry of the energy potential well, this ultimately results in an increased interatomic distance [238]. The amount of thermal expansion experienced by a crystal will be influenced by the strength and nature of its bonds and in general, crystals with predominately covalent bonds are expected to show a smaller thermal expansion than crystals of predominately ionic bonds, given as the former are stronger [239].

Composition	σ(800 °C) [S/cm]	Sintering temp. [°C]	E_A [eV]	Measurement range [°C]	Ref
$MnCo_2O_4$	51	1200	0.65	500-900	[228]
$MnCo_2O_4$	87	1000	0.53-0.59	500-900	[228]
$MnCo_2O_4$	90	1150-1350	0.25-0.33	RT-1000	[229]
$MnCo_2O_4$	83	1150	0.45	100-800	[192]
$MnCo_2O_4$	67	1200	0.44	RT-950	[164]
$MnCo_2O_4$	60	>1100	0.55	500-800	[27]
$MnCo_2O_4$	40	1300	0.76	600-900	[230]
$MnCo_2O_4$*	28	1000		100-900	[231]
$MnCo_2O_4$*	47	1200		100-900	[231]
$MnCo_2O_4$	34	1200	0.48	400-800	[232]
$Mn_{1.5}Co_{1.5}O_4$	60	1250		200-1050	[25]
$Mn_{1.5}Co_{1.5}O_4$	92	1200	0.52	500-900	[212]
$Mn_{1.5}Co_{1.5}O_4$	50	1150	0.42	100-800	[192]
$Mn_{1.5}Co_{1.5}O_4$	31	1250	0.45	500-800	[166]
$MnCo_{1.9}Fe_{0.1}O_4$	72	1200	0.38	RT-950	[164]
$MnCo_{1.9}Fe_{0.1}O_4$*	30/38	1000/1200		100-900	[231]
$MnCo_{1.85}Fe_{0.1}O_4$	85	1200	0.53-0.59	500-900	[228]
$MnCo_{1.75}Fe_{0.25}O_4$*	26/34	1000/1200		100-900	[231]
$MnCo_{1.66}Fe_{0.34}O_4$	60	1200	0.53-0.59	500-900	[228]
$MnCo_{1.5}Fe_{0.5}O_4$*	12/21	1000/1200		100-900	[231]
$MnCo_{1.5}Fe_{0.5}O_4$	48	1200	0.53-0.59	500-900	[228]
$MnCo_{1.3}Fe_{0.7}O_4$	34	1200	0.53-0.59	500-900	[228]
$MnCoFeO_4$*	6/8	1000/1200		100-900	[231]
$Mn_{0.2}Co_{0.2}Fe_{2.6}O_4$	90	1300	0.063	100-1300	[233]
$MnCrFeO_4$	0.3	1250-1550	0.45	227-1027	[234]
$MnCoCrO_4$	2.5	1200	0.57	500-900	[212]
$Mn_{0.75}Co_{0.75}Cr_{1.5}O_4$	0.45	1200	0.75	500-900	[212]
$Mn_{0.5}Co_{0.5}Cr_2O_4$	0.006	1200	1.0	500-900	[212]
$MnCr_2O_4$	0.004	1550	1.02	600-1000	[235]
$MnCr_2O_4$	0.03	1250-1550	0.89	227-1027	[234]
$Mn_{1.7}Cr_{1.3}O_4$	0.14	1550	0.95	600-1000	[235]
$MnCu_{0.5}Co_{1.5}O_4$	105.5[a]	950		500-800	[236]
$Mn_{1.4}Co_{1.4}Cu_{0.2}O_4$	53.7	1250	0.49	500-800	[166]

* = value was not corrected for the sample's porosity

[a] measured at 750 °C

Table 2.3: Electrical conductivity (σ) and activation energy for conductivity (E_A) of $(Mn,Co,M)_3O_4$ (M=Fe,Cu,Cr) spinel oxides reported in literature and the temperature at which the measured samples were sintered.

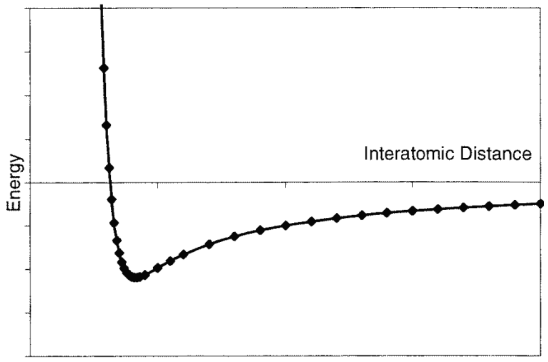

Figure 2.12: The interatomic potential energy as a function of interatomic distance between two atoms. Figure reprinted from [237].

The lattice thermal expansion coefficient (TEC) is defined as the relative change in unit *volume* with an unit change in temperature and can be obtained from the change in lattice parameter as a function of temperature by e.g. X-ray diffraction [239]. It is equally common to report TEC values as the bulk thermal expansion, which is defined as the relative change in unit *length* with a unit change in temperature. This can be written as:

$$\alpha_l = \frac{1}{L_0}\left(\frac{dL}{dT}\right) \tag{2.29}$$

where α_l is the thermal expansion coefficient with units K^{-1}, L is the sample length at temperature T and L_0 is the sample length at temperature $T = T_0$. Bulk thermal expansion coefficients can be determined by measuring the change in sample dimensions with temperature using e.g. a dilatometer. The bulk TEC is a macroscopic parameter, which means that in addition to the intrinsic lattice expansion, the measurement will reflect contributions from grain boundaries, voids and lattice defects [239]. If the expansion of the crystal is different in different directions, the results will be the average expansion of all directions unless a single crystal sample is used.

Some materials display dimensional changes upon heating that cannot be explained by the mechanism for thermal expansion described above. The term *chemical expansion* is used collectively for a number of different processes where the change in lattice dimensions is induced by a compositional change [240]. The change could either be gradual due to a gradual change in stoichiometry (stoichiometric expansion) or it can be sudden due to a change in crystal structure (phase change expansion) [241]. An example of the former is the anomalous increase in lattice

parameter observed in many perovskite oxides above 400 °C due to loss of oxygen accompanied by cation reduction [240]. Another example of chemical expansion has been reported for the spinel oxide Co_3O_4 above 600 K [242]. In this case, the anomalous expansion behavior has been explained by a spin-state transition of the octahedral Co^{3+} ions: $Co^{3+}(\text{LS}, 0.53\,\text{Å}) \longrightarrow Co^{3+}(\text{HS}, 0.61\,\text{Å})$ [243]. Co spin-state transitions have also been used to explain the anomalous expansion of $LaCoO_3$ [244].

TEC values for some $(Mn,Co,M)_3O_4$ (M=Fe,Cu,Cr) spinels reported in literature are given in Table 2.4. The scatter in the TEC values reported for the $MnCo_2O_4$ composition can probably be explained by the same factors as discussed in section 2.4.2 to explain the discrepancies in electrical conductivity. The overall range of values (10–$13.5 \cdot 10^{-6}$ K^{-1}) displayed by potential protective coating materials in Table 2.4 are in the same range as the TEC reported for Crofer 22 APU ($11.9 \cdot 10^{-6}$ K^{-1} between 20–800 °C [78]) and other commonly used materials in SOFC. It can however be noted that the TEC decreases with increasing Cr fraction, which is another argument for reducing the growth rate of the reaction layer between Cr_2O_3 and the coating.

Table 2.4: Thermal expansion coefficient (TEC) for various spinel compositions reported in literature and the temperature at which the tested samples were sintered. *= TEC curve appears to be non-linear in the temperature range for which the average TEC is calculated.

Composition	TEC [10^{-6} K^{-1}]	Range [K]	Sintering temp.	Ref.
$MnCo_2O_4$	11.7		1300	[230]
$MnCo_2O_4$	13.5	30-800	1000	[231]
$MnCo_2O_4$	13.1	30-800	1150	[229]
$MnCo_2O_4$	12.6	30-1000	1200	[245]
$MnCo_2O_4$	12.3	30-1000	1200	[232]
$MnCo_2O_4$	9.7	RT-1000	>1100	[27]
$Mn_{1.5}Co_{1.5}O_4$	11.7	30-800	no info	[246]
$Mn_{1.5}Co_{1.5}O_4$	10.8	30-1000	1200	[212]
$Mn_{1.5}Co_{1.5}O_4$	11.4	RT-800	1250	[247]
$Mn_{1.5}Co_{1.5}O_4$	10.6	RT-1000	1250	[166]
$MnCo_{1.9}Fe_{0.1}O_4$	11.9	20-1000	>1100	[248]
$MnCo_{1.9}Fe_{0.1}O_4$	13.4	30-800	1000	[231]
$MnCo_{1.75}Fe_{0.25}O_4$	12.3	30-800	1000	[231]
$MnCo_{1.5}Fe_{0.5}O_4$	10.7	30-800	1000	[231]
$MnCoFeO_4$	10.3	30-800	1000	[231]
$Mn_{1.25}Co_{1.25}Cr_{0.5}O_4$	10.0	30-1000	1200	[212]
$MnCoCrO_4$	8.7	30-1000	1200	[212]
$Mn_{0.5}Co_{0.5}Cr_2O_4$	6.7	30-1000	1200	[212]
$Mn_{1.4}Co_{1.4}Cu_{0.2}O_4$	11.8	RT-1000	1250	[166]
$Mn_{1.35}Co_{1.35}Cu_{0.3}O_4$	12.03	30-800	no info	[246]
$MnCo_{1.5}Cu_{0.5}O_4$	12.3*	30-1000	950	[236]

3. Manuscripts

Manuscript I

Thermal expansion and electrical conductivity of Fe and Cu doped $MnCo_2O_4$ spinel

Belma Talic[a,b], Peter Vang Hendriksen[b], Kjell Wiik[a], Hilde Lea Lein[a]

[a]*Department of Materials Science and Engineering, Norwegian University of Science and Technology*
[b]*Department of Energy Conversion and Storage, Technical University of Denmark*

Abstract. Manganese cobalt spinel oxides are promising coating materials for corrosion protection of metallic interconnects in solid oxide fuel cell (SOFC) stacks. This work investigates how iron and copper doping affect the crystal structure, thermal expansion and electrical conductivity of the $MnCo_{2-x}M_xO_4$ (M=Cu, Fe; x = 0.1, 0.3, 0.5) spinel oxides. Single phase cubic spinels were successfully prepared by spray pyrolysis. The lattice parameter increased with increasing iron content. The lattice parameter of the copper substituted materials varied greatly with the sample thermal history. The electrical conductivity between room temperature and 1000 °C increased with increasing copper content and decreased with increasing iron content. The thermal expansion coefficient (TEC) between 50 and 800 °C decreased from 14.4 to 11.0×10^{-6} K^{-1} from $MnCo_2O_4$ to $MnCo_{1.5}Fe_{0.5}O_4$, respectively. The TEC of copper substituted materials did not follow any obvious trend with composition and was likely influenced by precipitation of CuO during heating. For all materials the TEC was observed to increase above ca. 400 °C. The electrical conductivity and thermal expansion behavior is discussed on the basis of cation deficiency and spin-state transition of cobalt. Based on their physical properties, iron doped materials are the most attractive for application as SOFC interconnect coatings.

1. Introduction

The lifetime and performance of solid oxide fuel cell (SOFC) stacks is today among other factors limited by degradation of the ferritic stainless steel (FSS) interconnect [1,2]. Under SOFC operating conditions the FSS is oxidized to form a continuous surface scale typically composed of Cr_2O_3 and $MnCr_2O_4$ [3]. Due to the modest electrical conductivity of these materials [4,5], the resistance across the stack increases with time as the oxide scale grows thicker [6]. An additional challenge is the vaporization of Cr(VI) species from the scale surface by reaction with oxygen and water vapor present on the cathode side of the SOFC [7,8]. The volatile Cr(VI) species deposit on electrochemically active sites of the cathode, thereby causing significant performance degradation [9–11]. To mitigate these issues, the FSS may be coated with a protective material.

Some of the important requirements for the coating material are: sufficiently high electrical conductivity, thermal expansion coefficient (TEC) matching the FSS interconnect and other SOFC materials (typically 11-12×10^{-6} K^{-1} between 25 and 1000 °C), and low oxygen and chromium diffusion coefficients [12]. Several materials have been investigated for this purpose, including rare-earth oxides [13,14] and various lanthanum-based perovskites [15,16]. $(Mn,Co)_3O_4$ spinel oxides were first identified as possible coating materials by Larring and Norby [17], and have received increasing attention over the last decade [18–24]. Although these materials are not stable under the reducing conditions found on the anode side of the SOFC, they are considered promising coatings for the cathode side, due to an ability to reduce the oxidation rate of FSS and limit Cr-volatilization [25,26]. The most widely studied compositions in this system are $Mn_{1.5}Co_{1.5}O_4$ and $MnCo_2O_4$.

The AB_2O_4 spinel structure (space group *Fd-3m*) adopted by $MnCo_2O_4$ can be described as a nearly cubic close packed arrangement of oxygen ions where 1/8 of the available tetrahedral sites and 1/2 available octahedral sites are occupied by cations. The spinel structure is very flexible in terms of site occupancy and oxidation states of the elements, which makes characterization of the cation distribution complicated when transition metal cations are involved. Several suggestions for the cation distribution in $MnCo_2O_4$ have been put forth [27–34]. Most of these agree that tetrahedral sites primarily are occupied by Co^{2+}, while there is more debate about the oxidation states of Mn and Co occupying the octahedral sites. It was early shown by Yamamoto et al. [27] that the lattice parameter of $MnCo_2O_4$ is lower when synthesized by a low-temperature (80 °C) method compared to when synthesized by solid-state reaction at 1000 °C. At the time, this was attributed to a higher fraction of the tetrahedral sites being occupied by Mn^{2+} when prepared at low temperature. More recently it has been shown that preparation of $MnCo_2O_4$ below ca. 500-600°C yields a cation deficient spinel, with a smaller lattice parameter compared to the stoichiometric material [29,35–39]. For convenience, the cation deficiency is often designated as an excess of oxygen, i.e. $MnCo_2O_{4+\delta}$, with δ up to 0.6 reported [35]. Upon heating above ca. 500-700°C oxygen is released to form stoichiometric $MnCo_2O_4$ [35]. There are no reports about the process being reversible, i.e. that oxygen is taken up during cooling.

The small polaron hopping mechanism is generally accepted as the mechanism for electrical conductivity in spinel oxides containing transition metal cations [40,41]. Since the distance between octahedral sites is shorter than the distance between tetrahedral sites in the spinel structure, hopping takes place primarily between multivalent cations on the former [40]. For $MnCo_2O_4$, hopping is believed to take place mainly between Mn^{3+}/Mn^{4+} pairs on the octahedral sites, with a possible contribution due to hopping between Co^{2+}/Co^{III} pairs [42,43]. There is considerable scatter in literature regarding the magnitude of the electrical conductivity in this material, with values measured in air at 800 °C ranging from 34 to 132 S/cm [44–48]. There is also scatter in the reported thermal expansion

coefficient of $MnCo_2O_4$, ranging from 9.7-13.5×10^{-6} K^{-1} between room temperature and 800 °C [44–46,48,49].

There have been some attempts to improve the electrical conductivity and thermal expansion behavior by partially substituting Co with Ti [50], Ni [51], Fe [52], Cu [53,54] or Bi [55]. It is however not clear in all of the cases how doping affects the electrical conductivity. For example, addition of Fe is reported to both increase [52] and decrease [46] the electrical conductivity.

The aim of this work is obtain better understanding of the electrical and thermal behavior of the spinel oxides by providing a thorough characterization of these properties in $MnCo_{2-x}M_xO_4$ (M=Cu, Fe; x = 0.1, 0.3, 0.5). Iron and copper were chosen as substitutional elements based on an investigation of several binary spinels made by Petric and Ling [48], where it was shown that copper spinels exhibit appreciable electrical conductivities while ferrite spinels typically have TEC in the range of 11-12×10^{-6} K^{-1}, thus providing a good match with other SOFC components. Furthermore, diffusion couple experiments have indicated that both Cu and Fe doping of $(Mn,Co)_3O_4$ could be beneficial for reducing the scale growth rate and formation of a $(Mn,Co,Cr)_3O_4$ reaction layer between the coating and FSS interconnect [50,56]. The formation of $(Mn,Co,Cr)_3O_4$ is undesired due to this material's modest electrical conductivity and too low thermal expansion coefficient [57].

2. Experimental

2.1 Powder synthesis

$MnCo_{2-x}M_xO_4$ (M=Cu, Fe; x = 0, 0.1, 0.3, 0.5) powders were synthesized by spray pyrolysis using pilot-scale equipment. The details of this synthesis method have been described by Mokkelbost et al. [58]. Precursor solutions were prepared by dissolving metal nitrates, $Mn(NO_3)_2×H_2O$ (98 %, Aldrich), $Co(NO_3)_2×6H_2O$ (97.7 % min., Alfa Aesar), $Fe(NO_3)_3×9H_2O$ (> 98 %, Alfa Aesar) and $Cu(NO_3)_2×2.5H_2O$ (Rectapur, VWR), in distilled water by stirring overnight. The precursor solutions were filtered and their exact concentrations determined by thermogravimetrical analysis of the weight change after heating to 800 °C. They were then mixed in stoichiometric amounts according to target compositions (Table 1) and stirred overnight. The mixed solutions were atomized by spraying through a two-phase nozzle at a rate of 10 L/h into a rotating furnace set to a target temperature of 1000 °C. The high temperature causes the atomized droplets to decompose instantly, forming the oxides. The resulting powders were collected at the furnace outlet and calcined in air at 650 °C for 10 h to decompose any remaining organics. The heating and cooling rate (HCR) during calcination was 200 °C/h. The powders were subsequently ball milled overnight in 100 % ethanol (250 ml PE-bottles, Ø 10 mm YSZ milling balls), dried in a rotavapor, and sieved (250 μm).

Table 1: Target compositions of prepared spinel powders and abbreviations used throughout this text.

Composition	Abbr.
$MnCo_2O_4$	MC
$MnCo_{1.9}Fe_{0.1}O_4$	Fe1
$MnCo_{1.7}Fe_{0.3}O_4$	Fe3
$MnCo_{1.5}Fe_{0.5}O_4$	Fe5
$MnCo_{1.9}Cu_{0.1}O_4$	Cu1
$MnCo_{1.7}Cu_{0.3}O_4$	Cu3
$MnCo_{1.5}Cu_{0.5}O_4$	Cu5

2.2 Characterization

Structural characterization was performed on a Bruker DaVinchi X-ray diffractometer (XRD) with Cu-Kα radiation. Powder samples were mixed with ethanol and deposited on a silicon single crystal sample holder while solid samples were mounted in a large-cavity sample holder using molding clay. The diffractograms were recorded on rotating samples from 15-75° 2θ using a step size of 0.02° and a collection time of 1 s per step. Lattice parameters were refined by structure fitting of the diffraction patterns (Pawley method) using Topas software (Bruker).

Thermal expansion was characterized in a Netzsch DIL 402C dilatometer from 30-1000°C and reverse (HCR: 2 °C/min) under flowing (30 ml/min) synthetic air. All measurements were corrected against an Al_2O_3 standard. Dense pellets for the measurement were prepared from the spinel powders by uniaxial pressing in a Ø=5 mm steel die, sintering in air at 1100 °C for 5 h and subsequently annealing in air at 800 °C for 12 h (HCR: 2 °C/min). The annealing step was included to re-oxidize the spinel, which is partially decomposed when heated above 1050 °C in air [34,59]. The pellet ends were ground with #1200 SiC paper to make them parallel. Final pellet length was 8-11 mm. XRD was used to confirm that all materials were phase pure cubic spinels after the sintering procedure. For this purpose, larger pellets (Ø 20 mm) were prepared and sintered following the above described procedure. Before characterization, the pellets were ground with #500 SiC paper to remove 1-2 mm of the surface layer.

Thermogravimetric analysis (TGA) was performed using a TG 439 Thermo-Microbalance from Netzsch. The equipment consists of an electrically compensating symmetrical balance with two separate ovens for the sample and a counter weight, operating at identical heating and flow rates. The resolution with this equipment is 0.1 μm. Alumina crucibles containing the powders were suspended from the weighing beam using Pt30%Rh wires. Analysis was performed on ca. 15 mg of spinel powder with ca. 9.9 mg Al_2O_3 powder as the counter weight. Both the as-prepared spinel powder (calcined 650 °C) and powder

obtained by crushing a ceramic, sintered in air at 1100 °C (5 h) + 800 °C (12 h) as described above, were used. The mass change was recorded between room temperature and 800 °C in flowing air (10 ml/min) at various heating and cooling rates. A background correction was made for each temperature program by measuring with empty alumina crucibles. In theory, buoyancy effects should be eliminated by the experimental set-up, however, in practice a small influence could be detected in the background measurement. The background data are provided in Appendix A. After correcting for the background, the experimental results were fitted to a polynomial curve to reduce noise inherent to the measurement and improve readability of the figures. The original data and details about the noise reduction procedure may be found in Appendix A.

Electrical conductivity was characterized by the four-probe method on sintered rectangular bars. The bars were made by uniaxial pressing of the spinel powders in a steel die and sintering in air at 1050 °C for 5 h (HCR: 2 °C/min). The edges were cut to dimension (ca. 4×6×18 mm^3) using a diamond saw and lightly ground with #1200 SiC-paper. Pt-wires were attached to the sides of the bars, which were painted with Pt-paste and then heat treated at 1000 °C for ca. 10 min in air (HCR: 2 °C/min) to ensure good electrical contact. The electrical conductivity was measured in flowing air between room temperature and 1000 °C with 1 h dwell time for each 100 °C (HCR: 1 °C/min). Temperature was monitored by an S-type thermocouple placed close to the sample surface. Current was supplied by a Keithley 580 micro-ohmmeter and varied between 10-100 mA depending on the resistance. The current direction was switched at a frequency of ca. 1 Hz. The measured resistance was used to calculate the electrical conductivity according to:

$$\sigma = \frac{1}{R} \cdot \frac{L}{A} \tag{1}$$

where R is the resistance [Ω], L is the distance between the voltage probes [cm] and A is the cross sectional area of the sample bar [cm^2]. The average of the measured resistance in forward and reverse directions of passing current was used in order to eliminate any thermoelectric emf. The Bruggeman asymmetric model was used to correct the measured electrical conductivity for sample porosity according to [60,61]:

$$\sigma = \sigma_m \cdot \frac{1}{(1-p)^{\frac{3}{2}}} \tag{2}$$

where σ is the corrected conductivity, σ_m is the measured conductivity and p is the sample pore fraction. The porosity was determined by the Archimedes method according to ISO 5017:1998(E) using isopropanol as the solvent. The theoretical densities were calculated from XRD analysis of calcined powders. The phase purity of samples after the electrical conductivity measurement was checked by XRD of the crushed sample bars.

3. Results

3.1 Crystal structure

X-ray diffraction patterns of the as-prepared spinel powders after calcination at 650 °C in air are shown in Figure 1. All materials were identified as single phase cubic spinels. The lattice parameters were determined by fitting the XRD patterns to the cubic *Fd-3m* space group with the cation distribution set to[1] $(Co^{2+})[Co^{3+}Mn^{3+}]O_4^{2-}$. Both iron (as Fe^{3+}) and copper (as Cu^{2+}) were added to the octahedral position in place of cobalt. There was no significant difference in the goodness of fit by placing Fe/Cu on the tetrahedral sites or with different valence states. Lattice parameters obtained from the structure fit are plotted in Figure 2. Iron substitution increases the lattice parameter, while Cu substitution decreases the lattice parameter. This can also be seen in Figure 1 as a shifting of the diffraction peaks towards lower and higher 2θ angles, respectively. Neither of the substitutions result in a perfectly linear change in lattice parameter with compositions starting from the parent (MC) material.

XRD patterns of ceramics sintered at 1100 °C and annealed at 800 °C (provided in Appendix A) indicated that all materials remained single phase cubic spinels. The diffractograms were characterized by sharper peaks compared to Figure 1, reflecting the enhanced crystallinity and increase in particle size after heat treatment at higher temperature. The lattice parameters determined by structure fitting of these patterns are plotted in Figure 2. For nearly all of the materials, the lattice parameter after sintering at 1100 °C is higher than for the as-prepared powder (calcined 650 °C). The largest difference is for the Cu-doped materials, which after sintering show a trend of slightly increasing lattice parameter with increasing Cu substitution, i.e. the opposite of what is observed for the calcined powders. For the Fe-doped materials, the difference between the lattice parameters measured for the calcined powders and sintered ceramics decreases with increasing Fe substitution. The variation in lattice parameter from MC to Fe5 is linear for the sintered samples, in accordance with Vegard's law.

[1] In accordance with conventions for describing the cation distribution in spinel, the round brackets () designate cations in tetrahedral sites, while the square brackets [] designate cations in octahedral sites.

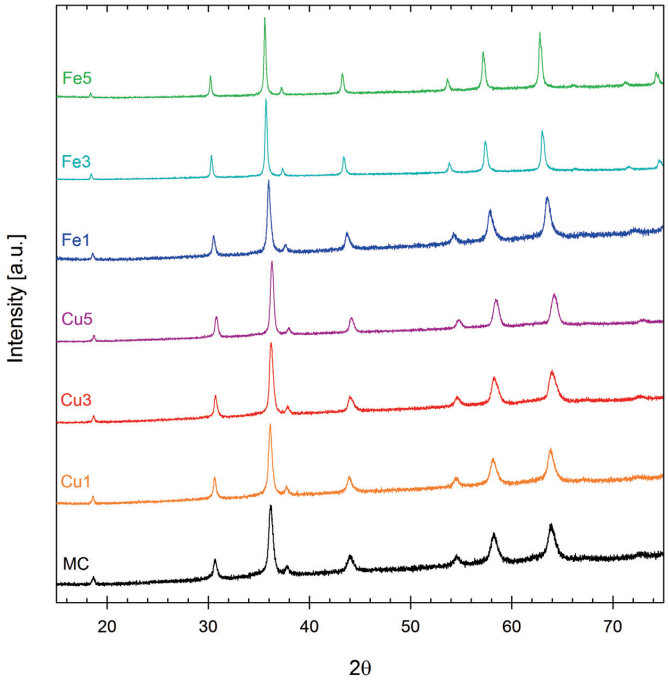

Figure 1. X-ray diffraction patterns of powders synthesized by spray pyrolysis after calcination at 650 °C in air. Individual patterns are normalized to the highest intensity peak.

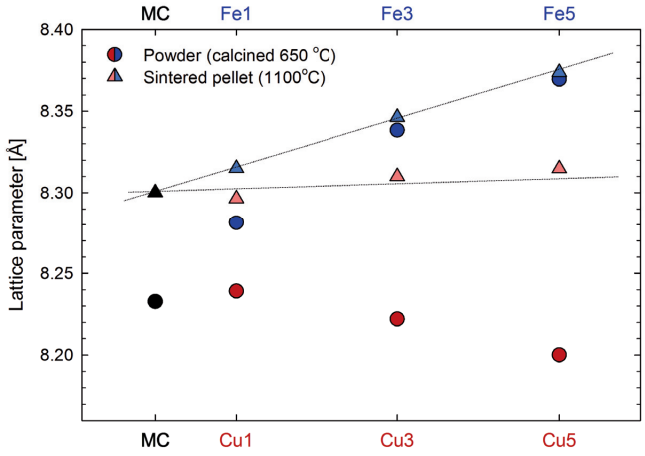

Figure 2. Lattice parameters determined by structure fitting of XRD patterns for as-prepared spinel powders, calcined at 650 °C, and pellets sintered at 1100 °C and annealed at 800 °C. MC is indicated by black symbols, Fe-doped by blue and Cu-doped by red. Stippled lines are added as guide to the eye.

3.2 Thermal expansion coefficient

Thermal expansion measured by dilatometry during heating in air (2 °C/min) is shown in Figure 3a. The thermal expansion is seen to decrease with increasing amount of Fe in the material. The addition of Cu results in an overall increase in thermal expansion, however, the variation with composition is more complicated and does not follow any obvious trend. For all materials, the expansion between room temperature and 800 °C fits well with two linear segments, as illustrated in Figure 3b for $MnCo_2O_4$. The transition between the two segments varies with composition, but is generally in the range of 300-500°C. The transition temperature for each material and the thermal expansion coefficients (TEC) calculated from the slopes of the curves in the different temperature segments are summarized in Table 2. Measuring the same sample more than one time generally resulted in a difference of < 5 % in TEC (values reported in Table 2 are based on the first measurement of each sample).

There was a small negative hysteresis between the expansion measured during heating and cooling for all materials. For clarity, only the heating curves are shown in Figure 3 (full measurement in Appendix A). The hysteresis decreased significantly when the measurement was performed between room temperature and 800 °C. This indicates that the hysteresis is due to creep or possibly an onset of partial reduction of Co in the materials [34]. The material containing the highest fraction of copper, Cu5, displayed a greater hysteresis compared to the other materials. A distinct change in the slope of thermal expansion above 800 °C can also be seen in Figure 3a. A XRD scan of the crushed sample after testing, shown in Figure 4, reveals small amounts of CuO secondary phase. This secondary phase is not detected in the sintered pellet (also shown in Figure 4), possibly because it was under the typical detection limit of XRD (~2 %) and/or this phase precipitated from the material with time at higher temperature.

Table 2: Thermal expansion coefficients (TEC) determined from linear fit of slopes in Figure 3a. Low temperature (LT) values are from 50 °C to the transition point, high temperature (HT) values are from the transition point to 800 °C. Sample density was determined by Archimedes method.

Comp.	LT-TEC [10^{-6} K^{-1}]	HT-TEC [10^{-6} K^{-1}]	Transition point [°C]	TEC 50-800°C [10^{-6} K^{-1}]	Sample density [%]
MC	12.9	15.3	410	14.4	91
Cu1	13.7	17.3	380	15.8	95
Cu3	12.7	16.3	330	15.1	95
Cu5	12.3	16.3	360	14.7	96
Fe1	11.4	14.8	350	13.6	95
Fe3	11.1	12.8	440	12.0	95
Fe5	9.9	11.2	440	11.0	96

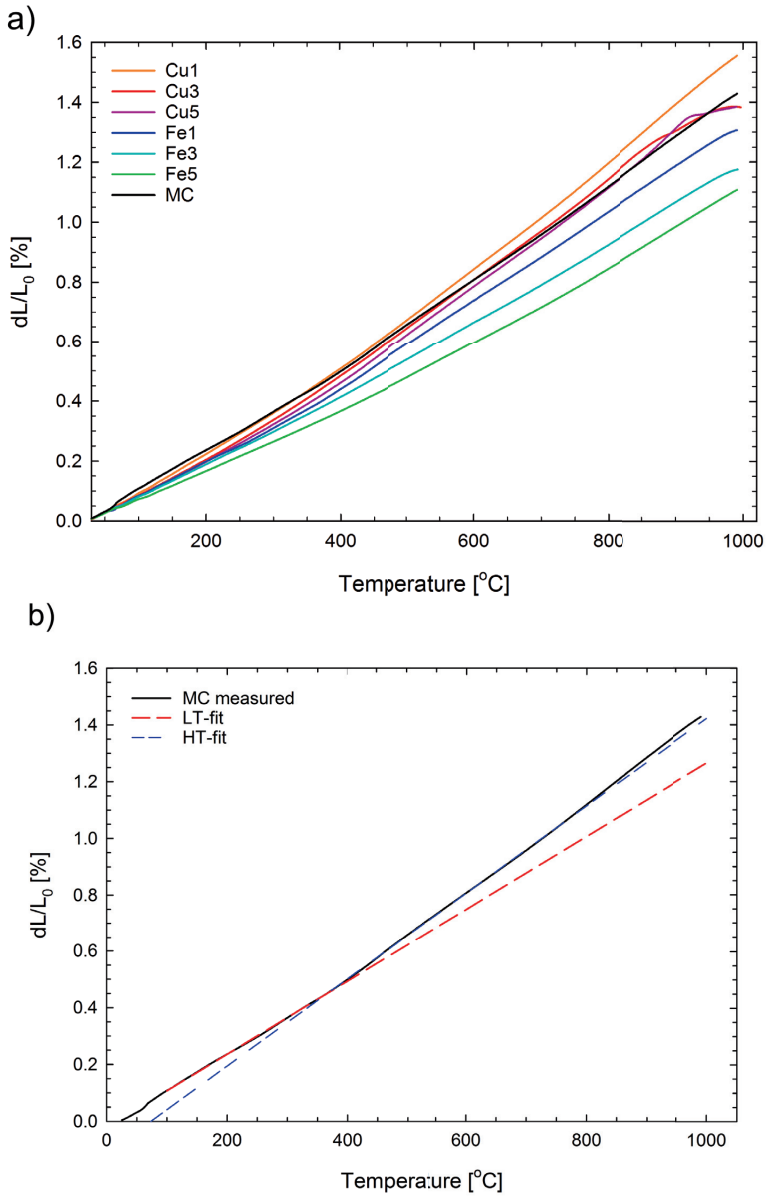

Figure 3. (a) Thermal expansion measured by dilatometry during heating in air, (b) Thermal expansion curve for the $MnCo_2O_4$ (MC) material showing linear fit of curve at low (LT) and high (HT) temperatures.

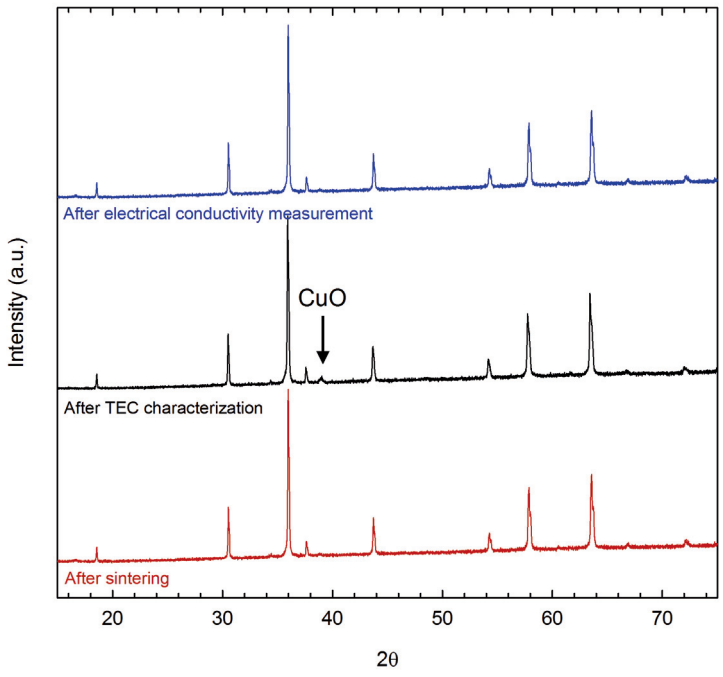

Figure 4. X-ray diffractograms of the $MnCo_{1.5}Cu_{0.5}O_4$ (Cu5) material after sintering (1100 °C + 800 °C, air), after thermal expansion characterization, and after electrical conductivity characterization. The peak belonging to CuO is highlighted, all other peaks belong to the cubic spinel phase.

3.3 Electrical conductivity

Figure 5 shows the electrical conductivity measured in air as a function of temperature. The results have been corrected for sample porosity using equation (2). All materials exhibit semiconducting behavior. The conductivity increases with increasing Cu-substitution and decreases with increasing Fe-substitution.

The temperature dependence can be described in accordance with the small polaron hopping model as [62]:

$$\sigma = \frac{\sigma_0}{T} \exp\left(-\frac{E_A}{kT}\right) \quad (3)$$

where T is the temperature [K], E_A is the activation energy for hopping [eV], and k is Boltzmann's constant [eV/K]. The pre-exponential factor, σ_0, is assumed to be constant. The slope of the ln(σT) vs 1/T curve (Fig. 5) can be fitted to two linear segments in similar temperature intervals as the thermal expansion, i.e. one segment between room temperature and ca. 400 °C and one at higher

temperatures. The high temperature activation energy decreases from 0.53 eV to 0.41 eV with increasing Cu-substitution, while Fe-substituted samples have the same activation energy as MC, namely 0.53 eV. The same trends are observed for the low temperature region, where Cu-substituted materials have activation energies in the range of 0.32-0.36 eV, while MC and the Fe-substituted materials have activation energies of 0.38-0.39 eV. The activation energy calculated from the slopes at high temperature together with the conductivity measured at 800 °C and the porosity of each sample are summarized in Table 3.

XRD of the crushed bars after measurement showed that all materials remained phase pure, cubic spinels. Unlike after TEC characterization, no CuO peaks could be detected in the diffractogram of the Cu5 material (see Figure 4). The lattice parameters of MC and Fe-substituted materials were equal to the lattice parameters obtained for the ceramics sintered at 1100 °C and annealed at 800 °C (see Figure 2). The lattice parameters for the Cu-substituted materials were in this case intermediate of those determined for calcined powder (650 °C) and sintered ceramic (1100 °C), decreasing from 8.286 Å for Cu1 to 8.274 Å for Cu5.

Table 3: Electrical conductivity (σ) measured at 800 °C, activation energy (E_A) and pre-exponential factor (σ_0) at high temperature (>400 °C) extracted from the Arrhenius plots. The conductivity values have been corrected for the measured sample density. σ_{uncorr} is the electrical conductivity at 800 °C before correcting for porosity.

Comp.	E_A [eV]	σ_0	σ (800 °C) [S/cm]	Sample density [%]	σ_{uncorr} [S/cm]
MC	0.53	17.2	89	72	55
Cu1	0.50	17.1	114	84	87
Cu3	0.44	16.7	142	95	131
Cu5	0.41	16.5	168	96	155
Fe1	0.53	17.1	77	77	52
Fe3	0.53	16.5	47	79	33
Fe5	0.53	16.2	31	81	23

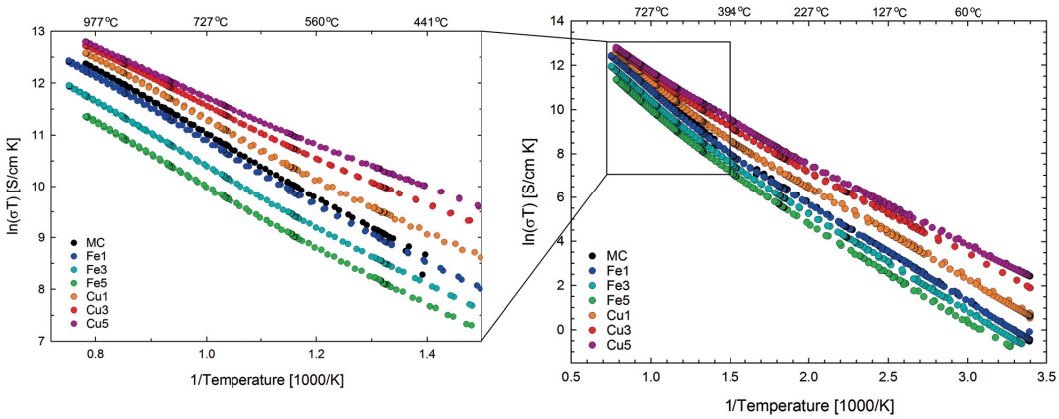

Figure 5. Arrhenius plot showing the natural logarithm of the electrical conductivity as a function of temperature. Results are corrected for sample porosity (specified in Table 3).

In most cases, there was negligible (< 1 %) hysteresis between the conductivity measured during heating and cooling, and no significant changes in the conductivity during the 1 h long isotherms. However, for the MC sample, the conductivity measured during the 1 h isotherm at 375 °C decreased considerably with time. When the sample was heated up to 1000 °C and cooled, the conductivity measured below 500 °C during cooling was higher than measured during heating. This manifested as a positive hysteresis, as seen in Figure 6a. A positive hysteresis was also observed when the isothermal steps were omitted, the heating and cooling rates increased from 1 °C/min to 3 °C/min, and the measurement reversed at 500 °C (Appendix A). Figure 6b shows that when holding the MC sample at constant temperature of 325 °C or 275 °C, the electrical conductivity continues to decrease for more than 40-50 h. In contrast, the electrical conductivity measured at 800 °C changes by less than 0.4 % over 25 h (Fig. 6b insert). A sample of the Cu1 material with 60 % density (sintered 10 h at 950 °C in air) also showed a hysteresis between the heating and cooling segments (Appendix A). This was not observed for the same material when the sample density was 87 % (sintered 5 h at 1050 °C in air), which suggests that the relaxation in conductivity at low temperature is related to the sample's interaction with the atmosphere.

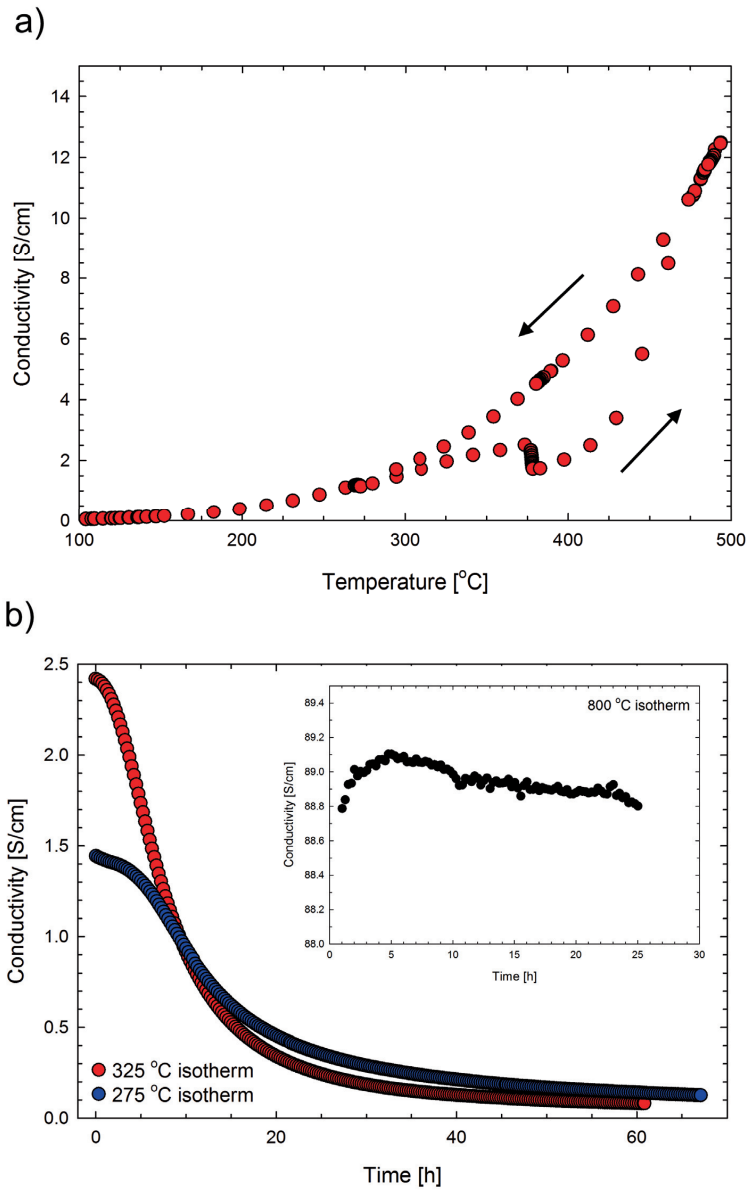

Figure 6. Anomalies in the electrical conductivity behavior of $MnCo_2O_4$. (a) Hysteresis in electrical conductivity measured during heating and cooling. The plot is an excerpt from a measurement between room temperature and 1000 °C. (b) Conductivity as a function of time, measured at constant temperature

3.4 Thermogravimetric analysis

The results of the thermogravimetrical analysis of MC powder obtained from a crushed ceramic sintered at 1100 °C and annealed at 800 °C are presented in Figure 7. When slowly heated (2 °C/min, Fig. 7a), the sample mass begins to increase above ca. 200 °C, reaching a maximum at 370 °C before it decreases again. Between 510 and 700 °C there is a plateau after which the mass decreases again. When the heating rate is increased to 10 °C/min (Fig. 7b) there is no mass uptake, but a distinct mass loss above 250 °C. The magnitude of the total mass loss at 10 °C/min between 250-650°C (0.24 %) is larger than at 2 °C/min between 370-510°C (0.10 %). The mass changes are not reversible upon cooling at 10 °C/min. However, when the same sample is re-heated at 1 °C/min (Fig. 7c), the sequence of mass uptake followed by loss can again be observed. The magnitude of both the mass uptake and loss at 1 °C/min are smaller than observed at 2 °C/min, but the mass change follows the same temperature trend. At 1 °C/min there is some mass gain upon cooling, however, this is shifted towards lower temperatures compared to the mass gain observed during heating.

Figure 8 shows TGA results for the calcined (650 °C) MC, Fe3 and Cu3 powders. The first cycle between room temperature and 800 °C was performed at a HCR of 10 °C/min (Fig. 8a). The initial mass loss below 200 °C can be attributed to evaporation of adsorbed water. After this, the mass change behavior is similar as for the MC powder heat treated at 1100 °C (Fig. 7b). Figure 8b shows the second cycle of the same materials performed at HCR of 1 °C/min. For all of the materials there is a peak in the mass change curve between 350 and 400 °C. The largest mass loss after this peak is for the Cu3 material. The mass loss during heating is partially reversible during cooling (stippled lines), resulting in a small hysteresis.

Overall, the mass changes are considerably larger for the powder calcined at 650 °C (Fig. 8) compared to the powder that has been heat treated up to 1100 °C (Fig. 7).

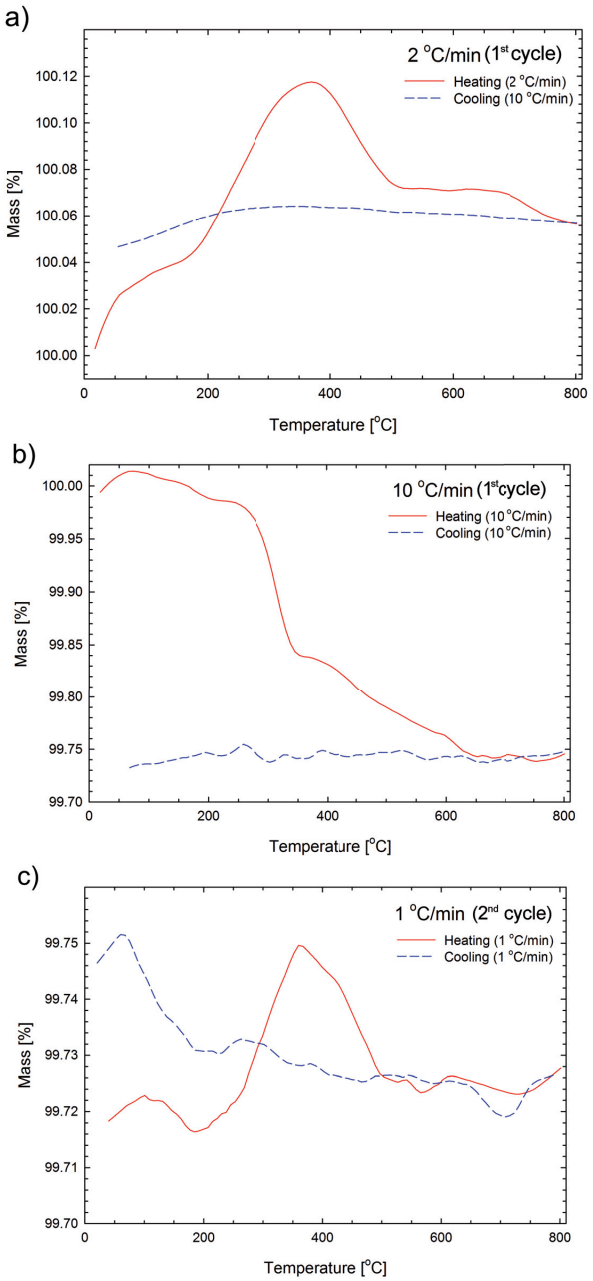

Figure 7. Thermogravimetric analysis of $MnCo_2O_4$ powder (heat treated 1100 °C+ 800 °C) showing relative weight change as a function of temperature in air. (a) heating rate 2 °C/min, cooling rate 10 °C/min, (b) heating and cooling rate 10 °C/min, (c) second cycle of sample in b), heating and cooling rate 1 °C/min. Note that the scale of the y-axis is different in the three graphs.

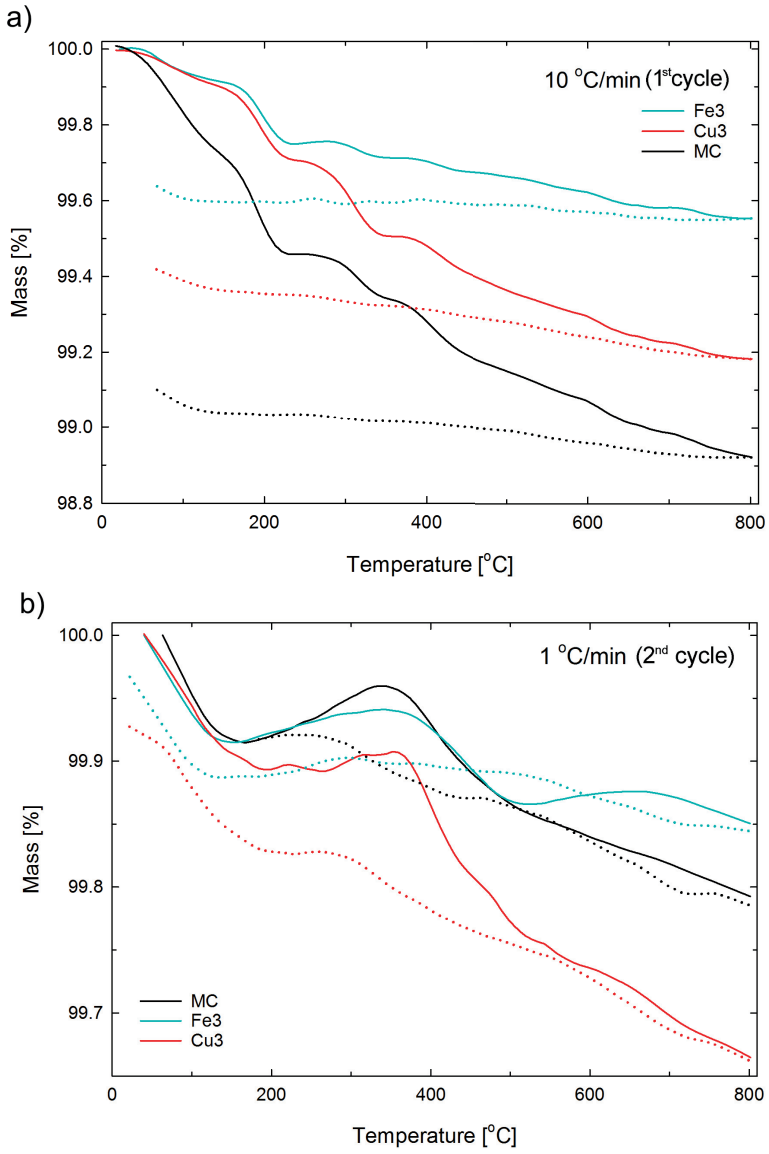

Figure 8. Thermogravimetric analysis of MC, Fe3 and Cu3 powders (calcined 650 °C) showing relative weight change during heating in air. Solid lines = heating, stippled lines = cooling. (a) heating and cooling rate 10 °C/min, (b) second cycle of samples in a) with heating and cooling rate 1 °C/min. The curves have been shifted to start at 100 % mass.

4. Discussion

4.1 Crystal structure

The smaller lattice parameter measured for most of the materials after calcination at 650 °C compared to after sintering at 1100 °C (Fig. 2) is consistent with the temperature dependence of the lattice parameter for $MnCo_2O_4$ reported in literature [27,39,63]. Comparing the value for MC powder calcined at 650 °C (8.233 Å) with the value given in PDF 23-1237 for presumably stoichiometric $MnCo_2O_4$ prepared at 720 °C (8.269 Å) indicates that the as-prepared powder might be slightly cation deficient. Nissinen et al. [35] reported $\delta = 0.1$ for $MnCo_2O_{4+\delta}$ calcined at 640 °C. With increasing Fe-substitution the difference between the lattice parameters after 650 °C and 1100 °C heat treatments decreases, suggesting that the temperature sensitivity is decreased by Fe-doping. This is corroborated by the TGA results (Fig. 8) showing smaller mass changes during heating in air for the Fe3 powder compared to the MC powder.

Due to the similar scattering factors of the elements in $MnCo_2O_4$, the cation distribution cannot be determined from XRD data. However, the most probable cation distribution may be estimated by comparing the lattice parameter determined by XRD with the theoretical lattice parameter for different cation distributions, following the method of O'Neill and Navrotsky [64]. The method is based on geometrical considerations of the spinel structure, described by Hill et al. [65], and assumes that ions can be considered as hard spheres. The average ionic radius is used when multiple cations occupy the same site. Based on an extensive review of binary spinels, O'Neill and Navrotsky [64] derived a set of effective ionic radii for cations in the spinel structure, which are used in the calculation. These radii are in most cases slightly smaller than those suggested by Shannon [66]. Since the electrical conductivity and thermal expansion was measured on sintered ceramics, we will compare the calculated lattice parameters for different distributions to the lattice parameters determined for samples sintered at 1100 °C.

For MC, Co^{2+} is assumed to be the only cation occupying tetrahedral sites, in accordance with majority of the cation distributions previously suggested in literature [27–34]. The cation distribution resulting in the closest match with that determined by XRD (8.298 Å) is $(Co^{2+})[Mn^{3+}_{0.54}Mn^{4+}_{0.46}Co^{III}_{0.54}Co^{2+}_{0.46}]O_4^{2-}$, which has a theoretical lattice parameter of 8.298 Å[2]. This distribution is very similar to that suggested by Bordeneuve et al. [34] based on neutron diffraction data on samples sintered at 750 °C and quenched to room temperature. The nearly 1:1 Mn^{3+}:Mn^{4+} ratio accounts for the high electrical conductivity of $MnCo_2O_4$ in the series of $Mn_xCo_{3-x}O_4$ spinels [42].

The calculations are complicated by the addition of a third element. However, taking the above suggested distribution as a starting point, two possibilities with

[2] Co^{III} designates the low spin state of Co^{3+}

an nearly equally good match between calculated and measured lattice parameters are obtained for the Fe-substituted materials. The first possibility is that Fe^{3+} (0.645 Å) replaces Co^{III} (0.53 Å) on the octahedral sites, and the second is that Fe^{3+} (0.485 Å) replaces Co^{2+} (0.58 Å) on tetrahedral sites. The latter requires a charge compensation by reduction of Co and Mn on the octahedral sites, resulting in the distribution $(Fe^{3+}_{0.5}Co^{2+}_{0.5})[Mn^{3+}_{0.5}Mn^{4+}_{0.5}Co^{2+}]O_4^{2-}$ for Fe5. Previous investigations of the cation distribution in $MnCo_{2-x}Fe_xO_4$ have suggested both a mixed occupancy of tetrahedral and octahedral sites [43], and that iron mainly occupies the latter [67]. Crystal field theory predicts that both Mn^{3+} and Co^{3+} have a stronger preference for the octahedral site than Fe^{3+} [68]. It is thus tempting to suggest that Fe^{3+} replaces Co^{2+} on tetrahedral sites in $MnCo_{2-x}Fe_xO_4$ and that the increase in lattice parameter is due to charge compensation by Co and Mn on the octahedral sites.

The lattice parameters of the Cu-substituted materials varied greatly with thermal history. The number of possibilities in terms of site occupancy and oxidation state of the elements are too numerous to use the method developed by O'Neill and Navrotsky to explain this variation. Investigations of $MnCoCuO_4$ have resulted in conflicting suggestions for the cation distribution. Brabers and Setten [69] suggested the distribution $(Cu^{+}_{0.65}Mn^{3+}_{0.35})[Cu^{2+}_{0.35}Co^{3+}Mn^{4+}_{0.65}]O^{2-}_4$, while others have suggested that both Cu^{2+} and Cu^{+} occupy tetrahedral sites and that octahedral sites are occupied by Co^{3+} and $Mn^{3+/4+}$ [70,71].

4.2 Possible non-stoichiometry

The TGA results showed a series of small but significant steps of mass gain and loss during heating of MC in air. It should be noted that the results in Figure 7 are for a powder obtained by crushing a ceramic that had been sintered at 1100 °C, annealed at 800 °C and cooled to room temperature at 2 °C/min. Thus, according to literature [35–38], the starting point should be stoichiometric $MnCo_2O_4$. Figure 7a and c clearly show that this material starts to take up oxygen at ca. 200 °C during slow heating in air. Assuming that the spinel initially is stoichiometric, the oxygen uptake measured between 200-370°C when heating at 2 °C/min (0.13 %) corresponds to $\delta = 0.02$. Again, it should be stressed that δ is related to the cation deficiency, as there is little room for interstitial oxygen in the close packed lattice of oxygen in the spinel structure. As far as we are aware, this is the first report of non-stoichiometry in $MnCo_2O_4$ spinel prepared at elevated temperatures. The mass changes are admittedly smaller than observed during heating of the non-stoichiometric material prepared at lower temperatures [35–38], however, they are still significant and may provide an explanation for the changes observed in electrical conductivity, as will be discussed later.

Oxidation accompanied by formation of cation vacancies has previously been reported for Mn-Cu and Mn-Ni-Fe spinel oxides [72,73]. The generalized oxidation reaction may be written in terms of Kroger-Vink notation as [72]:

$$\frac{1}{2}O_2 \rightarrow O_O^X + \frac{1}{4}V_A'' + \frac{1}{2}V_B''' + 2p^* \quad (4)$$

i.e. oxidation results in the formation of a new unit cell by creation of cation vacancies on the tetrahedral (A) and octahedral (B) sites, and results in two electron holes. Using X-ray absorption near edge structure (XANES) analysis, Bazuev et al. [63] demonstrated that the fraction Mn^{4+}/Mn^{3+} in $MnCo_2O_{4+\delta}$ spinel increases with increasing δ. Accordingly, it may be inferred that the electron holes are localized on manganese cations, i.e. $Mn^{3+} \rightarrow Mn^{4+}$ during oxidation. Above 370 °C the mass loss likely corresponds to reduction of Mn^{4+} to Mn^{3+}, as suggested previously for heating of cation-deficient $MnCo_2O_{4+\delta}$ [63]. Above 700 °C the sample heated at 2 °C/min experienced another small loss of oxygen. This is probably due to reduction of Co^{III} to Co^{2+} on the octahedral sites, considering that Co_3O_4 has the lowest decomposition temperature (900 °C) in the $Mn_xCo_{3-x}O_4$ series of spinels [34].

The whole series of oxidation and reduction steps believed to take place upon heating at 2 °C/min are summarized in Figure 9.

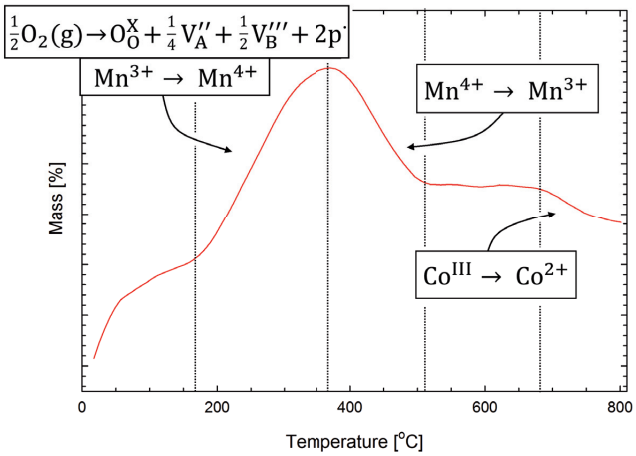

Figure 9. Suggestions for oxidation and reduction reactions to explain observed mass change of $MnCo_2O_4$ during heating in air at 2 °C/min.

The same series of reaction steps can be concluded to take place at 1 °C/min. However, the behavior at higher heating rates (10 °C/min) is different, with the first mass loss clearly shifted to lower temperatures and no distinct uptake of oxygen initially. It is also interesting to note that the total mass loss increases with

increasing heating rate. Kinetics are clearly important, however, more work will be needed to clarify the heating rate dependence of the different reactions.

The fact that the same sequence of mass changes, with a mass gain peak around 370 °C, is observed for the Fe- and Cu substituted materials strengthens the hypothesis that oxidation and reduction mainly involves manganese ions, since Fe and Cu replace Co in these materials. The magnitude of the mass change was greater for Cu3 and smaller for Fe3 compared to MC. These results fit well with the variations in lattice parameter, indicating that Fe-doped materials are less sensitive to thermal history and Cu-doped materials are more sensitive.

4.3 Electrical conductivity

The electrical conductivity of $MnCo_2O_4$ determined in this work is in the upper range of the values previously reported in literature. For example, [44] reported 34 S/cm at 800 °C in air for a sample sintered at 1200 °C and [74] reported 40 S/cm for a sample sintered at 1300 °C. As previously discussed by Liu et al. [43] some of the discrepancies found in literature are most likely due to the high temperature at which many of the investigated samples have been sintered. According to the Mn_3O_4-Co_3O_4 phase diagram reported by Aukrust and Muan [59], $MnCo_2O_4$ spinel is only stable up to ca. 1050 °C in air. Liu et al. [43] showed that $MnCo_2O_4$ sintered at 1200 °C had an electrical conductivity of 51 S/cm at 800 °C and contained significant amounts of rock salt secondary phases. When the same sample was annealed at 1000 °C for 72 h, the rock salt phases disappeared and the electrical conductivity at 800 °C increased to 87 S/cm. This is close to the value we obtained (89 S/cm) for the same material sintered at 1050 °C, which was confirmed to be phase pure by XRD.

The electrical conductivity decreased with increasing Fe-substitution, without any changes in the activation energy. If hopping between Co^{III}-Co^{2+} pairs on the octahedral sites contributes to the charge transfer in $MnCo_2O_4$, as suggested by Rousset et al. [42], both of the above suggested cation distributions for the Fe-substituted materials would explain why the electrical conductivity decreases. Irrespective of whether Fe^{3+} resides on the octahedral or tetrahedral sites in the spinel structure, the consequence of introducing Fe is a decrease in the concentration of Co^{III} (see section 4.1). Thus, there are fewer available sites for hopping as charge transfer is limited to hopping between the Mn^{3+}-Mn^{4+} pairs.

With increasing Cu-substitution the electrical conductivity increases and the activation energy decreases. The change in activation energy may indicate that copper ions participate in the charge transfer. Since small polaron hopping in the spinel structure is feasible only between equivalent sites, and the cation-cation distance is shortest between the octahedral sites, this would imply that both Cu^{+} and Cu^{2+} occupy the octahedral sites.

Time variation of the electrical conductivity, as shown in Figure 6, has previously been reported for nickel and copper ferrite spinels [75,76]. There it

was suggested that the cation distribution is a function of temperature and that the decrease in conductivity over time reflects re-distribution of the cations between octahedral and tetrahedral sites. More recently, Rousset el at. [42] investigated this so-called "aging" phenomenon in the $Mn_xCo_{3-x}O_4$-system at 125 °C and also attributed a decreasing electrical conductivity with time to cation re-distribution. However, aging was only appreciable for the end members of the system ($2.8<x<1.5$); for $MnCo_2O_4$ the change in electrical conductivity was less than 0.1 % over 500 h at 125 °C. Here we have shown a considerable aging effect also for the $MnCo_2O_4$ composition. Since the effect only was observed for this particular sample (with 72 % density) and a Cu1 sample sintered to low density (60%), it may be argued that the effect is connected to interactions with the atmosphere. It should be mentioned that the sample of $MnCo_2O_4$ investigated by Rousset et al. was prepared by spark plasma sintering, resulting in a density of 95 % [42].

The mass changes observed by TGA during heating at 2 °C/min and the reactions proposed to explain these changes (Fig. 9) provide a possible explanation for decrease in electrical conductivity. Below 370 °C the observed uptake of oxygen was proposed to result in the formation of cationic vacancies and electron holes. $MnCo_2O_4$ is a p-type conductor [77], so intuitively, it may be expected that the increase in hole concentration should result in an increase in electrical conductivity [40]. However, as discussed by Groen et al. [72], the mobility of the charge carriers is in this case more important than their concentration. The creation of cation vacancies reduces the number of available sites for hopping and consequently the mobility. When heated above 400 °C, oxygen is removed and cationic vacancies are annihilated, which results in an increase in the electrical conductivity. As seen from the TGA results (Fig. 7) oxygen uptake is not completely reversible during cooling, which explains the hysteresis in electrical conductivity below 500 °C (Fig. 6a).

4.4 Thermal expansion

All materials exhibited a change in the slope of thermal expansion above ca. 400 °C. Similar behavior may be observed upon examination of several previously published thermal expansion curves for $MnCo_2O_4$ and $MnCo_{2-x}Cu_xO_4$, although this was not recognized by the authors [44,45,78,79]. $MnCo_2O_4$ has no proven phase transitions in the temperature interval where the TEC is observed to increase. Some calculated phase diagrams of the Mn-Co-O system suggest the coexistence of $CoMnO_3$ with $MnCo_2O_4$ below ca. 600 °C and precipitation of MnO_2 below ca. 400 °C [48] . However, as far as we are aware, this has not been observed experimentally. Seeing as the TEC increases in the same temperature interval where a mass change was observed by TGA, it is possible that the extra expansion is related to reduction of Mn^{4+} (0.53 Å) to Mn^{3+} (0.645 Å) on the octahedral sites. However, considering the small magnitude of the mass change

observed for a finely crushed powder, it is arguable whether the dense (> 90 %) samples investigated by dilatometry interact sufficiently with the atmosphere to result in a significant increase in TEC. As discussed above, the relaxation effect in electrical conductivity was only observed for samples with a density below 72 %.

An alternative mechanism that would explain the increase in TEC is spin state transition of cobalt on the octahedral sites, which is responsible for the extra thermal expansion of Co_3O_4 observed above ca. 350 °C [80]. This can be described as Co^{3+}(LS) (0.545 Å) → Co^{3+}(HS) (0.61Å), where the numbers in parentheses are the Shannon ionic radii. Three-valent cobalt residing in the octahedral sites of $MnCo_2O_4$ is believed to be in the low spin state at room temperature [34], so a transition to high spin with increasing temperature is feasible. A mechanism involving spin state transition of cobalt would explain why the thermal expansion becomes more linear over the whole investigated temperature range when cobalt is replaced by iron. As discussed above, both of the most probable cation distributions for Fe-substituted $MnCo_2O_4$ involve a lower concentration of Co^{III} on octahedral sites. TGA results showed that the Fe-substituted materials behaved similarly as MC, thus, their more linear expansion behavior cannot be explained if instead oxidation is responsible for the extra expansion.

The thermal expansion behavior of materials containing copper is more complicated and the TEC does not follow any obvious trend with composition. Furthermore, the lattice parameter was found to vary significantly with thermal history. This could in part be due to precipitation of CuO as a secondary phase, which was observed for the sample containing the highest amount of Cu, namely $MnCo_{1.5}Cu_{0.5}O_4$.

4.5 Suitability as SOFC interconnect coating materials

As mentioned in the introduction, the most important criteria for selection of a suitable coating material for the protection of SOFC metallic interconnects are a close TEC match to the alloy and other SOFC components, a sufficiently high electrical conductivity and low oxygen and chromium diffusion coefficients through the coating. With respect to thermal expansion, the Fe-substituted materials show greatest promise. The average TEC of $MnCo_{1.7}Fe_{0.3}O_4$ (Fe3) between 50-800°C (12.0×10^{-6} K^{-1}) is very close to the TEC of Crofer 22 APU (11.9×10^{-6} K^{-1} [81]) in the same temperature interval, which is one of the commonly used interconnect alloys today. A closer match in TEC leads to less build-up of stresses during thermal cycling, thereby reducing the risk of cracking and/or spallation of the coating. Although the electrical conductivity was reduced by doping with iron, the conductivity remains several orders of magnitude higher than the typical electrical conductivity of the oxide scale formed on FSS [4]. The area specific resistance (ASR) across a coated interconnect will be given by the product of the thickness and resistivity of each layer. Assuming the scale is made

of Cr_2O_3 with an electrical conductivity of 0.1 S/cm at 800 °C, and that the coating is a 20 μm thick layer of Fe5 (31 S/cm at 800 °C), it can be shown that the chromia scale will dominate the ASR once this layer grows beyond 0.03μm. I.e. oxygen diffusion through the different materials will be a more important factor for reducing the ASR, since this influences the growth rate of the chromia scale under the coating. The oxidation of Crofer 22 APU coated with Fe and Cu doped $MnCo_2O_4$ is reported in [Manuscript II].

5. Conclusion

Single phase $MnCo_{2-x}M_xO_4$ (M=Cu, Fe; x = 0.1, 0.3, 0.5) materials of the cubic spinel structure were synthesized by spray pyrolysis. The electrical and thermal expansion properties were characterized in air between room temperature and 1000 °C. The thermal expansion behavior of all materials was characterized by a lower TEC between room temperature and ca. 400 °C compared to between ca. 400 °C and 800 °C. It was concluded that a spin state transition of Co^{3+} from low spin to high spin was the most likely origin of the extra expansion at elevated temperatures. Substitution with Fe resulted in a more linear expansion behavior in the whole temperature interval and an overall lower TEC. The thermal expansion behavior of Cu-substituted materials was likely influenced by precipitation of CuO secondary phases and was generally slightly higher than the thermal expansion of $MnCo_2O_4$.

The electrical conductivity decreased by substitution with Fe and increased by substitution with Cu. The electrical conductivity of $MnCo_2O_4$ decreased with time below 400 °C. This was related to the low density of the investigated sample, allowing for greater interaction with the atmosphere. Thermogravimetric analysis of the material revealed a complicated sequence of mass change with temperature, which provided an explanation for the observed anomaly in electrical conductivity. When slowly heated in air, $MnCo_2O_4$ picked up oxygen from the atmosphere resulting in the creation of cation vacancies, which decreased the electrical conductivity due to a reduction in the number of available sites for hopping.

Based on the closest match in TEC to other SOFC materials, Fe doped $MnCo_2O_4$ is considered most promising for the application as a protective coating on SOFC metallic interconnects.

References

[1] J.R. Mawdsley, J. David Carter, A. Jeremy Kropf, B. Yildiz, V.A. Maroni, Post-test evaluation of oxygen electrodes from solid oxide electrolysis stacks, *International Journal of Hydrogen Energy*. **34** 4198–4207 (2009).

[2] N.H. Menzler, D. Sebold, Q. Fang, Chromium-Related Degradation of Thin-Film Electrolyte Solid Oxide Fuel Cell Stacks, *ECS Transactions*. **68** 1815–1825 (2015).
[3] M. Palcut, L. Mikkelsen, K. Neufeld, M. Chen, R. Knibbe, P.V. Hendriksen, Corrosion stability of ferritic stainless steels for solid oxide electrolyser cell interconnects, *Corrosion Science*. **52** 3309–3320 (2010).
[4] A. Holt, P. Kofstad, Electrical conductivity and defect structure of Cr_2O_3. II. Reduced temperatures (< 1000 °C), *Solid State Ionics*. **69** 137–143 (1994).
[5] Z. Lu, J. Zhu, E. Andrew Payzant, M.P. Paranthaman, Electrical Conductivity of the Manganese Chromite Spinel Solid Solution, *Journal of the American Ceramic Society*. **88** 1050–1053 (2005).
[6] W.Z. Zhu, S.C. Deevi, Opportunity of metallic interconnects for solid oxide fuel cells: a status on contact resistance, *Materials Research Bulletin*. **38** 957–972 (2003).
[7] K. Hilpert, D. Das, M. Miller, D.H. Peck, R. Weiß, Chromium Vapor Species over Solid Oxide Fuel Cell Interconnect Materials and Their Potential for Degradation Processes, *Journal of The Electrochemical Society*. **143** 3642–3647 (1996).
[8] E.J. Opila, D.L. Myers, N.S. Jacobson, I.M.B. Nielsen, D.F. Johnson, J.K. Olminsky, et al., Theoretical and Experimental Investigation of the Thermochemistry of $CrO_2(OH)_2$(g), *The Journal of Physical Chemistry A*. **111** 1971–1980 (2007).
[9] H. Yokokawa, T. Horita, N. Sakai, K. Yamaji, M.E. Brito, Y.-P. Xiong, et al., Thermodynamic considerations on Cr poisoning in SOFC cathodes, *Solid State Ionics*. **177** 3193–3198 (2006).
[10] J.J. Bentzen, J.V.T. Høgh, R. Barfod, A. Hagen, Chromium Poisoning of LSM/YSZ and LSCF/CGO Composite Cathodes, *Fuel Cells*. **9** 823–832 (2009).
[11] J.W. Fergus, Effect of cathode and electrolyte transport properties on chromium poisoning in solid oxide fuel cells, *International Journal of Hydrogen Energy*. **32** 3664–3671 (2007).
[12] N. Shaigan, W. Qu, D.G. Ivey, W. Chen, A review of recent progress in coatings, surface modifications and alloy developments for solid oxide fuel cell ferritic stainless steel interconnects, *Journal of Power Sources*. **195** 1529–1542 (2010).
[13] K. Huang, P.Y. Hou, J.B. Goodenough, Reduced area specific resistance for iron-based metallic interconnects by surface oxide coatings, *Materials Research Bulletin*. **36** 81–95 (2001).
[14] S. Fontana, S. Chevalier, G. Caboche, Metallic interconnects for solid oxide fuel cell: Performance of reactive element oxide coating during long time exposure, *Materials and Corrosion*. **62** 650–658 (2011).
[15] Å.H. Persson, L. Mikkelsen, P.V. Hendriksen, M.A.J. Somers, Interaction mechanisms between slurry coatings and solid oxide fuel cell interconnect alloys during high temperature oxidation, *Journal of Alloys and Compounds*. **521** 16–29 (2012).
[16] M. Palcut, L. Mikkelsen, K. Neufeld, M. Chen, R. Knibbe, P.V. Hendriksen, Improved oxidation resistance of ferritic steels with LSM coating for high temperature electrochemical applications, *International Journal of Hydrogen Energy*. **37** 8087–8094 (2012).
[17] Y. Larring, T. Norby, Spinel and Perovskite Functional Layers Between Plansee Metallic Interconnect (Cr-5 wt % Fe-1 wt % Y_2O_3) and Ceramic $(La_{0.85}Sr_{0.15})_{0.91}MnO_3$ Cathode Materials for Solid Oxide Fuel Cells, *Journal of The Electrochemical Society*. **147** 3251–3256 (2000).

[18] B. Hua, J. Pu, W. Gong, J. Zhang, F. Lu, L. Jian, Cyclic oxidation of Mn–Co spinel coated SUS 430 alloy in the cathodic atmosphere of solid oxide fuel cells, *Journal of Power Sources*. **185** 419–422 (2008).
[19] T. Uehara, N. Yasuda, M. Okamoto, Y. Baba, Effect of Mn–Co spinel coating for Fe–Cr ferritic alloys ZMG232L and 232J3 for solid oxide fuel cell interconnects on oxidation behavior and Cr-evaporation, *Journal of Power Sources*. **196** 7251–7256 (2011).
[20] J.W. Stevenson, Z.G. Yang, G.G. Xia, Z. Nie, J.D. Templeton, Long-term oxidation behavior of spinel-coated ferritic stainless steel for solid oxide fuel cell interconnect applications, *Journal of Power Sources*. **231** 256–263 (2013).
[21] S.-I. Lee, J. Hong, H. Kim, J.-W. Son, J.-H. Lee, B.-K. Kim, et al., Highly Dense Mn-Co Spinel Coating for Protection of Metallic Interconnect of Solid Oxide Fuel Cells, *Journal of The Electrochemical Society*. **161** F1389–F1394 (2014).
[22] Z. Yang, G. Xia, S.P. Simner, J.W. Stevenson, Thermal Growth and Performance of Manganese Cobaltite Spinel Protection Layers on Ferritic Stainless Steel SOFC Interconnects, *Journal of The Electrochemical Society*. **152** A1896–A1901 (2005).
[23] N.V. Gavrilov, V.V. Ivanov, A.S. Kamenetskikh, A.V. Nikonov, Investigations of Mn–Co–O and Mn–Co–Y–O coatings deposited by the magnetron sputtering on ferritic stainless steels, *Surface and Coatings Technology*. **206** 1252–1258 (2011).
[24] H.H. Zhang, C.L. Zeng, Preparation and performances of Co–Mn spinel coating on a ferritic stainless steel interconnect material for solid oxide fuel cell application, *Journal of Power Sources*. **252** 122–129 (2014).
[25] H. Kurokawa, C.P. Jacobson, L.C. DeJonghe, S.J. Visco, Chromium vaporization of bare and of coated iron–chromium alloys at 1073 K, *Solid State Ionics*. **178** 287–296 (2007).
[26] L. Chen, E.Y. Sun, J. Yamanis, N. Magdefrau, Oxidation Kinetics of $Mn_{1.5}Co_{1.5}O_4$-Coated Haynes 230 and Crofer 22 APU for Solid Oxide Fuel Cell Interconnects, *Journal of The Electrochemical Society*. **157** B931–B942 (2010).
[27] N. Yamamoto, S. Higashi, S. Kawano, N. Achiwa, Preparation of $MnCo_2O_4$ by a wet method and its metal ion distribution, *Journal of Materials Science Letters*. **2** 525–526 (1983).
[28] S. Naka, M. Inagaki, T. Tanaka, On the formation of solid solution in $Co_{3-x}Mn_xO_4$ system, *Journal of Materials Science*. **7** 441–444 (1972).
[29] E. Rios, J.-L. Gautier, G. Poillerat, P. Chartier, Mixed valency spinel oxides of transition metals and electrocatalysis: case of the $Mn_xCo_{3-x}O_4$ system, *Electrochimica Acta*. **44** 1491–1497 (1998).
[30] A. Purwanto, A. Fajar, H. Mugirahardjo, J.W. Fergus, K. Wang, Cation distribution in spinel $(Mn,Co,Cr)_3O_4$ at room temperature, *Journal of Applied Crystallography*. **43** 394–400 (2010).
[31] H. Bordeneuve, C. Tenailleau, S. Guillemet-Fritsch, R. Smith, E. Suard, A. Rousset, Structural variations and cation distributions in $Mn_{3-x}Co_xO_4$ ($0 \leq x \leq 3$) dense ceramics using neutron diffraction data, *Solid State Sciences*. **12** 379–386 (2010).
[32] B. Boucher, R. Buhl, R. Di Bella, M. Perrin, Etude par des mesures de diffraction de neutrons et de magnétisme des propriétés cristallines et magnétiques de composés cubiques spinelles $Co_{3-x}Mn_xO_4$($0{,}6 \leq x \leq 1{,}2$), *Journal de Physique*. **31** 113–119 (1970).
[33] D.G. Wickham, W.J. Croft, Crystallographic and magnetic properties of several spinels containing trivalent JA-1044 manganese, *Journal of Physics and Chemistry of Solids*. **7** 351–360 (1958).

[34] H. Bordeneuve, A. Rousset, C. Tenailleau, S. Guillemet-Fritsch, Cation distribution in manganese cobaltite spinels $Co_{3-x}Mn_xO_4$ ($0 \leq x \leq 1$) determined by thermal analysis, *Journal of Thermal Analysis and Calorimetry*. **101** 137–142 (2010).
[35] T. Nissinen, M. Leskelä, M. Gasik, J. Lamminen, Decomposition of mixed Mn and Co nitrates supported on carbon, *Thermochimica Acta*. **427** 155–161 (2005).
[36] K. Uusi-Esko, E.-L. Rautama, M. Laitinen, T. Sajavaara, M. Karppinen, Control of Oxygen Nonstoichiometry and Magnetic Property of $MnCo_2O_4$ Thin Films Grown by Atomic Layer Deposition, *Chemistry of Materials*. **22** 6297–6300 (2010).
[37] J.L. Gautier, C. Cabezas, S. Barrato, Reduction electrochimique de $MnCo_2O_4$ prepare a basse et haute temperature, *Electrochimica Acta*. **26** 1377–1382 (1981).
[38] O.I. Gyrdasova, G.V. Bazuev, I.G. Grigorov, O.V. Koryakova, Preparation of $MnCo_2O_4$ whiskers and spheroids through thermal decomposition of $Mn_{1/3}Co_{2/3}C_2O_4 \cdot 2H_2O$, *Inorganic Materials*. **42** 1126–1132 (2006).
[39] A. Restovic, E. Ríos, S. Barbato, J. Ortiz, J.L. Gautier, Oxygen reduction in alkaline medium at thin $Mn_xCo_{3-x}O_4$ ($0 \leq x \leq 1$) spinel films prepared by spray pyrolysis. Effect of oxide cation composition on the reaction kinetics, *Journal of Electroanalytical Chemistry*. **522** 141–151 (2002).
[40] C.N.R. Rao, G.V. Subba Rao, Electrical conduction in metal oxides, *Physica Status Solidi (a)*. **1** 597–652 (1970).
[41] T.O. Mason, Electronic behavior and cationic defects in cubic transition metal oxides, *Physica B+C*. **150** 37–43 (1988).
[42] A. Rousset, C. Tenailleau, P. Dufour, H. Bordeneuve, I. Pasquet, S. Guillemet-Fritsch, et al., Electrical Properties of $Mn_{3-x}Co_xO_4$ ($0 \leq x \leq 3$) Ceramics: An Interesting System for Negative Temperature Coefficient Thermistors, *International Journal of Applied Ceramic Technology*. **10** 175–185 (2013).
[43] Y. Liu, J.W. Fergus, K. Wang, C.D. Cruz, Crystal Structure, Chemical Stabilities and Electrical Conductivity of Fe-Doped Manganese Cobalt Spinel Oxides for SOFC Interconnect Coatings, *Journal of The Electrochemical Society*. **160** F1316–F1321 (2013).
[44] D.R. Ou, M. Cheng, X.-L. Wang, Development of low-temperature sintered Mn–Co spinel coatings on Fe–Cr ferritic alloys for solid oxide fuel cell interconnect applications, *Journal of Power Sources*. **236** 200–206 (2013).
[45] A.D. Sharma, J. Mukhopadhyay, R.N. Basu, Synthesis and Characterization of Nanocrystalline $MnCo_2O_{4-\delta}$ Spinel for Protective Coating Application in SOFC, *ECS Transactions*. **35** 2509–2517 (2011).
[46] T. Kiefer, M. Zahid, F. Tietz, D. Stöver, H.R. Zerfass, Electrical conductivity and thermal expansion coefficientes of spinels in the series $MnCo_{2-x}Fe_xO_4$ for application as a protective layer in SOFC, *Proceedings of the 26th Risö International Symposium on Materials Science : Solid State Electrochemistry*. (2005).
[47] T. Brylewski, W. Kucza, A. Adamczyk, A. Kruk, M. Stygar, M. Bobruk, et al., Microstructure and electrical properties of $Mn_{1+x}Co_{2-x}O_4$ ($0 \leq x \leq 1.5$) spinels synthesized using EDTA-gel processes, *Ceramics International*. **40** 13873–13882 (2014).
[48] A. Petric, H. Ling, Electrical Conductivity and Thermal Expansion of Spinels at Elevated Temperatures, *Journal of the American Ceramic Society*. **90** 1515–1520 (2007).

[49] M.Y. Yoon, E.J. Lee, R.H. Song, H.J. Hwang, Preparation and properties of a $MnCo_2O_4$ for ceramic interconnect of solid oxide fuel cell via glycine nitrate process, *Metals and Materials International*. **17** 1039–1043 (2011).
[50] K. Wang, Y. Liu, J.W. Fergus, Interactions Between SOFC Interconnect Coating Materials and Chromia, *Journal of the American Ceramic Society*. **94** 4490–4495 (2011).
[51] B.-K. Park, J.-W. Lee, S.-B. Lee, T.-H. Lim, S.-J. Park, C.-O. Park, et al., Cu- and Ni-doped $Mn_{1.5}Co_{1.5}O_4$ spinel coatings on metallic interconnects for solid oxide fuel cells, *International Journal of Hydrogen Energy*. **38** 12043–12050 (2013).
[52] V. Miguel-Pérez, A. Martínez-Amesti, M.L. Nó, A. Larrañaga, M.I. Arriortua, The effect of doping $(Mn,B)_3O_4$ materials as protective layers in different metallic interconnects for Solid Oxide Fuel Cells, *Journal of Power Sources*. **243** 419–430 (2013).
[53] Y. Xu, Z. Wen, S. Wang, T. Wen, Cu doped Mn–Co spinel protective coating on ferritic stainless steels for SOFC interconnect applications, *Solid State Ionics*. **192** 561–564 (2011).
[54] J. Xiao, W. Zhang, C. Xiong, B. Chi, J. Pu, L. Jian, Oxidation behavior of Cu-doped $MnCo_2O_4$ spinel coating on ferritic stainless steels for solid oxide fuel cell interconnects, *International Journal of Hydrogen Energy*. (2016).
[55] M.E. dos Santos, R. Aparecido Ferreira, P. Noronha Lisboa-Filho, O. Peña, Cation distribution and magnetic characterization of the multiferroic cobalt manganese Co_2MnO_4 spinel doped with bismuth, *Journal of Magnetism and Magnetic Materials*. **329** 53–58 (2013).
[56] C.D. Kumar, A. Dekich, H. Wang, Y. Liu, W. Tilson, J. Ganley, et al., Transition Metal Doping of Manganese Cobalt Spinel Oxides for Coating SOFC Interconnects, *Journal of The Electrochemical Society*. **161** F47–F53 (2014).
[57] Y. Liu, J.W. Fergus, C.D. Cruz, Electrical Properties, Cation Distributions, and Thermal Expansion of Manganese Cobalt Chromite Spinel Oxides, *Journal of the American Ceramic Society*. **96** 1841–1846 (2013).
[58] T. Mokkelbost, Ø. Andersen, R.A. Strøm, K. Wiik, T. Grande, M.-A. Einarsrud, High-Temperature Proton-Conducting $LaNbO_4$-Based Materials: Powder Synthesis by Spray Pyrolysis, *Journal of the American Ceramic Society*. **90** 3395–3400 (2007).
[59] E. Aukrust, A. Muan, Phase Relations in the System Cobalt Oxide–Manganese Oxide in Air, *Journal of the American Ceramic Society*. **46** 511–511 (1963).
[60] D. a. G. Bruggeman, Berechnung verschiedener physikalischer Konstanten von heterogenen Substanzen. I. Dielektrizitätskonstanten und Leitfähigkeiten der Mischkörper aus isotropen Substanzen, *Annalen Der Physik*. **416** 636–664 (1935).
[61] R. Landauer, Electrical conductivity in inhomogeneous media, in: AIP Conf. Proc., AIP Publishing, 1978: pp. 2–45.
[62] N. Tsuda, K. Nasu, A. Fujimori, K. Siratori, Electronic Conduction in Oxides, Springer Berlin Heidelberg, Berlin, Heidelberg, 2000.
[63] G.V. Bazuev, A.V. Korolyov, Magnetic behavior of $MnCo_2O_{4+\delta}$ spinel obtained by thermal decomposition of binary oxalates, *Journal of Magnetism and Magnetic Materials*. **320** 2262–2268 (2008).
[64] H.S.C. O'Neill, A. Navrotsky, Simple spinels; crystallographic parameters, cation radii, lattice energies, and cation distribution, *American Mineralogist*. **68** 181–194 (1983).

[65] R.J. Hill, J.R. Craig, G.V. Gibbs, Systematics of the spinel structure type, *Physics and Chemistry of Minerals*. **4** 317–339 (1979).
[66] R.D. Shannon, Revised effective ionic radii and systematic studies of interatomic distances in halides and chalcogenides, *Acta Crystallographica Section A*. **32** 751–767 (1976).
[67] L.V. Gambino, A.B. Freeman, N.J. Magdefrau, M. Aindow, ALCHEMI studies of site occupancies in Cr-, Ni-, and Fe-substituted manganese cobaltite spinels, *Journal of Materials Science*. 1–13 (2015).
[68] D.S. McClure, The distribution of transition metal cations in spinels, *Journal of Physics and Chemistry of Solids*. **3** 311–317 (1957).
[69] V. a. M. Brabers, F. van Setten, X-ray photoelectron spectroscopy study of the ionic configuration of the spinel $CuMnCoO_4$, *Journal of Physics D: Applied Physics*. **16** L169 (1983).
[70] P.A. Wright, S. Natarajan, J.M. Thomas, P.L. Gai-Boyes, Mixed-metal amorphous and spinel phase oxidation catalysts: characterization by X-ray diffraction, X-ray absorption, electron microscopy, and catalytic studies of systems containing copper, cobalt, and manganese, *Chemistry of Materials*. **4** 1053–1065 (1992).
[71] B.L. Yang, S.F. Chan, W.S. Chang, Y.Z. Chen, Surface enrichment in mixed oxides of Cu, Co, and Mn, and its effect on CO oxidation, *Journal of Catalysis*. **130** 52–61 (1991).
[72] W.A. Groen, C. Metzmacher, P. Huppertz, S. Schuurman, Aging of NTC Ceramics in the System Mn-Ni-Fe-O, *Journal of Electroceramics*. **7** 77–87 (2001).
[73] Z. Wang, C. Zhao, P. Yang, L. Winnubst, C. Chen, Effect of annealing in O_2 or N_2 on the aging of $Fe_{0.5}Mn_{1.84}Ni_{0.66}O_4$ NTC-ceramics, *Solid State Ionics*. **177** 2191–2194 (2006).
[74] X. Chen, P. Hou, C. Jacobson, S. Visco, L. Dejonghe, Protective coating on stainless steel interconnect for SOFCs: oxidation kinetics and electrical properties, *Solid State Ionics*. **176** 425–433 (2005).
[75] E. Cuciureanu, S. Istrate, N. Rezlescu, On the Time Variation of the Conductivity in Nickel and Copper Ferrites, *Physica Status Solidi (a)*. **6** K37–K38 (1971).
[76] N. Rezlescu, E. Cuciureanu, C. Ioan, E. Luca, Time variation of the electrical conductivity in spinel ferrites, *Physica Status Solidi (a)*. **11** 351–359 (1972).
[77] A.D.D. Broemme, Physico-chemical investigations on Co-Mn-oxide spinels. PhD Thesis., Technische Universiteit Eindhoven, 1990.
[78] G.G. Xia, Z.G. Yang, J. Stevenson, Manganese-Cobalt Spinel Oxides as Surface Modifiers for Stainless Steel Interconnects of Solid Oxide Fuel Cells, *ECS Transactions*. **1** 325–332 (2006).
[79] J. Xiao, W. Zhang, C. Xiong, B. Chi, J. Pu, L. Jian, Oxidation of $MnCu_{0.5}Co_{1.5}O_4$ spinel coated SUS430 alloy interconnect in anode and cathode atmospheres for intermediate temperature solid oxide fuel cell, *International Journal of Hydrogen Energy*. **40** 1868–1876 (2015).
[80] V.A.M. Brabers, A.D.D. Broemme, Low-spin-high-spin transition in the Co_3O_4 spinel, *Journal of Magnetism and Magnetic Materials*. **104–107, Part 1** 405–406 (1992).
[81] Thyssen Krupp, Crofer 22 APU Material Data Sheet No. 4046, (2010).

Manuscript II

Iron and copper doped manganese cobalt spinel oxides as protective coatings for SOFC interconnects

Belma Talic[a,b], Sebastian Molin[b], Peter Vang Hendriksen[b], Kjell Wiik[a], Hilde Lea Lein[a]

[a]*Department of Materials Science and Engineering, Norwegian University of Science and Technology*
[b]*Department of Energy Conversion and Storage, Technical University of Denmark*

Abstract. Three spinel oxide coatings, $MnCo_2O_4$, $MnCo_{1.7}Cu_{0.3}O_4$ and $MnCo_{1.7}Fe_{0.3}O_4$ were investigated for high temperature corrosion protection of the metallic interconnect in solid oxide fuel cell (SOFC) stacks. The coatings were applied to Crofer 22 APU using electrophoretic deposition. Oxidation experiments were carried out in air at 700, 800 and 900 °C for up to 4000 h. All three coating materials reduced the oxidation rate considerably. The difference in oxidation rate between coated and uncoated alloy increased with increasing temperature. The area specific resistance (ASR) was measured in contact with $La_{0.85}Sr_{0.1}Mn_{1.1}O_3$ (LSM), simulating the interaction with the cathode in a SOFC stack. After 4300 h exposure to air at 800 °C the lowest ASR was measured for $MnCo_2O_4$ coated Crofer 22 APU (29 $m\Omega cm^2$). The ASR with iron and copper doped coatings was only marginally higher (31 $m\Omega cm^2$), while the ASR of uncoated Crofer 22 APU exceeded 100 $m\Omega cm^2$. LSM in contact with uncoated Crofer 22 APU contained significant amounts of Cr after the exposure. The spinel coatings effectively prevented Cr-diffusion into LSM. During oxidation, a complex $(Mn,Co,Cr)_3O_4$ reaction layer formed at the coating-alloy interface by diffusion of Co from the coating and Mn and Cr from the alloy.

1. Introduction

Ferritic stainless steels (FSS) are promising materials for the application as interconnects in planar solid oxide fuel cell (SOFC) stacks [1,2]. A number of new FSS grades specifically targeted towards this application have been developed in the recent years [3–5]. At SOFC operating conditions, these alloys typically form a dual layer scale consisting of Cr_2O_3 and $(Mn,Cr)_3O_4$. The formation of these oxides prevents excessive oxidation of the metal, however, due to a modest electrical conductivity, their growth also leads to an increase in area specific resistance (ASR) [6]. Another challenge is that these oxides are prone to form volatile Cr(VI)-

species, that have been shown to degrade the SOFC cathode performance [7,8]. A possible way to mitigate these challenges is to coat the FSS with a protective, electrically conductive material. $(Mn,Co)_3O_4$ spinels are considered promising coating materials for the air side of the interconnect, previously demonstrated to reduce both the ASR [9,10] and the rate of Cr-evaporation from the stainless steel [11]. The most extensively investigated compositions in this system are $MnCo_2O_4$ and $Mn_{1.5}Co_{1.5}O_4$. The former is a cubic spinel, while the latter is a dual phase mixture of cubic $MnCo_2O_4$ and tetragonal Mn_2CoO_4 that transform into a single phase cubic spinel above ca. 400 °C [12,13].

The protective action of these coatings has by some been attributed to their interaction with the thermally grown oxide scale, resulting in the formation of a Cr-rich $(Mn,Co,Cr)_3O_4$ reaction layer at the oxide scale/coating interface [14,15]. This layer is believed to reduce inward transport of oxygen and act as a barrier against outward transport of chromium [16]. However, the thermal expansion coefficient (TEC) decreases with increasing Cr-content in $(Mn,Co,Cr)_3O_4$, leading to an increasing TEC mismatch with the $(Mn,Co)_3O_4$ coating [14,17]. The electrical conductivity of Cr-rich spinel oxides is also orders of magnitude lower than the electrical conductivity of $(Mn,Co)_3O_4$ [14,17]. Due to these issues, there have been some concerns about the implications of this reaction layer on the long-term stability and ASR of $(Mn,Co)_3O_4$ coated interconnects.

Diffusion couple experiments have indicated that doping $(Mn,Co)_3O_4$ with Cu or Fe could be beneficial for reducing both oxidation of FSS and the formation of a $(Mn,Co,Cr)_3O_4$ reaction layer between the coating and alloy [18,19]. We have previously shown that the TEC of $MnCo_2O_4$ is reduced by replacing some of the Co with Fe, resulting in a better match with the other SOFC components [Manuscript I]. Although Fe-doping also reduces the electrical conductivity, the conductivity measured for $MnCo_{1.7}Fe_{0.3}O_4$ at 800 °C (47 S/cm) is still several orders of magnitude higher than the typically reported electrical conductivity of chromia (0.1-0.01 S/cm) [20,21]. Doping with Cu on the other hand improved the electrical conductivity [Manuscript I] and has by others been suggested to enhance densification of the coating [22]. There are a few previous studies where the ASR of FSS coated with Cu or Fe doped $(Mn,Co)_3O_4$ has been characterized. Most of these are limited to relatively short exposure times (< 500 h) and do not provided a detailed investigation of the interaction between the coating and thermally grown oxide scale [22–27]. Furthermore, since the ASR has been measured using different set-ups and contact electrodes in these studies, it is difficult to compare the performance of the different coating materials directly.

In this work we investigate the long term (4000 h) oxidation behavior and ASR of $MnCo_2O_4$, $MnCo_{1.7}Fe_{0.3}O_4$ and $MnCo_{1.7}Cu_{0.3}O_4$ coated Crofer 22 APU. The consequences of forming Cr-rich reaction layers on the ASR are discussed.

2. Experimental

2.1 Sample preparation

A 1 mm plate of Crofer 22 APU (Thyssen Krupp) with the composition given in Table 1 was cut into coupons of 20×20 mm. A 3 mm hole was drilled in one of the corners to allow for hanging in the oxidation furnace. The coupons were ground with SiC-paper, polished down to 1 μm using diamond abrasive, and cleaned in acetone and ethanol for 10 min each in an ultrasonic bath.

Table 1. Composition of Crofer 22 APU alloy used in this study in wt.%. Analyzed by Optical Emission Spectroscopy at Force Technology, Denmark.

Alloy	Fe	Cr	Mn	Ti	La	C	Si	Al
Crofer 22 APU	Bal.	23	0.42	0.068	0.04-0.20[1]	0.003	0.049[2]	0.007

[1]La was not measured by OES. Typical concentration according to manufacturer's datasheet
[2]Determination of Si content by OES is associated with large uncertainty

$MnCo_2O_4$ (MC), $MnCo_{1.7}Fe_{0.3}O_4$ (MCFe) and $MnCo_{1.7}Cu_{0.3}O_4$ (MCCu) spinel powders were prepared by spray pyrolysis of aqueous based nitrate solutions as described in detail elsewhere [Manuscript I]. The powders were calcined at 650 °C for 10 h in air, ball milled overnight in ethanol (Ø 10 mm YSZ milling media), dried, and sieved at 250 μm. The particle size of as-prepared powders was characterized using a Beckman coulter I/S particle size analyzer. Small amounts of each powder were dispersed in ethanol by ultrasonication before analysis.

The spinel powders were deposited on steel coupons using electrophoretic deposition (EPD). The EPD set-up consisted of a 150 ml Teflon box and two 4×4 cm plates of Crofer 22 APU serving as counter electrodes. Suspensions were made by ball milling 5 wt.% of powder in a 50/50 vol.% mixture of isopropanol and ethanol for 48 h (Ø 10 mm YSZ milling media, 500 ml PE-bottles). The steel coupon was mounted in parallel between the counter electrodes at a distance of 15 mm. A constant voltage of 35 V was supplied with the sample connected to the negative terminal. The deposition time was varied between 40-100 s. After drying in room temperature, coatings were sintered in a tubular furnace, first in N_2-H_2 at 900 °C for 2 h, then in air at 800 °C for 2 h. The heating and cooling rates were 120 °C/h. Gasses were bubbled through water at 5 °C to give a moisture content of ca. 1 %. Uncoated Crofer 22 APU was pre-oxidized under the same conditions to serve as a reference.

2.2 Characterization

The oxidation kinetics of spinel coated and bare, pre-oxidized Crofer 22 APU were studied in air at 700 °C, 800 °C and 900 °C in a chamber furnace. There was

no forced air flow (i.e. nearly stagnant conditions) and the humidity content in the furnace was not controlled. Three to five samples of each type were suspended vertically in the furnace. Every 250 h, the furnace was cooled to room temperature (180 °C/h) and the samples were weight on a scale with 0.00001 g accuracy (XS205 Mettler Toledo).

Area specific resistance (ASR) was characterized using the set-up illustrated in Figure 1. Crofer 22 APU was cut into 20×60 mm coupons and two 6 mm holes were drilled in the shorter ends for mounting purposes. A platinum wire (Ø 0.3 mm), was flattened on one end and welded to each coupon along the shorter edge. The coating was subsequently deposited and sintered as described above. Porous $La_{0.85}Sr_{0.1}Mn_{1.1}O_3$ (LSM) (20×20×1mm) plates were spray coated with a 50-60 µm layer of LSM (89 wt.%) and Co_3O_4 (11 wt.%) slurry mixture to serve as contacting plates. The steel coupons and LSM plates were arranged in a stack according to Figure 1a. Gold foil (0.3 mm) connected to gold wires, was placed on the top and bottom of the stack to distribute the current, and a dead load of 7 kg was put on top.

The stack was heated up to 800 °C in a vertical furnace in air and a current of 2 A, corresponding to 0.5 A/cm^2, was applied. The exposure comprised of 2000 h at 800 °C followed by 30 thermal cycles between 800 °C and 100 °C before the temperature was returned to 800 °C and kept for another 2000 h. Temperature was monitored by two S-type thermocouples, one positioned close to the center of the stack and one positioned close to the bottom, as illustrated in Figure 1a. The two thermocouples typically showed a difference of 10 °C at 800 °C. The current was monitored throughout the measurement by recording the voltage drop across an external resistor. The area specific resistance of the steel in contact with LSM was determined from the voltage drop between the Pt-wire connected to the steel and the Pt-wire between the LSM plates (see Figure 1b) according to:

$$ASR = \frac{\Delta V_{sample}}{I} \cdot A_{sample} \quad (1)$$

where ΔV_{sample} is the voltage drop, I is the current and A_{sample} is the nominal contact area (0.04 cm^2) between the steel coupon and LSM plate. Assuming Crofer 22 APU has negligible resistance, this set-up allows for measuring the ASR on each side of the sample independently (ΔV_1 and ΔV_2 in Figure 1b). As a reference, the voltage drop across one plate of LSM was also logged. Ohmic behavior was confirmed by varying the current between 0.1 A and 2 A during a short portion of the measurement.

Microstructural characterization was performed using a scanning electron microscope (SEM, Zeiss Supra 35 Field Emission SEM) equipped with an energy dispersive X-ray (EDX)-detector (Noran System SIX X-ray microanalysis system). Samples were cold vacuum embedded in epoxy, ground and polished in successive steps down to 1 µm, and carbon coated. EDX data were collected at an acceleration voltage of 15 kV and analyzed using the Noran System SIX software (Thermo

Scientific, ver. 2.3). Quantification of the collected spectra was performed by standardless analysis and the results must therefore be considered semi-quantitative. To avoid errors due to overlapping peaks, quantification was based on the K-lines for Cr, Mn, Co and Fe, and the L-lines for Sr and La.

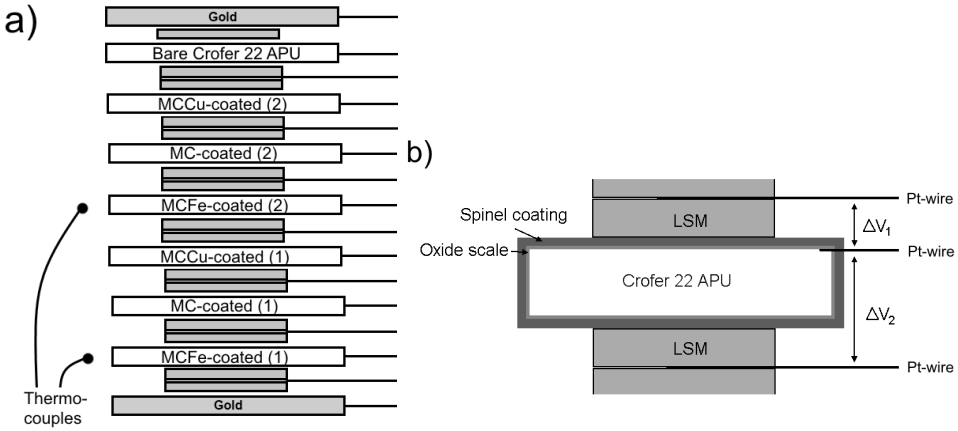

Figure 1. Illustration of set-up for measuring area specific resistance. (a) stacking order of steel samples and LSM plates. (b) illustration showing interfaces over which the voltage drop is measured on each steel sample.

3. Results

3.1 Characterization of as-prepared coatings

The resulting particle size distribution of all powders was bimodal, with median sizes (d_{50}) equal to 0.70 µm for MC, 0.63 µm for MCFe and 1.22 µm MCCu. Cross sectional SEM images of the as-prepared spinel coatings are shown in Figure 2. A ca. 0.6 µm oxide scale has formed at the coating/alloy interfaces due to the sintering heat treatment. The coating compositions, based on EDX analysis of the areas indicated by stippled rectangles in Figure 2, are presented in Table 2. The compositions of the MC and MCFe coatings was close to the nominal composition of the powders, i.e. $MnCo_2O_4$ and $MnCo_{1.7}Fe_{0.3}O_4$, although with a slightly lower Co/Mn fraction than target. The MCCu coating can be divided into roughly two parts based on differences in both composition and morphology. The 2-3 µm of the coating closest to the oxide scale are highly dense, while the remainder of the coating has a density similar to the MC and MCFe coatings. According to EDX analysis (Table 2), the dense part is rich in Fe and lean in Mn and Co, while the porous part contains more Mn and Cu relative to the nominal $MnCo_{1.7}Cu_{0.3}O_4$ composition. An EDX linescan of the oxide scale under the MCCu coating is shown in Figure 3. This reveals significant amounts of Fe in the oxide scale.

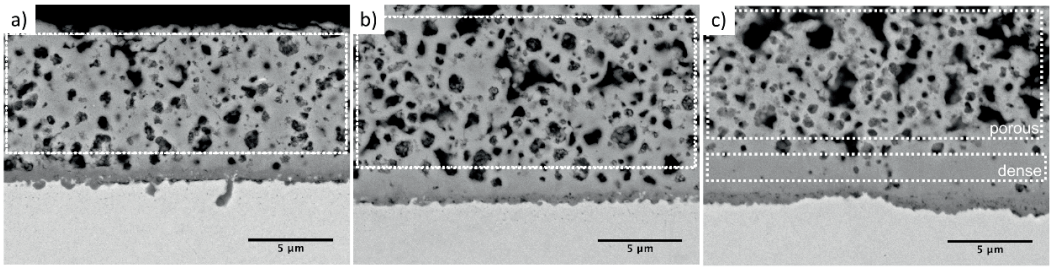

Figure 2: SEM backscatter images of spinel coatings on Crofer 22 APU after heat treatment at 900 °C in N_2-H_2 (2 h) and 800 °C in air (2 h). (a) MC (b) MCFe (c) MCCu. Stippled rectangles show areas analyzed by EDX in Table 2.

Table 2: Composition in wt.% of as-prepared spinel coatings on Crofer 22 APU. The results are integrated over the areas indicated by the stippled lines in Figure 2. The stoichiometry is calculated based on cation fractions.

Coating	Mn	Co	O	Fe	Cu	Cr	Stoichiometry
MC	25.7	45.2	27.9	0.7		0.5	$Mn_{1.12}Co_{1.83}Fe_{0.03}Cr_{0.02}O_4$
MCFe	26.5	40.4	24.1	8.5		0.5	$Mn_{1.09}Co_{1.55}Fe_{0.34}Cr_{0.02}O_4$
MCCu (porous)	27.5	35.2	25.7	0.6	10.6	0.4	$Mn_{1.17}Co_{1.41}Cu_{0.38}Fe_{0.03}Cr_{0.02}O_4$
MCCu (dense)	17.6	25.3	26.6	21.6	6.3	2.6	$Mn_{0.75}Co_{1.01}Cu_{0.23}Fe_{0.9}Cr_{0.12}O_4$

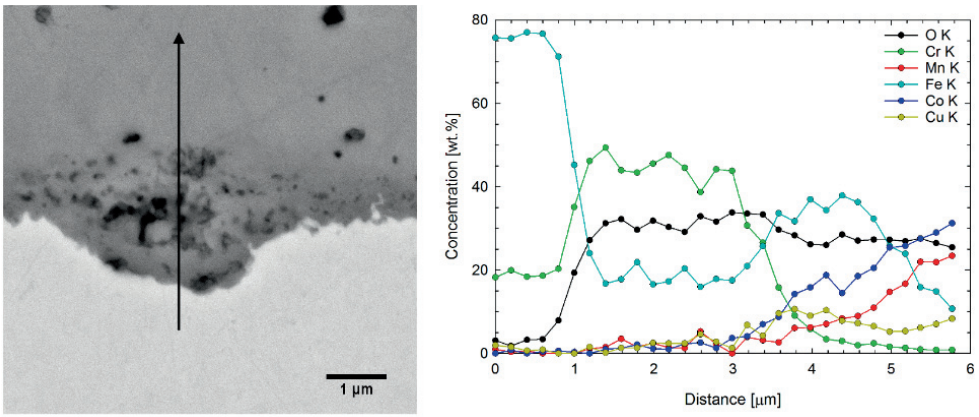

Figure 3: Closer magnification of the oxide scale under the MCCu coating and EDX linescan showing elemental distribution of Cr, Fe, O, Mn, Cu and Co.

3.2 Oxidation kinetics

Since sintering of the coatings leads to some initial mass gain of the underlying alloy substrate, uncoated Crofer 22 APU was heat treated under the same conditions to serve as a reference for the study of the oxidation kinetics. The mass gain of uncoated Crofer 22 APU after 2 h at 900 °C in N_2-H_2 and 2h at 800 °C in air was on average 0.09±0.03 mg/cm^2. Assuming all of this mass gain is oxygen uptake due to Cr_2O_3 formation and that the density of Cr_2O_3 is 5.21 g/cm^3, this mass gain corresponds to the formation of a 0.55 µm thick oxide scale, which is close to oxide scale observed at the coating/alloy interfaces after preparation (Fig. 2). Thus, the starting condition of the alloy should be the same for the pre-oxidized samples as for the spinel coated samples.

The gravimetrically measured mass change of spinel coated and bare, pre-oxidized Crofer 22 APU during cyclic oxidation in air at 700 °C, 800 °C and 900 °C is shown in Figure 4. After 2000 h at 900 °C the total mass gain of the all the spinel coated samples is less than half the mass gain of bare, pre-oxidized Crofer 22 APU. The benefit of the coating appears to decreases with decreasing temperature and at 700 °C the mass gain of some of the coated samples is even higher than the mass gain of the bare alloy. At 700 and 800 °C the mass gain increases in the order MC < MCFe < MCCu. At 900 °C, there is no significant difference between the different spinel coating materials.

The change in mass with time can to close approximation be described by parabolic kinetics:

$$(\Delta m/A)^2 = k_P t + C \qquad (2)$$

where Δm is the mass change [g], A is the sample area [cm^2], k_P is the parabolic rate constant [g^2/cm^{4}s], t is the time [s] and C is an integration constant. The parabolic rate constants were determined by a linear fit of the (mass gain)^2 vs time data and are summarized in Table 3. The mass gain during the first 250 h of oxidation was ignored to avoid potential contributions from transient oxidation kinetics [28]. The mass change during pre-oxidation/sintering of the spinel coatings was not included in the evaluation. The overall fit to the parabolic equation was good for all of the samples ($R^2 > 0.99$) with exception of Crofer 22 APU oxidized at 800 °C, in which case the results were better fitted to two segments: one between 250-1000 h ($k_P = 1.8\times10^{-14}$ g^2/cm^{4}s) and one between 1000-2000 h ($k_P = 2.9\times10^{-14}$ g^2/cm^{4}s). The increase in oxidation rate after 1000 h of exposure was found to correlate with the observation of local break-away oxidation on the sample edges of the uncoated alloy (see Appendix B).

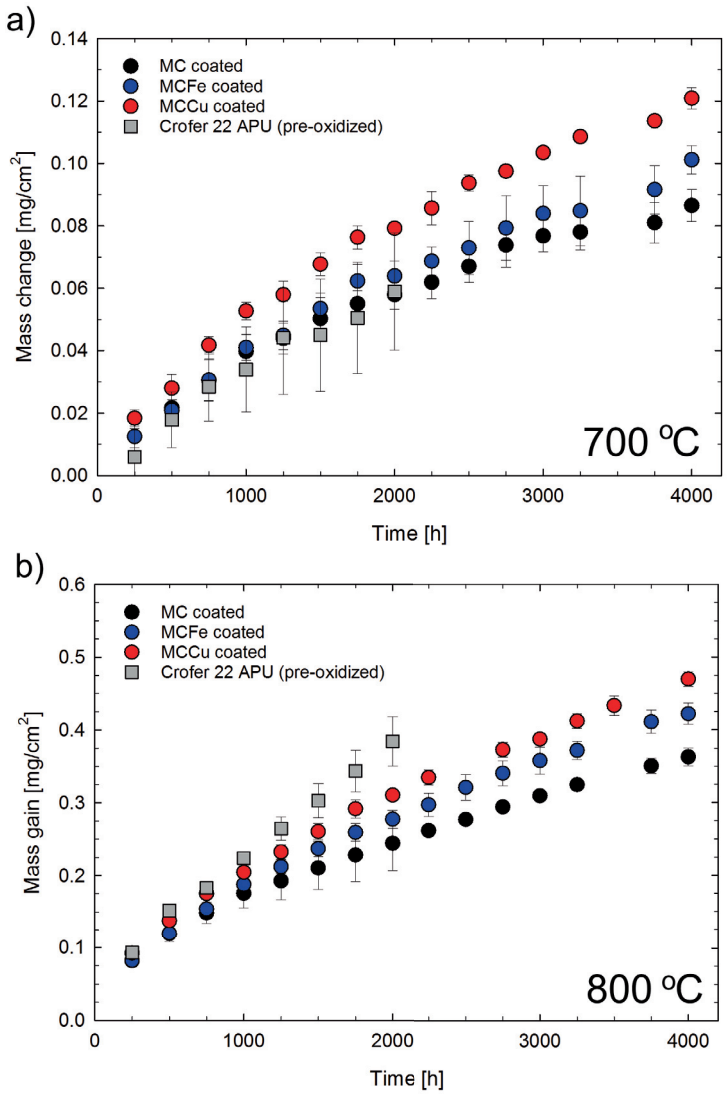

Figure 4: a-c) Mass gain of pre-oxidized and spinel coated Crofer 22 APU during cyclic oxidation in air at (a) 700 °C, (b) 800 °C, and (c) 900 °C. Each point shows the average value measured for 3-5 samples and the error bars show the standard deviation. (d) Arrhenius plot of parabolic rate constant (k_P) as a function of temperature inverse.

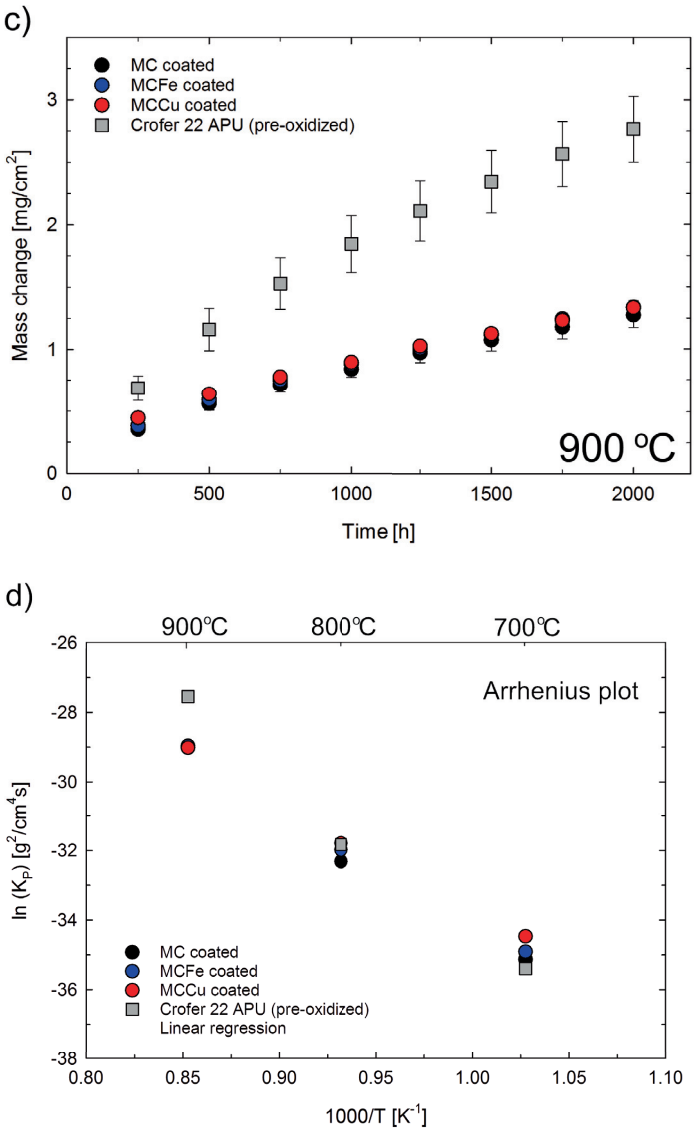

Figure 4. cont… (c) mass gain of pre-oxidized and spinel coated Crofer 22 APU during cyclic oxidation in air at 900 °C. Each point shows the average value measured for 3-5 samples and the error bars show the standard deviation. (d) Arrhenius plot of parabolic rate constant (k_P) as a function of temperature inverse.

Table 3. Parabolic rate constants (k_P) and activation energy for oxidation (E_A) of spinel coated and bare, pre-oxidized Crofer 22 APU in air. The k_P value for Crofer 22 APU was derived from 250-1000 h, after this the oxidation behavior deviated from parabolic kinetics.

Sample	k_p 700 °C [10^{-16} g^2/cm^{4}s]	k_p 800 °C [10^{-14} g^2/cm^{4}s]	k_p 900 °C [10^{-13} g^2/cm^{4}s]	E_A [kJ/mol]
MC coated	5.5	0.9	2.5	289
MCFe coated	6.9	1.3	2.6	281
MCCu coated	11	1.6	2.5	258
Crofer 22 APU	4.3	1.8	11	370

The activation energy for oxidation was determined by fitting the parabolic rate constants to an Arrhenius-type equation, described by:

$$k_P = k_0 \exp\left(-\frac{E_A}{RT}\right) \quad (3)$$

where E_A is the activation energy [kJ/mol], R is the gas constant [kJ/mol K], T is the temperature [K] and k_0 is a constant. The plots of k_P as function of temperature are shown in Figure 3d and the activation energies are listed in Table 3. The parabolic rate constants for the spinel coated samples display good linearity in the investigated temperature range and the obtained activation energies fall within the same range (258-289 kJ/mol). The behavior of uncoated Crofer 22 APU is less linear in the investigated temperature range and the activation energy obtained is significantly higher (370 kJ/mol).

3.3 Area specific resistance

Figure 6 shows ASR development representative for spinel coated and bare Crofer 22 APU in contact with LSM at 800 °C with an applied current density of 0.5 A/cm^2. The average ASR of all tested samples at the end of the measurement (4370 h) are given in Table 4. Note the time range in the figure: all samples were thermally aged at 800 °C for totally 3400 h and exposed to 30 thermal cycles between 800 °C and 100 °C before logging of the ASR was started. Degradation rates were estimated from a linear fit of the ASR curves the last 500 h of measurement and are presented in Table 4. The ASR of bare Crofer 22 increases with a higher rate than the ASR of the spinel coated samples and the final ASR value after 4370 h at 800 °C is more than three times higher. The spinel coated samples have nearly the same ASR value at the end, however, the rate at which the ASR increases, increases in the order MC < MCFe < MCCu. The MC coated sample has the both the lowest final ASR value and the lowest rate of degradation.

The ASR of the LSM reference plate decreases over the entire duration of the measurement.

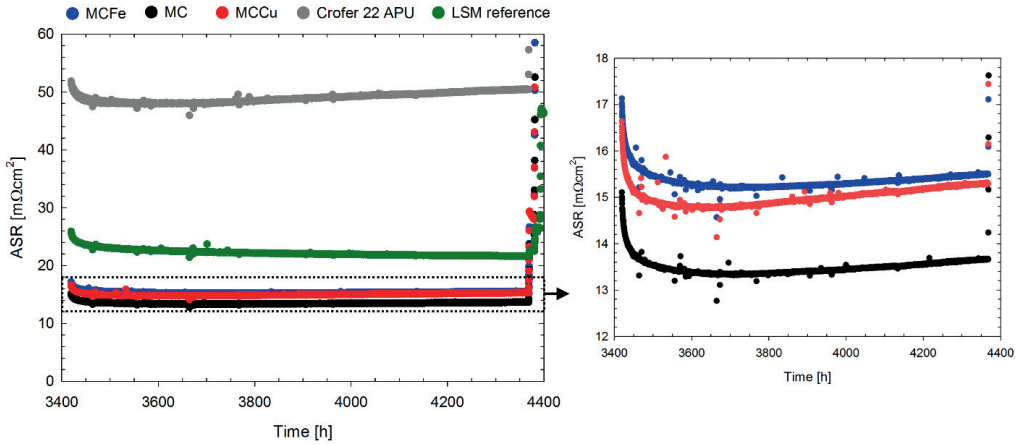

Figure 6: Area specific resistance of spinel coated and bare Crofer 22 APU measured in air at 800 °C using LSM as contacting plates and a current density of 0.5 A/cm^2. The plot to the right is an excerpt of the plot to the left, scaled to better display the difference between the spinel coated samples.

The temperature dependence of the ASR was determined by a step-wise cooling from 800 °C to 300 °C at the end of the measurement and is shown in Figure 7. Each temperature step was held for 10 h to allow for equilibration, however, the change in ASR during this period of time was negligible. The activation energies were determined from the slope of the curves according to:

$$\frac{ASR}{T} = A \cdot exp\left(\frac{E_a}{kT}\right) \tag{4}$$

where A is a pre-exponential factor [Ω/cm^2 K], E_a is the activation energy [kJ/mol], k is Boltzmann's constant [eV/K] and T is the temperature [K]. The temperature dependence of spinel coated and bare Crofer 22 APU was nearly linear over the whole temperature range and the activation energy for the coated samples (66-70 kJ/mol) is slightly larger than the activation energy for bare Crofer 22 APU (55 kJ/mol). The temperature dependence of the LSM reference plate is linear in the range of 300-700°C with an even lower activation energy (38 kJ/mol).

Table 4: Area specific resistance of spinel coated and bare Crofer 22 APU at the end of 4370 h measurement, the linear degradation rate calculated from the ASR slope with time and the activation energy (E_a) determined from the temperature dependence. Values for the spinel coated samples are the average and standard deviation of four individual sample surfaces (see Fig. 1 and Appendix B).

Sample	ASR after 4370 h [mΩcm^2]	Linear degr. rate [mΩcm^2/1000h]	E_a [kJ/mol]
MC coated	13.9±1.1	0.6±0.3	67.5
MCFe coated	15.7±1.9	0,9±0.6	70.4
MCCu coated	15.4±1.1	1.0±0.6	65.6
Bare Crofer 22 APU	50.4	3.6	55.0
LSM-reference	21.6	-1.1	37.6

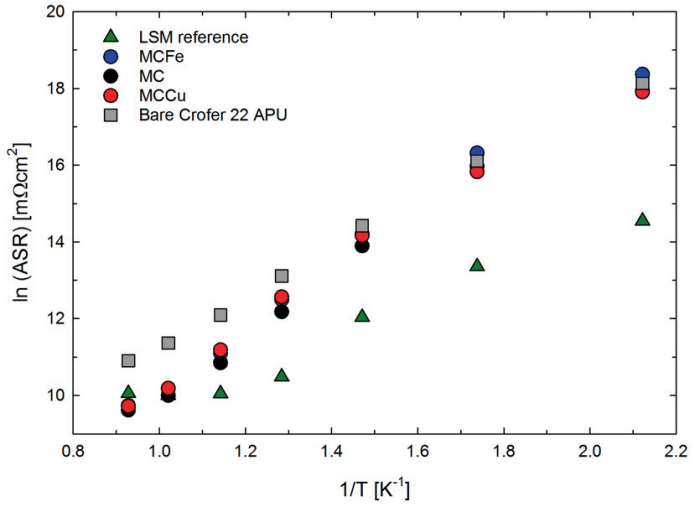

Figure 7: Area specific resistance as a function of temperature determined by step-wise cooling.

3.3 Microstructural characterization after oxidation

3.3.1 After oxidation at 900 °C

Figure 8a shows a cross sectional SEM image of bare Crofer 22 APU after 2000 h of oxidation at 900 °C. The thermally grown oxide scale is seen to consists of two layers, distinguishable by a contrasts difference in the BSE-SEM image. The outer layer was typically 2-4 µm thick with a composition close to $MnCr_2O_4$ according to EDX analysis. The inner layer was 10-13 µm thick and consisted primarily of Cr and O, with the exception of some parts closest to the interface with the alloy, which

were found to be enriched in Mn. The parts rich in Mn are distinguishable in the BSE-SEM images as areas of slightly higher brightness relative to the surrounding scale, and are highlighted in Figure 8a. Some of the Mn-rich oxides were observed to protrude into the alloy, as also seen in Figure 8a.

The typically observed microstructural features of the spinel coated samples after oxidation at 900 °C for 2000 h can be seen in Figures 8b-d. The morphology and thickness of the different layers varied significantly along the interface of all of the samples. The SEM images presented here illustrate this range of variation. In accordance with the mass gain results, the thermally grown oxide scale is significantly thinner for all of the coated samples in comparison with the uncoated alloy. Based on analysis of several representative SEM images, the average oxide scale was found to be slightly thinner under the MC coating (2.8±0.9 μm) than under the MCFe (3.9±1.0 μm) and MCCu (4.5±1.4 μm) coatings. However, the variations in the oxide scale thickness along the interfaces were large, as also indicated by the standard deviations. Similar to the uncoated alloy, the oxide scale consisted of primarily Cr_2O_3 with some enrichment of Mn in areas close to the interface with the alloy.

Figure 9 shows an EDX linescan of the MC coated sample taken across an area where the oxide scale was thin (see Fig. 8b). All of the coatings were found to contain significant amounts of Cr in such areas. From the linescan in Figure 9 it appears that the first 1-2 μm of the coating have a nearly constant composition with a stoichiometry close to $Mn_{0.5}CoCr_{1.5}O_4$. After this, the Cr-content decreases gradually outwards into the coating and drops to below 1 wt.% approximately 8 μm away from the interface with the chromia scale. The parts of the coating containing more than 5 wt.% Cr will from hereon be designated the reaction layer and have been highlighted with a stippled line in Figure 8b-d. The thickness of this reaction layer varied between 0.5-10 μm, with the thickest layers generally observed above the thinnest parts of the chromia scale and vice versa. The largest variations in reaction layer thickness were observed for the MCCu and MCFe coatings, for which a reaction layer was absent altogether along some portions of the interface. For this reason, the average reaction layer thickness could not be accurately determined. For the MC coated sample the reaction layer was more even along the interface, allowing for the average to be estimated to 5.1±1.5 μm.

The outer parts of the spinel coatings, containing less than 5 wt.% of Cr, were characterized by a higher porosity. The Co/Mn fraction in the coating decreased from the interface with the oxide scale to the outer surface, as also seen from the linescan in Figure 8. The Fe content in the MCCu coating after oxidation at 900 °C for 2000 h was nearly constant across the whole coating thickness and on average 5 wt.%. I.e. there was no indication that Fe continued to diffuse from the alloy and into the MCCu coating during oxidation.

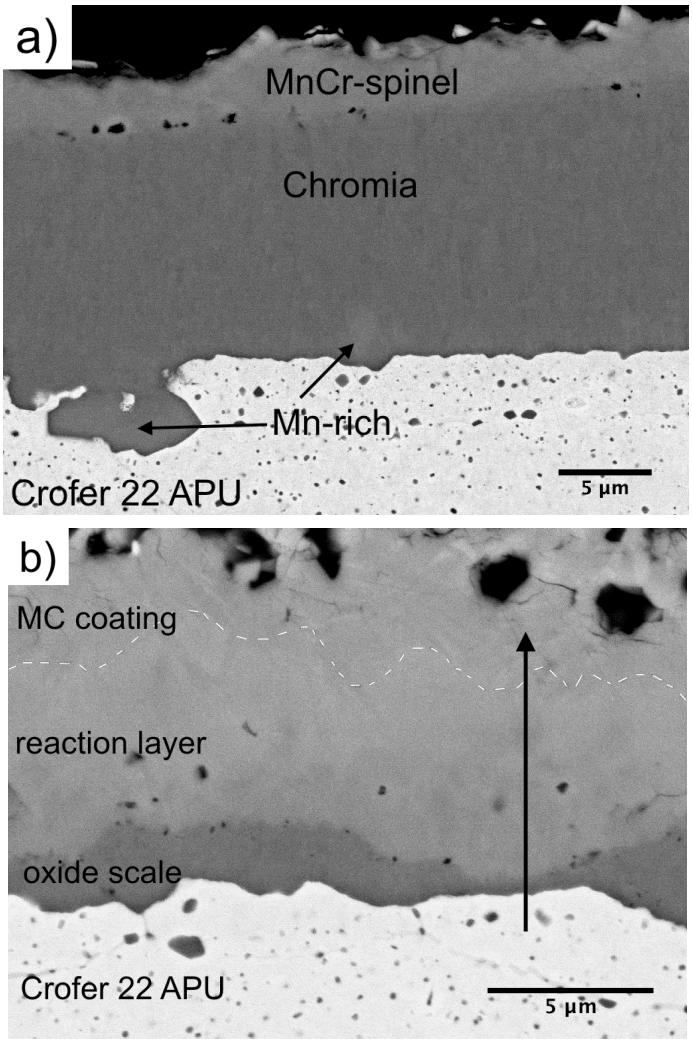

Figure 8: SEM backscatter images of spinel coated and uncoated Crofer 22 APU after 2000 h oxidation at 900 °C. (a) Uncoated Crofer 22 APU (note lower magnification), (b) MC coated (arrow shows position of EDX linescan in Figure 9), (c) MCFe coated, (d) MCCu coated. Stippled lines emphasize the interface between a Cr-containing reaction layer (> 5 wt.% Cr) and the coating.

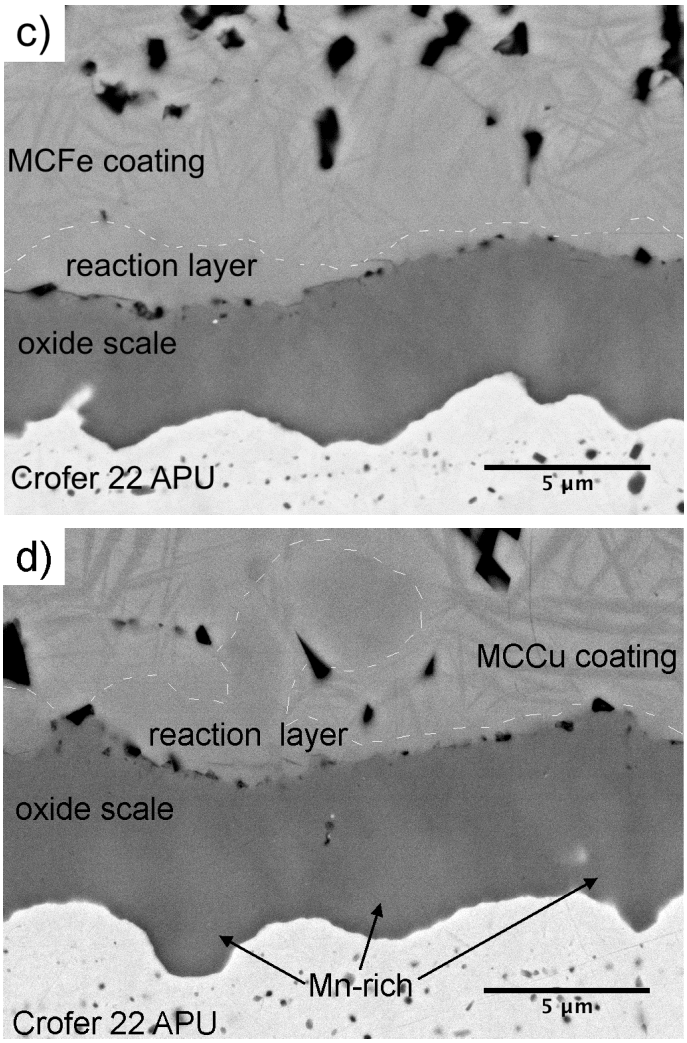

Figure 8. cont… SEM backscatter images of spinel coated Crofer 22 APU after 2000 h oxidation at 900 °C. (c) MCFe coated, (d) MCCu coated. Stippled lines emphasize the interface between a Cr-containing reaction layer (> 5 wt.% Cr) and the coating.

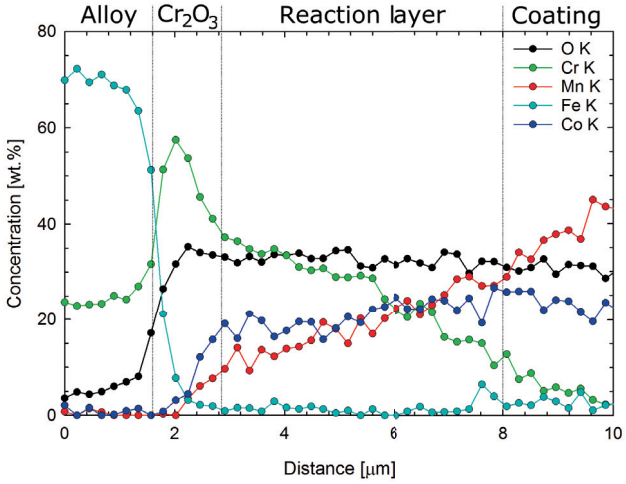

Figure 9. EDX compositional linescan across MC coated Crofer 22 APU after 2000 h oxidation at 900 °C. Figure 8b shows the area analyzed.

3.3.2 After oxidation at 800 °C

After 2000 h oxidation at 800 °C the average thickness of the oxide scale formed on bare Crofer 22 APU was 2.8±0.8 µm. The scale had the same composition as observed after oxidation at 900 °C, i.e. an outer $MnCr_2O_4$ layer, an inner Cr_2O_3 layer and MnCr-oxides along the scale/alloy interface.

Figure 10 shows a SEM image and EDX maps of bare Crofer 22 APU after the ASR measurement (ca. 4370 h at 800 °C). The average thickness of the oxide scale was 3.0±1.1 µm. The LSM contact plates coated with LSM/Co_3O_4 were well adherent to the sample. The EDX maps in Figure 10 reveal significant amounts of Cr in the LSM/Co_3O_4 contact layer and indicate that Cr primarily has reacted with Mn and Co. According to EDX point analysis the average Cr content in the first 20 µm of the contact layer above the oxide scale was 10 wt.%.

Figure 11 shows a SEM image and corresponding EDX maps for one of the MC coated Crofer 22 APU samples after ASR measurement. The results are representative also for the MCFe and MCCu coated samples in terms of coating morphology and overall elemental distribution. The adhesion between all of the coated samples and the LSM plates after measurement was poor. Inspection in SEM revealed that the detachment took place exclusively along the interface between the spinel coating and the LSM-Co_3O_4 contact paste. No delamination or spallation was observed in the coating or oxide scale layers. Based on differences in morphology and composition the coatings could be divided into two main parts. The first 3-5 µm above the chromia scale were highly dense and contained up to 25 wt.% of Cr (in the following referred to as the reaction layer). Above the reaction layer, the coatings were more porous and contained on average < 1 wt.% Cr. The Co content

was nearly constant throughout the whole coating thickness while the Mn content increased from the interface with the chromia scale towards the outer surface of the coating. The Co/Mn fraction in the porous part of the coating was nearly 1. The concentrations of Fe and Cu in the MCFe and MCCu coatings, respectively, were constant in the porous parts of the coatings and decreased towards the interface with the chromia scale. The whole MCCu coating (dense and porous parts) contained on average 6 wt.% Fe after 2000 h of cyclic oxidation and only 2 wt.% Fe after the ASR measurement. No chromium was detected in the first 30 µm of the LSM-Co_3O_4 contact layer in contact with any of the spinel coatings.

The average thickness of the oxide scales and Cr-rich reaction layers after 2000 h of cyclic oxidation and after the ASR measurement are presented in Figure 12. For the ASR samples there were no systematic differences between the oxide scale and coating on the two sides of the sample, i.e. the composition and morphology did not appear to depend on the direction in which the current was passed across the sample.

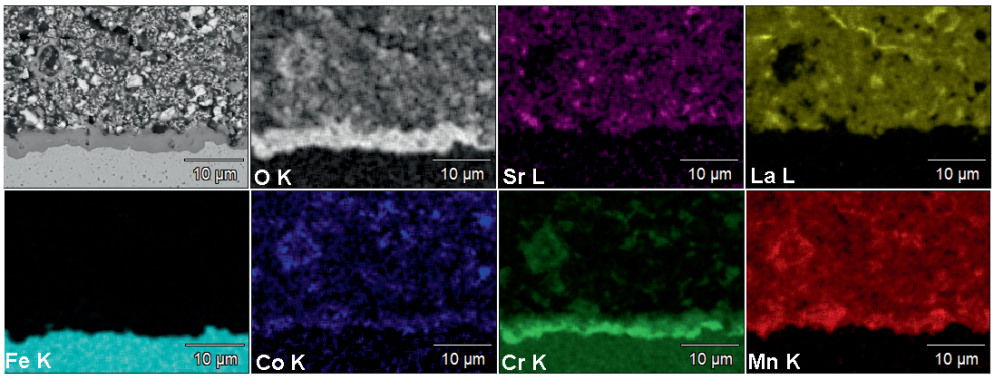

Figure 10: SEM image and EDX maps of bare Crofer 22 APU after area specific resistance measurement at 800 °C for ca. 4370 h.

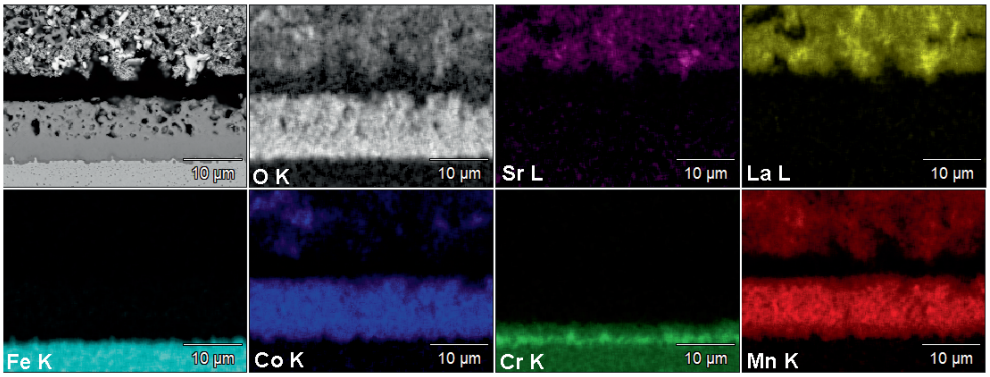

Figure 11: SEM image and EDX maps of MC coated Crofer 22 APU after area specific resistance measurement at 800 °C for ca. 4370 h.

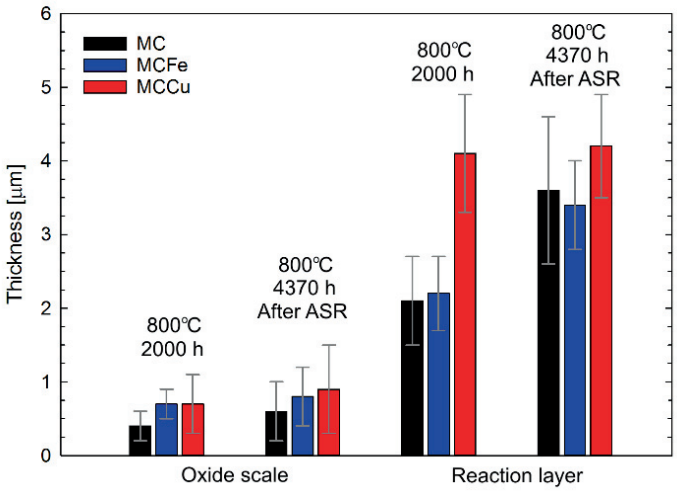

Figure 12: Thickness of oxide scale and Cr-rich reaction layer of spinel coated Crofer 22 APU oxidized in air at 800 °C. Measured after 2000 h of cyclic oxidation and after the ASR measurement.

4. Discussion

4.1 Oxidation kinetics and microstructural development

Assuming the mass gain measured during oxidation is due to oxygen uptake to form pure Cr_2O_3, the oxide scale thickness can be calculated from:

$$t_{Cr_2O_3} = \frac{(\Delta m/A) \cdot 3.167}{\rho(Cr_2O_3)} \quad (5)$$

where $\rho(Cr_2O_3)$ is the density of Cr_2O_3 (5.21 g/cm^3 [29]) and 3.167 is the stoichiometric factor for converting the mass of oxygen to the equivalent mass of Cr_2O_3. The total mass gain of bare Crofer 22 APU after 2000 h of oxidation at 800 °C (including mass gain during pre-oxidation) was 0.48 mg/cm^2, which according to the equation above corresponds to a 2.9 µm Cr_2O_3 scale. This value is very close to the oxide scale thickness measured on SEM images of the sample cross section after oxidation (2.8±0.8 µm). The calculated oxide scale thickness after 2000 h at 900 °C (17.2 µm) also agrees well with the observed oxide scale thickness (15±2 µm), considering that some of the mass gain can be attributed to internal oxidation and that the actual scale formed on the alloy is not pure Cr_2O_3.

For the spinel coated samples the same analysis results in a significantly higher calculated oxide scale thickness than observed on SEM images of the cross

sections. For example, the mass gain of MC-coated Crofer 22 APU after 2000 h at 800 °C (0.24 mg/cm^2) is equivalent to a 1.5 µm thick Cr_2O_3 scale, while the oxide scale thickness measured on SEM images is only 0.4±0.2 µm, i.e. effectively the same as the oxide scale thickness measured after sample preparation. Even after longer time of exposure at 800 °C the oxide scale thickness of MC-coated Crofer 22 APU remains virtually unchanged (0.6±0.4 µm after 4370 h ASR measurement). There is no reason to believe that the coated samples were oxidized more internally. Instead, the increase in mass can be accounted for by the growth of a Cr-containing reaction layer between the coating and oxide scale. The formation of this reaction layer can be described by the following reaction:

$$y\mathrm{Cr} + \left(\frac{3-y}{3}\right)\mathrm{MnCo_2O_4} + \left(\frac{2y}{3}\right)\mathrm{O_2} \rightarrow (\mathrm{MnCo_2})_{\frac{3-y}{3}}\mathrm{Cr}_y\mathrm{O_4} \qquad (6)$$

where it for simplicity is assumed that the Co:Mn fraction remains equal to 2. Assuming all the mass gain that cannot be attributed to growth of an oxide scale is due to formation of a reaction layer according to the equation above, the average amount of Cr in the reaction layer can be estimated from the measured reaction layer thickness by setting up a mass balance:

$$t_{rx(mass)} = t_{rx} \qquad (7)$$

where $t_{rx(mass)}$ is the reaction layer thickness calculated from the measured mass gain and t_{rx} is the reaction layer thickness measured on cross sectional SEM images. $t_{rx(mass)}$ can be calculated from an analogy to equation (5) above:

$$\frac{(\Delta m/A)_{ex} \cdot f}{\rho_{rx}} = t_{rx} \qquad (8)$$

$(\Delta m/A)_{ex}$ is the mass gain that cannot be attributed to growth of an oxide scale and ρ_{rx} is the density of the reaction layer, (estimated to 5.1 g/cm^3 based on the average reported for various $(Mn,Co)_{3-x}Cr_xO_4$ spinels [17]). f is the stoichiometric factor for converting oxygen uptake to the equivalent mass of the reaction layer, given by:

$$f = 3M_{rx}/4yM_O \qquad (9)$$

where M_{rx} is the molar mass of the reaction layer material, M_O is the molar mass of oxygen and y is the fraction of Cr in the reaction layer. The amount of Cr locked up in the reaction layer can then be found by solving for y.

For example, the thickness of the reaction layer measured on MC-coated Crofer 22 APU after 2000 h at 900 °C was 5.1±1.5 µm, the thickness of the oxide scale was 2.8±0.9 µm and the measured mass gain was 1.3±0.1 mg/cm^2. Putting these values into the mass balance results in an average Cr-content of 23±10 wt.% in a 5.1±1.5 µm reaction layer. This amount of Cr is equivalent to 1.8±0.5 µm Cr_2O_3.

Making the same analysis for MC-coated Crofer 22 APU oxidized at 800 °C for 2000 h result in an estimated Cr_2O_3 consumption of 0.45±0.08 μm due to formation of the reaction layer. In both cases, the total Cr_2O_3 thickness, i.e. the Cr_2O_3 thickness measured on SEM images and the Cr_2O_3 thickness estimated to have been consumed by formation of the reaction layer, is less than the oxide scale thickness measured on bare Crofer 22 APU. This infers that the thinner oxide scale observed on spinel coated samples is due to a reduction in the oxidation rate of the alloy.

Others have also reported that $(Mn,Co)_3O_4$ coatings reduce the oxidation rate of FSS [30–32]. On the other hand the same beneficial effect has not been reported for Co coatings, which first transform to Co_3O_4 and then $(Mn,Co)_3O_4$ by interaction with Mn-containing alloys [33,34]. Microstructural investigations of these coating after oxidation do not indicate any formation of a reaction layer between the coating and oxide scale [35]. We therefore suggest that the reduced oxidation rate of $(Mn,Co)_3O_4$ coated FSS may be attributed to the formation of a Cr-containing reaction layer. Horita et al. [16] showed that oxygen diffusion was slower through a Cr-containing reaction layer, formed at the interface between $MnCo_2O_4$ and chromia, than through both the $MnCo_2O_4$ coating and the chromia scale.

The growth of $(Mn,Co,Cr)_3O_4$ reaction layers has previously been studied by Wang et al. [18] using diffusion couples of Cr_2O_3 and $Mn_{1.5}Co_{1.5}O_4$ with Pt-markers at the interface. In this study, the reaction layer consisted of primarily $(Mn,Co)Cr_2O_4$ and was proposed to grow at the Cr_2O_3/$(Mn,Co)Cr_2O_4$ interface by inward diffusion of Mn and Co. Chromium diffused further outward from this reaction layer into the $Mn_{1.5}Co_{1.5}O_4$ pellet. A similar mechanism was proposed by Magdefrau et al. [15] who studied the microstructural development during oxidation of $Mn_{1.5}Co_{1.5}O_4$ coated Crofer 22 APU. According to Wang et al. [18] the growth rate of $(Mn,Co)Cr_2O_4$ is parabolic with a rate constant equal to 2.2×10^{-5} $\mu m^2/s$ at 800 °C. Although there is not enough data in the current study to estimate the growth rate of the reaction layer, it must clearly be lower than that reported by Wang, which predicts a 12.6 μm thick $(Mn,Co)Cr_2O_4$ layer to form after 2000 h at 800 °C. The difference could be due to the different Cr-sources, i.e. a sintered Cr_2O_3 pellet vs. an oxide scale thermally grown on FSS [19]. Magdefrau et al. [15] also reported thinner reaction layers after oxidation of $Mn_{1.5}Co_{1.5}O_4$ coated Crofer 22.

EDX analysis of the spinel coated samples after oxidation (see Fig. 9) revealed a decreasing Co/Mn fraction in the coating from the interface with the chromia scale to the outer surface. The reaction layer has a significantly higher Co/Mn fraction than the original coating, an observation also made in the previously mentioned studies [15,18]. Cation distribution studies of $MnCo_2O_4$ have shown that Mn primarily occupies the octahedral sites in the spinel structure while most of the tetrahedral sites are filled by Co, i.e. the distribution may be written as $(Co)[Mn,Co]O_4$, where the round brackets designate tetrahedral sites and the square brackets designate octahedral sites [12,36,37]. Chromium is known to have the strongest octahedral site preference among the transition metal cations [38,39] and is consequently expected to occupy only octahedral sites in $(Mn,Co,Cr)_3O_4$ [17,37].

The higher Co:Mn fraction in the reaction layer compared to the original spinel material suggests that Cr primarily replaces Mn in the coating. However, considering the growth mechanism suggested by Wang et al. [18], a contributing reason for the higher Co/Mn fraction in the reaction layer may also be faster diffusion of Co than Mn from the coating to the reaction layer/chromia interface. To the best of our knowledge, there are no available studies on the diffusion rates of Mn and Co in $(Mn,Co,Cr)_3O_4$ spinels. However, Lu and Dieckman [40,41] have shown that the diffusion of Co is slightly faster than the diffusion of Mn in several related spinel oxides at 1200 °C. The uneven thickness of the reaction layer along the interfaces may be related to local differences in composition as a result of the reduction heat treatment.

The higher mass gain of spinel coated samples relative to bare, pre-oxidized Crofer 22 APU at 700 °C is probably due to differences in Cr-evaporation rates from the two. We have previously shown that the Cr-evaporation rate from Crofer 22 APU at 800 °C in air-3% H_2O is reduced by a factor of 10-30 by the application of a MCFe coating [Manuscript IV]. The parabolic oxidation rate decreases by more than a factor of ten when the temperature is decreased from 800 °C to 700 °C (Fig. 4), while the rate of Cr-evaporation is known to be less dependent on temperature [42]. Thus, the relative influence of Cr-evaporation on the mass change increases with decreasing temperature. Due to the lack of information about the Cr-evaporation rates under the current conditions of nearly stagnant air, it is not possible to quantify the contribution from Cr-evaporation on the mass change results. Consequently, it is not possible to determine whether the spinel coating reduces the rate of oxide scale formation at 700 °C.

The activation energies for the oxidation of spinel coated samples are in the same range (258-289 kJ/mol) as previously reported for the oxidation of several uncoated FSS [4,42–44]. In these studies, the activation energy was compared to the reported activation energy for cation self-diffusion in Cr_2O_3 (255 kJ/mol [45]), to suggest that oxidation is takes place by outward diffusion of Cr through the oxide scale. The similar activation energy for the spinel coated samples may suggest that the same mechanism is prevalent. The activation energy of oxidation of bare, pre-oxidized Crofer 22 APU is significantly higher (370 kJ/mol) than previously reported for the same alloy by Palcut et al. [43]. This could be due to the influence of Cr-evaporation and/or the pre-oxidation treatment in the current study.

4.2 Area specific resistance

Since the electrical conductivity of spinel oxides decreases with increasing chromium content, there have been some concerns that a fast growing reaction layer could have negative effects on the long term ASR [17,18,46]. For example, at 800 °C the electrical conductivity of $MnCo_2O_4$ is 89 S/cm [Manuscript I], while the electrical conductivity of $Mn_{0.5}Co_{0.5}Cr_2O_4$ is 0.007 S/cm [17]. However, the ASR of spinel coated samples remained low, despite the formation of a reaction layer

considerably thicker than the chromia scale formed on bare Crofer 22 APU. The measured ASR values are in the same range as previously reported in long term studies of $Mn_{1.5}Co_{1.5}O_4$ coated Crofer 22 APU [10] and AISI441 [47] in contact with LSM. Based on the measured thickness of the oxide scale formed on bare Crofer 22 APU (ca. 3 μm) and the ASR measured after 4370 h at 800 °C (ca. 50 $m\Omega cm^2$), the conductivity of the oxide scale can be estimated to be 0.006 S/cm. Assuming the oxide scale on the MC coated sample has the same electrical conductivity, the measured scale thickness (0.6 μm) gives an estimated ASR of 10 $m\Omega cm^2$. If the difference between this estimate and the measured ASR (14 $m\Omega cm^2$) can be attributed to resistance across the reaction layer, the electrical conductivity of the ca. 3.5 μm thick reaction layer may be estimated to 0.09 S/cm. In reality, the electrical conductivity of the chromia scale formed on coated and bare alloy is likely different due to differences in impurity and defect level. The ASR will also be influenced by the contact area with the LSM electrode [48]. Nevertheless, these simple calculations indicate that the ASR mainly is controlled by the thickness of the chromia scale. I.e. the formation of a reaction layer by consumption of the chromia scale is favorable also for the electrical properties of the interconnect.

An acceptable ASR for the whole metallic interconnect during service is typically set to a limit of 100 $m\Omega cm^2$ [6]. As shown in Figure 5, this limit is exceeded by bare Crofer 22 APU already after 4370 h at 800 °C. By making an extrapolation of the linear degradation rates (Table 4), the ASR after 40 000 h at 800 °C is predicted to reach 36±12 $m\Omega cm^2$ for MC coated, 48±24 $m\Omega cm^2$ for MCFe coated, 51±23 $m\Omega cm^2$ for MCCu coated, and 180 $m\Omega cm^2$ for uncoated Crofer 22 APU. Thus, all spinel coated samples should be able to meet the electrical requirements for the interconnect, with MC showing the greatest promise. Besides ensuring a low and more stable ASR, the spinel coatings have the additional benefit of limiting Cr transport into the LSM/Co_3O_4 contact layer, as seen by comparing the EDX maps of uncoated (Fig. 10) and MC coated (Fig. 11) Crofer 22 APU. The protective action of the spinel coatings can be attributed to the formation of the reaction layer, which "binds up" outward diffusing Cr. Evaporation of chromium is typically modest in the conditions under which the ASR was measured, i.e. nearly stagnant air with relatively low $p(H_2O)$ [49]. Consequently, the high amount of Cr detected in LSM/Co_3O_4 that was in contact with uncoated Crofer 22 APU has most likely has been transported there by solid state diffusion and not by gas phase transport.

4.3 Effect of Fe and Cu doping

Both MCFe and MCCu coatings were effective in reducing the oxidation rate and improving the electrical properties of an interconnect alloy, however, at lower temperatures these materials appeared to be less protective than undoped $MnCo_2O_4$. In the as-prepared state, the inner 2-3 μm of the MCCu coating were of a

significantly higher density than the MC and MCFe coatings. Despite this higher initial density, the MCCu coating provided the least amount of protection. This indicates that the densified layer on MCCu, unlike the $(Mn,Co,Cr)_3O_4$ reaction layer formed after longer exposure, is not effective in reducing inward oxygen diffusion. The high density of the inner 2-3 μm of the MCCu coating can be attributed to a volume expansion due to incorporation of a large amount of iron, as seen by comparing the compositions of the dense and porous parts of the MCCu coating in Table 2. Low quantities of iron (< 5 wt.%) have previously been observed in $(Mn,Co)_3O_4$ coatings after sintering [15,50]. This was explained by rapid diffusion of Fe in Co-metal, which is formed during the first heat treatment step of the coating in reducing atmosphere [15,50]. The copper in the MCCu coating is likely reduced to its metallic state during the reduction step, in which the diffusivity of Fe is also known to be high [51]. The amount of Fe in the MCCu coating did not increase with time during subsequent oxidation in air. This indicates that the thermally grown oxide scale, which initially was porous and also contained significant amounts of Fe (Fig. 3), over time densified and impeded further diffusion of Fe outward from the alloy.

The average reaction layer thickness after oxidation at 900 °C could not be determined for MCCu and MCFe, nevertheless, these coatings appeared to overall have a thinner reaction layer than MC. This is in accordance with results from diffusion couple studies, showing that Fe and Cu doping of $Mn_{1.5}Co_{1.5}O_4$ reduces the reaction layer growth rate [18,19]. On the other hand, there was no apparent difference in the growth rate of the reaction layers on MC and MCFe coated samples during oxidation at 800 °C. The reason for these differences is not clear. However, as discussed above, the formation of a $(Mn,Co,Cr)_3O_4$ reaction layer is not necessarily a disadvantage, as this layer is proposed to slow down the inward diffusion of oxygen and consequently the oxidation rate of the alloy. The electrical conductivity of the reaction layer appears to be sufficiently high to not influence the ASR significantly. On the other hand, the impact of the reaction layer growth on the mechanical properties remains to be investigated. Although no spallation of the coating or oxide scale was observed during oxidation, this may become a risk with more rapid thermal cycling, considering that e.g. $Mn_{0.4}Co_{0.6}Cr_2O_4$ has a TEC of 6.8×10^{-6} K^{-1} (20-1000 °C [17]) and $MnCo_2O_4$ has a TEC of 14.4×10^{-6} K^{-1} (50-800 °C). With this in mind, the MCFe coating may be the preferred option, since this material has a TEC of 12.0×10^{-6} K^{-1} in the same temperature range.

5. Conclusion

The oxidation kinetics of Crofer 22 APU coated with MC, MCFe and MCCu have been compared. All of the spinel coatings were found to reduce the oxidation rate of the alloy in air at 800 °C and 900 °C, with the undoped material ($MnCo_2O_4$) resulting in the lowest mass gain at 800 °C. The protective effect of these coatings was attributed to the formation of a $(Mn,Co,Cr)_3O_4$ reaction layer between the

coating and oxide scale, believed to limit the inward diffusion of oxygen. At 700 °C it was not possible to determine whether or not the spinel coatings reduced the oxidation rate, in part because the oxidation rate of bare, pre-oxidized Crofer 22 APU was very low ($k_p = 4.3\times10^{-16}$ g^2/cm^4s).

The ASR of spinel coated and uncoated Crofer 22 APU in contact with LSM was measured over 4300 h in air at 800 °C. At the end of this measurement the ASR of all the spinel coated samples was more than three times lower than the ASR of bare Crofer 22 APU. Again, the MC material resulted in the lowest final ASR value and the lowest rate of ASR increase with time. The reaction layer thickness was concluded to have minor influences on the resistance across the interconnect in comparison with the thickness of the chromia scale. Based on extrapolation of the ASR results, Crofer 22 APU coated with any of the investigated spinel materials should be able to meet the requirement of ASR below 100 $m\Omega cm^2$ after 40 000 h service at 800 °C.

References

[1] P. Kofstad, R. Bredesen, High temperature corrosion in SOFC environments, *Solid State Ionics*. **52** 69–75 (1992).

[2] S. Linderoth, P.V. Hendriksen, M. Mogensen, N. Langvad, Investigations of metallic alloys for use as interconnects in solid oxide fuel cell stacks, *Journal of Materials Science*. **31** 5077–5082 (1996).

[3] R. Hojda, W. Heimann, W.J. Quadakkers, Production-capable materials concept for high-temperature fuel cells, *ThyssenKrupp Techforum*. (2003).

[4] A.W.B. Skilbred, R. Haugsrud, Sandvik Sanergy HT – A potential interconnect material for $LaNbO_4$-based proton ceramic fuel cells, *Journal of Power Sources*. **206** 70–76 (2012).

[5] T. Uehara, N. Yasuda, T. Ohno, A. Toji, Improvement of Oxidation Resistance of Fe-Cr Ferritic Alloy Sheets for SOFC Interconnects, *Electrochemistry*. **77** 131–133 (2009).

[6] W.Z. Zhu, S.C. Deevi, Opportunity of metallic interconnects for solid oxide fuel cells: a status on contact resistance, *Materials Research Bulletin*. **38** 957–972 (2003).

[7] J.J. Bentzen, J.V.T. Høgh, R. Barfod, A. Hagen, Chromium Poisoning of LSM/YSZ and LSCF/CGO Composite Cathodes, *Fuel Cells*. **9** 823–832 (2009).

[8] H. Yokokawa, T. Horita, N. Sakai, K. Yamaji, M.E. Brito, Y.-P. Xiong, et al., Thermodynamic considerations on Cr poisoning in SOFC cathodes, *Solid State Ionics*. **177** 3193–3198 (2006).

[9] Y. Larring, T. Norby, Spinel and Perovskite Functional Layers Between Plansee Metallic Interconnect (Cr-5 wt % Fe-1 wt % Y_2O_3) and Ceramic ($La_{0.85}Sr_{0.15}$)$_{0.91}MnO_3$ Cathode Materials for Solid Oxide Fuel Cells, *Journal of The Electrochemical Society*. **147** 3251–3256 (2000).

[10] F. Smeacetto, A. De Miranda, S. Cabanas Polo, S. Molin, D. Boccaccini, M. Salvo, et al., Electrophoretic deposition of $Mn_{1.5}Co_{1.5}O_4$ on metallic interconnect and interaction with glass-ceramic sealant for solid oxide fuel cells application, *Journal of Power Sources*. **280** 379–386 (2015).

[11] H. Kurokawa, C.P. Jacobson, L.C. DeJonghe, S.J. Visco, Chromium vaporization of bare and of coated iron–chromium alloys at 1073 K, *Solid State Ionics*. **178** 287–296 (2007).
[12] H. Bordeneuve, C. Tenailleau, S. Guillemet-Fritsch, R. Smith, E. Suard, A. Rousset, Structural variations and cation distributions in $Mn_{3-x}Co_xO_4$ ($0 \leq x \leq 3$) dense ceramics using neutron diffraction data, *Solid State Sciences*. **12** 379–386 (2010).
[13] T. Brylewski, W. Kucza, A. Adamczyk, A. Kruk, M. Stygar, M. Bobruk, et al., Microstructure and electrical properties of $Mn_{1+x}Co_{2-x}O_4$ ($0 \leq x \leq 1.5$) spinels synthesized using EDTA-gel processes, *Ceramics International*. **40** 13873–13882 (2014).
[14] J.W. Fergus, Synergism in the design of interconnect alloy–coating combinations solid for oxide fuel cells, *Scripta Materialia*. **65** 73–77 (2011).
[15] N.J. Magdefrau, L. Chen, E.Y. Sun, J. Yamanis, M. Aindow, Formation of spinel reaction layers in manganese cobaltite – coated Crofer22 APU for solid oxide fuel cell interconnects, *Journal of Power Sources*. **227** 318–326 (2013).
[16] T. Horita, H. Kishimoto, K. Yamaji, Y. Xiong, M.E. Brito, H. Yokokawa, et al., Diffusion of oxygen in the scales of Fe–Cr alloy interconnects and oxide coating layer for solid oxide fuel cells, *Solid State Ionics*. **179** 2216–2221 (2008).
[17] Y. Liu, J.W. Fergus, C.D. Cruz, Electrical Properties, Cation Distributions, and Thermal Expansion of Manganese Cobalt Chromite Spinel Oxides, *Journal of the American Ceramic Society*. **96** 1841–1846 (2013).
[18] K. Wang, Y. Liu, J.W. Fergus, Interactions Between SOFC Interconnect Coating Materials and Chromia, *Journal of the American Ceramic Society*. **94** 4490–4495 (2011).
[19] C.D. Kumar, A. Dekich, H. Wang, Y. Liu, W. Tilson, J. Ganley, et al., Transition Metal Doping of Manganese Cobalt Spinel Oxides for Coating SOFC Interconnects, *Journal of The Electrochemical Society*. **161** F47–F53 (2014).
[20] A. Holt, P. Kofstad, Electrical conductivity and defect structure of Cr_2O_3. II. Reduced temperatures (< 1000 °C), *Solid State Ionics*. **69** 137–143 (1994).
[21] J.A. Crawford, R.W. Vest, Electrical Conductivity of Single-Crystal Cr_2O_3, *Journal of Applied Physics*. **35** 2413 (1964).
[22] B.-K. Park, J.-W. Lee, S.-B. Lee, T.-H. Lim, S.-J. Park, C.-O. Park, et al., Cu- and Ni-doped $Mn_{1.5}Co_{1.5}O_4$ spinel coatings on metallic interconnects for solid oxide fuel cells, *International Journal of Hydrogen Energy*. **38** 12043–12050 (2013).
[23] X. Montero, F. Tietz, D. Sebold, H.P. Buchkremer, A. Ringuede, M. Cassir, et al., $MnCo_{1.9}Fe_{0.1}O_4$ spinel protection layer on commercial ferritic steels for interconnect applications in solid oxide fuel cells, *Journal of Power Sources*. **184** 172–179 (2008).
[24] O. Thomann, M. Pihlatie, M. Rautanen, O. Himanen, J. Lagerbom, M. Mäkinen, et al., Development and Application of HVOF Sprayed Spinel Protective Coating for SOFC Interconnects, *Journal of Thermal Spray Technology*. **22** 631–639 (2013).
[25] V. Miguel-Pérez, A. Martínez-Amesti, M.L. Nó, A. Larrañaga, M.I. Arriortua, The effect of doping $(Mn,B)_3O_4$ materials as protective layers in different metallic interconnects for Solid Oxide Fuel Cells, *Journal of Power Sources*. **243** 419–430 (2013).
[26] G. Chen, X. Xin, T. Luo, L. Liu, Y. Zhou, C. Yuan, et al., $Mn_{1.4}Co_{1.4}Cu_{0.2}O_4$ spinel protective coating on ferritic stainless steels for solid oxide fuel cell interconnect applications, *Journal of Power Sources*. **278** 230–234 (2015).

[27] J. Xiao, W. Zhang, C. Xiong, B. Chi, J. Pu, L. Jian, Oxidation behavior of Cu-doped $MnCo_2O_4$ spinel coating on ferritic stainless steels for solid oxide fuel cell interconnects, *International Journal of Hydrogen Energy*. (2016).
[28] S. Molin, M. Chen, P.V. Hendriksen, Oxidation study of coated Crofer 22 APU steel in dry oxygen, *Journal of Power Sources*. **251** 488–495 (2014).
[29] D.R. Lide, CRC Handbook of Chemistry and Physics, CRC Press, 1992.
[30] L. Chen, E.Y. Sun, J. Yamanis, N. Magdefrau, Oxidation Kinetics of $Mn_{1.5}Co_{1.5}O_4$-Coated Haynes 230 and Crofer 22 APU for Solid Oxide Fuel Cell Interconnects, *Journal of The Electrochemical Society*. **157** B931–B942 (2010).
[31] T. Uehara, N. Yasuda, M. Okamoto, Y. Baba, Effect of Mn–Co spinel coating for Fe–Cr ferritic alloys ZMG232L and 232J3 for solid oxide fuel cell interconnects on oxidation behavior and Cr-evaporation, *Journal of Power Sources*. **196** 7251–7256 (2011).
[32] H.H. Zhang, C.L. Zeng, Preparation and performances of Co–Mn spinel coating on a ferritic stainless steel interconnect material for solid oxide fuel cell application, *Journal of Power Sources*. **252** 122–129 (2014).
[33] J. Froitzheim, S. Canovic, M. Nikumaa, R. Sachitanand, L.G. Johansson, J.E. Svensson, Long term study of Cr evaporation and high temperature corrosion behaviour of Co coated ferritic steel for solid oxide fuel cell interconnects, *Journal of Power Sources*. **220** 217–227 (2012).
[34] A. Harthøj, T. Holt, P. Møller, Oxidation behaviour and electrical properties of cobalt/cerium oxide composite coatings for solid oxide fuel cell interconnects, *Journal of Power Sources*. **281** 227–237 (2015).
[35] S. Canovic, J. Froitzheim, R. Sachitanand, M. Nikumaa, M. Halvarsson, L.-G. Johansson, et al., Oxidation of Co- and Ce-nanocoated FeCr steels: A microstructural investigation, *Surface and Coatings Technology*. **215** 62–74 (2013).
[36] E. Rios, J.-L. Gautier, G. Poillerat, P. Chartier, Mixed valency spinel oxides of transition metals and electrocatalysis: case of the $Mn_xCo_{3-x}O_4$ system, *Electrochimica Acta*. **44** 1491–1497 (1998).
[37] A. Purwanto, A. Fajar, H. Mugirahardjo, J.W. Fergus, K. Wang, Cation distribution in spinel $(Mn,Co,Cr)_3O_4$ at room temperature, *Journal of Applied Crystallography*. **43** 394–400 (2010).
[38] A. Navrotsky, O.J. Kleppa, The thermodynamics of cation distributions in simple spinels, *Journal of Inorganic and Nuclear Chemistry*. **29** 2701–2714 (1967).
[39] H.S.C. O'Neill, A. Navrotsky, Cation distributions and thermodynamic properties of binary spinel solid solutions, *American Mineralogist*. **69** 733–753 (1984).
[40] F.-H. Lu, R. Dieckmann, Point defects and cation tracer diffusion in $(Co_xMn_{1-x})_{3-d}O_4$ spinels, *Solid State Ionics*. **67** 145–155 (1993).
[41] F.-H. Lu, R. Dieckmann, Point defects and cation tracer diffusion in $(Co, Fe, Mn)_{3-\delta}O_4$ spinels: I. Mixed spinels $(Co_xFe_{2y}Mn_y)_{3-\delta}O_4$, *Solid State Ionics*. **53–56, Part 1** 290–302 (1992).
[42] H. Falk-Windisch, J.E. Svensson, J. Froitzheim, The effect of temperature on chromium vaporization and oxide scale growth on interconnect steels for Solid Oxide Fuel Cells, *Journal of Power Sources*. **287** 25–35 (2015).
[43] M. Palcut, L. Mikkelsen, K. Neufeld, M. Chen, R. Knibbe, P.V. Hendriksen, Corrosion stability of ferritic stainless steels for solid oxide electrolyser cell interconnects, *Corrosion Science*. **52** 3309–3320 (2010).

[44] T. Brylewski, J. Dąbek, K. Przybylski, Oxidation kinetics study of the iron-based steel for solid oxide fuel cell application, *Journal of Thermal Analysis and Calorimetry*. **77** 207–216 (2004).
[45] P. Kofstad, K.P. Lillerud, On High Temperature Oxidation of Chromium II . Properties of and the Oxidation Mechanism of Chromium, *Journal of The Electrochemical Society*. **127** 2410–2419 (1980).
[46] Z. Lu, J. Zhu, E. Andrew Payzant, M.P. Paranthaman, Electrical Conductivity of the Manganese Chromite Spinel Solid Solution, *Journal of the American Ceramic Society*. **88** 1050–1053 (2005).
[47] J.W. Stevenson, Z.G. Yang, G.G. Xia, Z. Nie, J.D. Templeton, Long-term oxidation behavior of spinel-coated ferritic stainless steel for solid oxide fuel cell interconnect applications, *Journal of Power Sources*. **231** 256–263 (2013).
[48] S. Koch, P.V. Hendriksen, Contact resistance at ceramic interfaces and its dependence on mechanical load, *Solid State Ionics*. **168** 1–11 (2004).
[49] C. Key, J. Eziashi, J. Froitzheim, R. Amendola, R. Smith, P. Gannon, Methods to Quantify Reactive Chromium Vaporization from Solid Oxide Fuel Cell Interconnects, *Journal of The Electrochemical Society*. **161** C373–C381 (2014).
[50] L.V. Gambino, N.J. Magdefrau, M. Aindow, Microstructural effects of the reduction step in reactive consolidation of manganese cobaltite coatings on Crofer 22 APU, *Materials at High Temperatures*. **32** 142–147 (2015).
[51] D.B. Butrymowicz, J.R. Manning, M.E. Read, Fe diffusion in Cu and Cu-alloys, *J. Phys. Chem. Ref. Data*. **5** 103–149 (1976).

Manuscript III

Diffusion couple study of the interaction between Fe and Cu doped $MnCo_2O_4$ and Cr_2O_3

Belma Talic[a,b], Peter Vang Hendriksen[b], Kjell Wiik[a], Hilde Lea Lein[a]

[a]*Department of Materials Science and Engineering, Norwegian University of Science and Technology*
[b]*Department of Energy Conversion and Storage, Technical University of Denmark*

Abstract. Manganese cobalt spinel oxides are used to reduce chromium volatilization from metallic interconnects in solid oxide fuel cell (SOFC) stacks. When spinel oxide coated ferritic stainless steel (FSS) is exposed to the typical SOFC cathode atmosphere, a Cr-rich $(Mn,Co,Cr)_3O_4$ reaction layer forms between the oxide scale and coating. There is some concern that excessive growth of this layer may lead to coating and/or scale spallation. To obtain more knowledge on the reaction layer formation and growth kinetics, diffusion couples of sintered spinel oxide and chromia were studied. By using Pt-particles to mark the original interface, it was revealed that a reaction product rich in cobalt and chromium grows by diffusion of Co^{2+} from the spinel oxide to the chromia/reaction product interface. The growth of this reaction product followed parabolic kinetics. The growth rate decreased with Fe-doping of the $MnCo_2O_4$ spinel and increased with Cu-doping. There were considerable differences in the composition and thickness of the reaction product formed in the diffusion couple experiments compared to previous studies of spinel coated FSS. Possible reasons for these differences are discussed.

1. Introduction

Manganese cobalt spinel oxides are promising coating materials for corrosion protection of metallic interconnects in solid oxide fuel cell (SOFC) stacks [1]. One of the primary functions of these coatings is to reduce the volatilization of chromium at the interconnect surface [2,3]. Otherwise, volatile Cr(VI) species may be transported to and deposited at the cathode/air/electrolyte interface, blocking these electrochemically active sites for reaction and thereby degrading the fuel cell performance [4,5]. The spinel coating also aids in maintaining a low electrical resistivity across the interconnect and can reduce the oxidation rate of the interconnect alloy [6–8].

The protective action of $(Mn,Co)_3O_4$ coatings has by some been attributed to an interaction with the thermally grown oxide scale, resulting in the formation of a Cr-rich $(Mn,Co,Cr)_3O_4$ reaction layer at the oxide scale/coating interface [9,10]. This layer is believed to reduce inward transport of oxygen and act as a barrier

against the outward transport of chromium [10,11]. However, there have been some concerns about the implications of this reaction layer on the long-term stability and area specific resistance (ASR) of $(Mn,Co)_3O_4$ coated interconnects. With increasing Cr-content in $(Mn,Co,Cr)_3O_4$ the thermal expansion coefficient decreases, which leads to a greater TEC mismatch with the $(Mn,Co)_3O_4$ coating [9,12]. This could potentially lead to spallation of the coating or other mechanical damage during thermal cycling. The electrical conductivity of Cr-rich spinel oxides is orders of magnitude lower than the electrical conductivity of $(Mn,Co)_3O_4$ [9,12]. Thus, excessive growth of a $(Mn,Co,Cr)_3O_4$ reaction layer should be avoided.

There are only a few previous studies where the formation and growth of $(Mn,Co,Cr)_3O_4$ has been investigated. Magdefrau et al. [10] performed detailed transmission electron microscopy (TEM) analysis of the reaction product formed on $Mn_{1.5}Co_{1.5}O_4$ coated Crofer 22 APU. Chromium was reported to diffuse in a complicated sequence of fluxes, involving a change from initially outward diffusion from the alloy during sintering of the coating, to inward diffusion during initial exposure, to finally outward diffusion again during longer term exposure. Wang et al. [13] studied the interaction between $Mn_{1.5}Co_{1.5}O_4$ and Cr_2O_3 using diffusion couples. By applying Pt-markers at the original interface, they found that a $(Mn,Co,Cr)_3O_4$ layer grew by diffusion of Co and Mn towards the chromia surface. Wang reported that doping the spinel with Fe or Ti reduced the growth rate of the Cr-rich layer.

In [Manuscript II] we investigated the oxidation rate and ASR of Crofer 22 APU coated with $MnCo_2O_4$, $MnCo_{1.7}Cu_{0.3}O_4$ and $MnCo_{1.7}Fe_{0.3}O_4$. In air at 900 °C all three coatings were found to be equally effective in reducing the oxidation rate of the alloy, however, the thickness of the formed reaction layers was different with the different coating materials. Furthermore, the reaction layer formed on the $MnCo_2O_4$ coated alloy was more than two times thinner than the reaction layer thickness predicted based on the growth rate reported by Wang et al. [13]. To investigate possible reasons for these differences, we have in this work studied the interaction between the coating materials and chromia using diffusion couples. More knowledge about the formation and growth rate of the Cr-rich reaction layer is essential for a better prediction of the lifetime of $(Mn,Co)_3O_4$ coated interconnects.

2. Experimental

$MnCo_2O_4$ (MC), $MnCo_{1.7}Fe_{0.3}O_4$ (MCFe) and $MnCo_{1.7}Cu_{0.3}O_4$ (MCCu) spinel powders were prepared by spray pyrolysis of aqueous based nitrate solutions as described in detail elsewhere [Manuscript I]. After calcination at 650 °C for 10 h, the powders were ball milled overnight in 100 % ethanol (250 ml PE-bottle, Ø 10 mm YSZ balls), dried in a rotavapor and sieved at 250 μm. The particle size after milling was bimodal with the median (d_{50}) equal to 0.70 μm for MC, 0.63

μm for MCFe and 1.22 μm for MCCu [Manuscript II]. Pellets of the spinel powders were prepared by uniaxial pressing in a Ø=20 mm steel die (40 MPa) without use of binder. The spinel pellets were sintered in flowing air at 1100 °C for 5 h and subsequently annealed in air at 800 °C for 12 h (2 °C/min heating and cooling rate). The annealing step was included to re-oxidize the spinel, which is partially decomposed when heated above 1050 °C in air [14,15]. Cr_2O_3 powder was purchased from Alfa Aesar and used as-received (purity: 99 % on basis of metals, BET surface area: 3.4 m^2/g). Pellets were prepared by uniaxial pressing Cr_2O_3 powder in a Ø=20 mm steel die (40 MPa) without use of binder. The pressed pellets were sintered in flowing Ar-5%H_2 at 1500 °C for 2 h (3.3 °C/min heating and cooling rate). The sintered spinel and chromia pellets were ground with #500 SiC paper to make the faces parallel. One face was subsequently polished with diamonds in suspension in successive steps down to 1 μm. The density of the sintered pellets was determined by Archimedes method according to ISO 5017:1998(E) using isopropanol as the immersion liquid. The phase purity was checked on a Bruker D8 X-ray diffractometer (XRD) with Cu-Kα radiation. The pellets were mounted in a large-cavity sample holder using molding clay. Diffractograms were recorded on rotating samples from 15-75° 2θ using a step size of 0.02° and a collection time of 1 s per step.

The interaction of spinel oxides with chromia was studied by placing polished faces of the pellets against each other between two alumina plates. A load of ca. 0.1 MPa was put on top. The original interface between Cr_2O_3 and the spinels was marked by applying a thin layer of colloidal Pt paint (particle size < 0.1 μm) . The diffusion couples were annealed in a vertical furnace in stagnant air at 900 °C for 20-1000 h (heating and cooling rate 120 °C/h). After annealing, the couples were mounted in epoxy resin, cut by a diamond saw perpendicular to the reaction interface and polished with diamond abrasive in successive steps down to 1 μm. The thickness and composition of the reaction zone was characterized by scanning electron microscopy (SEM, Zeiss Supra 35 Field Emission SEM) and energy dispersive X-ray spectroscopy (EDX, Noran System SIX X-ray microanalysis system). EDX data were collected at an acceleration voltage of 15 kV and analyzed using the Noran System SIX software (Thermo Scientific, ver. 2.3). Quantification of the collected spectra was performed by standardless analysis and the results must therefore be considered semi-quantitative. To avoid errors due to overlapping peaks, quantification was based on the K-lines for Cr, Mn, Co, Cu and Fe.

3. Results

3.1 Characterization of starting materials

Figure 1 shows XRD patterns of all samples after sintering. The diffractogram of Cr_2O_3 could be matched to the database file of Cr_2O_3 (JCPDS 38-1479). XRD

patterns of MC, MCFe and MCCu could be indexed to the cubic spinel structure, with peak positions close to the database file of $MnCo_2O_4$ (JCPDS 84-0482). We have previously refined the lattice parameters of the spinel materials after sintering, obtaining 8.298 Å for MC, 8.346 Å for MCFe, and 8.310 Å for MCCu [Manuscript I]. Assuming the compositions are according to target, i.e. $MnCo_2O_4$, $MnCo_{1.7}Fe_{0.3}O_4$ and $MnCo_{1.7}Cu_{0.3}O_4$, the theoretical densities can be calculated to 5.51 g/cm^3, 5.39 g/cm^3 and 5.51 g/cm^3, respectively. With this as a reference, the density of the sintered ceramics were determined to 91 % for the MC pellet, and 95 % for the MCFe and MCCu pellets. The density of the sintered Cr_2O_3 pellet was determined to 95 % (using 5.21 g/cm^3 as the theoretical density [16]).

Figure 2 shows SEM images of the polished surfaces of the sintered spinel and chromia pellets, confirming the high density. The spinel samples have been thermally etched (10 min, 1000 °C, air) after polishing to reveal the grain boundaries. The grain size is generally in the range of 1-3 µm, with the MC sample on average having slightly larger grains that the MCFe and MCCu samples.

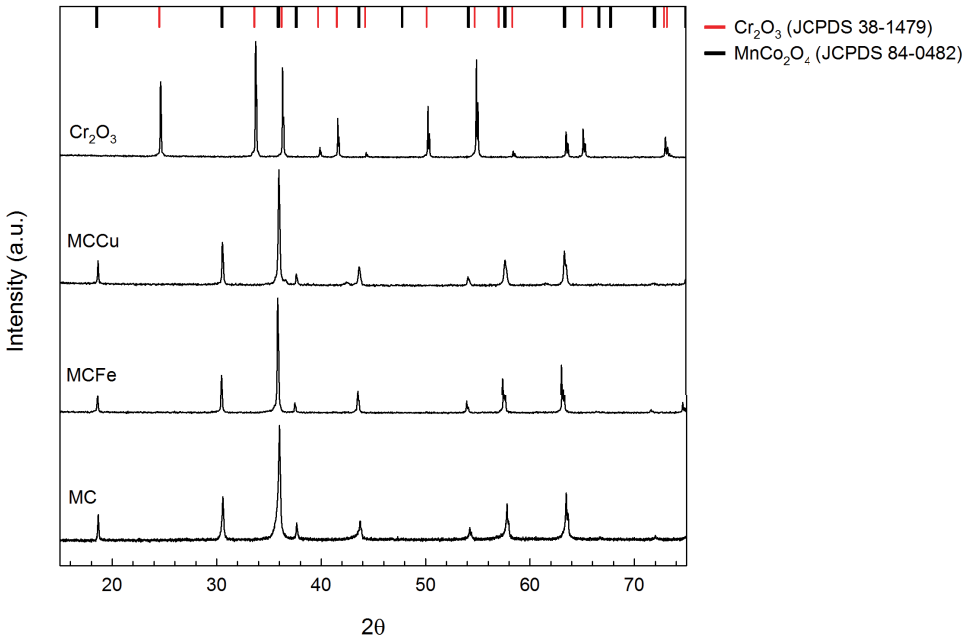

Figure 1. X-ray diffractograms of sintered spinel (air, 1100 °C+800 °C) and Cr_2O_3 (Ar-5%H_2, 1500 °C) pellets.

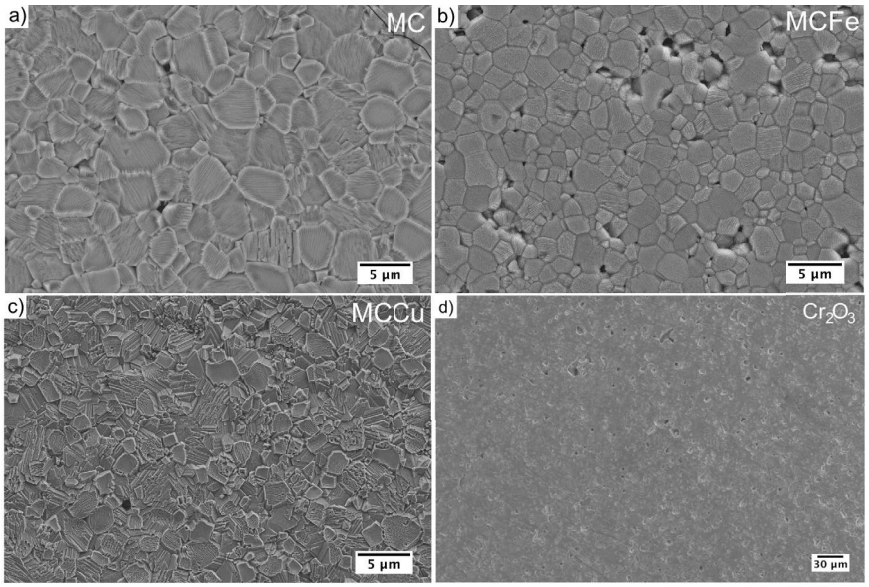

Figure 2. Polished surface of spinel and chromia pellets after sintering. The spinel pellets were thermally etched (1000 °C, 10 min, air) to reveal grain boundaries. (a) MC, (b) MCFe, (c) MCCu, (d) Cr_2O_3.

3.2 Characterization of reaction products

Figures 3 and 4 show representative cross sectional SEM backscatter electron (BSE) images and EDX linescans of the MC-Cr_2O_3 and MCFe-Cr_2O_3 diffusion couples after 300 h at 900 °C. The EDX linescans have been normalized to the total cation fraction based on atomic %. EDX gives inaccurate analysis of oxygen content in this situation, nevertheless, the linescans indicated a tendency for the oxygen content to decrease when going from chromia (ca. 64 at.%) to the spinel (ca. 57 at.%). The reaction product formed at the MC/Cr_2O_3 (Fig. 3) and MCFe/Cr_2O_3 (Fig. 4) interfaces is similar and consists of a single layer. This layer is visible in the SEM-BSE images as a medium gray phase between the lighter gray spinel and the darker gray chromia phases. The composition of the reaction layer according to EDX analysis is approximately $Co_{0.9}Mn_{0.2}Cr_{1.9}O_4$ ($\pm$ 0.1 for fraction of the different cations). The amount of Fe in the product of the MCFe-Cr_2O_3 couple totals to less than a fraction of 0.05 in the composition above. It should be noted that the reaction layer thickness, especially in case of the MCFe-Cr_2O_3 couple, is close to the spatial resolution of EDX. Thus, compositional analysis at the interfaces is not accurate. Nevertheless, there is a steep gradient in Cr-concentration between the product layers and the MC and MCFe spinels, indicating minimal diffusion of Cr into the MC and MCFe materials. The cation

fraction of Cr in MC and MCFe pellets ca. 1 μm from the interface with the reaction product is less than 0.03.

The morphology and composition of the formed reaction products did not change significantly with time (20-1000 h). After 20 h at 900 °C the MC and MCFe spinel pellets could be easily separated from the Cr_2O_3 pellet. The reaction product was then exclusively observed in contact with the spinel materials. After 150 h there was sufficient adhesion between the diffusion couples to allow mounting in epoxy without significant detachment of the two pellets. With extended annealing time, most of the diffusion couples partly cracked after cooling down to room temperature. In all cases, the spinel materials were more severely damaged than chromia, and the MCFe spinel was less damaged compared to the MC spinel.

The interface between MC/MCFe and the reaction product was mostly smooth, while the Cr_2O_3/product interface was wavy. Pt-makers were observed at both of these interfaces and at various locations within the reaction product, as seen in Figure 4. The majority of the Pt-markers were however observed at the spinel/reaction product interface, indicating that the reaction product grows at the Cr_2O_3/product interface. It is possible that the markers observed in other locations became displaced by the reaction front [17]. The composition and thickness of the reaction product did not vary with marker location, hence, it may be assumed that the Pt-markers did not influence the reaction.

Figure 5 shows a representative cross sectional SEM-BSE image and EDX linescan of the MCCu-Cr_2O_3 diffusion couple after 300 h at 900 °C. The reaction product formed in this case is clearly thicker and with a different morphology compared to the reaction product formed with the MC-Cr_2O_3 and MCFe-Cr_2O_3 diffusion couples. The contrast in the SEM-BSE image indicates a two-phase product. The EDX linescan shows that the amount of Cr in the reaction product increases slightly towards the interface with the chromia scale. The overall Cr-fraction in the reaction product is lower and the overall Mn fraction is slightly higher compared to the reaction products described above (cf. Fig. 3 and 4). The reaction layer additionally contains some Cu.

Compositional EDX maps of the MCCu-Cr_2O_3 interface are shown in Figure 6. These reveal that the brighter gray phase of the reaction product is more rich in Mn and lean in Cr compared to the darker gray phase. Based on contrast in the SEM-BSE image it appears that the "bands" of the Mn-rich phase extends nearly all the way to the Cr_2O_3/product interface, but become more narrow upon approaching this interface. It is possible that these bands are responsible for the slightly higher Mn-fraction and presence of Cu in the reaction layer indicated by the linescan (Fig. 5). Other than a relatively thick Mn-rich band located at a distance of 7-8 μm in the linescan, the bands are too narrow to be resolvable by EDX.

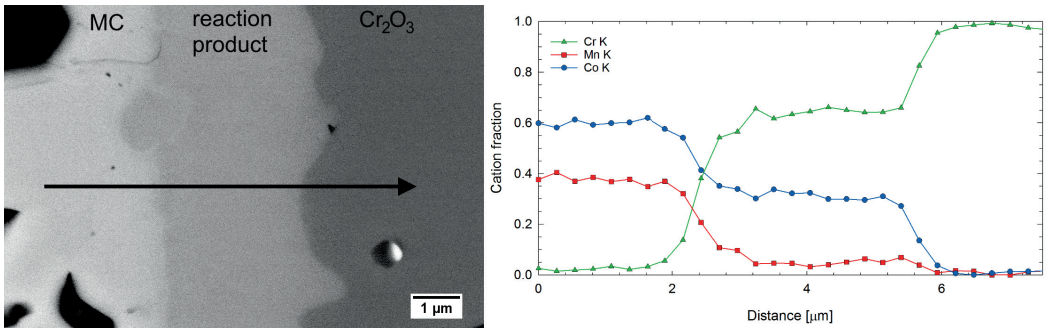

Figure 3. SEM-BSE image and EDX linescan across interface of a MC-Cr_2O_3 diffusion couple annealed 300 h at 900 °C. EDX results are normalized according to the total cation content.

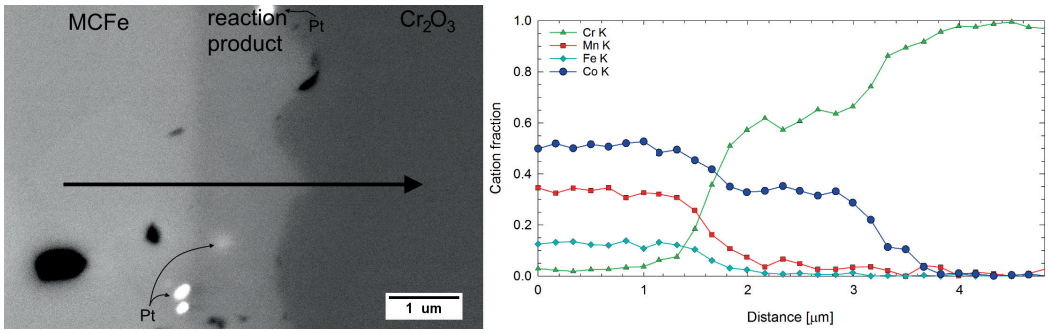

Figure 4. SEM-BSE image and EDX linescan across interface of a MCFe-Cr_2O_3 diffusion couple annealed 300 h at 900 °C. EDX results are normalized according to the total cation content.

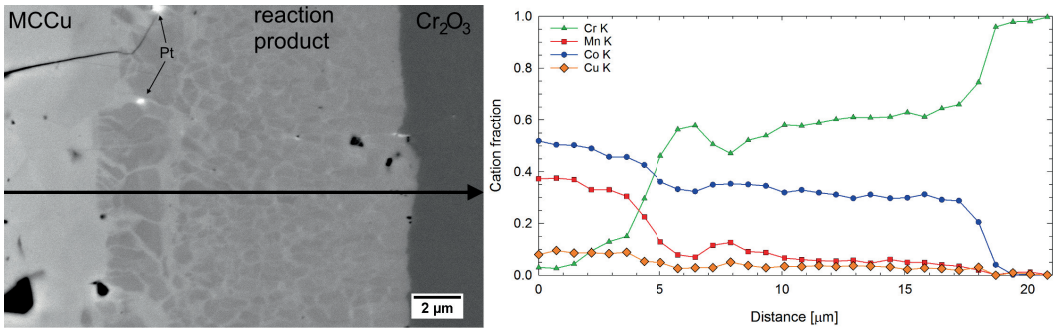

Figure 5. SEM-BSE image and EDX linescan across interface of a MCCu-Cr_2O_3 diffusion couple annealed 300 h at 900 °C. EDX results are normalized according to the total cation content.

Based on the compositional maps in Figure 6 the reaction product may be divided into two main parts. Closest to chromia is a thick layer consisting of Cr-rich "grains" surrounded by Mn-rich bands, while closest to the MCCu spinel is a thinner, apparently single phase, layer containing less Cr. The thin layer corresponds to the shoulder in the Cr-profile observed in Figure 5 (2-4 µm distance). The position of the Pt-markers indicates diffusion of Cr from the thicker layer rich in Cr into the MCCu spinel.

Figure 7a shows a SEM-BSE image of a MCCu-Cr_2O_3 diffusion couple annealed 500 h at 900 °C, in an area close to the outer edge of the couple. Going from left to right in the micrograph, the MCCu spinel is seen to be in close contact with the reaction product, which is followed by an epoxy-filled gap (black), a bright gray phase and finally Cr_2O_3. The bright gray phase was according to EDX point analysis rich in Cr and Cu (23 at.% Cr, 21 at% Cu, 55 at.% O, < 1 at% Co, Mn). This phase was also observed in a few scattered locations along the Cr_2O_3/reaction product interface where these layers were in close contact after mounting in epoxy. However, in such locations the Cu-Cr-rich phase was limited to isolated particles with a diameter of ca. 1-3 µm. A continuous layer of this phase, as seen in Figure 7a, was only observed close to the outer edge of the diffusion couple.

The MCCu material reacted with the alumina plate during annealing, making it difficult to separate the two at the end of experiment. The adhesion was strong already after 150 h of annealing at 900 °C. A SEM image overlaid with EDX maps of the MCCu/alumina plate interface after 500 h at 900 °C is shown in Figure 7b. This reveals precipitation of CuO in areas close to the contact plate.

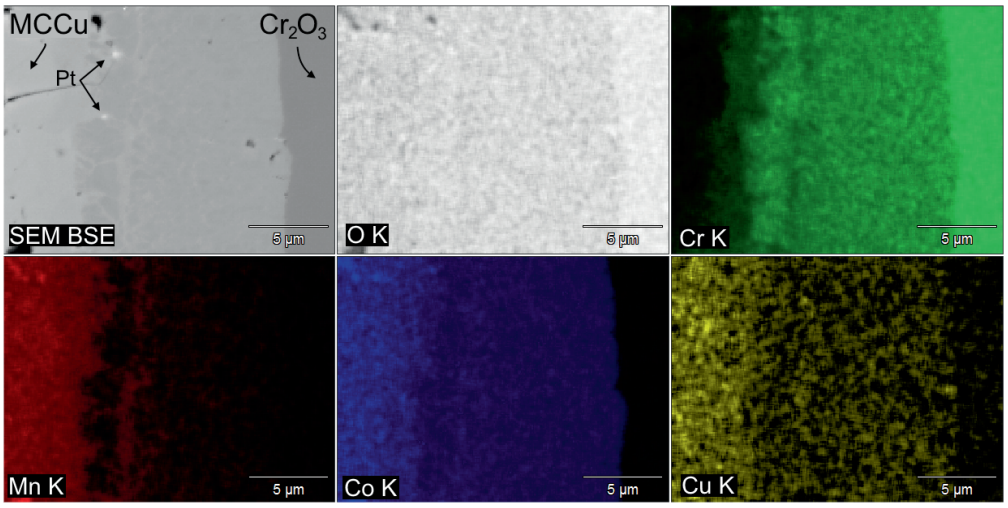

Figure 6. SEM-BSE image and compositional EDX maps of a MCCu-Cr_2O_3 diffusion couple annealed 300 h at 900 °C.

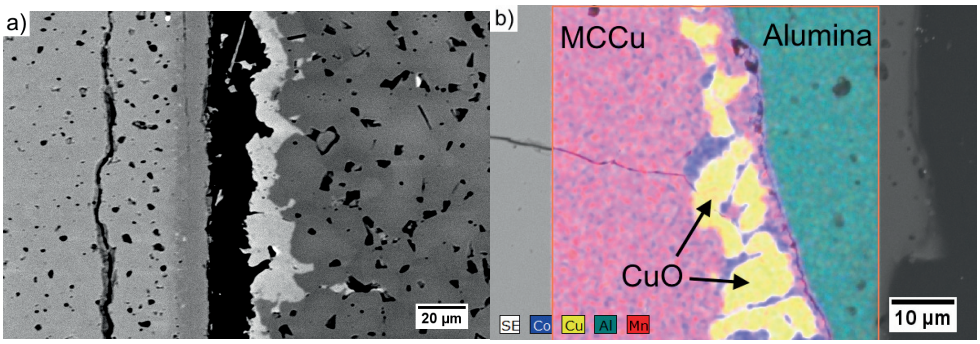

Figure 7. MCCu-Cr_2O_3 diffusion couple annealed 500 h at 900 °C. (a) SEM-BSE image of area close to the outer edge of the couple. Phases from left to right: MCCu, $(Mn,Co,Cu,Cr)_3O_4$ reaction product, epoxy-filled gap, Cr-Cu-rich phase, Cr_2O_3. (b) SEM image overlaid with EDX maps showing the interface between MCCu and the alumina contact plate.

After annealing of all diffusion couples, 5-20 µm sized particles rich in Fe and Cr could be observed in scattered locations within the chromia pellets. These were typically clustered together and located relatively far (> 50 µm) from the interface with the spinel. Since these secondary phases also were observed in chromia pellets annealed with Fe-free spinels (MC, MCCu), the as-received Cr_2O_3 powder likely contained some iron(oxide) impurities. It is not believed that the secondary phases affected the reactivity between chromia and the spinel oxides. No Fe was detected in the reaction layer formed between Cr_2O_3 and the MC and MCCu materials.

3.3 Kinetics of reaction layer formation

The thickness of the reaction product was measured in areas where all layers were in contact after mounting in epoxy. The exception to this was for the MC and MCFe diffusion couples annealed for 20 h, which were completely detached from the Cr_2O_3 pellet. In this cases, the thickness of the reaction product in contact with the spinel was measured. The MC-Cr_2O_3 diffusion couple annealed 1000 h could not be analyzed due to extensive cracking of the sample. For the MCCu-Cr_2O_3 diffusion couples, only the thickness of the Cr-rich spinel was measured.

The reaction layer thickness as a function of annealing time at 900 °C is shown in Figure 8. For all three materials the development of thickness with time can be described as approximately parabolic. Figure 9 shows the thickness plotted in parabolic units, from which the growth rate constants of the reaction product were determined to 1.2×10^{-4} µm^2/s for MCCu, 1.3×10^{-5} µm^2/s for MC, and 8.6×10^{-6} µm^2/s for MCFe. As seen in Figures 8 and 9b, the thickness of the

reaction product formed with the MC and MCFe diffusion couples after 300 h deviates from the otherwise parabolic behavior. These measurement points (shown as half-filled symbols in the plot) have been excluded from the fit of the data. However, including them does not significantly change the value of the rate constants (±1 on the last digit of the respective rate constants).

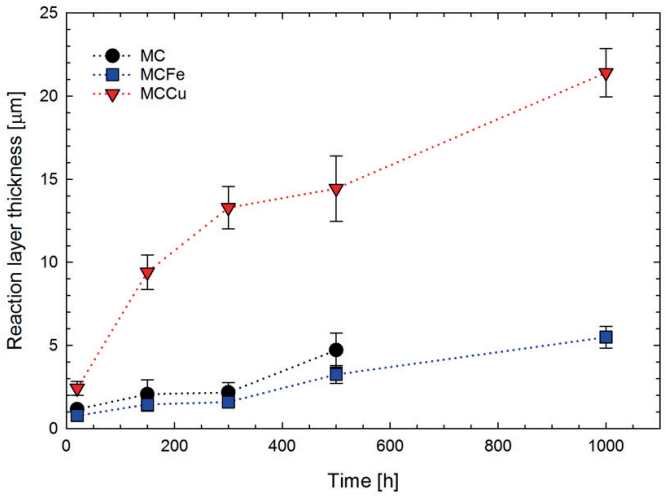

Figure 8. Thickness of reaction layer formed between MC, MCFe, and MCCu spinels and Cr_2O_3 as a function of annealing time at 900 °C in air. The stippled lines are added as a guide to the eye.

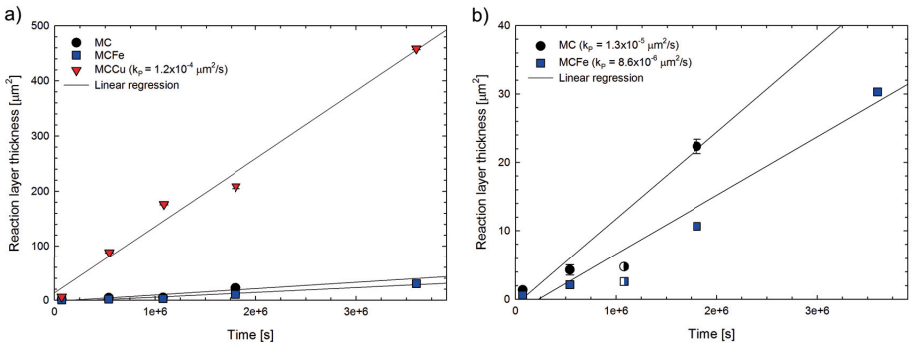

Figure 9. Thickness of reaction layer formed between MC, MCFe, and MCCu spinels and Cr_2O_3 as a function of time, plotted in parabolic units. (a) scaled to units of the MCCu diffusion couple, (b) scaled to units of the MC and MCFe diffusion couples. The half-filled symbols are excluded from the linear regression fit.

4. Discussion

4.1 Interaction between MC/MCFe and Cr_2O_3

The reaction product formed at the interface of the MC-Cr_2O_3 and MCFe-Cr_2O_3 diffusion couples after annealing at 900 °C was essentially the same, consisting of a single layer with a composition approximately equal to $Co_{0.9}Mn_{0.2}Cr_{1.9}O_4$ (Fig. 3, 4). The cationic fraction of Cr in this reaction product is close to the maximum permissible in spinel oxides. The AB_2O_4 spinel structure consists of a nearly cubic close packed arrangement of oxygen ions with 1/8 of the available tetrahedral sites occupied by A^{2+} cations and 1/2 of the available octahedral sites occupied by B^{3+} cations. Cr^{3+} is known to have a very strong preference for the octahedral (B) sites in this structure and is rarely ever found on the tetrahedral (A) sites under normal conditions [18–20]. The maximum cationic fraction of Cr in spinel oxides is therefore 2/3. Within the solid solution of $Co_xCr_{3-x}O_4$ ($1<x<3$), $CoCr_2O_4$ is the composition that is thermodynamically stable over the widest range of temperature and pO_2 [21]. The solubility of both Co and Mn in Cr_2O_3 is negligible [20,22].

The growth rate of $Co_{0.9}Mn_{0.2}Cr_{1.9}O_4$ obeyed parabolic kinetics, which indicates that the rate is controlled by diffusion in this reaction layer. Since a majority of the Pt markers were observed at the spinel/$Co_{0.9}Mn_{0.2}Cr_{1.9}O_4$ interface it may be inferred that the reaction layer grows at the interface with Cr_2O_3 by diffusion of Co^{2+} and Mn^{2+} through $Co_{0.9}Mn_{0.2}Cr_{1.9}O_4$. When reviewing literature on diffusion in $CoCr_2O_4$ and related spinel oxides this indeed seems more probable than a mechanism involving Cr^{3+} diffusion in the opposite direction. Sun [23] reported that the activation energy for Co^{2+} diffusion (51 kJ/mol) in $CoCr_2O_4$ was lower than the activation energy for Cr^{3+} diffusion (70 kJ/mol) in the temperature range of 1400-1600°C in air. The tracer diffusion coefficients of Cr, Co, Fe and Mn have been measured at 1200 °C in $(Mn,Co)_3O_4$ and $(Mn,Co,Fe)_3O_4$ by Lu and Dieckmann [24–26], and in $(Cr,Fe)_3O_4$ by Töpfer et al. [27]. In all of these materials, Cr has a diffusion coefficient three orders of magnitude lower than that of Mn, Co and Fe.

The Co/Mn fraction in the reaction product is considerably higher compared to the Co/Mn fraction in the original MC and MCFe spinels. According to calculations by Persson et al. [28] the Gibbs energy change for a mechanical mixture of Cr_2O_3, Mn_3O_4 and CoO to the equilibrium state at 900 °C becomes more negative with decreasing Mn content in the mixture. I.e. a reaction between the three components becomes thermodynamically more favorable with lower concentrations of Mn. With time however, any difference in diffusivity of Mn^{2+} and Co^{2+} in the reaction product will likely become more important than the thermodynamic driving force for reaction, seeing as the growth rate of the reaction layer is diffusion controlled. At 1200 °C, tracer diffusion coefficients of Co, Mn, and Fe in $(Mn,Co)_3O_4$, $(Mn,Co,Fe)_3O_4$ and $(Cr,Fe)_3O_4$ are within the same order of magnitude, nevertheless, the diffusivity of Co is slightly higher,

particularly at lower pO_2 [24–27]. Thus, kinetics will likely also favor the formation of $CoCr_2O_4$. The same arguments may explain the nearly negligible amount of Fe in the reaction product in case of the MCFe-Cr_2O_3 diffusion couple.

Since very similar reaction products were formed with the MC-Cr_2O_3 and MCFe-Cr_2O_3 diffusion couples, it is not clear why the growth rate was lower for the Fe-substituted material. A possible influencing factor could however be the access of oxygen at the two interfaces. When considering the reaction between Co^{2+} and Cr_2O_3 to form the interface product (omitting Mn for the sake of simplicity):

$$Co^{2+} + O^{2-} + Cr_2O_3 \rightarrow CoCr_2O_4 \quad (1)$$

it is clear that a supply oxygen is needed. The diffusivity of oxide ions is usually lower than the diffusivity of cations in spinel oxides [29]. The supply of oxygen to the reaction above is thus likely by diffusion through grain boundaries and/or cracks along the interfaces. Fewer cracks were observed in the case of the MCFe-Cr_2O_3 diffusion couple compared to MC-Cr_2O_3, thus the slower growth rate could be due to a more limited access of oxygen. The reason for the better mechanical stability of MCFe can be attributed to the closer match in thermal expansion coefficient between this material and chromia, compared to MC and chromia as previously shown in [Manuscript I].

Wang et al. [13] has performed a similar diffusion couple study of the interaction between Cr_2O_3 and $Mn_{1.5}Co_{1.5}O_4$ spinel. Also in their case, a Cr-rich reaction layer with a higher Co/Mn fraction than in the spinel was observed to form at the interface with Cr_2O_3. The parabolic growth rate of this layer was 6.9×10^{-5} $\mu m^2/cm$ at 900 °C. Wang also found a beneficial effect of Fe-substitution, reporting that the parabolic growth rate of the Cr-rich reaction layer decreased to 2.9×10^{-5} $\mu m^2/cm$ for a $MnCo_{1.66}Fe_{0.34}O_4$-Cr_2O_3 diffusion couple. The rate constants reported by Wang are slightly higher but nevertheless in the same order of magnitude as those we have measured for MC and MCFe interacting with Cr_2O_3.

4.1 Reaction layer formation with MCCu

A considerably thicker reaction product, consisting of two main layers, formed at the interface of the MCCu-Cr_2O_3 diffusion couple. The thickest part of this reaction product was observed to consist of two phases, namely Cr-rich grains surrounded by bands containing a relatively higher fraction Mn and Cu (Fig. 5-6). This type of morphology suggests a miscibility gap in the spinel solid solution [30]. The position of the Pt-markers indicates that this two-phase reaction layer grows by diffusion of Co^{2+} (and Mn^{2+}/$Cu^{+/2+}$) from the MCCu spinel to Cr_2O_3, i.e. the same as in the case of the MC-Cr_2O_3 and MCFe-Cr_2O_3 diffusion couples. However, based on the significantly faster growth rate, the diffusion rates

are clearly higher in the reaction layer formed with the MCCu-Cr_2O_3 diffusion couple. It is possible that the Mn-rich bands extending throughout this reaction layer act as fast diffusion paths for Co^{2+}.

The second reaction layer closest to MCCu contained ca. 15 % Cr (cation based). Based on location of the Pt-markers it appears that this layer grows by Cr^{3+} diffusion from the thicker Cr-rich layer into the MCCu spinel. This suggests that the MCCu material may not provide efficient protection against Cr-evaporation when applied as a coating on stainless steel. Grolig et al. [31,32] has measured the Cr-evaporation of ferritic stainless steel with Mn-Cu, Fe-Cu, and Cu-Fe metallic coatings, that are transformed to spinel oxides upon exposure to air at elevated temperatures. All of these coatings were less protective than a Co coating, which is transformed to a $(Mn,Co)_3O_4$ spinel by interaction with Mn diffusing outwards from the alloy.

Although the as-sintered MCCu sample was confirmed to be a phase pure, cubic spinel (Fig. 1), there are several observations questioning the stability of the Cu-substituted material. We have previously shown that CuO may precipitate from $MnCo_{1.5}Cu_{0.5}O_4$ during longer term exposure at elevated temperatures [Manuscript I]. In the current work, we also observed precipitation of CuO after annealing, primarily in areas close to the alumina contact plate (Fig. 7b). On the side of MCCu in contact with Cr_2O_3, a Cr-Cu-rich oxide phase formed at the interface between the $(Mn,Co,Cu,Cr)_3O_4$ reaction layer and Cr_2O_3. Based on EDX analysis results and thermodynamics of the Cr-Cu-O system, this phase is probably $CuCrO_2$ [33]. The amount of $CuCrO_2$ was significantly higher towards the edges of the diffusion couple, where there was a gap between this phase and the $(Mn,Co,Cu,Cr)_3O_4$ reaction product. It is not clear whether the gap was present initially due to poor contact between the MCCu and Cr_2O_3 pellets or whether the pellets separated with time due to formation of $CuCrO_2$. Either way, the access of oxygen can be assumed to be higher close to the edges of the diffusion couple relative to in the center, suggesting a close to atmospheric pO_2 is needed for this phase to form.

The MCCu-Cr_2O_3 diffusion couple results are in contradiction with the results presented by Kumar et al. [34] who studied the interaction between stainless steel 441 and sintered $Mn_{1.5}Co_{0.9}Cu_{0.6}O_4$ pellets. No Cr-rich spinel was observed at the interface after annealing this diffusion couple for 100 h at 900 °C. The reasons for these differences are not clear, but could be related to compositional differences of the Cu-substituted material or the source of Cr, namely sintered Cr_2O_3 vs. stainless steel.

4.3 Comparison to reaction products formed on spinel coated steel

Based on the parabolic growth rate determined for the MC-Cr_2O_3 diffusion couple, the reaction product should grow to ca. 9.7 μm after 2000 h at 900 °C. This is nearly twice the thickness of the reaction product previously observed on

MC coated Crofer 22 APU after 2000 h oxidation at 900 °C (5.1±1.5 µm) [Manuscript II]. As seen in Figure 3, the composition of the reaction product formed with the MC-Cr_2O_3 diffusion couple was $Co_{0.9}Mn_{0.2}Cr_{1.9}O_4$ and nearly constant across the whole layer thickness. This is also in contrast to the observations for the MC coated alloy, where the Cr-content and Co/Mn fraction in the reaction layer gradually decreased from the interface with the chromia scale and outwards.

The difference between the coated alloy and diffusion couple is even greater for the MCCu material. The reaction layer formed on MCCu coated Crofer 22 APU varied too much along the interface to determine an average thickness, however, the interaction was clearly less severe than for the MC coated sample. Furthermore, the two-phase mixture of a Cr-rich and Cr-lean product, and the formation of $CuCrO_2$ or CuO, was not observed in the case of the MCCu coated alloy.

There are a number of possible explanations for these considerable differences in the growth rate and composition of the reaction layer. First of all, the coating is deposited as a powder from suspension and needs to be sintered before exposure. In [Manuscript II] this was done by heat treating first in N_2-H_2 at 900 °C for 2 h and then in air at 800 °C for 2 h. During the first step, the MC spinel is decomposed to MnO and Co, and during the second step these components react to reform the spinel oxide [35,36]. After this sintering heat treatment, the MCCu coating contained ca. 20 wt.% Fe in a 2-3 µm layer closest to the alloy substrate. I.e. the coating effectively had a different composition than the MCCu pellet used in the diffusion couple study. The absence of any phase separations in the coating could indicate that the spinel phase is stabilized by Fe. Reduction and re-oxidation of the coating may as well have led to changes in local composition or defect chemistry of the MC and MCFe materials, affecting their reactivity with the thermally grown oxide scale.

Unlike the spinel pellets, which can be considered a semi-infinite source of $Co^{2+/}Mn^{2+}$ cations, the spinel coatings are relatively thin (< 20 µm). This means that the coating composition is subject to continuous change as Co and Mn cations diffuse into the oxide scale. The change in composition could have decreased the driving force for diffusion with time for the spinel coated samples. The higher porosity of the coating compared to the sintered spinel pellets should also be considered. An increased access of oxygen at the Cr_2O_3 surface could possibly have led to a greater influence by gaseous species, particularly Cr(VI), on the interaction mechanism [37].

Finally, it is important to consider that the thermally grown oxide scale on Crofer 22 APU is not pure Cr_2O_3. The alloy contains ca. 0.4 wt.% Mn and in the absence of a coating, $(Mn,Cr)_3O_4$ is typically formed on top of Cr_2O_3 [38,39]. Gambino et al. [36] showed that during the first step of coating sintering in reducing atmosphere, $(Mn,Cr)_3O_4$ is formed as the main component of the thermally grown oxide scale on Crofer 22 APU. Thus, during subsequent oxidation, the interactions in the alloy-coating system are primarily between

$(Mn,Cr)_3O_4$ and the coating material. This will obviously change the thermodynamic driving force for reaction. According to Östby and Chen [21], Gibbs energy change for the reaction $Co + Cr_2O_3 + ½ O_2 (g) = CoCr_2O_4$ is -47.4 kJ/mol at 1100 °C. Conversely, the exchange reaction $CoO + MnCr_2O_4 = MnO + CoCr_2O_4$ is estimated to have a Gibbs energy change of -9.2 kJ/mol at 1100 °C [40,41].

Suggested mechanisms for growth of a reaction layer in the MC/MCFe-Cr_2O_3 diffusion couple, and spinel coating-alloy systems are illustrated schematically in Figure 10. The growth mechanism for the diffusion couple (Fig. 10a) is similar to that proposed by Wang et al. [13]. As discussed above, $Co_{0.9}Mn_{0.2}Cr_{1.9}O_4$ is formed at the interface with Cr_2O_3 by diffusion of $Co^{2+/}Mn^{2+}$ through the existing layer of this product. The stippled line for Mn^{2+} indicates a slower diffusion of this species. Unlike in the mechanism proposed by Wang, we did not observe significant diffusion of chromium from the reaction product into the MC and MCFe spinels.

A suggested mechanism for forming a reaction layer in the coating-alloy system is illustrated in Figure 10b. Two-stage oxidation experiments with $^{16}O/^{18}O$ have shown that the oxide scale on Crofer 22 APU grows by predominant outward transport of cations [39,42]. I.e. Cr^{3+} and $Mn^{2+/3+}$ diffuse from the alloy to the scale/coating interface. Marker studies of the oxidation of $MnCo_2O_4$ coated E-brite have indicated that the reaction layer also in this case grows by inward diffusion of Co^{2+}/ Mn^{2+}[43]. At the oxide scale/coating interface Cr^{3+} and $Mn^{2+/3+}$ from the alloy may either combine directly with Co^{2+} from the coating or first be oxidized to Cr_2O_3 and/or $(Mn,Cr)_3O_4$ before the reaction product is formed. In both cases, oxygen is supplied via the spinel coating. The additional supply of $Mn^{2+/3+}$ from the alloy to the scale/coating interface is the most likely explanation for the relatively higher fraction of Mn in the reaction layer of spinel coated Crofer 22 APU compared to the reaction layer of the MC/MCFe-Cr_2O_3 diffusion couple.

Manganese cobalt spinel coatings have proved very effective in reducing Cr-evaporation from ferritic stainless steel, nevertheless, outward diffusion of Cr is not completely blocked [2,3]. Outward diffusion of chromium to the coating/atmosphere interface is indicated by the stippled line for Cr^{3+} in Figure 10b.

Although some important differences between the alloy-coating and spinel-Cr_2O_3 systems have been highlighted in the foregoing discussion, the existing results do not allow for a conclusion on the main reason(s) for the difference in reactivity. In particular, the effect of manganese needs to be more carefully investigated. A next step could therefore be to study diffusion couples between MC/MCFe/MCCu and $MnCr_2O_4$. More knowledge on the temperature and pO_2 dependence of the $CoO + MnCr_2O_4 = MnO + CoCr_2O_4$ exchange reaction would also be beneficial for a better understanding of the reactivity in this system.

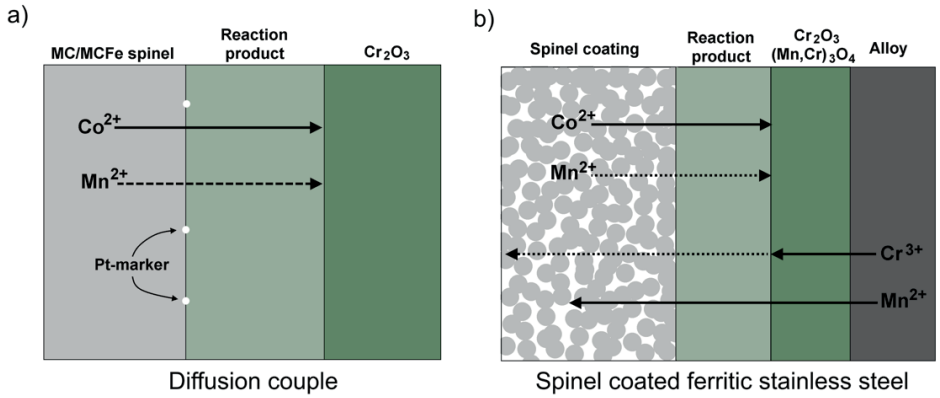

Figure 10. Proposed growth mechanism of a reaction layer for the system of (a) spinel-Cr_2O_3 diffusion couples (b) spinel coated alloy containing Mn.

5. Conclusion

The interaction between Fe and Cu doped $MnCo_2O_4$, and chromia was studied at 900 °C using diffusion couples. With the pure and Fe-doped material a single reaction product with approximately the composition $Co_{0.9}Mn_{0.2}Cr_{1.9}O_4$ formed during annealing. The growth rate of this product followed parabolic kinetics, with the rate constant determined to 1.3×10^{-5} $\mu m^2/s$ for the MC-Cr_2O_3 diffusion couple and 8.6×10^{-6} $\mu m^2/s$ for the MCFe-Cr_2O_3 diffusion couple. In case of the MCCu-Cr_2O_3 diffusion couple, the main reaction product consisted of Cr-rich grains surrounded by bands containing a relatively higher fraction Mn and Cu. The growth of this layer followed parabolic kinetics with a rate equal to 1.2×10^{-4} $\mu m^2/s$. Chromium was observed to diffuse from the Cr-rich reaction layer into the MCCu spinel. By use of Pt-markers it was shown that the reaction layer in all three systems grew by diffusion of Co^{2+} (and Mn/Fe/Cu) to the reaction layer/Cr_2O_3 interface.

The thickness and composition of the diffusion couple reaction layers were significantly different from what we have previously observed on spinel coated ferritic stainless steel after oxidation. Possible explanations for these differences were discussed. The fact that the outer oxide scale formed on most interconnect alloys is $(Mn,Cr)_3O_4$ and not Cr_2O_3 is believed to be particularly important.

References

[1] Y. Larring, T. Norby, Spinel and Perovskite Functional Layers Between Plansee Metallic Interconnect (Cr-5 wt % Fe-1 wt % Y_2O_3) and Ceramic

$(La_{0.85}Sr_{0.15})_{0.91}MnO_3$ Cathode Materials for Solid Oxide Fuel Cells, *Journal of The Electrochemical Society*. **147** 3251–3256 (2000).

[2] H. Kurokawa, C.P. Jacobson, L.C. DeJonghe, S.J. Visco, Chromium vaporization of bare and of coated iron–chromium alloys at 1073 K, *Solid State Ionics*. **178** 287–296 (2007).

[3] R. Trebbels, T. Markus, L. Singheiser, Investigation of Chromium Vaporization From Interconnector Steels With Spinel Coatings, *Journal of Fuel Cell Science and Technology*. **7** 011013–011013 (2009).

[4] K. Hilpert, D. Das, M. Miller, D.H. Peck, R. Weiß, Chromium Vapor Species over Solid Oxide Fuel Cell Interconnect Materials and Their Potential for Degradation Processes, *Journal of The Electrochemical Society*. **143** 3642–3647 (1996).

[5] S.P. Jiang, X. Chen, Chromium deposition and poisoning of cathodes of solid oxide fuel cells – A review, *International Journal of Hydrogen Energy*. **39** 505–531 (2014).

[6] L. Chen, E.Y. Sun, J. Yamanis, N. Magdefrau, Oxidation Kinetics of $Mn_{1.5}Co_{1.5}O_4$-Coated Haynes 230 and Crofer 22 APU for Solid Oxide Fuel Cell Interconnects, *Journal of The Electrochemical Society*. **157** B931–B942 (2010).

[7] J.W. Stevenson, Z.G. Yang, G.G. Xia, Z. Nie, J.D. Templeton, Long-term oxidation behavior of spinel-coated ferritic stainless steel for solid oxide fuel cell interconnect applications, *Journal of Power Sources*. **231** 256–263 (2013).

[8] F. Smeacetto, A. De Miranda, S. Cabanas Polo, S. Molin, D. Boccaccini, M. Salvo, et al., Electrophoretic deposition of $Mn_{1.5}Co_{1.5}O_4$ on metallic interconnect and interaction with glass-ceramic sealant for solid oxide fuel cells application, *Journal of Power Sources*. **280** 379–386 (2015).

[9] J.W. Fergus, Synergism in the design of interconnect alloy–coating combinations solid for oxide fuel cells, *Scripta Materialia*. **65** 73–77 (2011).

[10] N.J. Magdefrau, L. Chen, E.Y. Sun, J. Yamanis, M. Aindow, Formation of spinel reaction layers in manganese cobaltite – coated Crofer22 APU for solid oxide fuel cell interconnects, *Journal of Power Sources*. **227** 318–326 (2013).

[11] T. Horita, H. Kishimoto, K. Yamaji, Y. Xiong, M.E. Brito, H. Yokokawa, et al., Diffusion of oxygen in the scales of Fe–Cr alloy interconnects and oxide coating layer for solid oxide fuel cells, *Solid State Ionics*. **179** 2216–2221 (2008).

[12] Y. Liu, J.W. Fergus, C.D. Cruz, Electrical Properties, Cation Distributions, and Thermal Expansion of Manganese Cobalt Chromite Spinel Oxides, *Journal of the American Ceramic Society*. **96** 1841–1846 (2013).

[13] K. Wang, Y. Liu, J.W. Fergus, Interactions Between SOFC Interconnect Coating Materials and Chromia, *Journal of the American Ceramic Society*. **94** 4490–4495 (2011).

[14] E. Aukrust, A. Muan, Phase Relations in the System Cobalt Oxide–Manganese Oxide in Air, *Journal of the American Ceramic Society*. **46** 511–511 (1963).

[15] H. Bordeneuve, A. Rousset, C. Tenailleau, S. Guillemet-Fritsch, Cation distribution in manganese cobaltite spinels $Co_{3-x}Mn_xO_4$ ($0 \leq x \leq 1$) determined by thermal analysis, *Journal of Thermal Analysis and Calorimetry*. **101** 137–142 (2010).

[16] D.R. Lide, CRC Handbook of Chemistry and Physics, CRC Press, 1992.

[17] P. Kofstad, High Temperature Corrosion, 1988.

[18] D.S. McClure, The distribution of transition metal cations in spinels, *Journal of Physics and Chemistry of Solids*. **3** 311–317 (1957).

[19] H.S.C. O'Neill, A. Navrotsky, Cation distributions and thermodynamic properties of binary spinel solid solutions, *American Mineralogist*. **69** 733–753 (1984).

[20] A.N. Hansson, S. Linderoth, M. Mogensen, M.A.J. Somers, X-ray diffraction investigation of phase stability in the Co–Cr–O and the Fe–Co–Cr–O systems in air at 1323 K, *Journal of Alloys and Compounds*. **402** 194–200 (2005).
[21] J. Östby, M. Chen, Thermodynamic assessment of the CoOx–$CrO_{1.5}$ system, *Journal of Alloys and Compounds*. **485** 427–434 (2009).
[22] A. Naoumidis, H.A. Schulze, W. Jungen, P. Lersch, Phase studies in the chromium-manganese-titanium oxide system at different oxygen partial pressures, *Journal of the European Ceramic Society*. **7** 55–63 (1991).
[23] R. Sun, Diffusion of Cobalt and Chromium in Chromite Spinel, *The Journal of Chemical Physics*. **28** 290–293 (1958).
[24] F.-H. Lu, R. Dieckmann, Point defects and cation tracer diffusion in $(Co,Fe,Mn)_{3-\delta}O_4$ spinels: I. Mixed spinels $(Co_xFe_{2y}Mn_y)_{3-\delta}O_4$, *Solid State Ionics*. **53–56, Part 1** 290–302 (1992).
[25] F.-H. Lu, R. Dieckmann, Point defects and cation tracer diffusion in $(Co,Fe,Mn)_{3-\delta}O_4$ spinels: II. Mixed spinels $(Co_xFe_zMn_{2z})_{3-\delta}O_4$, *Solid State Ionics*. **59** 71–82 (1993).
[26] F.-H. Lu, R. Dieckmann, Point defects and cation tracer diffusion in $(Co_xMn_{1-x})_{3-d}O_4$ spinels, *Solid State Ionics*. **67** 145–155 (1993).
[27] J. Töpfer, S. Aggarwal, R. Dieckmann, Point defects and cation tracer diffusion in $(Cr_xFe_{1-x})_{3-\delta}O_4$ spinels, *Solid State Ionics*. **81** 251–266 (1995).
[28] Å.H. Persson, L. Mikkelsen, P.V. Hendriksen, M.A.J. Somers, Interaction mechanisms between slurry coatings and solid oxide fuel cell interconnect alloys during high temperature oxidation, *Journal of Alloys and Compounds*. **521** 16–29 (2012).
[29] H. Schmalzried, Chemical kinetics of solids, VCH, Weinheim ; New York, 1995.
[30] F.J.J. van Loo, Multiphase diffusion in binary and ternary solid-state systems, *Progress in Solid State Chemistry*. **20** 47–99 (1990).
[31] J.G. Grolig, H. Abdesselam, M. Gas, H.F. Windisch, J. Froitzheim, J.-E. Svensson, Copper Based Conversion Coatings on Ferritic Stainless Strip Steel as Solid Oxide Fuel Cell Interconnects: Oxidation Performance and Chromium Evaporation, *ECS Transactions*. **57** 2339–2347 (2013).
[32] J.G. Grolig, P. Alnegren, J. Froitzheim, J.-E. Svensson, Copper Iron Conversion Coating for Solid Oxide Fuel Cell Interconnects, *Journal of Power Sources*. **297** 534–539 (2015).
[33] P. Perrot, Chromium – Copper – Oxygen, in: G. Effenberg, S. Ilyenko (Eds.), Refractory Metal Systems, Springer Berlin Heidelberg, 2010: pp. 126–137.
[34] C.D. Kumar, A. Dekich, H. Wang, Y. Liu, W. Tilson, J. Ganley, et al., Transition Metal Doping of Manganese Cobalt Spinel Oxides for Coating SOFC Interconnects, *Journal of The Electrochemical Society*. **161** F47–F53 (2014).
[35] Z. Yang, G. Xia, S.P. Simner, J.W. Stevenson, Thermal Growth and Performance of Manganese Cobaltite Spinel Protection Layers on Ferritic Stainless Steel SOFC Interconnects, *Journal of The Electrochemical Society*. **152** A1896–A1901 (2005).
[36] L.V. Gambino, N.J. Magdefrau, M. Aindow, Microstructural effects of the reduction step in reactive consolidation of manganese cobaltite coatings on Crofer 22 APU, *Materials at High Temperatures*. **32** 142–147 (2015).
[37] E.J. Opila, D.L. Myers, N.S. Jacobson, I.M.B. Nielsen, D.F. Johnson, J.K. Olminsky, et al., Theoretical and Experimental Investigation of the Thermochemistry of $CrO_2(OH)_2(g)$, *The Journal of Physical Chemistry A*. **111** 1971–1980 (2007).

[38] M. Stanislowski, E. Wessel, K. Hilpert, T. Markus, L. Singheiser, Chromium Vaporization from High-Temperature Alloys I. Chromia-Forming Steels and the Influence of Outer Oxide Layers, *Journal of The Electrochemical Society*. **154** A295–A306 (2007).

[39] P. Huczkowski, N. Christiansen, V. Shemet, L. Niewolak, J. Piron-Abellan, L. Singheiser, et al., Growth Mechanisms and Electrical Conductivity of Oxide Scales on Ferritic Steels Proposed as Interconnect Materials for SOFC's, *Fuel Cells*. **6** 93–99 (2006).

[40] N. Koc, M. Timucin, Activity–Composition Relations in $MnCr_2O_4$–$CoCr_2O_4$ Solid Solutions and Stabilities of $MnCr_2O_4$ and $CoCr_2O_4$ at 1300°C, *Journal of the American Ceramic Society*. **88** 2578–2585 (2005).

[41] K.T. Jacob, K. Fitzner, Ion-exchange equilibria between (Mn, Co)O solid solution and (Mn, Co)Cr_2O_4 and (Mn, Co)Al_2O_4 spinel solid solutions at 1100 °C, *Journal of Materials Science*. **12** 481–488 (1977).

[42] S. Fontana, S. Chevalier, G. Caboche, Metallic Interconnects for Solid Oxide Fuel Cell: Performance of Reactive Element Oxide Coating During 10, 20 and 30 Months Exposure, *Oxidation of Metals*. **78** 307–328 (2012).

[43] S.L. Tobing, High temperature corrosion and corrosion protection of metallic interconnects for SOFC. PhD Thesis, Norwegian University of Science and Technology, 2015.

Manuscript IV

Effect of spinel coating density on oxidation resistance and Cr-vaporization from a stainless steel interconnect

Belma Talic[a,c], Hannes Falk-Windisch[b,] Vinothini Venkatachalam[c], Kjell Wiik[a]
Peter Vang Hendriksen[c], Hilde Lea Lein[a]

[a] *Department of Materials Science and Engineering, Norwegian University of Science and Technology, Norway*
[b]*Department of Chemistry and Chemical Engineering, Division of Energy and Materials, Chalmers University of Technology, Sweden*
[c]*Department of Energy Conversion and Storage, Technical University of Denmark, Risø Campus, Denmark*

Abstract. Manganese cobalt spinel oxides show promise as protective coatings for solid oxide fuel cell (SOFC) interconnects. For maximum density, such coatings are often sintered in a two-step procedure, involving heat treatment first in reducing and then in oxidizing atmospheres. Sintering the coating *in-situ* during heating of the SOFC stack would reduce production costs, however, this may result in lower coating density. This work investigates the effect of coating density on the oxidation kinetics and Cr-evaporation of $MnCo_{1.7}Fe_{0.3}O_4$ coated Crofer 22 APU. The oxidation behavior was evaluated over 5000 h at 800 °C in air. A coating sintered in air at 900 °C, equivalent to an *in-situ* heat treatment, reduced the oxidation rate of Crofer 22 APU sufficiently to meet SOFC lifetime requirements. The same coating reduced the Cr-evaporation rate in air-3% H_2O by 88 %. The protective action was attributed to partial densification of the coating with time, in interaction with the alloy. A highly dense coating that was achieved by the two step reduction and re-oxidation procedure reduced Cr-evaporation by 97 %.

1. Introduction

As the operating temperature of Solid Oxide Fuel Cells (SOFC) has been reduced over the last decades, ferritic stainless steels (FSS) have become the preferred choice for the interconnect material [1]. FSS offer several advantages over the previously used $LaCrO_3$-based ceramic interconnect such as lower costs, higher electrical and thermal conductivities and greater ease of manufacturing [2,3]. The use of FSS has however brought upon some new challenges. Under SOFC operating conditions, the steel oxidizes to form a Cr_2O_3 scale that continues to grow with time. Because of the modest electrical conductivity of Cr_2O_3, this leads to an increase in stack resistance [4]. Furthermore, the chromia scale in reaction with oxygen and water vapor forms volatile Cr(VI)-species that have been reported to "poison" SOFC cathodes [5,6]. There have been some attempts to develop new cathode materials with higher Cr-tolerance [7–9]. However, this will not eliminate the problem of high Cr-evaporation rates since Cr-depletion from the alloy to below a certain limit can lead to break-away type oxidation [10,11]. Cr-evaporation has a low activation energy and will therefore continue to be a challenge even if the operating temperature of SOFC is further reduced [12].

$(Mn,Co)_3O_4$ spinels have been identified as promising coating materials for reducing scale growth and Cr-evaporation from FSS [13–17]. Several methods to deposit these coatings are under consideration, including various slurry spraying methods [18–20], screen printing[21], electrophoretic deposition (EPD) [22,23], electroplating [24] and atmospheric plasma spraying [25,26]. EPD is particularly promising as it is a fast and cheap method that offers good control of layer thickness and the opportunity to coat geometrically complex structures [27]. However, a common element for powder-based methods such as EPD is that the coating needs to sinter after deposition. To ensure maximum coating density while avoiding excessive oxidation of the steel substrate, spinel coatings have typically been sintered by a two-step procedure [15,21]. The first step is heat treatment in N_2+H_2 or some other reducing atmosphere where the spinel oxide decomposes into MnO and Co [28]. During the second step of heat treatment in air the spinel phase is re-formed and densification is promoted by a reaction-sintering type mechanism [29,30]. The two-step sintering procedure has in some assessments been estimated to make up approximately 20 % of the total interconnect coating costs [31,32]. From a commercial point-of-view, it would therefore be beneficial if the coating instead could be densified in-situ during startup of the SOFC stack. However, as shown by Lee et al. [21], very little densification of $(Mn,Co)_3O_4$ is achieved in air at moderate temperatures: according to their dilatometry measurements, the linear sintering shrinkage of $Mn_{1.5}Co_{1.5}O_4$ below 1000 °C is less than 3 %.

Only few studies have investigated how a lower $(Mn,Co)_3O_4$ coating density affects Cr-evaporation and oxidation of FSS interconnects. Kurokawa et al. [13] measured the Cr-vaporization rate of $MnCo_2O_4$ coated SS430 where two different levels of coating density were achieved by different powder manufacturing

methods. After 24 h of exposure at 800 °C, they found that although vaporization was reduced by a factor of three with a porous coating, the denser coating was ten times more effective [13]. Akanda et al. [32] compared the ASR of SS441 coated with $(Mn,Co)_3O_4$ that was sintered either by the reduction and re-oxidation procedure or by heat treating in air only. They concluded that a dense coating, achieved by including the reduction heat treatment step, was necessary to avoid excessive scale growth leading to unacceptably high ASR. Their conclusion was however made after accelerated testing at 900 °C, while the results from 1000 h measurement at 800 °C actually show a low and stable ASR for the sample that was only sintered in air. Thus, there appear to be indications in literature that even a porous spinel coating will provide some protection of the steel substrate. There is however a lack of long term studies at realistic SOFC operating temperatures where the effect of coating density is evaluated.

In this work, we have investigated long term (5000 h) oxidation behavior of Crofer 22 APU with $MnCo_{1.7}Fe_{0.3}O_4$ coatings that were sintered to produce different degrees of porosity. In addition, Cr-evaporation from Crofer 22 APU with coatings of different porosity has been measured during the first 500 h of exposure to humidified air. The $MnCo_{1.7}Fe_{0.3}O_4$ composition was chosen as the coating because the thermal expansion coefficient (TEC) of this material between room temperature and 800 °C (12.0×10^{-6} K^{-1}) is lower than that of $MnCo_2O_4$ (14.4×10^{-6} K^{-1}) [Manuscript I]. The lower value provides a better match to the TEC of Crofer 22 APU (11.9×10^{-6} K^{-1} [33]). This is reduces the build-up stresses during thermal cycling, consequently reducing the risk of coating spallation.

2. Experimental

A plate of 1 mm thick Crofer 22 APU (Thyssen Krupp) with the composition given in Table 1 was cut into coupons of 20×20 mm. A 3 mm hole was drilled in one of the corners to allow for hanging in the oxidation furnace. The samples were ground with SiC-paper, polished down to 1 μm using diamond abrasive and cleaned in acetone and ethanol for 10 minutes each in an ultrasonic bath. Sample thickness measured after grinding was typically 0.8-0.9 mm.

Table 1. Composition of Crofer 22 APU alloy used in this study in wt.%. Analyzed by Optical Emission Spectroscopy (OES) at Force Technology, Denmark.

Alloy	Fe	Cr	Mn	Ti	La	C	Si	Al
Crofer 22 APU	Bal.	23	0.42	0.068	0.04-0.20[1]	0.003	0.049[2]	0.007

[1]La was not analyzed by OES. Concentration according to the manufacturer's datasheet
[2]Determination of Si content by OES is associated with large uncertainty

The steel coupons were coated by electrophoretic deposition (EPD). $MnCo_{1.7}Fe_{0.3}O_4$ powder was synthesized by spray pyrolysis of an aqueous based nitrate solution as described in [Manuscript I]. The powder was calcined at 650 °C for 5 h and subsequently ball milled (250 ml PE-bottle, Ø 10 mm YSZ milling balls) overnight in 100 % ethanol before use. The particle size distribution after milling was bimodal with a median size (d_{50}) equal to 0.63 μm [Manuscript II]. The EPD suspension was prepared by ball milling 5 wt.% spinel powder in a 50/50 vol.% mixture of ethanol and isopropanol for 48 h (500 ml PE-bottle, Ø 10 mm YSZ milling balls). Two larger plates of Crofer 22 APU were used as counter electrodes. The sample coupon was place in the center between these two plates at a distance of 15 mm. A constant voltage of 35 V was applied for 90 s with the negative terminal connected to the sample coupon to deposit approximately 7.6 mg/cm^2 of powder.

The three different procedures under which the coated samples were heat treated are described in Table 2. The heating and cooling rates were 120 °C/h. Gases were bubbled through water at 5 °C to give a moisture content of ca. 1 %. Bare Crofer 22 APU was heat treated under the same conditions to estimate the mass change during coating sintering.

Table 2. Heat treatment procedures for sintering $MnCo_{1.7}Fe_{0.3}O_4$ coating on Crofer 22 APU and abbreviation for each method, used throughout this text.

Abbreviation	1: Reduction step (R)	2: Oxidation step (O)
O900		2 h at 900 °C in air
R900+O800	2 h at 900 °C in N_2-9%H_2	2 h at 800 °C in air
R1100+O800	5 h at 1100 °C in N_2-9%H_2	5 h at 800 °C in air

Oxidation was studied in air at 800 °C for 5000 h in a chamber furnace. There was no forced air flow to the furnace (i.e. nearly stagnant conditions) and the humidity content was not controlled. Polished Crofer 22 APU without any coating was oxidized under the same conditions for 2000 h. At least three samples of each type were suspended vertically (hanging from an alumina rod). Every 250 h, the furnace was cooled to room temperature (180 °C/h) and the samples were weight on a scale with 0.00001 g accuracy (XS205 Mettler Toledo). One sample of each type was taken out after 2000 and 5000 h of oxidation for inspection by scanning electron microscopy (SEM, Zeiss Supra 35 field emission-SEM and Zeiss Merlin field emission-SEM) and energy dispersive X-ray spectroscopy (EDX, Bruker X-Flash 6160). The EDX data were collected at an acceleration voltage of 15 kV and analyzed using Esprit software (Bruker). Quantification (standardless) was performed using only the Kα lines for Cr, Mn, Co and Fe.

Additional samples were oxidized in flowing air with 3 % H_2O while measuring chromium evaporation using the Denuder method. The method has been described in detail in [34], where it was determined to have a 95±5 % collection efficiency. The moisture content was achieved by passing cleaned, dry

air through a membrane (Perma Pure FC-Series humidifier) connected to a water bath at 24.4 °C. The flow rate of the gas was set to 6000 ml/min. A porous Al_2O_3 flow restrictor was placed in front of the samples to ensure a uniform flow pattern. A quartz tube (Ø 6 mm) coated with Na_2CO_3 was placed behind the samples to act as the gas outlet. Volatile Cr species react with the carbonate to form chromate according to reaction (1):

$$CrO_2(OH)_2(g) + Na_2CO_3(s) \rightarrow Na_2CrO_4(s) + H_2O\,(g) + CO_2(g) \quad (1)$$

At regular intervals, the quartz tubes were exchanged and rinsed with distilled water to dissolve the sodium chromate. The amount of chromate in the solution was quantified by spectrophotometry (Evolution 60S, Thermo Scientific).

For the O900 samples, Cr-evaporation was also measured during sintering. The coated samples were placed in the furnace at 150 °C, heated to 900 °C for 2 h and cooled to 500 °C before exchanging and analyzing the quartz tube. This was done to obtain a measure for the total Cr-evaporation if the coating is sintered *in-situ* during start-up of a SOFC stack. Subsequent exposure of the O900 samples, those sintered ex-situ (R1100+O800) and bare Crofer 22 APU was made by placing samples in the furnace at 300 °C and heating to 800 °C (heating rate 240 °C/h). The exposure was continuous for 500 h while exchanging the quartz tubes approximately every 100 h. The samples were examined by SEM-EDX after exposure. All measurements were performed in two different furnaces to check for reproducibility. The total surface area of samples in each of the measurements was 15.7 cm^2.

3. Results

3.1 Microstructure after coating preparation

SEM cross sections of $MnCo_{1.7}Fe_{0.3}O_4$ coated Crofer 22 APU after the three different sintering procedures are shown in Figure 1. The coating porosity was estimated based on five such micrographs of each sample using ImageJ software [35] and is given in Table 3 together with the average chromia scale thickness determined from the micrographs. The measured mass gain of bare Crofer 22 APU after the same heat treatments is also given in Table 3. EDX analysis indicated that the average composition of the coating after heat treatment was $Mn_{1.1}Co_{1.6}Fe_{0.3}O_4$, i.e. the Mn/Co fraction is slightly higher than the nominal powder composition of $MnCo_{1.7}Fe_{0.3}O_4$. There was no significant difference in coating composition after the different sintering heat treatments (< 3 wt.% difference on analysis of cations). All of the coatings contained trace amounts of Cr (< 0.5 wt.%).

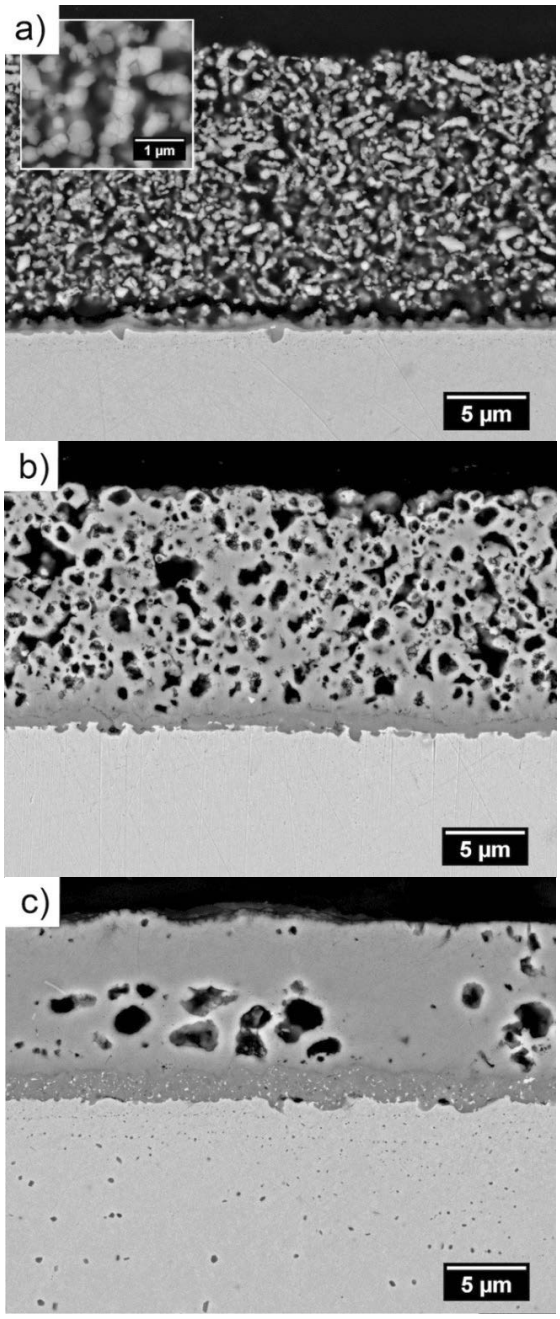

Figure 1. SEM backscatter electron images of $MnCo_{1.7}Fe_{0.3}O_4$ coating on Crofer 22 APU after different sintering heat treatment procedures (a) O900 (b) R900+O800 (c) R1100+O800.

Figure 1a shows that heat treatment in air at 900 °C was only sufficient to initiate neck formation between the ceramic particles. The adhesion of the coating appears to be poor as it detached from the steel substrate during mounting in epoxy. Heat treatment in reducing atmosphere at 900 °C before re-oxidation in air lead to slight improvement in both densification and adhesion as evident from Figure 1b. A thin continuous layer of densified spinel appears to cover most of the chromia scale, while the porosity of the bulk part of the coating is still high. Densification of the coating was considerably enhanced by increasing the temperature during the reduction step to 1100 °C (Fig. 1c). The remaining few pores in the coating all appear to be isolated. However, the increase in temperature from 900 °C to 1100 °C also resulted in a three times thicker chromia scale (Table 3).

Bright particles were observed in the chromia scale of both samples heat-treated in reducing atmosphere. EDX point analysis showed that the particles contained more Fe and less O compared to the surrounding scale, indicating that they are metallic inclusions.

Table 3. Chromia scale thickness and coating porosity measured on SEM images of $MnCo_{1.7}Fe_{0.3}O_4$ coated Crofer 22 APU after sintering. Mass gain of bare Crofer 22 APU is after being heat treated under the same conditions.

Sample	Cr_2O_3 thickness [μm]	Coating porosity [%]	Mass gain of bare Crofer 22 APU [mg/cm^2]
O900	0.3±0.2	53±5	0.06
R900+O800	0.6±0.2	35±5	0.10
R1100+O800	1.8±0.3	17±3	0.56

3.2 Oxidation in air

The mass change measured during oxidation in air at 800 °C is shown in Figure 2a. During the first 250 h of oxidation, the mass gain of the two samples heat-treated under reducing conditions (R900+O800 and R1100+O800) is larger than the mass gain of the sample heat treated in air only (O900), possibly due to continued re-oxidation of the coating. For all of the coated samples, mass change over time followed to close approximation parabolic oxidation kinetics, described by:

$$(\Delta m/A)^2 = k_P t + C \qquad (2)$$

where Δm is the measured mass change [g], A is the sample area [cm^2], k_P is the parabolic rate constant [g^2/cm^{4}s], t is the time [s] and C is an integration constant. The mass change of Crofer 22 APU deviated slightly from parabolic behavior after 1000 h oxidation. The oxidation constants were obtained from a linear fit of

the (mass gain)^2 vs time data, as shown in Figure 2b and are summarized in Table 4. The mass gain during the first 250 h was ignored to avoid potential contributions from continued re-oxidation of the coating or initial non-parabolic oxidation behavior [36]. For bare Crofer 22 APU, only the mass change between 250 h and 1000 h (parabolic region) was used to determine the rate constant. The lowest oxidation rate is found for the sample with the densest coating (R1100+O800), however, the other coatings also reduce the oxidation rate significantly relative to bare Crofer 22 APU.

Table 4. Parabolic rate constant of bare and $MnCo_{1.7}Fe_{0.3}O_4$ coated Crofer 22 APU in air at 800 °C calculated from mass gain measured over 5000 h (coated samples) or 1000 h (bare Crofer 22 APU) of oxidation.

Sample	k_p [10^{-14} g^2/cm^{4}s]
O900	1.4
R900+O800	1.3
R1100+O800	0.34
Bare Crofer 22 APU	4.2

3.3 Cr-evaporation

The total amount of chromium species evaporated and the rate of Cr-evaporation during continuous exposure to flowing air-3%H_2O is shown in Figure 3a and b, respectively. Note that in both curves, the first value for the O900 samples corresponds to the 2 h exposure at 900 °C (*in-situ* sintering). During this short period the Cr-evaporation rate is the same as for bare Crofer 22 APU measured at 800 °C. After the temperature is lowered to 800 °C, the rate initially decreases with time before it after 250 h stabilizes at a value ten times lower than in case of bare Crofer 22 APU. The evaporation rate from samples with dense coatings (R1100+O800) is nearly constant over time and on average three times lower than measured for the porous coating (O900).

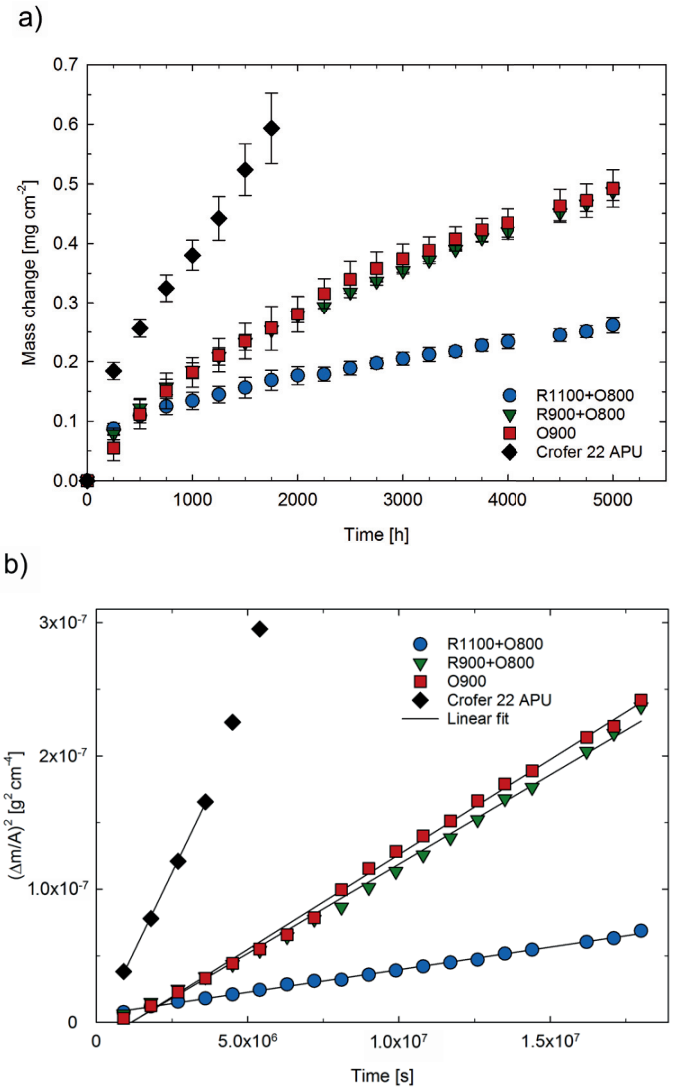

Figure 2. (a) Mass change of bare and spinel coated Crofer 22 APU during oxidation at 800 °C in air. Each point is the average of 2-5 samples and the error bars are equal to one standard deviation. (b) Parabolic rate plot showing the best linear fit of the (mass change)^2 vs time data.

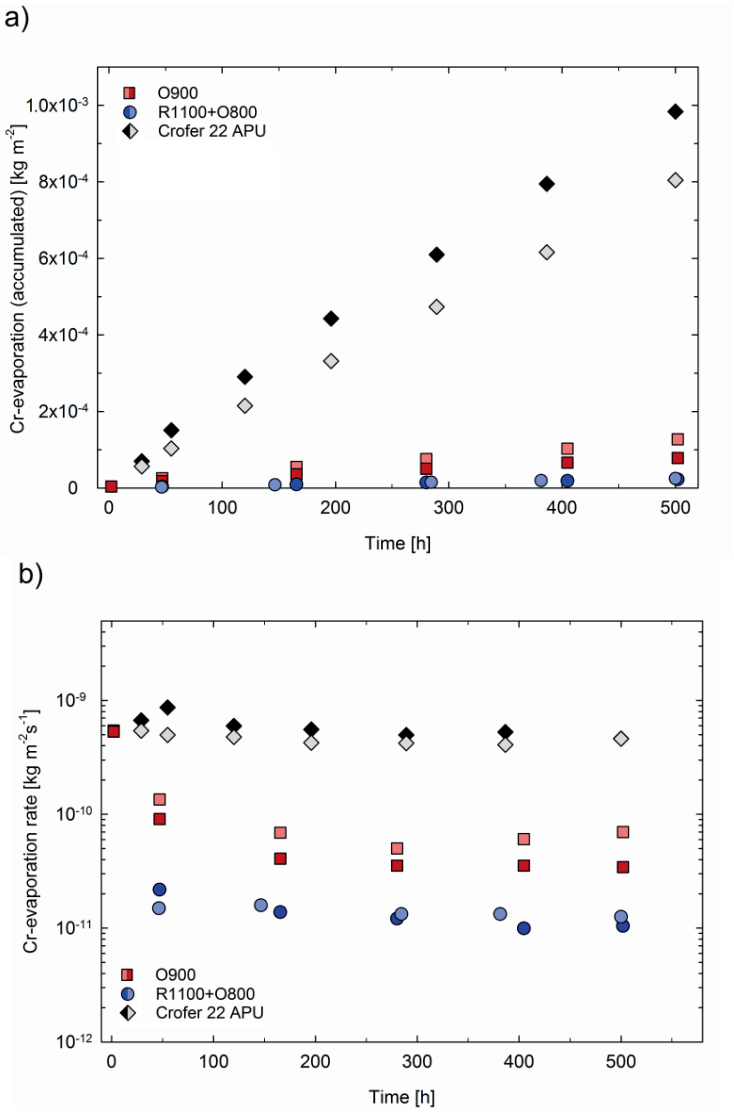

Figure 3. Cr evaporation from bare and spinel coated Crofer 22 APU measured at 800 °C in flowing air-3%H_2O. Both parallels measured in two different furnaces under identical conditions are shown. The first value (at 2 h exposure time) for the O900 sample was measured at 900 °C. (a) Total amount of Cr-species evaporated (b) Rate of Cr-evaporation vs. time.

3.4 Microstructure after oxidation

The microstructural and compositional development during oxidation at 800 °C in air is seen from the SEM images and EDX maps in Figure 4. Figure 4a shows that a 2-4 μm dense layer has formed along the interface between the initially highly porous coating (O900) and the chromia scale. The EDX maps do not reveal any compositional differences between this layer and the bulk of the coating. Quantitative point analysis showed that the amount of chromium in the densified layer was 3-5 wt.%, while the overall amount in the porous portion of the coating was ≤ 1wt.%. There were no apparent changes in the concentration of Co, Mn and Fe between the dense and porous portions of the coating. Because the dense layer was narrow relative to the EDX spatial resolution, it was not possible to determine its composition and how it changed over time more precisely. The overall Co/Mn fraction in the whole coating decreased with increasing oxidation time from 1.7 in the as-prepared coating, to 1.4 after 2000 h at 800 °C, and finally to1.2 after 5000 h at 800 °C (fractions are based on wt.%). The total amount of Fe in the coating remained constant (8±1 wt.%). A similar microstructure was observed when inspecting the O900 samples exposed to air-3% H_2O for 500 h during Cr-evaporation measurement. The thickness of the densified region was slightly thinner for these samples, while it did not increase noticably from 2000 to 5000 h of oxidation in air. The adhesion between the coating and the alloy substrate appears to have improved during oxidation.

EDX maps of coatings that were heat treated under reducing atmosphere (R900+O800 and R1100+O800) reveal a distinct reaction layer consisting of Mn, Cr, Co, Fe and O between the chromia scale and spinel coating (Fig. 4b and c). The thickness of this layer was typically 3-5 μm, however with large variation along the interface. The variation in reaction layer thickness was generally opposite the variation in oxide scale thickness, i.e. a thinner reaction layer was observed where the oxide scale was thicker and vice versa. In areas where the reaction layer was thick, the interfaces between the oxide scale, reaction layer and coating appeared more diffuse. Where there was no distinct reaction layer, micro-pores could be observed along the oxide scale/coating interface. These features are all seen in Figure 4b. By making EDX linescans across the thickest parts of the reaction layer, a compositional plateau close to the composition of $Mn_{0.5}CoFe_{0.3}Cr_{1.1}O_4$ was found. I.e. for coatings that were heat treated under reducing atmosphere (R900+O800 and R1100+O800) the reaction layer contained significantly larger amounts of Cr (< 25 wt.%) than the densified layer of the coating only heat treated in air (Cr < 5 wt.%). The overall Cr-content in the bulk part of the R900+O800 and R1100+O800 coatings was generally < 1 wt.%.

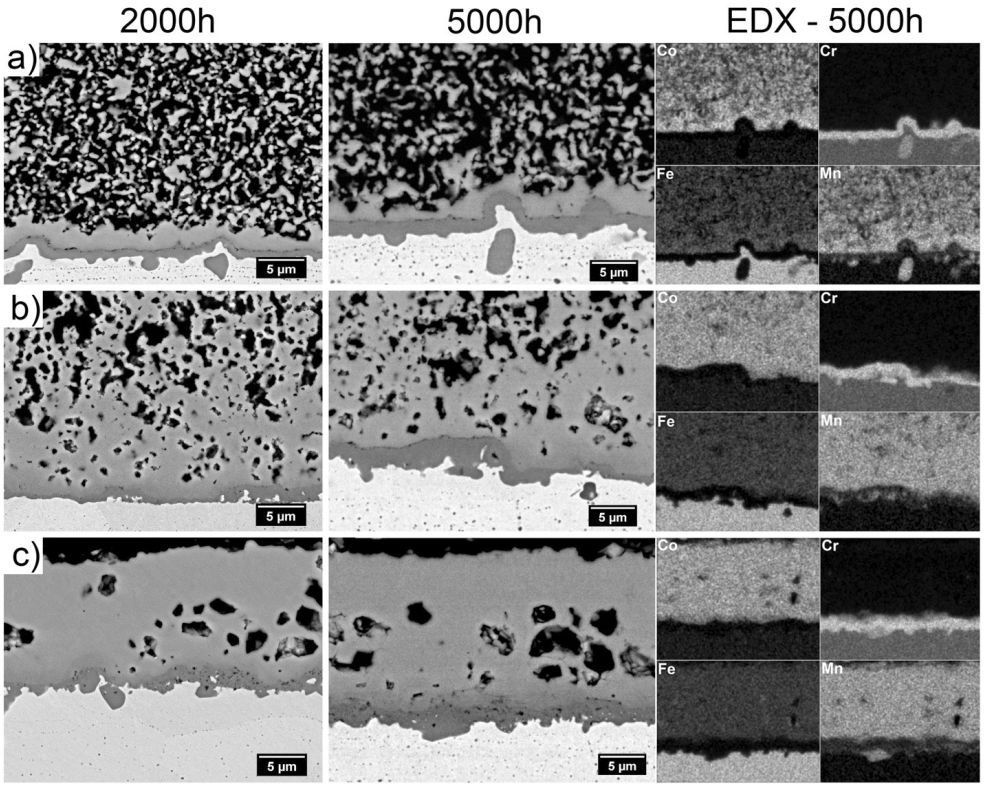

Figure 4. SEM backscatter electron images of samples after oxidation at 800 °C in air for 2000 and 5000 h, and corresponding EDX maps after 5000 h. (a) O900, (b) R900+O800, (c) R1100+O800.

The thickness of the oxide scale varied along the interface for all samples, but was most uniform under the R900 coating. The average thickness was determined by measuring every 2 µm along the cross section of at least five different, representative SEM images at the same magnification as shown in Figure 4 and is summarized in Table 5. The average oxide scale thickness under the O900 coating increases at a higher rate than the oxide scale under the R900+O800 coating. The oxide scale under the R1100+O800 coating appears to slightly decrease during oxidation. Figure 4c shows that the oxide scale under R1100+O800 is more porous after oxidation than it was directly after sintering (Fig. 1c). Metallic inclusions in the chromia scale are still visible, but in significantly lower quantities.

In all of the samples, $(Mn,Cr)_3O_4$ was detected at the scale/alloy interface. Internal oxides rich in Ti were detected further below the alloy surface. No cracking or spallation of the coating was observed for any of the samples after oxidation.

Table 5. Oxide scale thickness measured on SEM micrographs after 2000 h and 5000 h oxidation at 800 °C in air.

	Oxide scale thickness [μm]	
Sample	2000 h	5000 h
O900	0.8±0.3	1.3±0.4
R900+O800	0.8±0.4	1.1±0.6
R1100+O800	1.7±0.7	1.5±0.5

4. Discussion

4.1 Oxidation kinetics

After 5000 h of exposure to air at 800 °C, the sample with the densest coating (R1100+O800) has the lowest mass gain, albeit the thickest chromia scale. This is because initial growth of the chromia scale during the different sintering procedures is not accounted for in the mass change plot (Fig. 2a). Figure 5 shows a recalculation of the results where this has been included. The recalculation was made by adding the mass change during sintering to the mass change measured at 800 °C and adjusting for the "equivalent age". The mass change of bare Crofer 22 APU (Table 2) was used as an estimate, as it was difficult to determine this accurately for the coated samples. Thus, it is assumed that the coating does not provide any significant protection during sintering. This was found to be a fair assumption when comparing the chromia scale thickness of bare and coated Crofer 22 APU after the same heat treatment. The equivalent age is here defined as the amount of time bare Crofer 22 APU is oxidized at 800 °C before obtaining the same mass gain. For example, the equivalent age of R1100+O800 is ca. 1650 h since the mass gain during the R1100+O800 heat treatment was 0.56 mg/cm^2 and bare Crofer 22 APU had to be oxidized for approximately 1650 h before gaining this amount of mass (see Fig. 2a).

The recalculated results allow for a more fair comparison of the protective action of the different coatings. Figure 5 shows that after 5000 h, the total mass gain of R1100+O800 is 10 % higher than the total mass gain of O900. These results agree with the oxide scale thickness measured on SEM images (Table 5). Nevertheless, the lowest *rate* of oxidation is displayed by R1100+O800. Accordingly, the total mass gain of these samples should become lower than the total mass gain of the O900 samples after a certain period of time. To predict when this will occur, the mass gain beyond 5000 h has been estimated using the parabolic rate constants (Table 2). The results are plotted as lines in Figure 5 and show that the same total mass gain should be reached after approximately 15 000 h at 800 °C in air. Hence, up to 15 000 h the interconnect alloy will be less degraded with the O900 coating, whereas after this point, the alloy with the

R1100+O800 coating will be less degraded. Considering the target lifetime of SOFCs usually is > 40 000 h, the extrapolation analysis points to that the dense coating will provide a slight benefit on the long term. The reduction in oxidation rate is large enough to make up for the stronger initial oxidation of the alloy that occurs at the high temperature needed to sinter the coating. Nevertheless, Figure 5 clearly shows that in the long run, the difference in mass gain due to different coating density is minor compared to the large reduction in mass gain of Crofer 22 APU with any of the coatings. If the SOFC operating temperature is decreased below 800 °C, the benefit of a dense coating might however diminish, as decreasing the temperature 100 °C typically leads to a 10-30 times decrease in the oxidation rate of ferritic stainless steels [12,37,38].

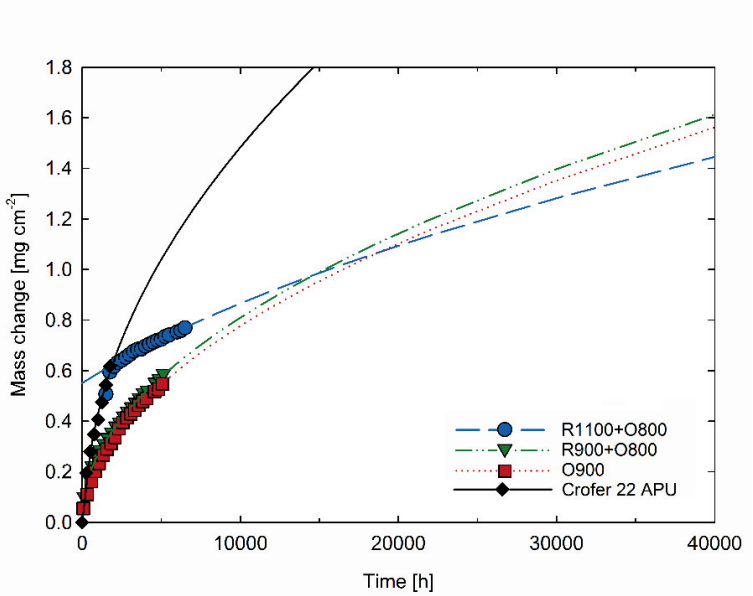

Figure 5. Mass change at 800 °C in air recalculated to include initial mass change during heat treatment of coatings and the "equivalent age". Lines show an extrapolation of the mass change based on the parabolic rate constants.

4.2 Cr-evaporation

The Cr-evaporation rate of Crofer 22 APU was reduced by a factor of 30 with a dense $MnCo_{1.7}Fe_{0.3}O_4$ coating (Fig. 3b), which is in line with what has previously been reported for $(Mn,Co)_3O_4$ coatings [13,20,39]. It should be mentioned that approximately 1 % of the surface area of the samples was without coating due to it being covered by the electrode clip during EPD. Assuming this area has the same Cr-evaporation rate as measured for bare Crofer 22 APU, it could make up to 45 % of the measured Cr-evaporation for the R1100+O800 samples. Differences in the exact size of this area vary slightly from sample to

sample, which can account for some of the scatter in the measured results. Nevertheless, since EDX analysis after oxidation showed up to 1 wt.% Cr in the outer parts of the coating, some portion of the collected Cr must have diffused through the coating as well. Thus, although the spinel obviously is highly effective in reducing Cr outward diffusion, it does not block it entirely. This is in contradiction to what has been reported in some other studies of $(Mn,Co)_3O_4$ coated Crofer 22 APU where no Cr was found in the coating layer close to the gas interface after oxidation [40,41]. The discrepancy could be due to the shorter oxidation time (400 h) or lower temperature (700 °C) investigated in these studies. Other longer term studies at 800 °C confirm up to 1 wt.% incorporation of Cr in the outer layers of $(Mn,Co)_3O_4$ based spinel coatings [15,42].

While greatest reduction in Cr-evaporation was achieved with a dense coating, even the highly porous coating reduced the evaporation rate by 10 times relative to bare Crofer 22 APU. The decreasing Cr-evaporation rate over time, and the observation that a dense layer formed between the chromia scale and otherwise porous coating after 500 h of exposure, suggest that the protective action primarily is due to formation of this densified layer. The amount of Cr released to the atmosphere is reduced due to reaction of outward diffusing Cr with the $MnCo_{1.7}Fe_{0.3}O_4$ spinel coating. Another likely contribution to the reduced evaporation rate is slower Cr-diffusion through the $(Mn,Co,Fe,Cr)_3O_4$ reaction layer compared to the $(Cr,Mn)_3O_4$ layer typically formed on the outer surface of Crofer 22 APU [43]. The even lower Cr-evaporation rate with a dense coating can be attributed to the presence of the dense $MnCo_{1.7}Fe_{0.3}O_4$ layer above this Cr-containing reaction layer, acting as further barrier against Cr outward diffusion.

Kurokawa et al. [13] has also reported that a highly porous $MnCo_2O_4$ coating can reduce Cr-vaporization. However, in their study the denser coating was ten times more effective while we found the difference to be only a factor of three. It should be mentioned that their measurements were performed with a higher content of H_2O in the gas (10 %), which is known to increase the rate of Cr-vaporization [44,45]. Nevertheless, since they report Cr-evaporation rates for the bare alloy (9.8×10^{-10} kg/m^{2}s) and with a highly dense spinel coating (2.3×10^{-11} kg/m^{2}s) that are comparable to those measured in the current work, it is interesting to compare the results for the more porous coatings as well. The Cr-evaporation rate we have measured for the porous coated sample after 47 h of exposure is three times lower than that reported by Kurokawa et al. after 72 h at the same temperature. The different coating densities in the work by Kurokawa et al. were attributed to different particle size distributions in the spinel powders used to fabricate the coatings, the sintering heat treatment was the same for all samples. Powder prepared by co-precipitation and calcined at 800 °C had a finer particle size (ca. 0.3 μm) and thus better sinterability than powder prepared by GNP and calcined at 1100 °C (particle size 0.3-3 μm). No dense layer between the coating and chromia scale is visible in their SEM micrographs of the porous coating after exposure, which strengthens the hypothesis that the formation of a

dense layer between the chromia scale and otherwise porous coating is critical for the coatings protective abilities.

4.3 Microstructural development

The $MnCo_{1.7}Fe_{0.3}O_4$ coating density increased by more than 25 % when heat-treated in N_2-H_2 at 900 °C compared to when heat-treated in air at the same temperature. This is in accordance with previous studies, in which the improved densification in reducing atmosphere was attributed to a reaction-sintering type mechanism [21,28]. The bright particles observed in the thermally grown oxide scale are most likely metallic inclusions, caused by stress build-up due to internal oxidation [46]. For Crofer 22 APU, internal oxidation of Ti and $(Mn,Cr)_3O_4$ formation at the scale/alloy interface are likely origins of the stress build-up [29,47]. Although $(Mn,Cr)_3O_4$ usually is reported to form above the chromia scale during oxidation of Crofer 22 APU and similar alloys, $(Mn,Cr)_3O_4$ has also previously been observed at the alloy/scale interface [42,47]. Thermodynamically, $(Mn,Cr)_3O_4$ is stable down to lower oxygen partial pressures than Cr_2O_3, thus, its presence at the alloy/oxide scale interface is feasible [48,49].

The parabolic oxidation rate of Crofer 22 APU was reduced by more than a factor of four by the two most porous spinel coatings (O900 and R900+O800). The initial porosity of both of these coatings is above the 30 % proposed as minimum for physical gas permeability in similar systems [50,51], which suggests that none of them provide a proper physical barrier against the oxidizing gas. However, with time, the coatings were observed to densify in a 2-4 μm region above the thermally grown oxide scale. It is unlikely that continued sintering is responsible for this densification, seeing as the temperature of exposure was low (800 °C) and the coatings mainly were observed to densify in a narrow region above the oxide scale.

The densified region of the R900+O800 coating contained up to 25 wt.% Cr. The improved density with time may therefore be attributed to a volume expansion due to incorporation of Cr. In case of the O900 coating however, the maximum amount of Cr in the densified region was only 5 wt.%. The large difference in Cr concentration in the two densified regions may be explained on basis of the compositional changes taking place during the two sintering heat treatments. Gambino et al. [29] showed that during heat treatment of $Mn_{1.5}Co_{1.5}O_4$ coated Crofer 22 APU in N_2-H_2 at 900 °C, $Mn_{1.5}Co_{1.5}O_4$ is reduced to MnO and Co. Simultaneously, a ca. 3 μm thick Cr_2O_3 + $(Mn,Cr)_3O_4$ scale is formed at the coating/alloy interface. A transmission electron microscopy study of the $Mn_{1.5}Co_{1.5}O_4$ coating after re-oxidation showed that the interface between chromia and the coating comprises Mn, Cr, Co and Fe [42]. I.e. during re-oxidation of the coating, Mn in $(Mn,Cr)_3O_4$ is partially replaced by Co and Fe to form the Cr-rich reaction layer. Based on results in the current study, it may be argued that the formation of $(Mn,Cr)_3O_4$ is a prerequisite for the formation of the Cr-rich reaction

layer. Gambino et al. [29] proposed that Cr_2O_3 is formed first on Crofer 22 APU and that the $(Mn,Cr)_3O_4$ spinel grows with time due to outward diffusion of Mn from the alloy. We suggest that another contribution to growth of $(Mn,Cr)_3O_4$ is a reaction between thermally grown Cr_2O_3 and MnO from the reduced coating. This reaction would allow for the formation of a thicker spinel layer due to the more accessible source of Mn. The proposed microstructural development is summarized schematically in Figure 6.

The lower amount of Cr in the densified region of the O900 coating is due to an initially thinner $(Mn,Cr)_3O_4$ layer. Since this coating is not reduced to MnO and Co, $(Mn,Cr)_3O_4$ can only form by diffusion of Mn from the alloy. The O900 coating was found to overall contain more Mn after oxidation compared to in the as-prepared state. This can only be due to diffusion of Mn from the alloy. Although there were no detectable differences in the Co/Mn ratio between the dense and porous parts of the coating, it is possible that the local densification of this coating in part is due to reaction with outward diffusing Mn. Higher resolution microscopy will be necessary to investigate this mechanism further.

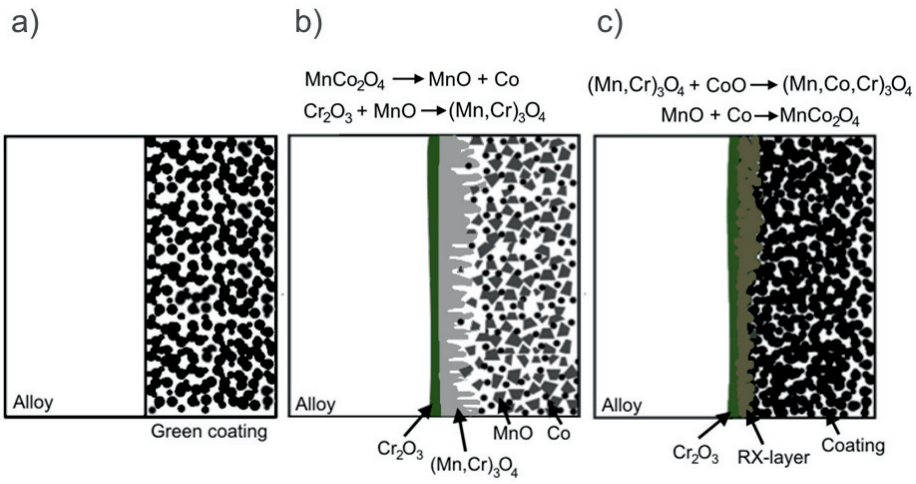

Figure 6. Schematic illustration of the microstructural development during oxidation of spinel coated Crofer 22 APU heat treated by the two-step procedure. (a) As deposited coating, (b) After heat treatment in reducing atmosphere (re-drawn from [29]), (c) After re-oxidation and continued exposure to air. Iron has been omitted for simplicity.

It may be noted that although the O900 and R900+O800 coated samples experienced the same mass gain during oxidation (Fig. 2), the oxide scale thickness was slightly smaller on the R900+O800 coated samples (Table 5). Horita et al. [52] showed that ^{18}O diffusivity in a $(Mn,Co,Cr)_3O_4$ reaction layer formed during oxidation of $MnCo_2O_4$ coated FSS, is lower than the diffusivity in both the coating and the thermally grown oxide scale. From this it may be inferred

that the thinner oxide scale under the R900+O800 coating is due a higher amount of Cr in the densified region. This would explain why Akanda et al. [32] observed considerably faster scale growth at 900 °C in air under a $Mn_{1.5}Co_{1.5}O_4$ coating sintered only in air compared to a coating sintered by the two-step reduction and re-oxidation procedure.

The even greater reduction in oxidation rate for the densest coating (R1100+O800) is probably due to the presence of a dense $MnCo_{1.7}Fe_{0.3}O_4$ spinel layer above the Cr-rich reaction layer. This reduces the oxygen partial pressure at the reaction layer/coating interface, which consequentially decreases the driving force for oxidation [53]. Another possibility is that the high temperature heat treatment used to sinter the coating has modified the properties of the formed chromia scale and thereby affected the oxidation kinetics. It is know that diffusion in Cr_2O_3 can vary with grain size and presence of minor impurities [54,55]. There is however limited information available on how pre-oxidation of Crofer 22 APU at different temperatures and in different atmospheres affects subsequent oxidation behavior in air [56,57]. At this point it is not possible to resolve how much of the improved oxidation resistance is due to a denser coating and how much is due to pre-oxidation of the alloy. This will be investigated in [Manuscript V].

4.4 Implications for long-term performance as protective coatings

One way of evaluating the lifetime of interconnect alloys is based on the time it takes to decrease the concentration of Cr in the alloy beneath a critical level where break-away oxidation occurs. This can be used as a criteria for determining whether the spinel coating is protective enough. For ferritic stainless steels such as Crofer 22 APU, the critical Cr concentration before break-away has been determined to be approximately 16 wt.% [10]. Quadakkers et al. [58] derived an expression for the time to break-away for alumina forming steel, which Huczkowski et al. [10] later showed was applicable for chromia forming alloys. For a rectangular sheet of infinite width and breadth, it can be shown that the time to break-away is given by:

$$t_B = \left\{\left[(C_0 - C_B) \cdot \rho_{alloy} \cdot d \cdot 2.3 \cdot 10^{-3}\right] - w_{pre}\right\}^2 \cdot 1/k_P \qquad (3)$$

where C_0 and C_B are the initial and final Cr-concentrations in the alloy, ρ_{alloy} is the density of the alloy, d is the alloy thickness, w_{pre} is the initial mass gain during sintering of the coating and k_P is the parabolic rate constant. In the following, it is assumed that all of the measured mass gain is due to oxidation of Cr to Cr_2O_3, that oxide spallation does not occur and that k_P is independent of the component thickness. For oxidation of bare Crofer 22 APU at 800 °C the last assumption has been found to be valid as long as the thickness is between 0.3 and 2 mm; below this the parabolic rate constant increases with decreasing alloy thickness [10].

Figure 7 shows the time to break-away with the different coatings as a function of alloy thickness. The calculations indicate that a plate of Crofer 22 APU with the most porous spinel coating (O900) only needs to be > 0.15 mm thick to withstand 40 000 h at 800 °C. Without any coating, the required thickness nearly doubles. This is without taking evaporation of the scale into account. Sachitanand et al. [11] has shown that the time for break-away of 0.2 mm thick Sandvik HT at 850 °C decreases by a factor of two when exposed to high flow rate conditions, compared to when Cr evaporation is suppressed. Although Cr-evaporation will decrease the lifetime of the porous coated samples as well, the influence will be considerably smaller due to the 10 times lower Cr-evaporation rate compared to bare Crofer 22 APU.

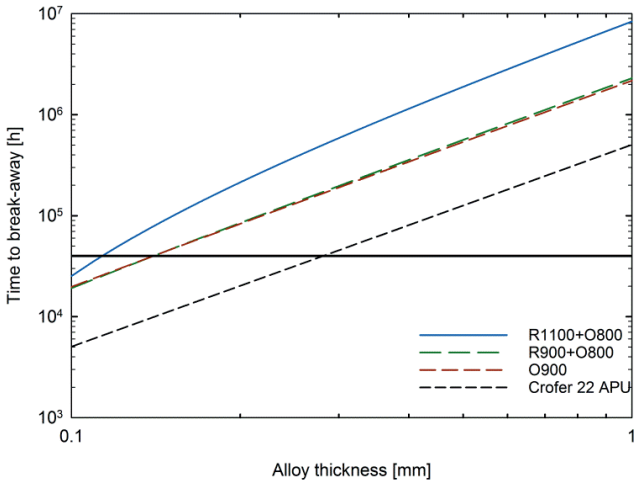

Figure 7. Time to break-away oxidation as a function of component thickness for bare and spinel coated Crofer 22 APU calculated based on measured oxidation rate at 800 °C in air. The black horizontal line marks 40 000 h.

Based on the oxidation behavior alone it can be concluded that even a porous $MnCo_{1.7}Fe_{0.3}O_4$ coating, which results from heat treatment in air at 900 °C, will provide sufficient protection of an interconnect alloy like Crofer 22 APU to meet SOFC lifetime requirements. The predicted mass gain difference between the dense and porous coating is less than 10 % after 40 000 h, which is not expected to result in a large enough difference in ASR to make up for the extra costs of *ex-situ* sintering. In terms of thermo-mechanical properties, porous coatings could even prove to be better than dense by providing strain tolerance [28,59]. The main uncertainty with the use of porous coatings is whether the higher rate of Cr-evaporation will lead to unacceptably high degradation of the SOFC cathode. Stanislowski et al. [60] estimated that the voltage of a typical SOFC stack with a $La_xSr_yMnO_3$ (LSM) cathode operated at Research Center Juelich would degrade

by 1 % for every 3.96 µg/cm^2 of Cr released from the interconnect. From the measured Cr-vaporization rates in the current study, this corresponds to a voltage degradation rate of 43 %/1000 h for bare Crofer 22 APU, 4.7 %/1000 h with the coating sintered in air (O900) and 1.7 %/1000 h with the coating sintered by the two-step procedure (R1100+O800). The estimated degradation rates indicate that not even the highly dense coating is protective enough. This is surprising considering that more recent SOFC stack test at Juelich show a voltage degradation rate of only 0.5 %/1000 h with $MnCo_{1.9}Fe_{0.1}O_4$ coated Crofer 22 APU [61]. The estimated degradation rates by Stanislowski et al. are probably not relevant for the current state-of-the-art stack technology. Thus, the question about whether the highly porous coating will be protective enough in terms of reducing the Cr-evaporation remains to be resolved.

5. Conclusion

The effect of $MnCo_{1.7}Fe_{0.3}O_4$ spinel coating density on the oxidation kinetics and Cr-evaporation of Crofer 22 APU has been investigated. In line with previous reports, it was found that denser coatings could be achieved by heat treating first in reducing and then in oxidizing atmospheres, compared to heat treating in air only.

The oxidation rate measured at 800 °C in air was four times lower with a highly dense coating compared to a more porous one. However, to produce the dense coating, high temperatures were needed during the reduction heat treatment step, which lead to higher initial oxidation of the steel. The implication of this was that even after 5000 h of oxidation at 800 °C, the total mass gain of samples with dense coatings was 20 % higher than the total mass gain of samples with initially porous coatings. If the lifetime is assessed on a Cr-depletion criterion alone, it was shown that even a highly porous $MnCo_{1.7}Fe_{0.3}O_4$ spinel coating provides sufficient protection of Crofer 22 APU to survive 40 000 h service at 800 °C.

The potential drawback with a porous coating is the higher Cr-evaporation rate. Although the Cr-evaporation rate was reduced ten times relative to bare Crofer 22 APU, it was still three times higher than what was measured for the dense coating. Whether this slightly higher amount of released chromium will be damaging for the cathode performance remains to be resolved.

References

[1] W.Z. Zhu, S.C. Deevi, Development of interconnect materials for solid oxide fuel cells, *Materials Science and Engineering: A*. **348** 227–243 (2003).

[2] S. Linderoth, P.V. Hendriksen, M. Mogensen, N. Langvad, Investigations of metallic alloys for use as interconnects in solid oxide fuel cell stacks, *Journal of Materials Science*. **31** 5077–5082 (1996).
[3] J.W. Fergus, Metallic interconnects for solid oxide fuel cells, *Materials Science and Engineering: A*. **397** 271–283 (2005).
[4] W.Z. Zhu, S.C. Deevi, Opportunity of metallic interconnects for solid oxide fuel cells: a status on contact resistance, *Materials Research Bulletin*. **38** 957–972 (2003).
[5] K. Hilpert, D. Das, M. Miller, D.H. Peck, R. Weiß, Chromium Vapor Species over Solid Oxide Fuel Cell Interconnect Materials and Their Potential for Degradation Processes, *Journal of The Electrochemical Society*. **143** 3642–3647 (1996).
[6] J.W. Fergus, Effect of cathode and electrolyte transport properties on chromium poisoning in solid oxide fuel cells, *International Journal of Hydrogen Energy*. **32** 3664–3671 (2007).
[7] L. Zhao, S. Amarasinghe, S.P. Jiang, Enhanced chromium tolerance of $La_{0.6}Sr_{0.4}Co_{0.2}Fe_{0.8}O_{3-\delta}$ electrode of solid oxide fuel cells by $Gd_{0.1}Ce_{0.9}O_{1.95}$ impregnation, *Electrochemistry Communications*. **37** 84–87 (2013).
[8] E. Park, S. Taniguchi, T. Daio, J.-T. Chou, K. Sasaki, Comparison of chromium poisoning among solid oxide fuel cell cathode materials, *Solid State Ionics*. **262** 421–427 (2014).
[9] M. Yang, E. Bucher, W. Sitte, Effects of chromium poisoning on the long-term oxygen exchange kinetics of the solid oxide fuel cell cathode materials $La_{0.6}Sr_{0.4}CoO_3$ and Nd_2NiO_4, *Journal of Power Sources*. **196** 7313–7317 (2011).
[10] P. Huczkowski, V. Shemet, J. Piron-Abellan, L. Singheiser, W.J. Quadakkers, N. Christiansen, Oxidation limited life times of chromia forming ferritic steels, *Materials and Corrosion*. **55** 825–830 (2004).
[11] R. Sachitanand, J.-E. Svensson, J. Froitzheim, The Influence of Cr Evaporation on Long Term Cr Depletion Rates in Ferritic Stainless Steels, *Oxidation of Metals*. **84** 241–257 (2015).
[12] H. Falk-Windisch, J.E. Svensson, J. Froitzheim, The effect of temperature on chromium vaporization and oxide scale growth on interconnect steels for Solid Oxide Fuel Cells, *Journal of Power Sources*. **287** 25–35 (2015).
[13] H. Kurokawa, C.P. Jacobson, L.C. DeJonghe, S.J. Visco, Chromium vaporization of bare and of coated iron–chromium alloys at 1073 K, *Solid State Ionics*. **178** 287–296 (2007).
[14] J. Malzbender, P. Batfalsky, R. Vaßen, V. Shemet, F. Tietz, Component interactions after long-term operation of an SOFC stack with LSM cathode, *Journal of Power Sources*. **201** 196–203 (2012).
[15] J.W. Stevenson, Z.G. Yang, G.G. Xia, Z. Nie, J.D. Templeton, Long-term oxidation behavior of spinel-coated ferritic stainless steel for solid oxide fuel cell interconnect applications, *Journal of Power Sources*. **231** 256–263 (2013).
[16] Y. Larring, T. Norby, Spinel and Perovskite Functional Layers Between Plansee Metallic Interconnect (Cr-5 wt % Fe-1 wt % Y_2O_3) and Ceramic $(La_{0.85}Sr_{0.15})_{0.91}MnO_3$ Cathode Materials for Solid Oxide Fuel Cells, *Journal of The Electrochemical Society*. **147** 3251–3256 (2000).
[17] F. Smeacetto, A. De Miranda, S. Cabanas Polo, S. Molin, D. Boccaccini, M. Salvo, et al., Electrophoretic deposition of $Mn_{1.5}Co_{1.5}O_4$ on metallic interconnect and interaction with glass-ceramic sealant for solid oxide fuel cells application, *Journal of Power Sources*. **280** 379–386 (2015).

[18] Å.H. Persson, L. Mikkelsen, P.V. Hendriksen, M.A.J. Somers, Interaction mechanisms between slurry coatings and solid oxide fuel cell interconnect alloys during high temperature oxidation, *Journal of Alloys and Compounds*. **521** 16–29 (2012).
[19] L. Chen, E.Y. Sun, J. Yamanis, N. Magdefrau, Oxidation Kinetics of $Mn_{1.5}Co_{1.5}O_4$-Coated Haynes 230 and Crofer 22 APU for Solid Oxide Fuel Cell Interconnects, *Journal of The Electrochemical Society*. **157** B931–B942 (2010).
[20] R. Trebbels, T. Markus, L. Singheiser, Investigation of Chromium Vaporization From Interconnector Steels With Spinel Coatings, *Journal of Fuel Cell Science and Technology*. **7** 011013–011013 (2009).
[21] S.-I. Lee, J. Hong, H. Kim, J.-W. Son, J.-H. Lee, B.-K. Kim, et al., Highly Dense Mn-Co Spinel Coating for Protection of Metallic Interconnect of Solid Oxide Fuel Cells, *Journal of The Electrochemical Society*. **161** F1389–F1394 (2014).
[22] M. Mirzaei, A. Simchi, M.A. Faghihi-Sani, A. Yazdanyar, Electrophoretic deposition and sintering of a nanostructured manganese–cobalt spinel coating for solid oxide fuel cell interconnects, *Ceramics International*. **42** 6648–6656 (2016).
[23] Y. Zhang, A. Javed, M. Zhou, S. Liang, P. Xiao, Fabrication of Mn–Co Spinel Coatings on Crofer 22 APU Stainless Steel by Electrophoretic Deposition for Interconnect Applications in Solid Oxide Fuel Cells, *International Journal of Applied Ceramic Technology*. **11** 332–341 (2014).
[24] M.R. Bateni, P. Wei, X. Deng, A. Petric, Spinel coatings for UNS 430 stainless steel interconnects, *Surface and Coatings Technology*. **201** 4677–4684 (2007).
[25] E. Saoutieff, G. Bertrand, M. Zahid, L. Gautier, APS Deposition of $MnCo_2O_4$ on Commercial Alloys K41X used as Solid Oxide Fuel Cell Interconnect: The Importance of Post Heat-treatment for Densification of the Protective Layer, *ECS Transactions*. **25** 1397–1402 (2009).
[26] J. Puranen, M. Pihlatie, J. Lagerbom, T. Salminen, J. Laakso, L. Hyvärinen, et al., Influence of powder composition and manufacturing method on electrical and chromium barrier properties of atmospheric plasma sprayed spinel coatings prepared from $MnCo_2O_4$ and $Mn_2CoO_4 + Co$ powders on Crofer 22 APU interconnectors, *International Journal of Hydrogen Energy*. **39** 17246–17257 (2014).
[27] L. Besra, M. Liu, A review on fundamentals and applications of electrophoretic deposition (EPD), *Progress in Materials Science*. **52** 1–61 (2007).
[28] Z. Yang, G. Xia, S.P. Simner, J.W. Stevenson, Thermal Growth and Performance of Manganese Cobaltite Spinel Protection Layers on Ferritic Stainless Steel SOFC Interconnects, *Journal of The Electrochemical Society*. **152** A1896–A1901 (2005).
[29] L.V. Gambino, N.J. Magdefrau, M. Aindow, Microstructural effects of the reduction step in reactive consolidation of manganese cobaltite coatings on Crofer 22 APU, *Materials at High Temperatures*. **32** 142–147 (2015).
[30] N.J. Magdefrau, L. Chen, E.Y. Sun, M. Aindow, The effect of $Mn_{1.5}Co_{1.5}O_4$ coatings on the development of near surface microstructure for Haynes 230 oxidized at 800 °C in air, *Surface and Coatings Technology*. **242** 109–117 (2014).
[31] N.J. Kidner, Nextech Coatings, Protective Coatings for Metallic SOFC Components, (2012).
[32] S.R. Akanda, N.J. Kidner, M.E. Walter, Spinel coatings on metallic interconnects: Effect of reduction heat treatment on performance, *Surface and Coatings Technology*. **253** 255–260 (2014).
[33] Thyssen Krupp, Crofer 22 APU Material Data Sheet No. 4046, (2010).

[34] J. Froitzheim, H. Ravash, E. Larsson, L.G. Johansson, J.E. Svensson, Investigation of Chromium Volatilization from FeCr Interconnects by a Denuder Technique, *Journal of The Electrochemical Society*. **157** B1295–B1300 (2010).
[35] C.A. Schneider, W.S. Rasband, K.W. Eliceiri, NIH Image to ImageJ: 25 years of image analysis, *Nature Methods*. **9** 671–675 (2012).
[36] S. Molin, M. Chen, P.V. Hendriksen, Oxidation study of coated Crofer 22 APU steel in dry oxygen, *Journal of Power Sources*. **251** 488–495 (2014).
[37] H. Hindam, D.P. Whittle, Microstructure, adhesion and growth kinetics of protective scales on metals and alloys, *Oxidation of Metals*. **18** 245–284 (1982).
[38] M. Palcut, L. Mikkelsen, K. Neufeld, M. Chen, R. Knibbe, P.V. Hendriksen, Corrosion stability of ferritic stainless steels for solid oxide electrolyser cell interconnects, *Corrosion Science*. **52** 3309–3320 (2010).
[39] C. Collins, J. Lucas, T.L. Buchanan, M. Kopczyk, A. Kayani, P.E. Gannon, et al., Chromium volatility of coated and uncoated steel interconnects for SOFCs, *Surface and Coatings Technology*. **201** 4467–4470 (2006).
[40] Z. Yang, G.-G. Xia, X.-H. Li, J.W. Stevenson, $(Mn,Co)_3O_4$ spinel coatings on ferritic stainless steels for SOFC interconnect applications, *International Journal of Hydrogen Energy*. **32** 3648–3654 (2007).
[41] J. Puranen, M. Pihlatie, J. Lagerbom, G. Bolelli, J. Laakso, L. Hyvärinen, et al., Post-mortem evaluation of oxidized atmospheric plasma sprayed Mn–Co–Fe oxide spinel coatings on SOFC interconnectors, *International Journal of Hydrogen Energy*. **39** 17284–17294 (2014).
[42] N.J. Magdefrau, L. Chen, E.Y. Sun, J. Yamanis, M. Aindow, Formation of spinel reaction layers in manganese cobaltite – coated Crofer22 APU for solid oxide fuel cell interconnects, *Journal of Power Sources*. **227** 318–326 (2013).
[43] M. Stanislowski, E. Wessel, K. Hilpert, T. Markus, L. Singheiser, Chromium Vaporization from High-Temperature Alloys I. Chromia-Forming Steels and the Influence of Outer Oxide Layers, *Journal of The Electrochemical Society*. **154** A295–A306 (2007).
[44] E.J. Opila, N.S. Jacobson, D.L. Myers, E.H. Copland, Predicting oxide stability in high-temperature water vapor, *JOM*. **58** 22–28 (2006).
[45] C. Key, J. Eziashi, J. Froitzheim, R. Amendola, R. Smith, P. Gannon, Methods to Quantify Reactive Chromium Vaporization from Solid Oxide Fuel Cell Interconnects, *Journal of The Electrochemical Society*. **161** C373–C381 (2014).
[46] J. Issartel, S. Martoia, F. Charlot, V. Parry, G. Parry, R. Estevez, et al., High temperature behavior of the metal/oxide interface of ferritic stainless steels, *Corrosion Science*. **59** 148–156 (2012).
[47] P. Huczkowski, N. Christiansen, V. Shemet, L. Niewolak, J. Piron-Abellan, L. Singheiser, et al., Growth Mechanisms and Electrical Conductivity of Oxide Scales on Ferritic Steels Proposed as Interconnect Materials for SOFC's, *Fuel Cells*. **6** 93–99 (2006).
[48] L. Mikkelsen, M. Chen, P.V. Hendriksen, Å. Persson, N. Pryds, K. Rodrigo, Deposition of $La_{0.8}Sr_{0.2}Cr_{0.97}V_{0.03}O_3$ and $MnCr_2O_4$ thin films on ferritic alloy for solid oxide fuel cell application, *Surface and Coatings Technology*. **202** 1262–1266 (2007).
[49] I.-H. Jung, Critical evaluation and thermodynamic modeling of the Mn–Cr–O system for the oxidation of SOFC interconnect, *Solid State Ionics*. **177** 765–777 (2006).

[50] H.L. Lein, T. Tezuka, T. Grande, M.-A. Einarsrud, Asymmetric proton conducting oxide membranes and fuel cells prepared by aqueous tape casting, *Solid State Ionics*. **179** 1146–1150 (2008).
[51] M. Weirich, J. Gurauskis, V. Gil, K. Wiik, M.-A. Einarsrud, Preparation of lanthanum tungstate membranes by tape casting technique, *International Journal of Hydrogen Energy*. **37** 8056–8061 (2012).
[52] T. Horita, H. Kishimoto, K. Yamaji, Y. Xiong, M.E. Brito, H. Yokokawa, et al., Diffusion of oxygen in the scales of Fe–Cr alloy interconnects and oxide coating layer for solid oxide fuel cells, *Solid State Ionics*. **179** 2216–2221 (2008).
[53] M. Palcut, L. Mikkelsen, K. Neufeld, M. Chen, R. Knibbe, P.V. Hendriksen, Efficient dual layer interconnect coating for high temperature electrochemical devices, *International Journal of Hydrogen Energy*. **37** 14501–14510 (2012).
[54] P. Kofstad, K.P. Lillerud, On High Temperature Oxidation of Chromium II . Properties of and the Oxidation Mechanism of Chromium, *Journal of The Electrochemical Society*. **127** 2410–2419 (1980).
[55] K. Hoshino, N.L. Peterson, Cation Self-Diffusion in Cr_2O_3, *Journal of the American Ceramic Society*. **66** c202–c203 (1983).
[56] N.J. Magdefrau, L. Chen, E.Y. Sun, M. Aindow, Effects of alloy heat treatment on oxidation kinetics and scale morphology for Crofer 22 APU, *Journal of Power Sources*. **241** 756–767 (2013).
[57] W. Wongpromrat, G. Berthomé, V. Parry, S. Chandra-ambhorn, W. Chandra-ambhorn, C. Pascal, et al., Reduction of chromium volatilisation from stainless steel interconnector of solid oxide electrochemical devices by controlled preoxidation, *Corrosion Science*. **106** 172–178 (2016).
[58] W.J. Quadakkers, K. Bongartz, The prediction of breakaway oxidation for alumina forming ODS alloys using oxidation diagrams, *Materials and Corrosion*. **45** 232–241 (1994).
[59] X. Montero, N. Jordán, J. Pirón-Abellán, F. Tietz, D. Stöver, M. Cassir, et al., Spinel and Perovskite Protection Layers Between Crofer22APU and $La_{0.8}Sr_{0.2}FeO_3$ Cathode Materials for SOFC Interconnects, *Journal of The Electrochemical Society*. **156** B188–B196 (2009).
[60] M. Stanislowski, J. Froitzheim, L. Niewolak, W.J. Quadakkers, K. Hilpert, T. Markus, et al., Reduction of chromium vaporization from SOFC interconnectors by highly effective coatings, *Journal of Power Sources*. **164** 578–589 (2007).
[61] L. Blum, U. Packbier, I.C. Vinke, L.G.J. de Haart, Long-Term Testing of SOFC Stacks at Forschungszentrum Jülich, *Fuel Cells*. **13** 646–653 (2013).

Manuscript V

Effect of pre-oxidation on the oxidation resistance of Crofer 22 APU

Belma Talic[a,b], Sebastian Molin[b], Peter Vang Hendriksen[b], Hilde Lea Lein[a]

[a] *Department of Materials Science and Engineering, Norwegian University of Science and Technology, Norway*
[b]*Department of Energy Conversion and Storage, Technical University of Denmark, Risø Campus, Denmark*

Abstract. Ferric stainless steels such as Crofer 22 APU are attractive for the use as interconnects in solid oxide fuel cell (SOFC) stacks. This work investigates the effect of pre-oxidation on the oxidation behavior of Crofer 22 APU. Pre-oxidation heat treatments were performed in air, N_2-9%H_2 or H_2 to either form an oxide scale on the surface or increase the alloy grain size. Oxidation kinetics were evaluated in air based on mass gain measurements. Oxide scale composition and morphology was characterized by scanning electron microscopy, energy dispersive X-ray spectroscopy and X-ray diffraction. The oxidation rate in air at 800 °C was reduced by a short (< 5 h) heat treatment at higher temperatures in either air or N_2-9%H_2. Increasing the grain size of the alloy had an adverse effect on the oxidation resistance. In all cases the scale formed on Crofer 22 APU consisted of an outer $(Mn,Cr)_3O_4$ layer, an inner Cr_2O_3 layer and sub-scale $(Mn,Cr)_3O_4$ nodules. The ratio of the different oxidation products varied with heat treatment procedure and the effect of pre-oxidation is discussed on the basis of this variation.

1. Introduction

Solid oxide fuel cells (SOFC) offer an environmentally friendly way of converting the chemical energy in fuels such as H_2 to electrical energy with a high electrical conversion efficiency [1]. The operating principle may be described by the following reaction:

$$H_2\,(g) + ½\,O_2\,(g) \rightarrow H_2O + \text{electrical energy} + \text{heat}$$

A single SOFC unit consists of two porous electrodes separated by a dense, ionically conductive electrolyte and has an open circuit potential of ca. 1 V [1]. To obtain higher voltages several cells are stacked together in series. Interconnects are then used between the electrodes of adjacent cells to provide a path for the current and separate the fuel supplied to one cell from the oxidant supplied to the other. In addition to being electrically conductive and stable in the fuel and oxidant atmospheres, the interconnect material should be chemically compatible with the

electrode materials, have a thermal expansion coefficient matching the other SOFC components, easy to manufacture and shape, and affordable [2,3].

Ferritic stainless steels (FSS) are promising for this application as they satisfy many of the above mentioned criteria [4,5]. In recent years, a number of new alloys specifically targeted towards the application as interconnects have been developed [6–8]. These have several common features such as: a high Cr-content (20-24 wt.%) to ensure a sufficiently large "Cr-reservoir" for long-term stability [9], minor additions of Mn (< 1 wt.%) to form an outer $(Mn,Cr)_3O_4$ scale that reduces Cr-volatilization [10], and additions of reactive elements such as La and Zr for improved scale adherence and oxidation resistance [11,12].

However, despite the development of highly specialized alloys, there are still some challenges limiting the use of pure FSS as the interconnect material. For corrosion resistance these alloys rely on forming a chromia scale, which has only a moderate electrical conductivity [13]. Consequently, as the chromia scale thickens with time, the resistance across the SOFC stack increases [14]. Another challenge is the volatilization of Cr(VI) species, which have been found to deposit on the electrochemically active sites of the oxygen electrode and thereby degrade its electrochemical activity [15,16]. Due to these challenges, the FSS will need to be coated in order to survive the envisioned service lifetime of 40 000 h of stack operation [17].

$(Mn,Co)_3O_4$ spinels are promising coating materials, demonstrated to limit Cr-volatilization and reduce the oxidation rate and electrical resistance of the FSS [18–21]. In [Manuscript IV] we investigated how the protective capabilities of spinel coatings are affected by the initial density of the coating. $MnCo_{1.7}Fe_{0.3}O_4$ coated Crofer 22 APU was heat treated in air or N_2-9%H_2 at different temperatures to create different levels of porosity in the coating. The parabolic oxidation rate of Crofer 22 APU in air at 800 °C was reduced by more than a factor of 10 by a highly dense coating (produced by heat-treating at 1100 °C in N_2-9%H_2 followed by 800 °C in air). Comparably, an initially highly porous coating (produced by heat-treating at 900 °C in air only) reduced the oxidation rate by a factor of 3. The difference in oxidation resistance was believed to be mainly due to the difference in coating porosity, however, it was speculated whether pre-oxidation of the alloy also could have some influence.

Magdefrau et al. [22] showed that the parabolic oxidation rate of Crofer 22 APU in air at 800 °C could be reduced by a factor of 3.5 by a heat treatment that increased the alloy grain size from ca. 16 to 250 μm. The beneficial effect of the heat treatment was attributed to an increased proportion and grain size of the $MnCr_2O_4$ scale layer formed on top of Cr_2O_3. Others have reported that pre-oxidation of Crofer 22 APU in air is beneficial for improving the oxidation resistance during subsequent exposure to H_2-H_2O [23]. Conversely, pre-oxidation in H_2-H_2O was found beneficial for reducing erosion-corrosion of Incoloy 800H in air at 500 °C with silica as the erodent [24]. Literature on the effect of pre-oxidation of chromia forming alloys is otherwise limited.

In this work we investigate the effect of pre-oxidation on the oxidation resistance of Crofer 22 APU in air. The conditions for pre-oxidation were chosen based on the heat treatment procedures previously used in [Manuscript IV] to densify the spinel coatings. This is to elucidate whether some of the apparent dependence of oxidation rate on coating density in reality should be attributed to modifications of the alloy. We have additionally included samples where Crofer 22 APU was heat treated to increase the alloy grain size without forming an external oxide scale. This was to investigate whether the improved oxidation resistance could be due to an increase of the alloy grain size, as previously suggested [22].

2. Experimental

Crofer 22 APU (Thyssen Krupp) with the composition as given in Table 1 was used for this study. This batch belongs to the newer batches of Crofer 22 APU, with low Si and Al contents. The 1 mm sheet was laser cut into 20×20 mm coupons. A 3 mm hole was drilled in one of the corners of each coupon to allow for hanging in the oxidation furnace. The coupons were ground with SiC-paper, polished down to 1 μm using diamond abrasive and cleaned in acetone and ethanol for 10 minutes each in an ultrasonic bath. Typically thickness after polishing was 0.8-0.9 mm.

Table 1. Composition of Crofer 22 APU alloy used in this study in wt.%. Analyzed by Optical Emission Spectroscopy (OES) at Force Technology, Denmark.

Alloy	Fe	Cr	Mn	Ti	La	C	Si	Al
Crofer 22 APU	Bal.	23	0.42	0.068	0.04-0.20[1]	0.003	0.049[2]	0.007

[1]La was not analyzed by OES. Concentration is according to manufacturer's datasheet
[2]Determination of Si content by OES is associated with large uncertainty

The coupons were heat treated to either grow an oxide layer or increase the grain size of the alloy. Some coupons were also left in the as-received state, i.e. only polished and cleaned. An overview of the heat treatment procedures and sample abbreviations used throughout this text is given in Table 2. All heat treatments were performed in tubular furnaces with the coupons suspended vertically (hanging from an alumina rod) and with heating and cooling rates of 120 °C/h. Air and N_2-9%H_2 were bubbled through water at 5 °C to achieve a water vapor content of ca. 1%. During the H1100 heat treatment, the furnace tube was (for safety reasons) initially purged with Ar and heated at 50 °C for 3 min before pure H_2 was introduced. During cooling the gas was again switched to Ar below 425 °C. The flow rate of both gasses was 13 L/min. The pO_2 in the furnace at 1100 °C was ca. 10^{-21} atm. The H1100 samples were re-polished after heat treatment.

Table 2. Overview of heat treatment procedures and sample abbreviation used throughout this text.

Abbreviation	Heat treatment
As received	
O900	900 °C, air-1%H_2O, 2h
R900+O800	900 °C, N_2-9%H_2-1%H_2O, 2h + 800 °C, air-1%H_2O, 2h
R1100+O800	1100 °C, N_2-9%H_2-1%H_2O, 5h + 800 °C, air-1%H_2O, 5h
H1100	1100 °C, H_2 (pO_2 10^{-21} atm), 2h

Oxidation behavior was studied in stagnant air at 700 °C, 800 °C and 900 °C. Three to five alloy coupons of each type were suspended vertically in a chamber furnace. The humidity content in the furnace was not controlled. Every 250 h, the furnace was cooled to room temperature (180 °C/h) and the coupons were weight on a scale with 0.00001 g accuracy (XS205 Mettler Toledo).

Microstructural characterization was made using a scanning electron microscope (SEM, Zeiss Supra 35 Field Emission SEM) equipped with an energy dispersive X-ray spectroscopy detector (EDX, Noran System SIX X-ray microanalysis system). For cross sectional analysis the steel coupons were cold vacuum embedded in epoxy, ground and polished in successive steps down to 1 µm, and finally carbon coated. EDX data were collected at an acceleration voltage of 15 kV and analyzed using the Noran System SIX software (Thermo Scientific, ver. 2.3). Quantification of the collected spectra was performed by standardless analysis and the results are therefore semi-quantitative.

To reveal the alloy grains, epoxy mounted, polished samples were etched for 40 s by immersion in a mixture (by volume) of 1 part HNO_3, 3 parts glycerol and 5 parts HCl. The etched samples were inspected in an optical microscope (Leitz Aristomet) and the grain size was quantified by the linear intercept method on images of 1200×900 µm. At least four lines on four representative images were analyzed for each sample.

3. Results

3.1 Microstructural characterization after pre-oxidation

SEM backscatter electron (BSE) images of the R900+O800 sample after pre-oxidation are shown in Figure 1. The surface is observed for the most part to be covered by an oxide of sub-micron (100-200 nm) sized grains. The cross sectional micrograph (Fig. 1b) reveals a 0.3-0.8 µm thick oxide scale that contains significant amounts of iron in addition to chromium and manganese according to EDX analysis. Pre-oxidation at 900 °C in air (O900) lead to the formation of a 0.1-0.3 µm thick oxide scale with an otherwise similar grain size. XRD analysis (Fig. 2) shows peaks belonging to the alloy and a cubic spinel oxide for both O900 and

R900+O800. The intensity of the peaks belonging to the oxide were weaker for O900 than for R900+O800, reflecting the difference in oxide scale thickness on the two.

SEM images of the surface and cross section of the R1100+O800 sample after pre-oxidation are shown in Figure 3. The oxide scale on the surface has a plate and whisker-like morphology, characteristic for oxide scales formed in reducing atmospheres [10,25,26]. The cross sectional micrograph shows an oxide scale of approximately 2.8-3.0 µm thickness. According to EDX analysis (not shown) the top and bottom part of the scale were rich in Mn, while the center was nearly pure Cr_2O_3. Alloy inclusions in the scale are also visible in Figure 3b. XRD analysis (Fig. 2) reveals in this case peaks belonging to Cr_2O_3 in addition to the alloy and a cubic spinel.

No visible oxide scale was formed after heat treatment in pure hydrogen (H1100). The sample surface still had a metallic shine and XRD (Fig. 2) shows peaks belonging to the alloy only.

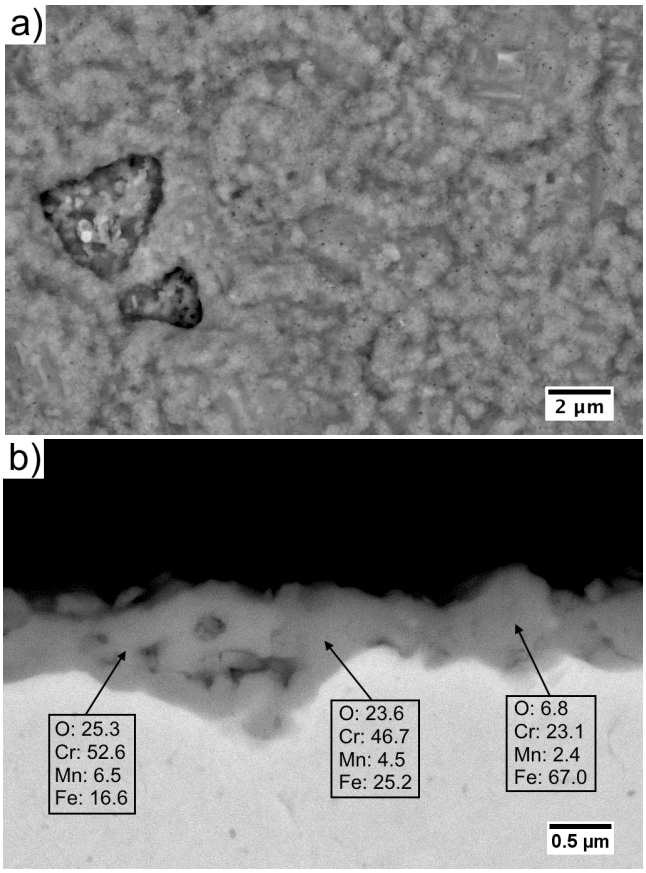

Figure 1. SEM-BSE micrographs of R900+O800 after pre-oxidation heat treatment. (a) surface, (b) cross section and EDX point analysis results (in wt.%).

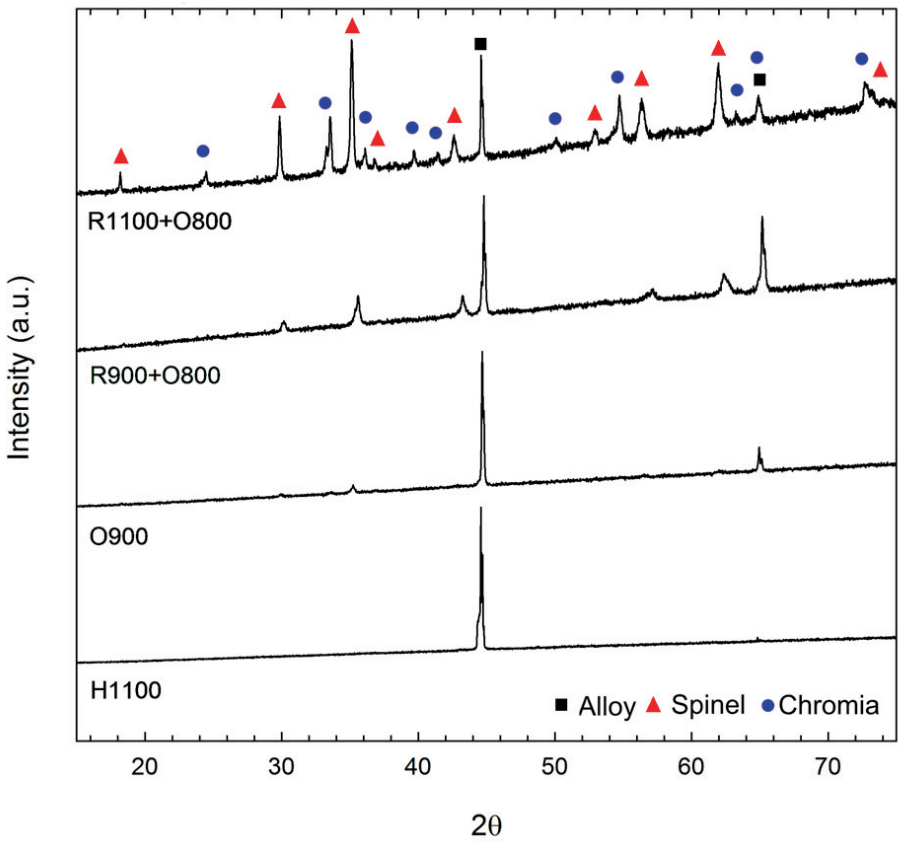

Figure 2. X-ray diffractograms of Crofer 22 APU after pre-oxidation heat treatment. Alloy = PDF 65-4664, Spinel = PDF 75-1614, Chromia = PDF 38-1479.

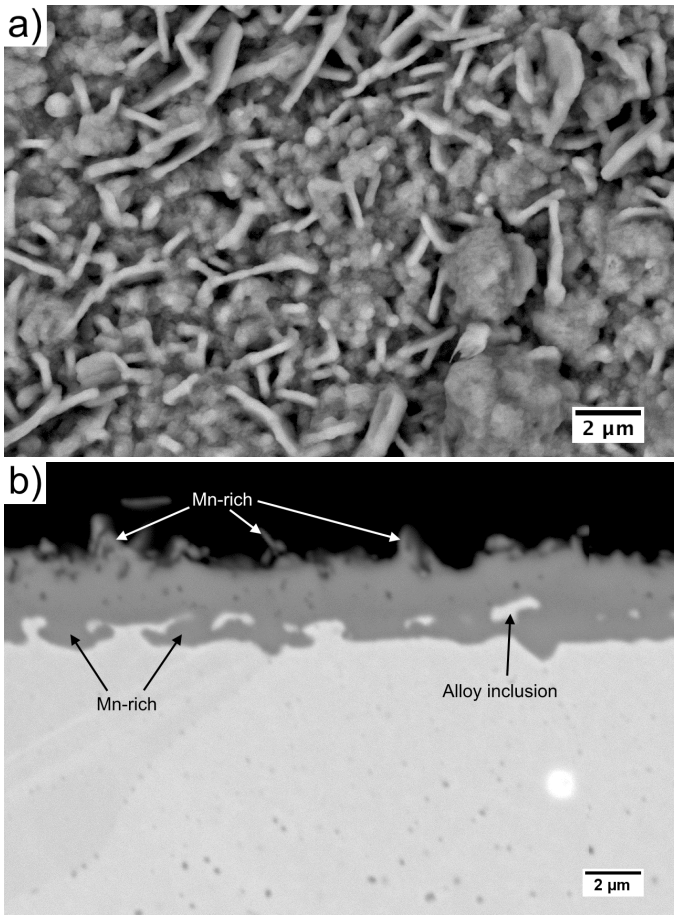

Figure 3. SEM-BSE micrographs of R1100+O800 after pre-oxidation heat treatment. (a) surface, (b) cross section.

Optical micrographs of etched cross sections of as-received Crofer 22 APU and after the H1100 and R1100+O800 heat treatments are shown in Figure 4. The average grain size, determined by the linear intercept method, was 35 µm for the as-received sample, 380 µm for H1100 and 230 µm for R1100+O800. Heat treatment at 900 °C did not lead to any significant grain growth, i.e. the grain size of the O900 and R900+O800 samples after pre-oxidation was essentially the same as in the as-received alloy.

As seen in Figure 4, the alloy grains in the R1100+O800 sample are smaller in the near-surface region of the coupon compared to in the center, while the grains of the H1100 sample are of more uniform size across the whole sample thickness. This can be attributed to the formation of an oxide scale on the surface of R1100+O800, which inhibited grain-growth in the near-surface region of the alloy.

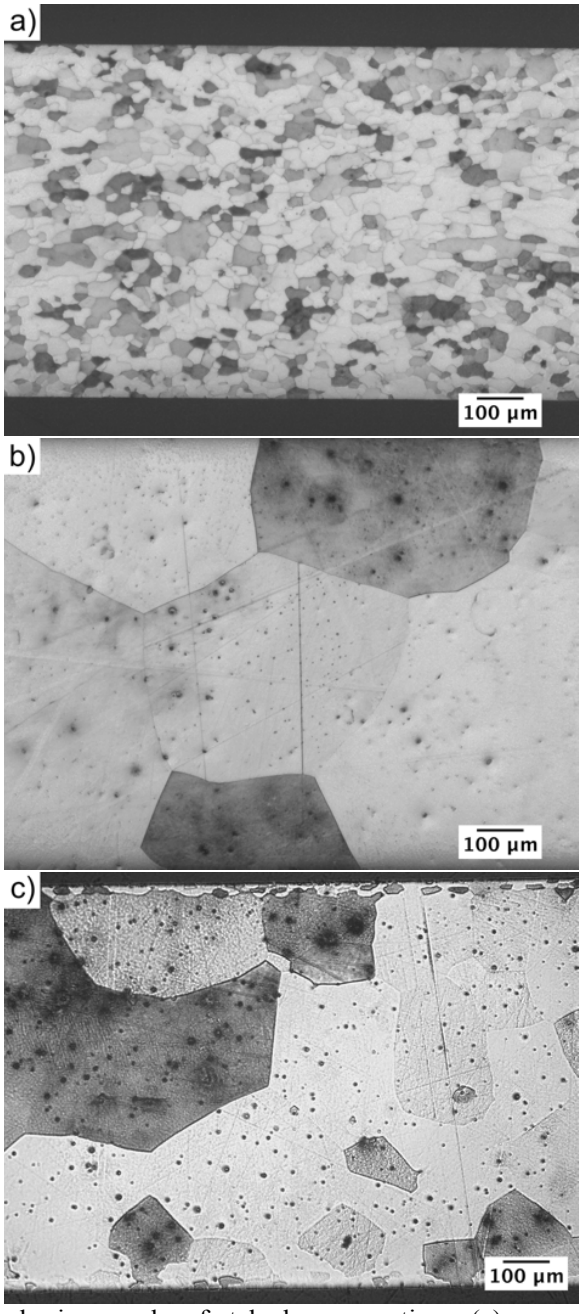

Figure 4. Optical micrographs of etched cross sections. (a) as-received Crofer 22 APU, (b) after H1100 heat treatment, (c) after R1100+O800 pre-oxidation heat treatment.

3.2 Oxidation kinetics

The average mass gain after pre-oxidation heat treatment was 0.055 mg/cm^2 for O900, 0.096 mg/cm^2 for R900+O800, and 0.556 mg/cm^2 for R1100+O800. Heat treatment in pure hydrogen (H1100) resulted in an average mass loss of 0.024 mg/cm^2. The mass change of all samples during subsequent oxidation in air at 800 °C is shown in Figure 5. In Figure 6, these results have been re-calculated to include the mass gain during pre-oxidation. The curves have also been shifted along the x-axis to adjust for the "equivalent age" of the sample due to the pre-oxidation heat treatment. The equivalent age is taken as the length of time as-received Crofer 22 APU was oxidized in air at 800 °C before acquiring the same mass gain as during the pre-oxidation heat treatment. For example, the mass gain after R1100+800 pre-oxidation was 0.556 mg/cm^2, and as-received Crofer 22 APU was oxidized ca. 1650 h at 800 °C before gaining the same mass. Thus, the equivalent age of the R1100+O800 pre-oxidation is 1650 h. By making this adjustment, the existing oxide scale on pre-oxidized samples is accounted when comparing the oxidation results.

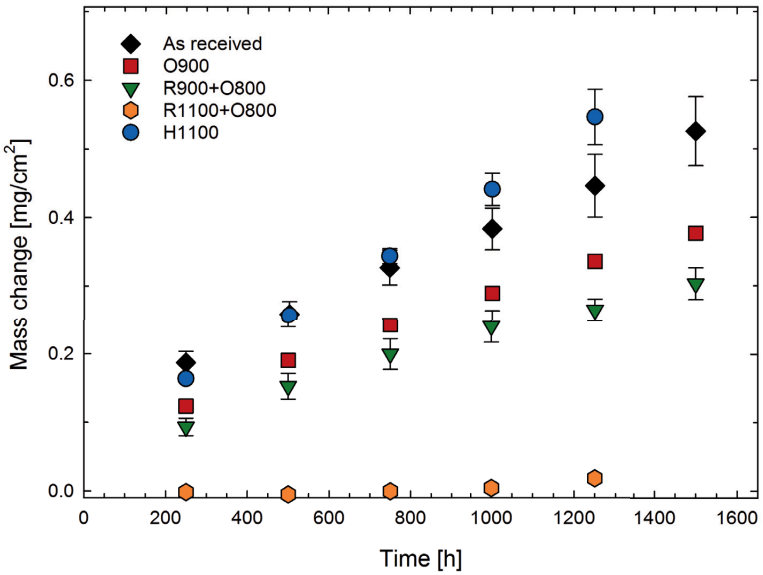

Figure 5. Mass change of Crofer 22 APU during cyclic oxidation in air at 800 °C.

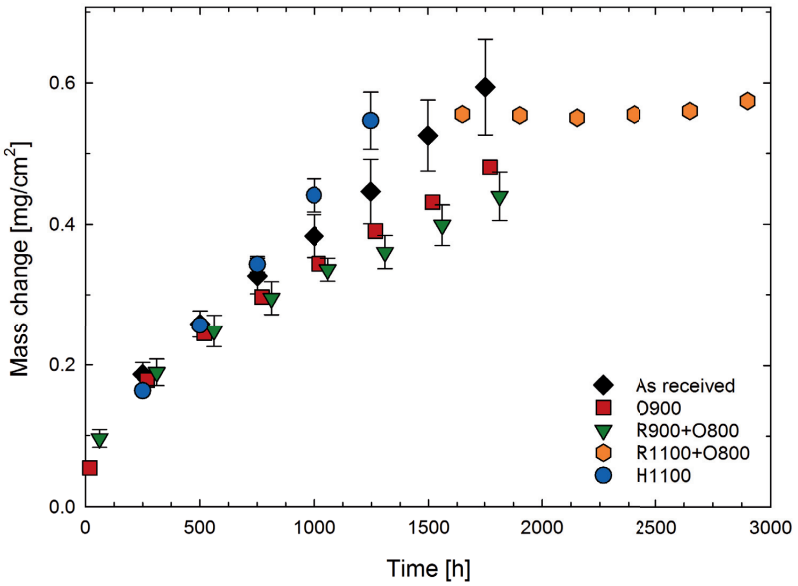

Figure 6. Mass change of Crofer 22 APU during cyclic oxidation in air at 800 °C, recalculated to account for mass gain during pre-oxidation.

During the first 1000 h of oxidation the kinetics of the as-received, O900 and R900+O800 samples are in approximate agreement with the parabolic rate law, described by:

$$(\Delta m/A)^2 = k_P t + C$$

where $\Delta m/A$ is the mass change per unit area [mg/cm^2], t is the time [s], k_P is the parabolic rate constant [g^2/cm^{4}s] and C is an integration constant. The parabolic rate constants were determined by a linear fit of the slope of a $(\Delta m/A)^2$ vs t plot based on mass change measured between 250 and 1000 h oxidation, as shown in Figure 7. Note that the slopes are evaluated based on the recalculated mass changes. The rate constants were 4.2×10^{-14} g^2/cm^{4}s for the as-received sample, 3.2×10^{-14} g^2/cm^{4}s for O900 and 2.9×10^{-14} g^2/cm^{4}s for R900+O800. I.e. pre-oxidation in both air and N_2-H_2 at 900 °C appear to slightly lower the oxidation rate of Crofer 22 APU at 800 °C in air. After ca. 1000 h, the mass change started to deviate from parabolic behavior for all three sets of samples. Localized break-away oxidation was observed on the edges of samples taken out after 2000 h oxidation at 800 °C (Appendix B).

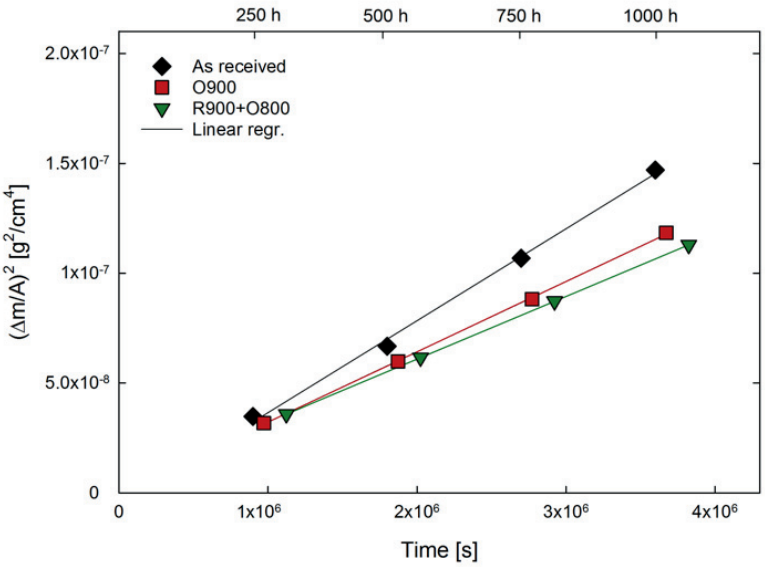

Figure 7. Mass change of Crofer 22 APU at 800 °C in air, plotted in parabolic units to determine the rate constants.

The mass change of the R1100+O800 and H1100 samples deviated strongly from parabolic oxidation kinetics also the first 1000 h of oxidation. Initially, the mass gain of H1100 is slightly lower than the mass gain of the as-received sample, however, after ca. 500 h of oxidation the reverse becomes true. After 1000 h at 800 °C the average mass gained by H1100 samples was 0.44 mg/cm^2, while the average mass gained by the as-received samples was 0.38 mg/cm^2. By fitting the mass change of H1100 to the general rate equation, $(\Delta m/A)^m = k_m t + C$, the coefficient m was determined to ca. 1.4. This is indicative of oxidation kinetics intermediate between linear and parabolic [27]. The same analysis could not be made using the R1100+O800 data, partly because the mass change per sample was close to the sensitivity of the scale used (0.01 mg). Nevertheless, from Figure 6 it is clear that the oxidation rate after the R1100+O800 pre-oxidation is considerably decreased compared to the as-received alloy.

To investigate whether the beneficial grain size effect reported by Magdefrau et al. [22] could be due to internal oxidation or depletion of Mn from the alloy, some of the R1100+O800 samples were re-polished after pre-oxidation to remove the formed oxide scale. The average mass gain of these sample after 1000 h at 800 °C was 0.32 mg/cm^2 (measurement before 1000 h may be found in Appendix C).

The as-received and R900+O800 samples were additionally oxidized in air at 700 °C and 900 °C. The mass change, recalculated to include mass gain during pre-oxidation, is shown in Figure 8. After re-calculation, there is no significant difference in the mass change of the as-received and pre-oxidized samples. Parabolic oxidation kinetics are obeyed at both temperatures with the rate constants determined to be 1.8×10^{-15} g^2/cm^4s at 700 °C and 1.3×10^{-12} g^2/cm^4s at 900 °C.

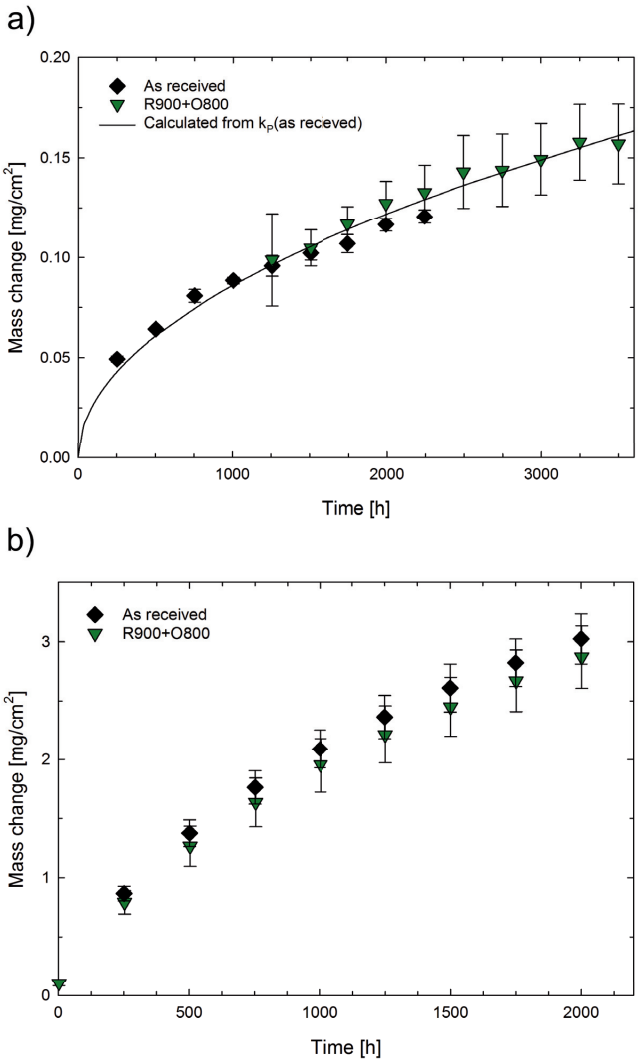

Figure 8. Mass change during cyclic oxidation in air. (a) at 700 °C, showing also the parabolic fit to the mass change of the as-received sample, (b) at 900 °C.

3.3 Microstructural characterization after oxidation at 800 °C

X-ray diffractograms of all samples after 1000 h oxidation at 800 °C in air are shown in Figure 9. Peaks identified as belonging to chromia, $(Mn,Cr)_3O_4$ spinel and the alloy can be observed for all samples. The H1100 sample shows slightly stronger reflections for chromia compared to the other samples, otherwise the differences are minor.

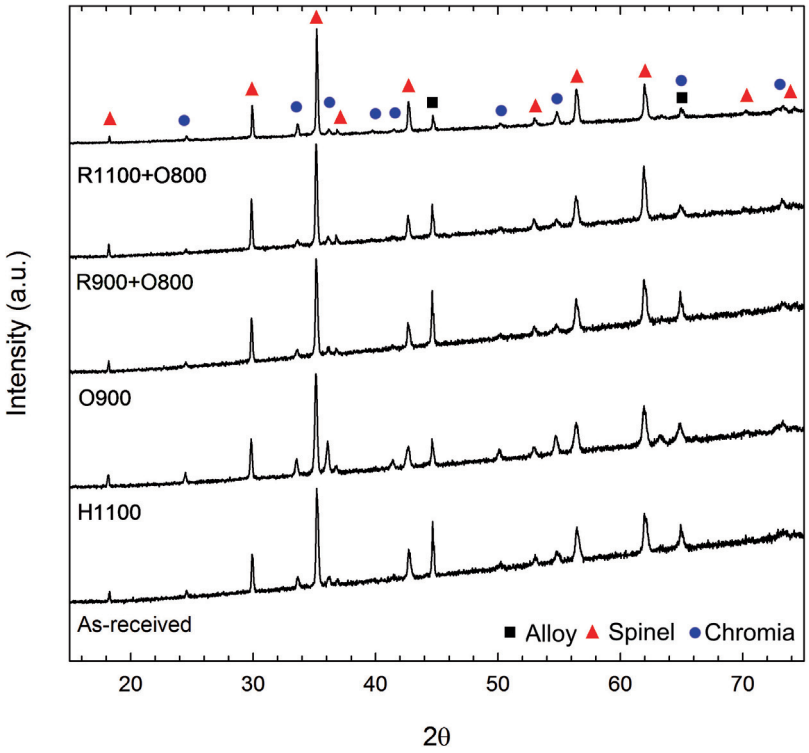

Figure 9. X-ray diffractograms of Crofer 22 APU after 1000 h oxidation in air at 800 °C. Alloy = PDF 65-4664, Spinel = PDF 75-1614, Chromia = PDF 38-1479.

Figure 10a shows SEM micrographs of the surface of as-received Crofer 22 APU after 1000 h oxidation at 800 °C in air. The morphology is characterized by oxide ridges arranged in a pattern resembling the grain structure of the alloy (cf. Fig. 4a). The high magnification insert shows oxide grains in the range of 200-300 nm. A similar surface morphology was observed for the O900 and R900+O800 samples, although with slightly fewer ridges covering the surface of the latter.

Figure 10b shows a cross sectional SEM image of the same as-received sample. From measurements on at least five representative SEM images with the same magnification, the average oxide scale thickness was determined to 1.8±0.3 µm.

The thickness of the scale measured on the O900 and R900+O800 samples was 1.7±0.4 µm and 1.6±0.3 µm, respectively. For all three, the oxide scale appeared to be overall dense and well adherent to the alloy. At periodic intervals of ca. 20-40 µm, oxide nodules protruding into the alloy could be observed. These typically had a diameter of ca. 2-5 µm and are highlighted in Figure 10b. The scale above these nodules was buckled and slightly thicker than the scale on the flat parts. The distance between the oxide nodules corresponds well with the distance between the ridges observed on the sample surface (cf. Fig. 10a). The insert in Figure 10b shows an optical micrograph of the same sample after chemical etching, demonstrating that the oxide nodules are located on alloy grain boundaries.

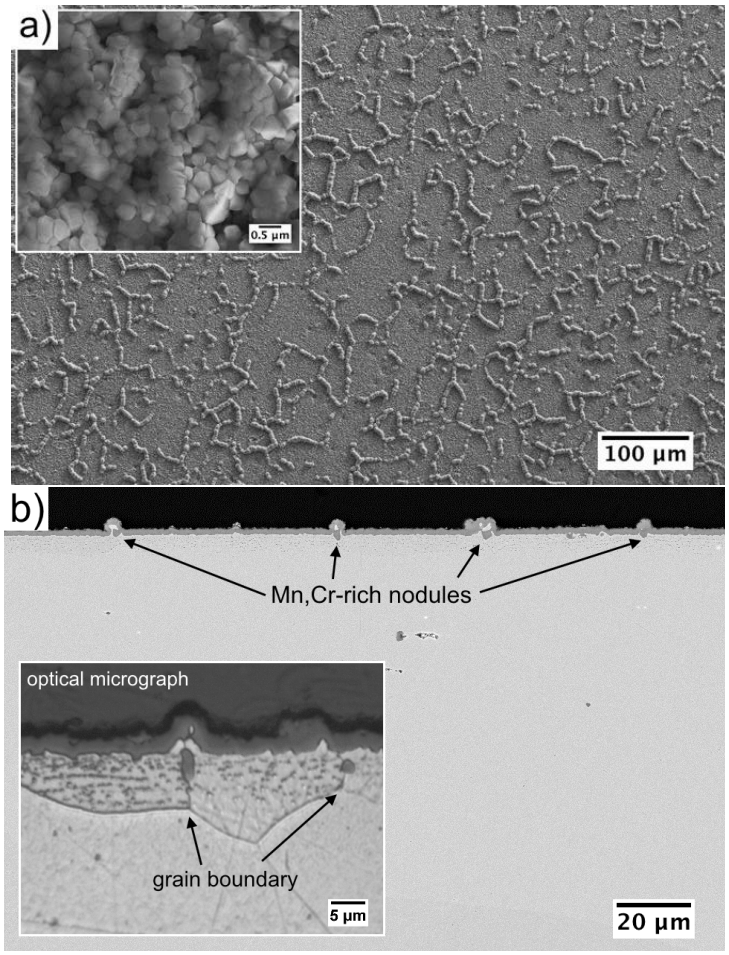

Figure 10. Micrographs of as-received Crofer 22 APU after 1000 h oxidation at 800 °C in air. (a) SEM-SE surface, (b) SEM-BSE of cross section and (insert) optical micrograph of etched cross section.

Figure 11 shows compositional EDX maps of the oxide scale on the as-received sample. These show that the nodules beneath the scale are rich in Mn and Cr. Quantitative EDX point analysis revealed a Cr/Mn atomic ratio close to 2/1. The scale above these nodules is seen to consists of an inner Cr_2O_3 layer and an outer $(Mn,Cr)_3O_4$ layer. Smaller internal oxides rich in Ti can also be identified in the EDX map. These were observed in the 30-40 µm subsurface region of all samples after oxidation (visible in SEM-BSE images by darker contrast compared to alloy).

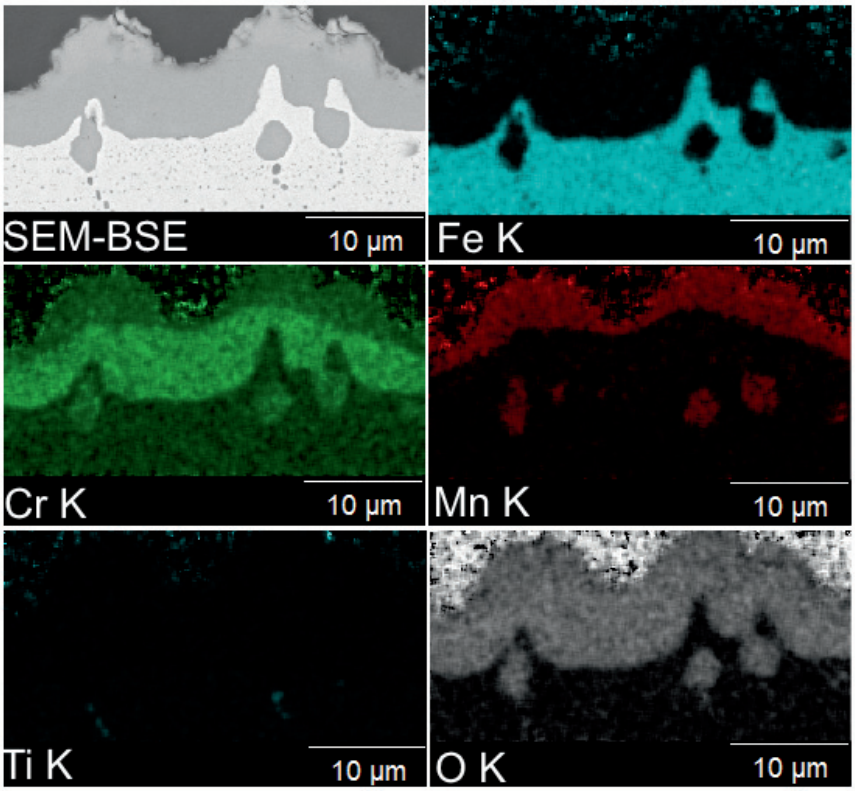

Figure 11. Cross section SEM-BSE micrograph and EDX maps of as-received sample after 1000 h oxidation at 800 °C in air.

Figure 12 shows SEM images of the surface and cross section of the H1100 sample after 1000 h oxidation at 800 °C in air. The grain size of the oxide on the surface is approximately 200-400 µm. Oxide ridges can again be observed on the surface (Fig. 12a), however, the distance between these is clearly greater than the distance between the ridges on the as received sample (cf. Fig. 10a). Correspondingly, fewer oxide nodules protruding into the alloy can be seen in the cross sectional image (Fig. 12b). Considering the larger grain size of this sample

before oxidation (Fig. 4b), this further verifies that the nodules primarily are formed at alloy grain boundaries.

The average oxide scale thickness after 1000 h oxidation at 800 °C in air was determined to 2.1±0.4 µm. The cross sectional BSE micrograph (Fig. 12b) reveals small bright spots distributed in the alloy, also far below the surface. These were observed in all of the samples and found to be rich in La according to EDX analysis.

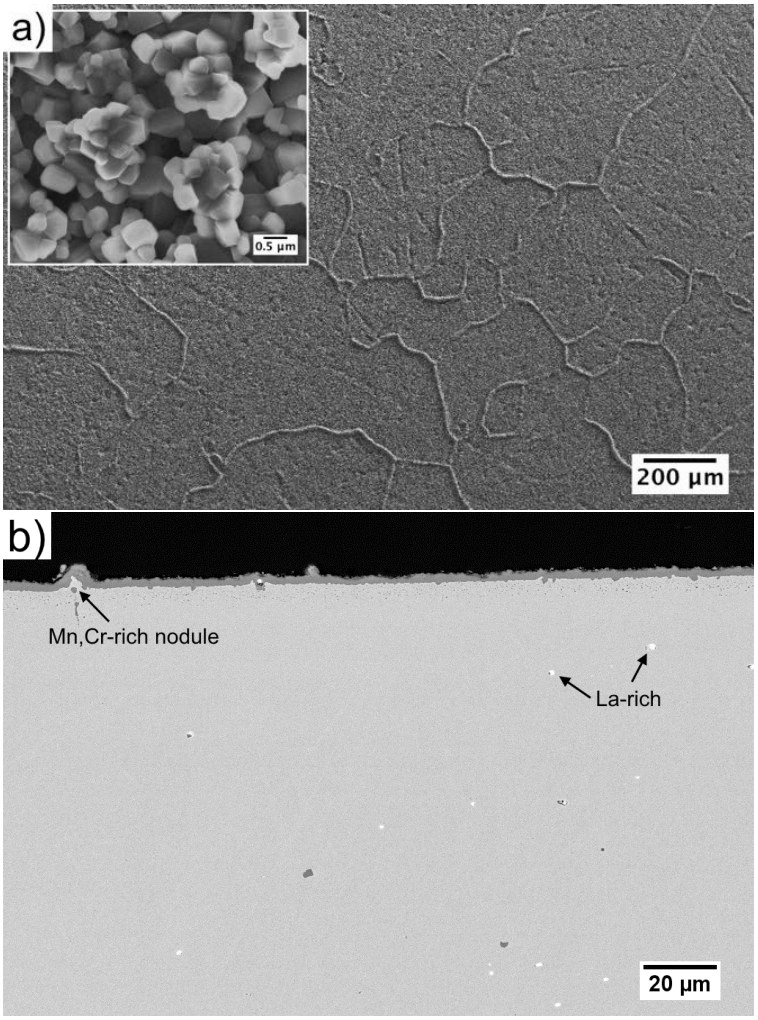

Figure 12. Surface (a) and cross sectional (b) SEM micrographs of H1100 sample after 1000 h oxidation at 800 °C in air.

The composition of the flat part of the oxide scale, i.e. areas free of subscale nodules, was different for the as-received and H1100 samples. Compositional EDX linescans of the two samples are shown in Figure 13. In both cases, the scale consist of an inner Cr_2O_3 layer and an outer $(Mn,Cr)_3O_4$ layer. However, the $Cr_2O_3/(Mn,Cr)_3O_4$ thickness ratio is clearly greater for H1100. For the as-received sample, it may also be noted that the fraction of spinel is greater in this flat part of the scale compared to above the oxide nodules (cf. Fig. 11).

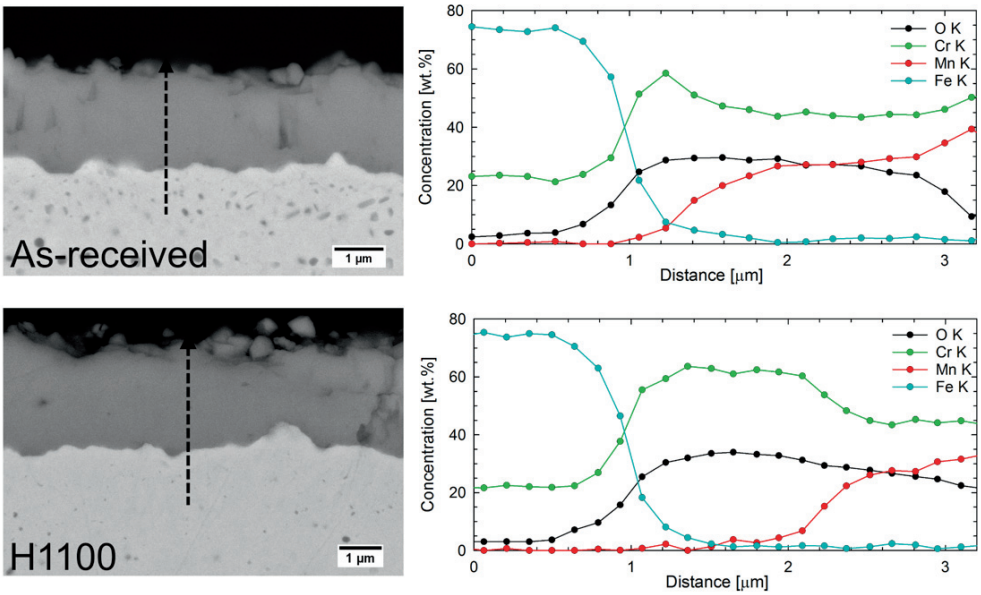

Figure 13. Cross sectional SEM-EDX images and EDX compositional linescans of the as-received (top) and H1100 (bottom) samples after 1000 h oxidation at 800 °C in air.

Surface and cross sectional SEM images of the R1100+O800 sample after 1000 h oxidation at 800 °C in air are shown in Figure 14. In this case, the surface is without any distinct oxide ridges. The high magnification insert in Figure 14a indicates a more faceted oxide scale compared to the as-received and H1100 samples, with grains in the range of 300-800 nm. The average thickness of the oxide scale was determined to 2.91±0.3 µm. Very few oxide nodules protruding into the alloy were found along the length of the sample. Alloy inclusions could be observed in the center of the scale. EDX mapping of the cross section (Fig. 15) reveals that the oxide scale below the alloy inclusions consist of a nearly continuous layer of $(Mn,Cr)_3O_4$, while the scale above the inclusions consists of an inner Cr_2O_3 layer and an outer $(Mn,Cr)_3O_4$ layer.

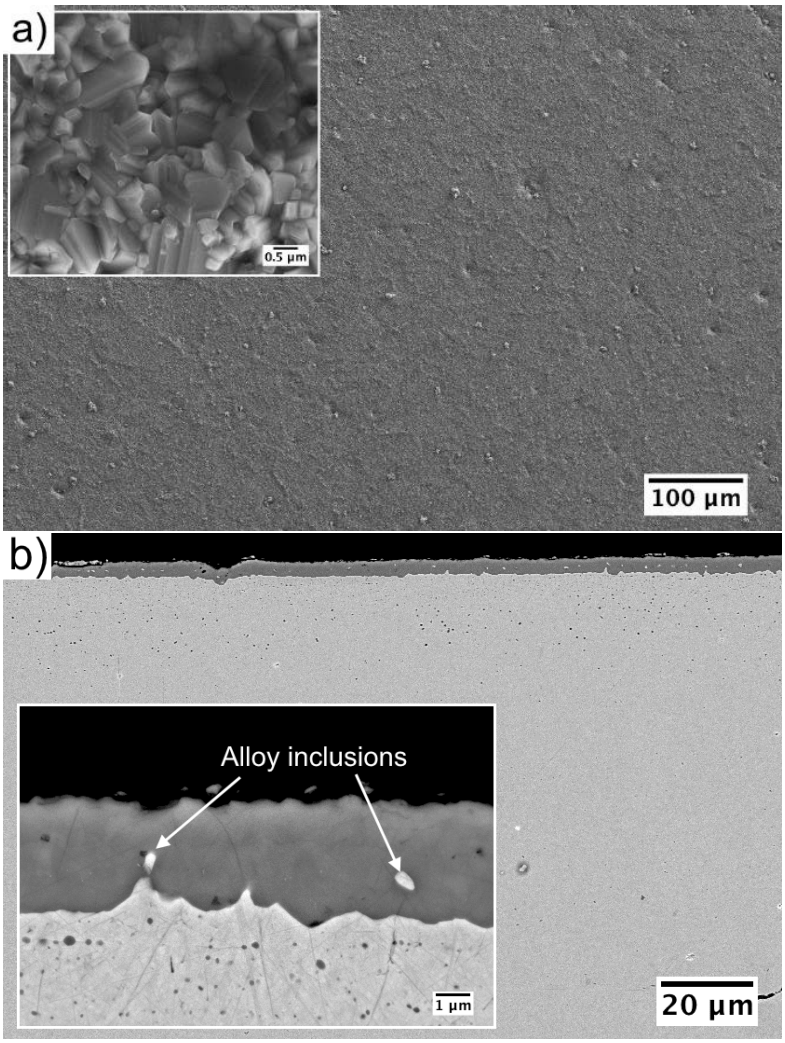

Figure 13. Surface (a) and cross sectional (b) SEM micrographs of R1100+O800 sample after 1000 h oxidation at 800 °C in air

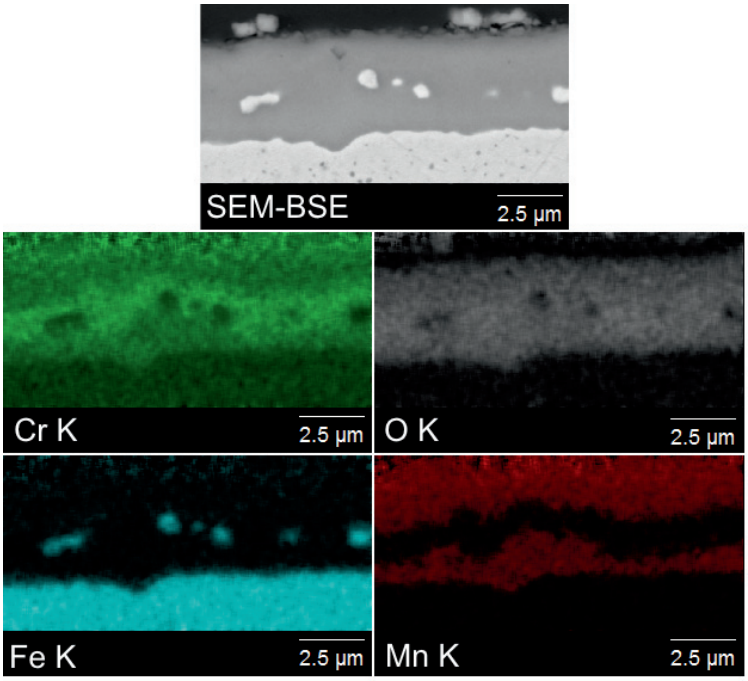

Figure 14. SEM-BSE micrograph and EDX maps of R1100+O800 sample after 1000 h oxidation at 800 °C in air.

4. Discussion

4.1 Effect of pre-oxidation

The results show that the oxidation rate of Crofer 22 APU at 800 °C in air can be significantly reduced by pre-oxidation in reducing atmosphere above this temperature. Conversely, heat treating the alloy to increase the grain size, without forming an oxide scale, has a negative effect on the oxidation resistance. The different heat treatments also had a marked influence on the composition and morphology of the formed oxide scale.

We will first consider oxidation of as-received Crofer 22 APU. The mass gain followed parabolic kinetics, indicating that growth of the oxide scale is controlled by solid state diffusion [27]. The parabolic rate constant determined after 1000 h at 800 °C is in line with what has previously been reported for the oxidation of Crofer 22 APU under similar conditions [22,25,28]. Two-stage oxidation experiments in air with $^{16}O/^{18}O$ have shown that the oxide scale on Crofer 22 APU grows

predominantly by outward transport of cations, with a minor contribution from inward transport of oxygen [29,30].

After 1000 h at 800 °C in air the scale on the as-received sample was characterized by a thin inner Cr_2O_3 layer, a thicker outer $(Mn,Cr)_3O_4$ layer, and subscale $(Mn,Cr)_3O_4$ oxide nodules. The sub-scale $(Mn,Cr)_3O_4$ nodules have been observed in a number of previous oxidation studies of Crofer 22 APU and similar ferritic stainless steels [10,11,22,25,31,32]. Nevertheless, it is more common that a continuous layer of $(Mn,Cr)_3O_4$ forms on the outer surface of the scale. Thermodynamically, the presence of manganese chromium spinel at the alloy/scale interface is to be expected. Gibbs energy for formation of MnO is more negative than for formation of Cr_2O_3, and $MnCr_2O_4$ is the most stable compound at elevated temperatures and at the low pO_2 prevalent at the alloy/scale interface [33]. The reason why a greater portion of $(Mn,Cr)_3O_4$ usually is observed at the scale/atmosphere interface can be attributed to the high oxygen affinity of Mn^{2+} and the greater diffusivity of Mn^{2+} compared to Cr^{3+} in thermally grown chromia [34,35].

The spinel nodules are clearly formed preferentially along the grain boundaries of the alloy, indicating that these are fast diffusion paths for manganese. Zhu et al. [36] estimated that the volume diffusion coefficient of Mn is twice that of Fe and Cr in ferrite at 800 °C. It was hypothesized that the difference in diffusivity should be even greater along the grain boundaries. Others have suggested that a fast transport of Mn to the surface is due to initial segregation of Mn at the alloy grain boundaries [37]. In either case, the more continuous band of $(Mn,Cr)_3O_4$ formed at the alloy/scale interface after the R1100+O800 pre-oxidation heat treatment can be explained by an overall smaller difference between volume and grain boundary diffusivity with increasing temperature [38]. Stott et al. [39] predicted that due to the high oxygen affinity of Mn^{2+}, any $(Mn,Cr)_3O_4$ initially present at the alloy/scale interface should decompose with time, unless Mn supply from the alloy is sustained. In the current case, it is safe to assume that Mn has not been depleted from the alloy after 1000 h oxidation at 800 °C. With a 1 mm thick sample and 0.42 wt.% Mn in the alloy (Table 1), there is enough Mn to form a ca. 14 μm thick $MnCr_2O_4$ layer. I.e. the supply of Mn may be sustained for a longer time.

The mass change of the R1100+O800 pre-oxidized samples was too small to evaluate the oxidation kinetics. However, if diffusion control may be assumed, it is considered unlikely that the nearly continuous $(Mn,Cr)_3O_4$ layer at the alloy/scale interface is responsible for the improved oxidation resistance. Cation diffusivity is generally greater in $MnCr_2O_4$ compared to Cr_2O_3 [35,40]. Thus, if oxidation of R1100+O800 is controlled by outward diffusion of cations from the alloy, as in the case of as-received Crofer 22 APU, transport of cations through the chromia scale should be rate-determining.

The beneficial effect of the R1100+O800 pre-oxidation heat treatment may instead be related to changes in the transport properties of chromia due to a modification of the defect structure and/or the grain size of the oxide. The diffusivity of Cr along grain boundaries is several orders of magnitude larger than

the diffusivity in the lattice [41], and consequently, the oxidation rate should decrease if the grain size of the chromia scale is increased. From previous work on ferritic stainless steels and Ni-based alloys, it is known that the chromia scale formed in H_2-H_2O is different from that formed in air [24,28,31,42]. Although the results are conflicting about whether the oxidation rate in H_2-H_2O is increased or decreased compared to the oxidation rate in air, there is a general consensus in these studies that the oxide scales formed in H_2-H_2O are better adherent and have lower residual growth stresses. Galerie et al. [43] showed that also the defect chemistry of thermally grown chromia is affected by the oxidation atmosphere. Oxidation in air forms Cr_2O_3 having p-type character at the scale/atmosphere interface and n-type character on the scale/alloy interface, while oxidation in Ar-H_2O mixtures forms Cr_2O_3 with n-type character exclusively.

If a modification of the defect chemistry is responsible for the improved oxidation resistance after heat treatment in N_2-H_2-H_2O, the effect should only be transient until the scale is equilibrated with air. The results here do not indicate that this is the case, however, the oxidation behavior will need to be studied over a longer period of time to confirm this. More careful analysis of the oxide scale (e.g. by transmission electron microscopy) will be necessary to clarify the reason for the beneficial effect of pre-oxidation.

Although it is not believed to be the main factor, a contribution to the reduced oxidation rate after pre-oxidation can be attributed to the lower number of sub-scale $(Mn,Cr)_3O_4$ nodules formed on the pre-oxidized samples. The formation of these nodules is associated with a volume increase that results in tensile stresses in the external scale [44]. This is evident from the observed buckling of the alloy and scale above the nodules (Fig. 10). Unless the tensile stresses can be alleviated by creep, the oxide scale above the nodules will likely become damaged by cracking [45]. Cracks in the scale expose fresh alloy surface to the oxidizing gas, which leads to an increase in the oxidation rate. No cracks were directly observed by inspection in SEM after oxidation, however, this could be due to rapid healing of the cracks by formation of new oxide. Indeed, this seems plausible when noting that the oxide scale above the nodules generally was thicker and had a greater $Cr_2O_3/(Mn,Cr)_3O_4$ thickness ratio compared to the scale on the flat parts (compare Fig. 11 and 13). The scale formed after pre-oxidation at R1100+O800 was nearly free of sub-scale spinel nodules and overall more flat. The risk of cracking is considerably lower with this type of morphology compared to that observed for the as-received sample. Crack formation and healing would also contribute to explain the increase in oxidation rate for the as-received, O900 and R900+O800 samples beyond 1000 h of oxidation at 800 °C.

The R900+O800 pre-oxidation heat treatment had no apparent effect on the oxidation resistance of Crofer 22 APU in air at 700 °C and 900 °C, in contrast to what was observed at 800 °C. The reasons for this are not apparent. However, it can be noted that the mass gain at 700 °C is very low and close to the sensitivity of the scale used in this study. Investigation of R1100+O800 pre-oxidation heat treatment at 700 °C was not viable since the mass gain during pre-oxidation (0.556

mg/cm^2) is equal to an estimated equivalent age of > 40 000 h based on extrapolation of the mass gain for the as-received sample ($k_P = 1.8\times10^{-15}$ g^2/cm^{4}s).

4.2 Effect of increasing the alloy grain size

Following the earlier discussion, one might expect the sample with increased alloy grain size (H1100) to have a lower oxidation rate due to formation of fewer spinel nodules. However, as seen in Figure 5, the H1100 sample had the highest measured mass gain in air at 800°C. Furthermore, the mass change of H1100 did not obey parabolic oxidation kinetics. The behavior was instead intermediate between parabolic and linear, suggesting that growth of the oxide scale in part is controlled by some interfacial reaction [27]. From the present results, it is not clear what this reaction could be. The observation that the oxidation rate increases after increasing the alloy grain size is however in accordance with established theory. It is usually reported that the transition to selective oxidation of chromium takes place at lower chromium contents for alloys with a smaller grain size or for alloys that have been cold-worked to induce dislocations in the subsurface [27,46]. This is attributed to the more rapid diffusion of chromium along grain boundaries, dislocations and similar short-circuit paths in the alloy, leading to faster formation of a protective scale.

These results are in contradiction with those presented by Magdefrau et al. [22], where the parabolic oxidation rate of Crofer 22 APU in air at 800 °C was reduced by a factor of 3.5 by increasing the grain size of the alloy from ca. 16 to 250 μm. In their case, the grain size was increased by heat treating in argon at 1050 °C. The pO_2 in this atmosphere is not stated in the paper and there is no information about the mass change during heat treatment. However, the authors report the presence of internal Ti-oxide precipitates in the near-surface region of the alloy and that the samples were polished after heat treatment. Based on this information, we suggest an alternative explanation for the reduced oxidation rate with increased grain size observed by Magdefrau et al. Assuming the pO_2 during the heat treatment was sufficiently high to also oxidize Mn, the heat treatment and subsequent surface polishing would essentially decrease the concentration of Mn in the alloy. From literature it is known that the oxidation rate of ferritic stainless steels decreases with decreasing concentration of Mn in the alloy [47,48]. This hypothesis is corroborated by the mass gain results for the R1100+O800 samples polished after pre-oxidation to remove the oxide scale. The mass gain of these samples after 1000 h at 800 °C (0.32 mg/cm^2) was slightly lower than measured for both the as-received (0.38 mg/cm^2) and H1100 (0.44 mg/cm^2) samples. It should be mentioned that although the addition of Mn to the alloy leads to an increase in oxidation rate, the formation of an outer $(Mn,Cr)_3O_4$ scale is beneficial for reducing Cr-volatilization [10].

4.3 Comparison with spinel coated Crofer 22 APU

In [Manuscript IV] we investigated the oxidation resistance of $MnCo_{1.7}Fe_{0.3}O_4$ coated Crofer 22 APU, heat treated to produce three different levels of porosity in the coating. The heat treatment procedures were identical to those used here to pre-oxidize the uncoated alloy, i.e. O900, R900+O800 and R1100+O800. We found that even an initially highly porous coating, obtained by heat treating in air at 900 °C, reduced the oxidation rate compared to uncoated Crofer 22 APU. A highly dense coating, obtained by the two-step R1100+O800 heat treatment procedure, provided the greatest protection. However, it was not clear how much of the difference in oxidation resistance could be attributed to different coating densities and how much was influenced by pre-oxidation of the alloy.

In Figure 15, the mass change of spinel coated and bare, pre-oxidized Crofer 22 APU during oxidation in air at 800 °C can be directly compared. The results presented in these graphs are the raw data, i.e. not corrected for pre-oxidation or equivalent age, since the bare and coated samples have undergone the exact same heat treatments. For the O900 and R900+O800 heat treatments it is evident that the spinel coating contributes to reducing the oxidation rate, since bare Crofer 22 APU pre-oxidized under the same conditions as the coated samples has the highest mass gain. However, spinel coated samples sintered R1100+O800 have a higher mass gain than the bare, pre-oxidized alloy. In [Manuscript IV] it was shown that the Cr-evaporation rate of Crofer 22 APU was reduced by a factor of 30 by this spinel coating. The lower mass gain of uncoated Crofer 22 APU may therefore in part be due to a higher mass loss caused by Cr-evaporation. During oxidation, the $MnCo_{1.7}Fe_{0.3}O_4$ coating reacted with the scale on the alloy to form $(Mn,Co,Fe,Cr)_3O_4$. This contributes to some of the mass gain of the spinel coated sample, without necessarily involving oxidation of the alloy. Nevertheless, it is clear that also pre-oxidation of Crofer 22 APU must has a profound influence. Based on the comparison in Figure 15, it may be speculated whether the higher density of the coating sintered R1100+O800 really provides any added protection compared to the more porous coatings.

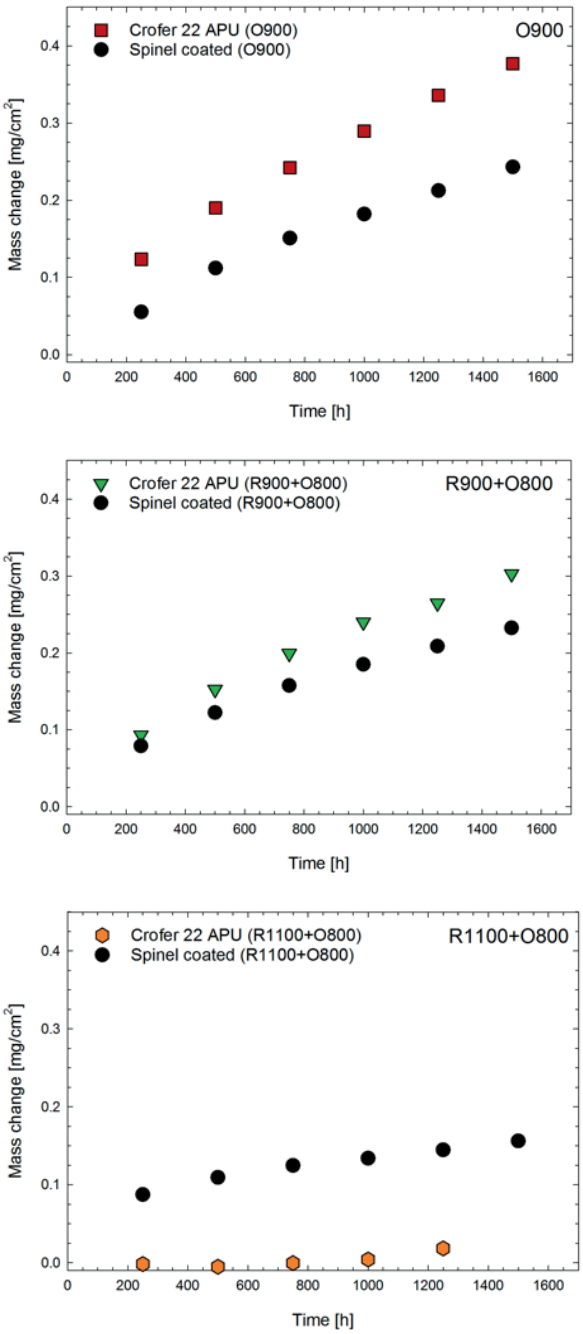

Figure 15. Mass change of $MnCo_{1.7}Fe_{0.3}O_4$ coated and bare Crofer 22 APU during oxidation in air at 800 °C. The samples (coated and bare) were pre-oxidized as indicated in the figures.

5. Conclusion

The effect of pre-oxidation and alloy grain size on the oxidation resistance of Crofer 22 APU in air was investigated. By pre-oxidizing in N_2-H_2 for 2h at 900 °C, the parabolic oxidation rate during subsequent oxidation in air at 800 °C decreased from 4.2×10^{-14} to 2.9×10^{-14} g^2/cm^4s, respectively. Pre-oxidation in air at 900 °C for 2 h decreased to parabolic rate to 3.2×10^{-14} g^2/cm^4s. The greatest reduction in oxidation rate was after pre-oxidation at 1100 °C in N_2-H_2 for 5h (R1100+O800). The mass change of these samples during subsequent oxidation in air at 800 °C was too low to determine the rate constant and whether or not parabolic kinetics were prevalent.

Sub-scale $(Mn,Cr)_3O_4$ nodules formed at the alloy grain boundaries, leading to buckling of the nearby alloy and surface scale. These nodules are believed to cause cracking of the surface scale and thereby an increase of the oxidation rate. The R1100+O800 pre-oxidized sample had instead of the oxide nodules a nearly continuous layer of $(Mn,Cr)_3O_4$ at the scale/alloy interface. The beneficial effect of pre-oxidation is believed to be a combination of fewer sub-scale oxide nodules and a possible change in the defect chemistry and/or grain size of the oxide scale formed at higher temperature and in reducing atmosphere.

By heat treating as-received Crofer 22 APU in pure H_2 at 1100 °C the alloy grain size was increased from 35 to 380 μm. The increased grain size had a negative effect on the oxidation resistance of Crofer 22 APU in air at 800 °C. The rate was intermediate between linear and parabolic and the scale contained a relatively higher fraction of Cr_2O_3 than $(Mn,Cr)_3O_4$ compared to the scale formed on the as-received alloy.

References

[1] S.C. Singhal, Solid Oxide Fuel Cells: Past, Present and Future, in: J.T.S. Irvine, P. Connor (Eds.), Solid Oxide Fuels Cells: Facts and Figures, Springer London, 2013: pp. 1–23.

[2] J.W. Fergus, Metallic interconnects for solid oxide fuel cells, *Materials Science and Engineering: A*. **397** 271–283 (2005).

[3] W.J. Quadakkers, J. Prion-Abellan, V. Shemet, L. Singheiser, Metallic interconnectors for solid oxide fuel cells – a review, *Materials at High Temperatures*. **20** 115–127 (2003).

[4] S. Linderoth, P.V. Hendriksen, M. Mogensen, N. Langvad, Investigations of metallic alloys for use as interconnects in solid oxide fuel cell stacks, *Journal of Materials Science*. **31** 5077–5082 (1996).

[5] P. Kofstad, R. Bredesen, High temperature corrosion in SOFC environments, *Solid State Ionics*. **52** 69–75 (1992).

[6] R. Hojda, W. Heimann, W.J. Quadakkers, Production-capable materials concept for high-temperature fuel cells, *ThyssenKrupp Techforum*. (2003).

[7] A.W.B. Skilbred, R. Haugsrud, Sandvik Sanergy HT – A potential interconnect material for $LaNbO_4$-based proton ceramic fuel cells, *Journal of Power Sources*. **206** 70–76 (2012).
[8] T. Uehara, N. Yasuda, T. Ohno, A. Toji, Improvement of Oxidation Resistance of Fe-Cr Ferritic Alloy Sheets for SOFC Interconnects, *Electrochemistry*. **77** 131–133 (2009).
[9] P. Huczkowski, V. Shemet, J. Piron-Abellan, L. Singheiser, W.J. Quadakkers, N. Christiansen, Oxidation limited life times of chromia forming ferritic steels, *Materials and Corrosion*. **55** 825–830 (2004).
[10] M. Stanislowski, E. Wessel, K. Hilpert, T. Markus, L. Singheiser, Chromium Vaporization from High-Temperature Alloys I. Chromia-Forming Steels and the Influence of Outer Oxide Layers, *Journal of The Electrochemical Society*. **154** A295–A306 (2007).
[11] D.E. Alman, P.D. Jablonski, Effect of minor elements and a Ce surface treatment on the oxidation behavior of an Fe–22Cr–0.5Mn (Crofer 22 APU) ferritic stainless steel, *International Journal of Hydrogen Energy*. **32** 3743–3753 (2007).
[12] P.Y. Hou, J. Stringer, The effect of reactive element additions on the selective oxidation, growth and adhesion of chromia scales, *Materials Science and Engineering: A*. **202** 1–10 (1995).
[13] A. Holt, P. Kofstad, Electrical conductivity and defect structure of Cr_2O_3. II. Reduced temperatures (< 1000 °C), *Solid State Ionics*. **69** 137–143 (1994).
[14] W.Z. Zhu, S.C. Deevi, Opportunity of metallic interconnects for solid oxide fuel cells: a status on contact resistance, *Materials Research Bulletin*. **38** 957–972 (2003).
[15] S. Taniguchi, M. Kadowaki, H. Kawamura, T. Yasuo, Y. Akiyama, Y. Miyake, et al., Degradation phenomena in the cathode of a solid oxide fuel cell with an alloy separator, *Journal of Power Sources*. **55** 73–79 (1995).
[16] J.J. Bentzen, J.V.T. Høgh, R. Barfod, A. Hagen, Chromium Poisoning of LSM/YSZ and LSCF/CGO Composite Cathodes, *Fuel Cells*. **9** 823–832 (2009).
[17] N. Shaigan, W. Qu, D.G. Ivey, W. Chen, A review of recent progress in coatings, surface modifications and alloy developments for solid oxide fuel cell ferritic stainless steel interconnects, *Journal of Power Sources*. **195** 1529–1542 (2010).
[18] Y. Larring, T. Norby, Spinel and Perovskite Functional Layers Between Plansee Metallic Interconnect (Cr-5 wt % Fe-1 wt % Y_2O_3) and Ceramic $(La_{0.85}Sr_{0.15})_{0.91}MnO_3$ Cathode Materials for Solid Oxide Fuel Cells, *Journal of The Electrochemical Society*. **147** 3251–3256 (2000).
[19] H. Kurokawa, C.P. Jacobson, L.C. DeJonghe, S.J. Visco, Chromium vaporization of bare and of coated iron–chromium alloys at 1073 K, *Solid State Ionics*. **178** 287–296 (2007).
[20] X. Montero, F. Tietz, D. Sebold, H.P. Buchkremer, A. Ringuede, M. Cassir, et al., $MnCo_{1.9}Fe_{0.1}O_4$ spinel protection layer on commercial ferritic steels for interconnect applications in solid oxide fuel cells, *Journal of Power Sources*. **184** 172–179 (2008).
[21] L. Chen, E.Y. Sun, J. Yamanis, N. Magdefrau, Oxidation Kinetics of $Mn_{1.5}Co_{1.5}O_4$-Coated Haynes 230 and Crofer 22 APU for Solid Oxide Fuel Cell Interconnects, *Journal of The Electrochemical Society*. **157** B931–B942 (2010).
[22] N.J. Magdefrau, L. Chen, E.Y. Sun, M. Aindow, Effects of alloy heat treatment on oxidation kinetics and scale morphology for Crofer 22 APU, *Journal of Power Sources*. **241** 756–767 (2013).
[23] S. Fontana, M. Vuksa, S. Chevalier, G. Caboche, P. Piccardo, On the Effect of Surface Treatment to Improve Oxidation Resistance and Conductivity of Metallic

Interconnects for SOFC in Operating Conditions, *Materials Science Forum*. **595-598** 753–762 (2008).
[24] M.M. Stack, F.H. Stott, G.C. Wood, The effect of pre-oxidation of chromia and alumina forming alloys on erosion in laboratory simulated fluidized-bed conditions, *Corrosion Science*. **33** 965–983 (1992).
[25] P. Huczkowski, S. Ertl, J. Piron-Abellan, N. Christiansen, T. Höfler, V. Shemet, et al., Effect of component thickness on lifetime and oxidation rate of chromia forming ferritic steels in low and high pO2 environments, *Materials at High Temperatures*. **22** 253–262 (2005).
[26] Y. Liu, Performance evaluation of several commercial alloys in a reducing environment, *Journal of Power Sources*. **179** 286–291 (2008).
[27] P. Kofstad, High Temperature Corrosion, 1988.
[28] M. Palcut, L. Mikkelsen, K. Neufeld, M. Chen, R. Knibbe, P.V. Hendriksen, Corrosion stability of ferritic stainless steels for solid oxide electrolyser cell interconnects, *Corrosion Science*. **52** 3309–3320 (2010).
[29] P. Huczkowski, N. Christiansen, V. Shemet, L. Niewolak, J. Piron-Abellan, L. Singheiser, et al., Growth Mechanisms and Electrical Conductivity of Oxide Scales on Ferritic Steels Proposed as Interconnect Materials for SOFC's, *Fuel Cells*. **6** 93–99 (2006).
[30] S. Fontana, S. Chevalier, G. Caboche, Metallic Interconnects for Solid Oxide Fuel Cell: Performance of Reactive Element Oxide Coating During 10, 20 and 30 Months Exposure, *Oxidation of Metals*. **78** 307–328 (2012).
[31] L. Niewolak, D.J. Young, H. Hattendorf, L. Singheiser, W.J. Quadakkers, Mechanisms of Oxide Scale Formation on Ferritic Interconnect Steel in Simulated Low and High pO2 Service Environments of Solid Oxide Fuel Cells, *Oxidation of Metals*. **82** 123–143 (2014).
[32] S. Canovic, J. Froitzheim, R. Sachitanand, M. Nikumaa, M. Halvarsson, L.-G. Johansson, et al., Oxidation of Co- and Ce-nanocoated FeCr steels: A microstructural investigation, *Surface and Coatings Technology*. **215** 62–74 (2013).
[33] I.-H. Jung, Critical evaluation and thermodynamic modeling of the Mn–Cr–O system for the oxidation of SOFC interconnect, *Solid State Ionics*. **177** 765–777 (2006).
[34] M.G.C. Cox, B. McEnaney, V.D. Scott, Kinetics of initial oxide growth on Fe-Cr alloys and the role of vacancies in film breakdown, *Philos Mag*. **31** 331–338 (1975).
[35] R.E. Lobnig, H.P. Schmidt, K. Hennesen, H.J. Grabke, Diffusion of cations in chromia layers grown on iron-base alloys, *Oxidation of Metals*. **37** 81–93 (1992).
[36] J. Zhu, L.M.F. Diaz, G.R. Holcomb, P.D. Jablonski, C.J. Cowen, D.E. Laughlin, et al., On the Relation Between Oxide Ridge Evolution and Alloy Surface Grain Boundary Disorientation in Fe–22 wt % Cr Alloys, *Journal of The Electrochemical Society*. **157** B655–B664 (2010).
[37] C. Thorning, S. Sridhar, Grain boundary ridge formation during initial high temperature oxidation of Mn/Al TRIP steel, *Philosophical Magazine*. **87** 3479–3499 (2007).
[38] H. Mehrer, Diffusion in solids: fundamentals, methods, materials, diffusion-controlled processes, Springer Science & Business Media, 2007.
[39] F.H. Stott, F.I. Wei, C.A. Enahoro, The influence of manganese on the High-temperature oxidation of iron-chromium alloys, *Materials and Corrosion*. **40** 198–205 (1989).

[40] J. Gilewicz-Wolter, J. Dudała, Z. Żurek, M. Homa, J. Lis, M. Wolter, Diffusion of chromium, manganese, and iron in $MnCr_2O_4$ spinel, *Journal of Phase Equilibria and Diffusion*. **26** 561–564 (2005).
[41] P. Kofstad, Defects and transport properties of metal oxides, *Oxidation of Metals*. **44** 3–27 (1995).
[42] T. Brylewski, M. Nanko, T. Maruyama, K. Przybylski, Application of Fe–16Cr ferritic alloy to interconnector for a solid oxide fuel cell, *Solid State Ionics*. **143** 131–150 (2001).
[43] A. Galerie, J.P. Petit, Y. Wouters, J. Mougin, A. Srisrual, P.Y. Hou, Water Vapour Effects on the Oxidation of Chromia-Forming Alloys, *Materials Science Forum*. **696** 200–205 (2011).
[44] D.J. Young, High temperature oxidation and corrosion of metals, Elsevier, 2008.
[45] M. Schütze, Deformation and cracking behavior of protective oxide scales on heat-resistant steels under tensile strain, *Oxidation of Metals*. **24** 199–232 (1985).
[46] M.K. Hossain, Effects of alloy microstructure on the high temperature oxidation of an Fe-10% Cr alloy, *Corrosion Science*. **19** 1031–1045 (1979).
[47] B. Hua, Y. Kong, W. Zhang, J. Pu, B. Chi, L. Jian, The effect of Mn on the oxidation behavior and electrical conductivity of Fe–17Cr alloys in solid oxide fuel cell cathode atmosphere, *Journal of Power Sources*. **196** 7627–7638 (2011).
[48] A.L. Marasco, D.J. Young, The oxidation of Iron-Chromium-Manganese alloys at 900°C, *Oxidation of Metals*. **36** 157–174 (1991).

4. Summary and concluding remarks

The use of $(Mn, Co)_3O_4$ spinels as protective coatings on SOFC metallic interconnects has been explored for more than a decade since first being proposed by Larring and Norby [18]. The promising potential of these coatings to improve area specific resistance (ASR) and reduce Cr-volatilization has been demonstrated in some previous studies [17, 19, 20], and confirmed in the present work. Yet, there is limited knowledge about in which way these coatings improve the oxidation resistance, and some uncertainty connected to whether they will be protective enough to ensure a sufficiently long service lifetime of a ferritic stainless steel (FSS) interconnect. This thesis has sought out to obtain better understanding of these issues by studying the degradation of $MnCo_2O_4$ coated ferritic stainless steel. Attempts were made to further improve the coating by partially substituting Co in $MnCo_2O_4$ with Fe or Cu. Finally, the potential of reducing coating costs by simplifying the spinel coating heat treatment procedure was investigated. The following chapter will summarize and link the main results and conclusions of the experimental work presented in the preceding manuscripts.

The first part of this thesis investigated the effect of iron and copper substitutions in $MnCo_2O_4$. Phase pure $MnCo_{2-x}M_xO_4$ (M = Cu, Fe;x = 0, 0.1, 0.3, 0.5) materials were successfully synthesized by spray pyrolysis (Manuscript I). Fe-substituted materials displayed a more linear thermal expansion behavior and a thermal expansion coefficient (TEC) closer matching that of other commonly used SOFC materials. The average TEC of $MnCo_{1.7}Fe_{0.3}O_4$ (MCFe) between 50 and 800 °C was $12.0 \cdot 10^{-6}$ K^{-1}, which is very close to the TEC of Crofer 22 APU ($11.9 \cdot 10^{-6} K^{-1}$ [78]). In comparison, the average TEC of $MnCo_2O_4$ (MC) was $14.4 \cdot 10^{-6}$ K^{-1}. A closer match in TEC is beneficial for reducing build-up of stresses during thermal cycling, which potentially can lead to cracking or spallation of the coating. The current work did not reveal any apparent differences in mechanical stability of the MC and MCFe coatings on Crofer 22 APU (Manuscript II). However, it was observed that a densely sintered MCFe ceramic generally was more intact than a densely sintered MC ceramic after being heat treated in close contact with sintered Cr_2O_3 (Manuscript III). The benefit of a more suitable TEC offered by the MCFe material will therefore likely become apparent first after longer term exposure or under more harsh conditions of rapid thermal cycling. The electrical conductivity was found to decrease with increasing Fe-substitution. Nevertheless, the conductivity of MCFe (47 S/cm at 800 °C) is sufficiently high for the application as a protective coating material for SOFC interconnects. This was evident from the ASR measurements, which showed a comparable contact resist-

ance for MC and MCFe coated Crofer 22 APU after 4300 h at 800 °C (Manuscript II).

Although XRD showed that the synthesized Cu-substituted materials were phase pure and crystallized in the cubic spinel structure, there were several observation throughout this work pointing towards a poor stability of the $MnCo_{2-x}Cu_xO_4$ solid solution. The lattice parameter of Cu-substituted materials varied significantly with thermal history, without following any obvious trend. CuO was observed to precipitate from $MnCo_{1.5}Cu_{0.5}O_4$ during thermal cycling, causing a large hysteresis in the thermal expansion behavior (Manuscript I). The diffusion couple experiment also showed precipitation of CuO from $MnCo_{1.7}Cu_{0.3}O_4$ (MCCu) and formation of a very thick, multi-phase reaction product in contact with Cr_2O_3 (Manuscript III). The main beneficial effect of Cu-substitution was that the electrical conductivity was increased; from 89 $\mathrm{S/cm}$ for MC to 168 $\mathrm{S/cm}$ for $MnCo_{1.5}Cu_{0.5}O_4$ at 800 °C. The ASR of MCCu coated Crofer 22 APU was however slightly higher than MC coated. After the reduction and re-oxidation heat treatment procedure used to densify the coating (900 °C N_2-9%H_2 + 800 °C air), the MCCu coating contained ca. 20 wt.% iron in the 2-3 $\mu\mathrm{m}$ of the coating closest to the oxide scale. This was attributed to outward diffusion of Fe during the reduction heat treatment step and may be taken as another sign of the poor stability of the Cu-substituted materials. Incorporation of iron in the coatings had the beneficial effect of greatly improving the coating density in the area close to the interface with the alloy. Despite this density improvement, the MCCu coated samples displayed a slightly greater mass gain during oxidation and a greater rate of ASR increase than the MC and MCFe coated samples.

Overall, the changes in ASR and oxidation rate of Crofer 22 APU resulting from doping the $MnCo_2O_4$ coating with Fe or Cu were minor. A 97 % reduction in Cr-evaporation was measured for MCFe coated Crofer 22 APU (Manuscript IV). This is in line with the reductions previously reported with a $MnCo_2O_4$ coating [17] and with a metallic Co coating, which is transformed to $(Mn,Co)_3O_4$ during exposure [172]. The capability of the MCCu material to reduce Cr-volatilization was not quantified. From microstructural characterization of MCCu coated Crofer 22 APU after oxidation there is no reason to believe that this material should provide significantly better or worse protection than MC and MCFe. Comparably low amounts of Cr were detected in the three coating materials after long term (4000 h) exposure of coated Crofer 22 APU to air at 800 °C. In conclusion, MC, MCFe and MCCu spinels may all three be suitable candidates as the interconnect coating material. The MCFe material is however probably the safest choice, due to the closer match in thermal expansion to other commonly used SOFC materials.

To ensure high density while avoiding excessive damage of the FSS interconnect,

$(Mn, Co)_3O_4$ spinel coatings have after deposition typically been sintered in a two-step reduction and re-oxidation procedure. The reduction firing step has in some assessments been estimated to make up ca. 20 % of the total interconnect coating costs [167, 249]. From a commercial perspective it would therefore be an advantage if the spinel coating instead could be sintered *in-situ* during warm-up of the SOFC stack. The results in this thesis indicate that this may be a viable option (Manuscript IV). A highly porous MCFe coating, resulting from sintering in air at 900 °C for 2 h, reduced the Cr-evaporation from Crofer 22 APU by 88 % in air-3%H_2O at 800 °C. The protective action was attributed to partial densification of the coating with time, in interaction with the alloy. A highly dense coating, with only closed porosity, was achieved by first reducing the coating in N_2-9%H_2 at 1100 °C and then re-oxidizing it in air at 800 °C. This coating resulted in a 97 % reduction in Cr-evaporation from Crofer 22 APU. The parabolic oxidation rate of Crofer 22 APU at 800 °C in air was reduced by a factor of 12 and 3 by the highly dense and highly porous coatings, respectively. However, the high sintering temperature required to densify the coating lead to considerably greater initial oxidation of the alloy. Consequently, after 5000 h oxidation at 800 °C, the *total* mass gain of the sample with a dense coating was 20 % higher than the mass gain of a sample with a porous coating. These differences are however minor compared to the large reduction in oxidation rate of Crofer 22 APU provided by any of the spinel coatings.

The interaction between spinel coatings and the thermally grown oxide scale on FSS was a reoccurring topic throughout this thesis. Microstructural characterization was made on both spinel coated Crofer 22 APU after oxidation, and on diffusion couples of densely sintered spinel oxides and chromia. The results revealed that the reactivity depends on a number of factors, including coating composition, how the coating is sintered after deposition, and the exposure temperature. In most cases, a reaction layer rich in Co and Cr formed at the interface between the spinel coatings and the thermally grown oxide scale on the alloy. Or, in case of the diffusion couples, at the interface between spinel oxide and chromia pellets. In case of the coated alloy, this reaction product contained a considerably lower amount of Cr and apparently grew at a slower rate than the reaction product formed with the diffusion couples.

The Co and Cr rich reaction product was proposed to grow by diffusion of Co^{2+} from the spinel oxide to the chromia/reaction product interface. For the diffusion couples, this mechanism was confirmed by using Pt-particles to mark the original interface. It is believed to be the dominant mechanism in the alloy-coating system as well, based on available literature reporting that the diffusion of Co is orders of magnitude faster than the diffusion of Cr in related spinel oxides [250–253]. The

reason for the different growth rate and Cr-content in the two systems is probably connected to the source of Cr and oxygen. It is well known, and also observed in the current work, that the outer scale formed on uncoated Crofer 22 APU consists of $(Mn,Cr)_3O_4$. Thus, in the coating-alloy system, the interaction between the spinel oxide coating and $(Mn,Cr)_3O_4$ is probably more important than the interaction between the spinel oxide coating and Cr_2O_3. This is supported by the observation that the reaction product formed on the coated alloy contained significantly larger amounts of Mn than the reaction product formed with the diffusion couples. Previous studies have shown that the oxide scale on uncoated Crofer 22 APU grows by outward transport of cations [12, 154]. Accordingly, the growth rate of the reaction layer on the coated alloy may be limited by outward transport of Cr from the alloy to the oxide scale/reaction product interface. In this respect it is worth noting that the activation energy for oxidation of spinel coated Crofer 22 APU is the same as previously reported for oxidation of several uncoated FSSs [107]. This activation energy was related to the activation energy for Cr diffusion in chromia, to suggest that the parabolic oxidation rate is controlled by outward diffusion of chromium. For the spinel coated samples oxidized at 800 °C the mass gain (oxygen uptake) followed parabolic kinetics, however, the oxide scale thickness remained nearly unchanged over 4000 h of exposure (Manuscript II). The mass gain was instead related to growth of the Cr-rich reaction layer. Thus, the growth of this reaction layer may be controlled by outward diffusion of chromium.

Due to decreasing electrical conductivity and thermal expansion coefficient of spinel oxides with increasing Cr content, there have been some concerns that the formation of Cr-rich reaction layers might have negative consequences on the ASR of spinel coated FSS [24, 254]. By comparing the development in oxide scale and reaction layer thickness with the development in ASR, it was concluded that the reaction layer has a minimal influence on increasing the ASR (Manuscript II). Instead, it may be argued that the formation of the Cr-containing reaction layer is beneficial for reducing the ASR of the coated interconnect since formation of this layer consumes the oxide scale that is thermally grown on the alloy.

Fe-substitution in $MnCo_2O_4$ reduced the growth rate of the reaction layer between the spinel oxide and chromia (Manuscript III), in accordance with earlier reports by Wang et al. [28]. Fe-substitution also reduced the thickness of the Cr-rich reaction product formed on spinel coated Crofer 22 APU after oxidation at 900 °C (Manuscript II). However, when the oxidation temperature was lowered to 800 °C, there was minimal difference between the thickness of the reaction product formed with MC and MCFe coated Crofer 22 APU. Surprisingly, the reaction layer formed on MCFe coated samples after oxidation at 800 °C was more continuous and thicker

than the reaction layer formed after oxidation at 900 °C. Another interesting observation was that less Cr was found to incorporate in the coating when it was heat treated in air only, compared to when it was heat treated in reducing atmosphere first (Manuscript IV). The reason for this complicated behavior is not clear. However, the observations may provide an explanation to why, in some studies, the $(Mn, Co)_3O_4$ spinel coating has been reported to *not* have any beneficial effect on the oxidation resistance and/or ASR of the FSS interconnect [26, 163, 172, 174]. Horita et al. [255] has shown that ^{18}O diffusion is slower in $(Mn, Co, Cr)_3O_4$ than in both $MnCo_2O_4$ and the thermally grown oxide scale on FSS. The formation of the Cr-rich reaction layer is therefore probably responsible for the reduction in oxidation rate observed on spinel coated FSS. In situations where formation of the reaction layer is hindered, which appears to be the case if the coating is heat treated in air only, the coating is less effective in decreasing the oxidation rate. On the other hand, it was also shown that pre-oxidation of uncoated Crofer 22 APU can have a significant influence on the oxidation rate (Manuscript V). Pre-oxidizing in reducing atmosphere was found to have greater effect than pre-oxidizing in air at the same temperature. Thus, the reduction in oxidation rate cannot be ascribed to a protective effect by the spinel coating and Cr-rich reaction layer alone.

5. Outlook

The experimental work in this thesis has confirmed the promising potential of $MnCo_2O_4$ based spinels as protective coatings for SOFC interconnects, and provided some insight to the relevant interaction mechanisms in this system. There are nevertheless many topics that will require further exploration. Some of the remaining questions are listed below.

- Thermogravimetric analysis of the spinel oxide materials indicated a series of reduction and oxidation processes taking place during heating in air (Manuscript I). These reactions took place mainly below 700 °C, thus they are not expected to have any implications on the function of the spinel oxide as a coating material for SOFC interconnects. However, $MnCo_2O_4$ is being explored for the use in a number of lower temperature applications, for example as a termistor [226] and for electrocatalysis [208]. For these applications, the possible cation deficiency and the suggested influence it has on the electrical conductivity is of importance. The first step to resolve the reasons for the anomalous electrical conductivity behavior would be to confirm that there are no phase changes taking place in the relevant temperature interval. Although this has not been observed experimentally, calculated phase diagrams suggest a phase transition around 400 °C [27]. Further thermogravimetric analysis should be conducted, with changes in atmosphere and more cycles on the same powder sample to establish the reversibility of the oxidation and reduction reactions.

- The formation of a chromium rich reaction layer by interaction of the spinel coating with the thermally grown oxide scale on the alloy was suggested to be beneficial for reducing the ASR of FSS interconnects (Manuscript II). However, it is unclear how the growth of this reaction layer will influence the mechanical properties of the coated alloy. This is a concern due to the low thermal expansion coefficient of Cr-rich spinel oxides [254]. Previous studies that have investigated the mechanical properties of $MnCo_2O_4$ coated Crofer 22 APU have not taken the formation of such reaction layers into account [21, 256].

- Diffusion couples of sintered spinel oxides and chromia did not serve as a satisfactory model for studying the interaction between spinel coatings and the thermally grown oxide scale on FSS (Manuscript III). Since the outer oxide scale formed on most interconnect alloys is $(Mn, Cr)_3O_4$, the next step could be to study diffusion couples of the spinel oxides in contact with this material instead. The temperature dependence of the reactivity will also be important to establish. With the long lifetimes of SOFC, use of higher temperatures for ac-

celerated testing is desirable. However, in order to translate the obtained results to service temperature, knowledge about the activation energies for reactions is essential.

- It was demonstrated that even a highly porous spinel oxide coating could reduce the Cr-vaporization from Crofer 22 APU considerably (Manuscript IV). The challenge remains in determining whether the measured reduction in Cr-evaporation is sufficient to avoid detrimental influence on the SOFC cathode performance. This will require comparing performance of interconnects with highly dense and porous coatings in operation in a stack, or using a half-cell set-up where the cathode performance can be monitored. The ideal would be if a systematic study of several cathode materials under controlled conditions could be performed to establish fairly simple relationships between the Cr-evaporation rate from the interconnect and degradation of the cathode material. With development of the transpiration and Denuder methods, quantification of Cr released from candidate interconnect materials can be done on a near routine basis [94]. Although this is useful for comparing different interconnect candidates, stack tests are still required to confirm whether a candidate material is good *enough*.
- A significant improvement of the oxidation resistance of uncoated Crofer 22 APU could be achieved by pre-oxidation (Manuscript V). To understand the reasons for this beneficial effect, more careful characterization of the microstructure, preferably by transmission electron microscopy [257], is needed. It will also be necessary to extend the oxidation testing time to establish whether the effect of pre-oxidation is transient or provides a long-term beneficial effect.

References

[1] IPCC Fifth Assessment Report.

[2] Greenhouse gas emissions by economic activity, 2013. eurostat. url: http://ec.europa.eu/eurostat/statistics-explained/index.php/greenhousegas_emissions_by_industries_and_households.

[3] 2050 Energy strategy - European Commission url: https://ec.europa.eu/energy/en/topics/energy-strategy/2050-energy-strategy.

[4] S. Becker, B. A. Frew, G. B. Andresen, T. Zeyer, S. Schramm, M. Greiner, and M. Z. Jacobson. Features of a fully renewable US electricity system: Optimized mixes of wind and solar PV and transmission grid extensions. *Energy*, 72:443–458, August 2014.

[5] C. F. Schœnbein. X. On the voltaic polarization of certain solid and fluid substances. *Philosophical Magazine Series 3*, 14(85):43–45, January 1839.

[6] W. R. Grove Esq M.A. XXIV. On voltaic series and the combination of gases by platinum. *Philosophical Magazine Series 3*, 14(86):127–130, February 1839.

[7] R. Payne, J. Love, and M. Kah. Generating Electricity at 60% Electrical Efficiency from 1 - 2 kWe SOFC Products. *ECS Transactions*, 25(2):231–239, September 2009.

[8] M. Mogensen, S. Højgaard Jensen, A. Hauch, I. Chorkendorff, and T. Jacobsen. Reversible solid oxide cells. In *Ceram. Eng. Sci. Proc*, volume 28, pages 91–101, 2008.

[9] D. J. L. Brett, A. Atkinson, D. Cumming, E. Ramírez-Cabrera, R. Rudkin, and N. P. Brandon. Methanol as a direct fuel in intermediate temperature (500–600 °C) solid oxide fuel cells with copper based anodes. *Chemical Engineering Science*, 60(21):5649–5662, November 2005.

[10] J. Lawrence and M. Boltze. Auxiliary power unit based on a solid oxide fuel cell and fuelled with diesel. *Journal of Power Sources*, 154(2):479–488, March 2006.

[11] P. Singh and N. Q. Minh. Solid Oxide Fuel Cells: Technology Status. *International Journal of Applied Ceramic Technology*, 1(1):5–15, January 2004.

[12] P. Huczkowski, N. Christiansen, V. Shemet, L. Niewolak, J. Piron-Abellan, L. Singheiser, and W. J. Quadakkers. Growth Mechanisms and Electrical Conductivity of Oxide Scales on Ferritic Steels Proposed as Interconnect Materials for SOFC's. *Fuel Cells*, 6(2):93–99, April 2006.

[13] W. Z. Zhu and S. C. Deevi. Opportunity of metallic interconnects for solid oxide fuel cells: a status on contact resistance. *Materials Research Bulletin*, 38(6):957–972, 2003.

[14] K. Hilpert, D. Das, M. Miller, D. H. Peck, and R. Weiß. Chromium Vapor Species over Solid Oxide Fuel Cell Interconnect Materials and Their Potential for Degradation Processes. *Journal of The Electrochemical Society*, 143(11):3642–3647, November 1996.

[15] J. W. Fergus. Effect of cathode and electrolyte transport properties on chromium poisoning in solid oxide fuel cells. *International Journal of Hydrogen Energy*, 32(16):3664–3671, November 2007.

[16] L. Chen, E. Y. Sun, J. Yamanis, and N. Magdefrau. Oxidation Kinetics of $Mn_{1.5}Co_{1.5}O_4$-Coated Haynes 230 and Crofer 22 APU for Solid Oxide Fuel Cell Interconnects. *Journal of The Electrochemical Society*, 157(6):B931–B942, June 2010.

[17] H. Kurokawa, C. P. Jacobson, L. C. DeJonghe, and S. J. Visco. Chromium vaporization of bare and of coated iron–chromium alloys at 1073 K. *Solid State Ionics*, 178(3–4):287–296, February 2007.

[18] Y. Larring and T. Norby. Spinel and Perovskite Functional Layers Between Plansee Metallic Interconnect (Cr–5 wt % Fe–1 wt % Y_2O_3) and Ceramic $(La_{0.85}Sr_{0.15})_{0.91}MnO_3$ Cathode Materials for Solid Oxide Fuel Cells. *Journal of The Electrochemical Society*, 147(9):3251–3256, September 2000.

[19] F. Smeacetto, A. De Miranda, S. Cabanas Polo, S. Molin, D. Boccaccini, M. Salvo, and A. R. Boccaccini. Electrophoretic deposition of $Mn_1 \cdot 5\,Co_1 \cdot 5\,O_4$ on metallic interconnect and interaction with glass-ceramic sealant for solid oxide fuel cells application. *Journal of Power Sources*, 280:379–386, April 2015.

[20] J. W. Stevenson, Z. G. Yang, G. G. Xia, Z. Nie, and J. D. Templeton. Long-term oxidation behavior of spinel-coated ferritic stainless steel for solid oxide fuel cell interconnect applications. *Journal of Power Sources*, 231:256–263, June 2013.

[21] W. N. Liu, X. Sun, E. Stephens, and M. A. Khaleel. Life prediction of coated and uncoated metallic interconnect for solid oxide fuel cell applications. *Journal of Power Sources*, 189(2):1044–1050, April 2009.

[22] S. R. Akanda, M. E. Walter, N. J. Kidner, and M. M. Seabaugh. Lifetime prediction for manganese cobalt spinel oxide coatings on metallic interconnects. *Thin Solid Films*, 565:237–248, August 2014.

[23] N. J. Magdefrau, L. Chen, E. Y. Sun, J. Yamanis, and M. Aindow. Formation of spinel reaction layers in manganese cobaltite – coated Crofer22 APU for solid oxide fuel cell interconnects. *Journal of Power Sources*, 227:318–326, April 2013.

[24] J. W. Fergus. Synergism in the design of interconnect alloy–coating combinations solid for oxide fuel cells. *Scripta Materialia*, 65(2):73–77, July 2011.

[25] Z. Yang, G. G. Xia, X. H. Li, and J. W. Stevenson. $(Mn,Co)_3O_4$ spinel coatings on ferritic stainless steels for SOFC interconnect applications. *International Journal of Hydrogen Energy*, 32(16):3648–3654, November 2007.

[26] J. Puranen, M. Pihlatie, J. Lagerbom, G. Bolelli, J. Laakso, L. Hyvärinen, M. Kylmälahti, J. Himanen, O.and Kiviaho, L. Lusvarghi, and P. Vuoristo. Post-mortem evaluation of oxidized atmospheric plasma sprayed Mn–Co–Fe oxide spinel coatings on SOFC interconnectors. *International Journal of Hydrogen Energy*, 39(30):17284–17294, 2014.

[27] A. Petric and H. Ling. Electrical Conductivity and Thermal Expansion of Spinels at Elevated Temperatures. *Journal of the American Ceramic Society*, 90(5):1515–1520, 2007.

[28] K. Wang, Y. Liu, and J. W. Fergus. Interactions Between SOFC Interconnect Coating Materials and Chromia. *Journal of the American Ceramic Society*, 94(12):4490–4495, December 2011.

[29] CJ Dileep Kumar, A. Dekich, H. Wang, Y. Liu, W. Tilson, J. Ganley, and J. W. Fergus. Transition Metal Doping of Manganese Cobalt Spinel Oxides for Coating SOFC Interconnects. *Journal of The Electrochemical Society*, 161(1):F47–F53, 2014.

[30] S. C. Singhal. Solid Oxide Fuel Cells: Past, Present and Future. In John T. S. Irvine and Paul Connor, editors, *Solid Oxide Fuels Cells: Facts and Figures*, Green Energy and Technology, pages 1–23. Springer London, 2013.

[31] Sakurambo. Diagram of a solid oxide fuel cell. Wikimedia Commons. https://commons.wikimedia.org/wiki/file:solid_oxide_fuel_cell.svg accessed 20-06-2016.

[32] W. Nernst. Über die elektrolytische Leitung fester Körper bei sehr hohen Temperaturen. *Zeitschrift für Elektrochemie*, 6(2):41–43, July 1899.

[33] H. G. Scott. Phase relationships in the zirconia-yttria system. *Journal of Materials Science*, 10(9):1527–1535, September 1975.

[34] D. W. Strickler and W. G. Carlson. Ionic Conductivity of Cubic Solid Solutions in the System CaO–Y_2O_3–ZrO_2. *Journal of the American Ceramic Society*, 47(3):122–127, March 1964.

[35] T. Ishihara, H. Matsuda, and Y. Takita. Doped $LaGaO_3$ Perovskite Type Oxide as a New Oxide Ionic Conductor. *Journal of the American Chemical Society*, 116(9):3801–3803, May 1994.

[36] M. Feng, J. B. Goodenough, K. Huang, and C. Milliken. Fuel cells with doped lanthanum gallate electrolyte. *Journal of Power Sources*, 63(1):47–51, November 1996.

[37] B. C. H. Steele. Appraisal of $Ce_{1-y}Gd_yO_{2-y/2}$ electrolytes for IT-SOFC operation at 500 °C. *Solid State Ionics*, 129(1–4):95–110, April 2000.

[38] M. Mogensen, N. M. Sammes, and G. A. Tompsett. Physical, chemical and electrochemical properties of pure and doped ceria. *Solid State Ionics*, 129(1–4):63–94, April 2000.

[39] T. Setoguchi, K. Okamoto, K. Eguchi, and H. Arai. Effects of Anode Material and Fuel on Anodic Reaction of Solid Oxide Fuel Cells. *Journal of The Electrochemical Society*, 139(10):2875–2880, October 1992.

[40] M. Mogensen and S. Skaarup. Kinetic and geometric aspects of solid oxide fuel cell electrodes. *Solid State Ionics*, 86–88, Part 2:1151–1160, July 1996.

[41] Y. Matsuzaki and I. Yasuda. The poisoning effect of sulfur-containing impurity gas on a SOFC anode: Part I. Dependence on temperature, time, and impurity concentration. *Solid State Ionics*, 132(3–4):261–269, July 2000.

[42] O. A. Marina, N. L. Canfield, and J. W. Stevenson. Thermal, electrical, and electrocatalytical properties of lanthanum-doped strontium titanate. *Solid State Ionics*, 149(1–2):21–28, July 2002.

[43] A. Hauch. Power point lecture from course 45100 SOFC and Electrolysis (F12) at DTU, 2012.

[44] S. P. Jiang. Development of lanthanum strontium manganite perovskite cathode materials of solid oxide fuel cells: a review. *Journal of Materials Science*, 43(21):6799–6833, October 2008.

[45] San Ping Jiang. A review of wet impregnation—An alternative method for the fabrication of high performance and nano-structured electrodes of solid oxide fuel cells. *Materials Science and Engineering: A*, 418(1–2):199–210, February 2006.

[46] Y. Ji, J. A. Kilner, and M. F. Carolan. Electrical properties and oxygen diffusion in yttria-stabilised zirconia (YSZ)–$La_{0.8}Sr_{0.2}MnO_{3-\delta}$ (LSM) composites. *Solid State Ionics*, 176(9–10):937–943, March 2005.

[47] C. C. T. Yang, W. C. J. Wei, and A. Roosen. Electrical conductivity and microstructures of $La_{0.65}Sr_{0.3}MnO_3$–8 mol% yttria-stabilized zirconia. *Materials Chemistry and Physics*, 81(1):134–142, July 2003.

[48] S. P. Simner, M. D. Anderson, M. H. Engelhard, and J. W. Stevenson. Degradation Mechanisms of La–Sr–Co–Fe–O_3 SOFC Cathodes. *Electrochemical and Solid-State Letters*, 9(10):A478–A481, October 2006.

[49] Y. Leng, S. H. Chan, and Q. Liu. Development of LSCF–GDC composite cathodes for low-temperature solid oxide fuel cells with thin film GDC electrolyte. *International Journal of Hydrogen Energy*, 33(14):3808–3817, July 2008.

[50] J. J. Choi, D. S. Park, B. G. Seong, and H. Y. Bae. Low-temperature preparation of dense $(Gd, Ce)O_{2-\delta}$–Gd_2O_3 composite buffer layer by aerosol deposition for YSZ electrolyte-based SOFC. *International Journal of Hydrogen Energy*, 37(12):9809–9815, June 2012.

[51] S. Taniguchi, M. Kadowaki, H. Kawamura, T. Yasuo, Y. Akiyama, Y. Miyake, and T. Saitoh. Degradation phenomena in the cathode of a solid oxide fuel cell with an alloy separator. *Journal of Power Sources*, 55(1):73–79, May 1995.

[52] J. J. Bentzen, J. V. T. Høgh, R. Barfod, and A. Hagen. Chromium Poisoning of LSM/YSZ and LSCF/CGO Composite Cathodes. *Fuel Cells*, 9(6):823–832, December 2009.

[53] E. Park, S. Taniguchi, J. T. Daio, T.and Chou, and K. Sasaki. Comparison of chromium poisoning among solid oxide fuel cell cathode materials. *Solid State Ionics*, 262:421–427, September 2014.

[54] E. Konysheva, H. Penkalla, E. Wessel, J. Mertens, U. Seeling, L. Singheiser, and K. Hilpert. Chromium Poisoning of Perovskite Cathodes by the ODS Alloy Cr5Fe1Y_2O_3 and the High Chromium Ferritic Steel Crofer22APU. *Journal of The Electrochemical Society*, 153(4):A765–A773, April 2006.

[55] S. C. Paulson and V. I. Birss. Chromium Poisoning of LSM-YSZ SOFC Cathodes I. Detailed Study of the Distribution of Chromium Species at a Porous, Single-Phase Cathode. *Journal of The Electrochemical Society*, 151(11):A1961–A1968, November 2004.

[56] S.P. Jiang, S. Zhang, and Y.D. Zhen. Early interaction between Fe–Cr alloy metallic interconnect and Sr-doped $LaMnO_3$ cathodes of solid oxide fuel cells. *Journal of Materials Research*, 20(03):747–758, March 2005.

[57] S. P. Jiang and X. Chen. Chromium deposition and poisoning of cathodes of solid oxide fuel cells – A review. *International Journal of Hydrogen Energy*, 39(1):505–531, January 2014.

[58] L. Zhao, S. Amarasinghe, and S. P. Jiang. Enhanced chromium tolerance of $La_{0.6}Sr_{0.4}Co_{0.2}Fe_{0.8}O_{3-\delta}$ electrode of solid oxide fuel cells by $Gd_{0.1}Ce_{0.9}O_{1.95}$ impregnation. *Electrochemistry Communications*, 37:84–87, December 2013.

[59] W. Z. Zhu and S. C. Deevi. Development of interconnect materials for solid oxide fuel cells. *Materials Science and Engineering: A*, 348(1–2):227–243, May 2003.

[60] M. C. Tucker. Progress in metal-supported solid oxide fuel cells: A review. *Journal of Power Sources*, 195(15):4570–4582, August 2010.

[61] DoITPoMS - TLP Library Fuel Cells url: http://www.doitpoms.ac.uk/tlplib/fuel-cells/printall.php accessed: 20.04.16.

[62] W. J. Quadakkers, J. Prion-Abellan, V. Shemet, and L. Singheiser. Metallic interconnectors for solid oxide fuel cells – a review. *Materials at High Temperatures*, 20(2):115–127, 2003.

[63] J. W. Fergus. Metallic interconnects for solid oxide fuel cells. *Materials Science and Engineering: A*, 397(1–2):271–283, April 2005.

[64] J. W. Fergus. Lanthanum chromite-based materials for solid oxide fuel cell interconnects. *Solid State Ionics*, 171(1–2):1–15, June 2004.

[65] H. Yokokawa, N. Sakai, T. Kawada, and M. Dokiya. Chemical Thermodynamic Considerations in Sintering of $LaCrO_3$–Based Perovskites. *Journal of The Electrochemical Society*, 138(4):1018–1027, April 1991.

[66] P. Kofstad and R. Bredesen. High temperature corrosion in SOFC environments. *Solid State Ionics*, 52(1–3):69–75, 1992.

[67] S. Linderoth, P. V. Hendriksen, M. Mogensen, and N. Langvad. Investigations of metallic alloys for use as interconnects in solid oxide fuel cell stacks. *Journal of Materials Science*, 31(19):5077–5082, January 1996.

[68] Z. Yang. Recent advances in metallic interconnects for solid oxide fuel cells. *International Materials Reviews*, 53(1):39–54, January 2008.

[69] U. Diekmann and H. Ringel. Current collector for a SOFC fuel-cell pile, July 2001. Patent nr. US6268076 B1.

[70] J. Piron-Abellan, F. Tietz, A. Gil, L. Singheiser, W. J. Quadakkers, T. Ladwein, and V. Shemet. Long term oxidation behaviour and compatibility with contact materials of newly developed ferritic interconnector steel. In *Proceedings 5th European Solid Oxide Fuel Cell Forum*, Luzerne, Switzerland, 2002.

[71] R. Hojda, W. Heimann, and W. J. Quadakkers. Production-capable materials concept for high-temperature fuel cells. *ThyssenKrupp techforum*, (JUL), 2003.

[72] M. Stanislowski, E. Wessel, K. Hilpert, T. Markus, and L. Singheiser. Chromium Vaporization from High-Temperature Alloys I. Chromia-Forming Steels and the Influence of Outer Oxide Layers. *Journal of The Electrochemical Society*, 154(4):A295–A306, April 2007.

[73] G. R. Holcomb and D. E. Alman. The effect of manganese additions on the reactive evaporation of chromium in Ni–Cr alloys. *Scripta Materialia*, 54(10):1821–1825, May 2006.

[74] D. E. Alman and P. D. Jablonski. Effect of minor elements and a Ce surface treatment on the oxidation behavior of an Fe–22Cr–0.5Mn (Crofer 22 APU) ferritic stainless steel. *International Journal of Hydrogen Energy*, 32(16):3743–3753, November 2007.

[75] P. Y. Hou and J. Stringer. The effect of reactive element additions on the selective oxidation, growth and adhesion of chromia scales. *Materials Science and Engineering: A*, 202(1–2):1–10, November 1995.

[76] L. Gambino, N. Magdefrau, and M. Aindow. Analysis of Titanium Microalloying in As-Received and Oxidized Crofer® 22 APU. *Microscopy and Microanalysis*, 20(Supplement S3):892–893, August 2014.

[77] J. Froitzheim, G. H. Meier, L. Niewolak, P. J. Ennis, H. Hattendorf, L. Singheiser, and W. J. Quadakkers. Development of high strength ferritic steel for interconnect application in SOFCs. *Journal of Power Sources*, 178(1):163–173, March 2008.

[78] Thyssen Krupp. Crofer 22 APU Material Data Sheet No. 4046, May 2010.

[79] Hitachi. ZMG 232l Material Data Sheet.

[80] Sandvik Materials Technology. Sandvik Sanergy HT 441 Materials Data Sheet.

[81] Thyssen Krupp. Crofer 22 H Material Data Sheet No. 4050, June 2010.

[82] P. Kofstad. *High Temperature Corrosion*. Elsevier Science Publishing Co. Inc., 1988.

[83] S. Chevalier. Mechanisms and Kinetics of Oxidation A2. In B. Stott, M. Cottis, R. Graham, S. Lindsay, T. Lyon, D. Richardson, and H. Scantlebury, editors, *Shreir's Corrosion*, pages 132–152. Elsevier, Oxford, 2010.

[84] E. S. Machlin. Chapter III - Free Energy and Phase Diagrams. In *An Introduction to Aspects of Thermodynamics and Kinetics Relevant to Materials Science (Third Edition)*, pages 91–116. Elsevier Science Ltd, Oxford, 2007.

[85] C. Wagner. Beitrag zur theorie des anlaufvorgangs. *Z. Phys. Chem. B*, 21:25–41, 1933.

[86] P. Sarrazin, A. Galerie, and M. Caillet. Contribution to understanding parabolic oxidation kinetics of dilute alloys. Part II: Oxides with metal deficit or oxygen excess. *Oxidation of metals*, 46(3-4):299–312, 1996.

[87] G. C. Wood. High-temperature oxidation of alloys. *Oxidation of Metals*, 2(1):11–57, 1970.

[88] N. Birks, G. H. Meier, and F. S. Pettit. *Introduction to the High Temperature Oxidation of Metals*. Cambridge University Press, March 2006.

[89] D. J. Young. *High temperature oxidation and corrosion of metals*, volume 1. Elsevier, 2008.

[90] B. B. Ebbinghaus. Thermodynamics of gas phase chromium species: The chromium oxides, the chromium oxyhydroxides, and volatility calculations in waste incineration processes. *Combustion and Flame*, 93(1–2):119–137, April 1993.

[91] E. J. Opila, D. L. Myers, N. S. Jacobson, I.M. B. Nielsen, D. F. Johnson, J. K. Olminsky, and M.D. Allendorf. Theoretical and Experimental Investigation of the Thermochemistry of $CrO_2(OH)_2$(g). *The Journal of Physical Chemistry A*, 111(10):1971–1980, March 2007.

[92] C. S. Tedmon. The Effect of Oxide Volatilization on the Oxidation Kinetics of Cr and Fe–Cr Alloys. *Journal of The Electrochemical Society*, 113(8):766–768, August 1966.

[93] G. R. Holcomb. Calculation of Reactive-evaporation Rates of Chromia. *Oxidation of Metals*, 69(3-4):163–180, April 2008.

[94] C. Key, J. Eziashi, J. Froitzheim, R. Amendola, R. Smith, and P. Gannon. Methods to Quantify Reactive Chromium Vaporization from Solid Oxide Fuel Cell Interconnects. *Journal of The Electrochemical Society*, 161(9):C373–C381, 2014.

[95] K. P. Lillerud and P. Kofstad. On High Temperature Oxidation of Chromium I . Oxidation of Annealed, Thermally Etched Chromium at 800 °–1100 °C.

Journal of The Electrochemical Society, 127(11):2397–2410, November 1980.

[96] D. Caplan, Alma Harvey, and M. Cohen. Oxidation of chromium at 890 °–1200 °C. *Corrosion Science*, 3(3):161–IN8, January 1963.

[97] W. C Hagel. Factors controlling the high-temperature oxidation of chromium. *Journal of the electrochemical society*, 109(3):C78–C78, 1962.

[98] W. C. Hagel and A. U. Seybolt. Cation Diffusion in Cr_2O_3. *Journal of The Electrochemical Society*, 108(12):1146–1152, December 1961.

[99] J. H. Park, W. E. King, and S. J. Rothman. Cation Tracer Diffusion in Cr_2O_3 and Cr_2O_3-0.09 wt% Y_2O_3. *Journal of the American Ceramic Society*, 70(12):880–885, December 1987.

[100] S. C. Tsai, A. M. Huntz, and C. Dolin. Diffusion of ^{18}O in massive Cr_2O_3 and in Cr_2O_3 scales at 900 °C and its relation to the oxidation kinetics of chromia forming alloys. *Oxidation of Metals*, 43(5-6):581–596, June 1995.

[101] A. M. Huntz and S. C. Tsai. Diffusion in oxide scales: application to Cr_2O_3 scales. *Journal of Materials Science Letters*, 13(11):821–825, January 1994.

[102] C. Greskovich. Deviation from Stoichiometry in Cr_2O_3 at High Oxygen Partial Pressures. *Journal of the American Ceramic Society*, 67(6):C–111, June 1984.

[103] A. C. S. Sabioni, A. M. Huntz, J. Philibert, B. Lesage, and C. Monty. Relation between the oxidation growth rate of chromia scales and self-diffusion in Cr_2O_3. *Journal of materials science*, 27(17):4782–4790, 1992.

[104] D. Caplan and G. I. Sproule. Effect of oxide grain structure on the high-temperature oxidation of Cr. *Oxidation of Metals*, 9(5):459–472, October 1975.

[105] L. Singheiser, P. Huczkowski, T. Markus, and W. J. Quadakkers. High Temperature Corrosion Issues for Metallic Materials in Solid Oxide Fuel Cells A2. In Stott, B., Cottis, M., Graham, R., Lindsay, S., Lyon, T., Richardson, D., and Scantlebury, H., editors, *Shreir's Corrosion*, pages 482–517. Elsevier, Oxford, 2010.

[106] A. W. B. Skilbred and R. Haugsrud. Sandvik Sanergy HT – A potential interconnect material for $LaNbO_4$-based proton ceramic fuel cells. *Journal of Power Sources*, 206:70–76, May 2012.

[107] M. Palcut, L. Mikkelsen, K. Neufeld, M. Chen, R. Knibbe, and P. V. Hendriksen. Corrosion stability of ferritic stainless steels for solid oxide electrolyser cell interconnects. *Corrosion Science*, 52(10):3309–3320, 2010.

[108] T. Brylewski, M. Nanko, T. Maruyama, and K. Przybylski. Application of Fe–16Cr ferritic alloy to interconnector for a solid oxide fuel cell. *Solid State Ionics*, 143(2):131–150, June 2001.

[109] S. Fontana, R. Amendola, S. Chevalier, P. Piccardo, G. Caboche, M. Viviani, R. Molins, and M. Sennour. Metallic interconnects for SOFC: Characterisation of corrosion resistance and conductivity evaluation at operating temperature of differently coated alloys. *Journal of Power Sources*, 171(2):652–662, September 2007.

[110] E. A. Polman, T. Fransen, and P. J. Gellings. The reactive element effect; ionic processes of grain-boundary segregation and diffusion in chromium oxide scales. *Journal of Physics: Condensed Matter*, 1(28):4497, 1989.

[111] H. Liu, M. M. Stack, and S. B. Lyon. Reactive element effects on the ionic transport processes in Cr_2O_3 scales. *Solid State Ionics*, 109(3–4):247–257, June 1998.

[112] B. A. Pint. Experimental observations in support of the dynamic-segregation theory to explain the reactive-element effect. *Oxidation of Metals*, 45(1-2):1–37, February 1996.

[113] C. Asensio-Jimenez, L. Niewolak, H. Hattendorf, B. Kuhn, P. Huczkowski, L. Singheiser, and W. J. Quadakkers. Effect of Specimen Thickness on the Oxidation Rate of High Chromium Ferritic Steels: The Significance of Intrinsic Alloy Creep Strength. *Oxidation of Metals*, 79(1-2):15–28, February 2013.

[114] P. Huczkowski, V. Shemet, J. Piron-Abellan, L. Singheiser, W. J. Quadakkers, and N. Christiansen. Oxidation limited life times of chromia forming ferritic steels. *Materials and Corrosion*, 55(11):825–830, November 2004.

[115] T. Uehara, N. Yasuda, T. Ohno, and A. Toji. Improvement of Oxidation Resistance of Fe-Cr Ferritic Alloy Sheets for SOFC Interconnects. *Electrochemistry*, 77(2):131–133, 2009.

[116] R. Sachitanand, J.-E. Svensson, and J. Froitzheim. The Influence of Cr Evaporation on Long Term Cr Depletion Rates in Ferritic Stainless Steels. *Oxidation of Metals*, 84(3-4):241–257, May 2015.

[117] N. Yasuda, T. Uehara, M. Okamoto, C. Aoki, T. Ohno, and A. Toji. Improvement of Oxidation Resistance of Fe-Cr Ferritic Alloy Sheets for SOFC Interconnects. *ECS Transactions*, 25(2):1447–1453, September 2009.

[118] H. Falk-Windisch, J. E. Svensson, and J. Froitzheim. The effect of temperature on chromium vaporization and oxide scale growth on interconnect steels for Solid Oxide Fuel Cells. *Journal of Power Sources*, 287:25–35, August 2015.

[119] Y. Liu. Performance evaluation of several commercial alloys in a reducing environment. *Journal of Power Sources*, 179(1):286–291, April 2008.

[120] P. Huczkowski, S. Ertl, J. Piron-Abellan, N. Christiansen, T. Höfler, V. Shemet, L. Singheiser, and W.j. Quadakkers. Effect of component thickness on lifetime and oxidation rate of chromia forming ferritic steels in low and high po_2 environments. *Materials at High Temperatures*, 22(3-4):253–262, January 2005.

[121] M. Linder, T. Hocker, L. Holzer, K. A. Friedrich, B. Iwanschitz, A. Mai, and J. A. Schuler. Cr_2O_3 scale growth rates on metallic interconnectors derived from 40,000 h solid oxide fuel cell stack operation. *Journal of Power Sources*, 243:508–518, December 2013.

[122] P. Alnegren, M. Sattari, J. Froitzheim, and J-E. Svensson. Degradation of ferritic stainless steels under conditions used for solid oxide fuel cells and electrolyzers at varying oxygen pressures. *Corrosion Science*, 2016.

[123] L. Niewolak, D. J. Young, H. Hattendorf, L. Singheiser, and W. J. Quadakkers. Mechanisms of Oxide Scale Formation on Ferritic Interconnect Steel in Simulated Low and High po_2 Service Environments of Solid Oxide Fuel Cells. *Oxidation of Metals*, 82(1-2):123–143, August 2014.

[124] S. Molin, M. Chen, J. R. Bowen, and P. V. Hendriksen. Diffusion of Nickel into Ferritic Steel Interconnects of Solid Oxide Fuel/Electrolysis Stacks. *ECS Transactions*, 57(1):2245–2252, October 2013.

[125] M. Stygar, T. Brylewski, A. Kruk, and K. Przybylski. Oxidation properties of ferritic stainless steel in dual Ar–H_2–H_2O/air atmosphere exposure with regard to SOFC interconnect application. *Solid State Ionics*, 262:449–453, September 2014.

[126] Z. Yang, M. S. Walker, P. Singh, and J.W. Stevenson. Anomalous Corrosion Behavior of Stainless Steels under SOFC Interconnect Exposure Conditions. *Electrochemical and Solid-State Letters*, 6(10):B35–B37, October 2003.

[127] P. Alnegren, M. Sattari, J. E. Svensson, and J. Froitzheim. Severe dual atmosphere effect at 600 °C for stainless steel 441. *Journal of Power Sources*, 301:170–178, January 2016.

[128] Y. Zhao and J. W. Fergus. Oxidation of Alloys 430 and 441 in SOFC Dual Atmospheres: Effects of Flow Rate and Humidity. *Journal of The Electrochemical Society*, 159(3):C109–C113, January 2012.

[129] M. R. Ardigo, I. Popa, L. Combemale, S. Chevalier, F. Herbst, and P. Girardon. Dual atmosphere study of the K41X stainless steel for interconnect application in high temperature water vapour electrolysis. *International Journal of Hydrogen Energy*, 40(15):5305–5312, April 2015.

[130] Z. Yang, M. S. Walker, P. Singh, J. W. Stevenson, and T. Norby. Oxidation Behavior of Ferritic Stainless Steels under SOFC Interconnect Exposure Conditions. *Journal of The Electrochemical Society*, 151(12):B669–B678, December 2004.

[131] G. R. Holcomb, M. Ziomek-Moroz, S. D. Cramer, B. S. Covino, and S. J. Bullard. Dual-environment effects on the oxidation of metallic interconnects. *Journal of Materials Engineering and Performance*, 15(4):404–409, August 2006.

[132] J. Rufner, P. Gannon, P. White, M. Deibert, S. Teintze, R. Smith, and H. Chen. Oxidation behavior of stainless steel 430 and 441 at 800 °C in

single (air/air) and dual atmosphere (air/hydrogen) exposures. *International Journal of Hydrogen Energy*, 33(4):1392–1398, February 2008.

[133] H. Kurokawa, K. Kawamura, and T. Maruyama. Oxidation behavior of Fe–16Cr alloy interconnect for SOFC under hydrogen potential gradient. *Solid State Ionics*, 168(1–2):13–21, March 2004.

[134] P. Gannon and R. Amendola. High-Temperature, Dual-Atmosphere Corrosion of Solid-Oxide Fuel Cell Interconnects. *JOM*, 64(12):1470–1476, October 2012.

[135] N.H. Menzler, Peter Batfalsky, Sonja Groß, Vladimir Shemet, and Frank Tietz. Post-Test Characterization of an SOFC Short-Stack after 17,000 Hours of Steady Operation. In *Electrochemcial Transactions*, pages 195–206, 2011.

[136] J. Mougin, A. Galerie, M. Dupeux, N. Rosman, G. Lucazeau, A.-M. Huntz, and L. Antoni. In-situ determination of growth and thermal stresses in chromia scales formed on a ferritic stainless steel. *Materials and Corrosion*, 53(7):486–490, July 2002.

[137] W. J. Quadakkers and K. Bongartz. The prediction of breakaway oxidation for alumina forming ODS alloys using oxidation diagrams. *Materials and Corrosion*, 45(4):232–241, April 1994.

[138] H. Al-Badairy, G. J. Tatlock, and M. J. Bennett. A comparison of breakaway oxidation in wedge-shaped and parallel sided coupons of FeCrAl alloys. *Materials at High Temperatures*, 17(1):101–107, January 2000.

[139] A. Holt and P. Kofstad. Electrical conductivity and defect structure of Cr_2O_3 . I. High temperatures (>1000 °C). *Solid State Ionics*, 69(2):127–136, July 1994.

[140] A. Holt and P. Kofstad. Electrical conductivity and defect structure of Cr_2O_3 II. Reduced temperatures (< 1000 °C). *Solid State Ionics*, 69(2):137–143, 1994.

[141] J. A. Crawford and R. W. Vest. Electrical Conductivity of Single–Crystal Cr_2O_3. *Journal of Applied Physics*, 35(8):2413–2418, August 1964.

[142] H. Nagai, T. Fujikawa, and K. Shoji. Electrical Conductivity of Cr_2O_3 doped with La_2O_3, Y_2O_3 and NiO. *Transactions of the Japan Institute of Metals*, 24(8):581–588, 1983.

[143] M. Linder, T. Hocker, L. Holzer, K. A. Friedrich, B. Iwanschitz, A. Mai, and J. A. Schuler. Model-based prediction of the ohmic resistance of metallic interconnects from oxide scale growth based on scanning electron microscopy. *Journal of Power Sources*, 272:595–605, December 2014.

[144] K. Kawamura, T. Nitobe, H. Kurokawa, M. Ueda, and T. Maruyama. Effect of Electric Current on Growth of Oxide Scale on Fe–25Cr Alloy for SOFC Interconnect at 1073 K. *Journal of the Electrochemical Society*, 159(3):B259–B264, 2012.

[145] P. Kodjamanova, Q. Fu, and L. Gautier. Electric Current Effects on the Corrosion Behaviour of High Chromium Ferritic Steels. *Oxidation of Metals*, 79(1-2):53–64, February 2013.

[146] K. Huang, P. Y. Hou, and J. B. Goodenough. Characterization of iron-based alloy interconnects for reduced temperature solid oxide fuel cells. *Solid State Ionics*, 129(1–4):237–250, April 2000.

[147] W. Wu, G. L. Wang, W. B. Guan, Y. F. Zhen, and W. G. Wang. Effect of Contact Method between Interconnects and Electrodes on Area Specific Resistance in Planar Solid Oxide Fuel Cells. *Fuel Cells*, 13(5):743–750, 2013.

[148] Z. Yang, G. Xia, P. Singh, and J. W. Stevenson. Electrical contacts between cathodes and metallic interconnects in solid oxide fuel cells. *Journal of Power Sources*, 155(2):246–252, April 2006.

[149] S. Megel, E. Girdauskaite, V. Sauchuk, M. Kusnezoff, and A. Michaelis. Area specific resistance of oxide scales grown on ferritic alloys for solid oxide fuel cell interconnects. *Journal of Power Sources*, 196(17):7136–7143, September 2011.

[150] J. G. Grolig, J. Froitzheim, and J.-E. Svensson. Coated stainless steel 441 as interconnect material for solid oxide fuel cells: Evolution of electrical properties. *Journal of Power Sources*, 284:321–327, June 2015.

[151] M. Stanislowski, J. Froitzheim, L. Niewolak, W. J. Quadakkers, K. Hilpert, T. Markus, and L. Singheiser. Reduction of chromium vaporization from SOFC interconnectors by highly effective coatings. *Journal of Power Sources*, 164(2):578–589, February 2007.

[152] N. Shaigan, W. Qu, D. G. Ivey, and W. Chen. A review of recent progress in coatings, surface modifications and alloy developments for solid oxide fuel cell ferritic stainless steel interconnects. *Journal of Power Sources*, 195(6):1529–1542, March 2010.

[153] K. Huang, P. Y. Hou, and J. B. Goodenough. Reduced area specific resistance for iron-based metallic interconnects by surface oxide coatings. *Materials Research Bulletin*, 36(1–2):81–95, January 2001.

[154] S. Fontana, S. Chevalier, and G. Caboche. Metallic Interconnects for Solid Oxide Fuel Cell: Performance of Reactive Element Oxide Coating During 10, 20 and 30 Months Exposure. *Oxidation of Metals*, 78(5-6):307–328, July 2012.

[155] M. Sattari, R. Sachitanand, J. Froitzheim, J. E. Svensson, and T. Jonsson. The effect of Ce on the high temperature oxidation properties of a Fe–22%Cr steel: microstructural investigation and EELS analysis. *Materials at High Temperatures*, 32(1-2):118–122, January 2015.

[156] S. Canovic, J. Froitzheim, R. Sachitanand, M. Nikumaa, M. Halvarsson, L. G. Johansson, and J. E. Svensson. Oxidation of Co- and Ce-nanocoated FeCr steels: A microstructural investigation. *Surface and Coatings Technology*, 215:62–74, January 2013.

[157] W. J. Quadakkers, H. Greiner, M. Hänsel, A. Pattanaik, A. S. Khanna, and W. Malléner. Compatibility of perovskite contact layers between cathode and metallic interconnector plates of SOFCs. *Solid State Ionics*, 91(1–2):55–67, October 1996.

[158] Z. Yang, G. G. Xia, G. D. Maupin, and J. W. Stevenson. Conductive protection layers on oxidation resistant alloys for SOFC interconnect applications. *Surface and Coatings Technology*, 201(7):4476–4483, December 2006.

[159] C. Gindorf, K. Hilpert, and L. Singheiser. Determination of Chromium Vaporization Rates of Different Interconnect Alloys by Transpiration Experiments. In *Proceedings of the Seventh International Symposium*, Electrochemical Society Proceedings Volume 2001-16, pages 793–802, Tsukuba, Ibaraki, Japan, June 2001.

[160] M. Palcut, L. Mikkelsen, K. Neufeld, M. Chen, R. Knibbe, and P. V. Hendriksen. Efficient dual layer interconnect coating for high temperature electrochemical devices. *International Journal of Hydrogen Energy*, 37(19):14501–14510, 2012.

[161] M. V. F. Schlupp, J. W. Kim, A. Brevet, C. Rado, K. Couturier, U. F. Vogt, F. Lefebvre-Joud, and A. Züttel. Avoiding chromium transport from stainless steel interconnects into contact layers and oxygen electrodes in intermediate temperature solid oxide electrolysis stacks. *Journal of Power Sources*, 270:587–593, December 2014.

[162] B. Hua, J. Pu, W. Gong, J. Zhang, F. Lu, and L. Jian. Cyclic oxidation of Mn–Co spinel coated SUS 430 alloy in the cathodic atmosphere of solid oxide fuel cells. *Journal of Power Sources*, 185(1):419–422, October 2008.

[163] N.V. Gavrilov, V.V. Ivanov, A.S. Kamenetskikh, and A.V. Nikonov. Investigations of Mn–Co–O and Mn–Co–Y–O coatings deposited by the magnetron sputtering on ferritic stainless steels. *Surface and Coatings Technology*, 206(6):1252–1258, December 2011.

[164] V. Miguel-Pérez, A. Martínez-Amesti, M. L. Nó, A. Larrañaga, and M. I. Arriortua. The effect of doping $(Mn, B)_3O_4$ materials as protective layers in different metallic interconnects for Solid Oxide Fuel Cells. *Journal of Power Sources*, 243:419–430, December 2013.

[165] T. Uehara, N. Yasuda, M. Okamoto, and Y. Baba. Effect of Mn–Co spinel coating for Fe–Cr ferritic alloys ZMG232l and 232J3 for solid oxide fuel cell interconnects on oxidation behavior and Cr-evaporation. *Journal of Power Sources*, 196(17):7251–7256, September 2011.

[166] B.K. Park, J.W. Lee, S.B. Lee, T.H. Lim, S.J. Park, C.O. Park, and R.H. Song. Cu- and Ni-doped $Mn_{1.5}Co_{1.5}O_4$ spinel coatings on metallic interconnects for solid oxide fuel cells. *International Journal of Hydrogen Energy*, 38(27):12043–12050, September 2013.

[167] S. R. Akanda, N. J. Kidner, and M. E. Walter. Spinel coatings on metallic interconnects: Effect of reduction heat treatment on performance. *Surface and Coatings Technology*, 253:255–260, August 2014.

[168] P. Wei, M. R. Bateni, and A. Petric. Conversion of copper and manganese metallic films to spinel coating. *Journal of Materials Science*, 47(13):5205–5215, March 2012.

[169] M. R. Bateni, P. Wei, X. Deng, and A. Petric. Spinel coatings for UNS 430 stainless steel interconnects. *Surface and Coatings Technology*, 201(8):4677–4684, January 2007.

[170] W. Zhang, B. Hua, N. Duan, J. Pu, B. Chi, and J. Li. Cu-Fe Spinel Coating as Oxidation Barrier for Fe-16Cr Metallic Interconnect in Solid Oxide Fuel Cells. *Journal of The Electrochemical Society*, 159(9):C388–C392, January 2012.

[171] J. G. Grolig, P. Alnegren, J. Froitzheim, and J.E. Svensson. Copper Iron Conversion Coating for Solid Oxide Fuel Cell Interconnects. *Journal of Power Sources*, 297:534–539, November 2015.

[172] J. Froitzheim, S. Canovic, M. Nikumaa, R. Sachitanand, L. G. Johansson, and J. E. Svensson. Long term study of Cr evaporation and high temperature corrosion behaviour of Co coated ferritic steel for solid oxide fuel cell interconnects. *Journal of Power Sources*, 220:217–227, December 2012.

[173] A. Harthøj, T. Holt, and P. Møller. Oxidation behaviour and electrical properties of cobalt/cerium oxide composite coatings for solid oxide fuel cell interconnects. *Journal of Power Sources*, 281:227–237, 2015.

[174] Å.H. Persson, L. Mikkelsen, P.V. Hendriksen, and M.A.J. Somers. Interaction mechanisms between slurry coatings and solid oxide fuel cell interconnect alloys during high temperature oxidation. *Journal of Alloys and Compounds*, 521:16–29, April 2012.

[175] S.I. Lee, J. Hong, H. Kim, J.W. Son, J.H. Lee, B.K. Kim, H.W. Lee, and K.J. Yoon. Highly Dense Mn-Co Spinel Coating for Protection of Metallic Interconnect of Solid Oxide Fuel Cells. *Journal of The Electrochemical Society*, 161(14):F1389–F1394, January 2014.

[176] M. Mirzaei, A. Simchi, M. A. Faghihi-Sani, and A. Yazdanyar. Electrophoretic deposition and sintering of a nanostructured manganese–cobalt spinel coating for solid oxide fuel cell interconnects. *Ceramics International*, 42(6):6648–6656, 2016.

[177] Y. Zhang, A. Javed, M. Zhou, S. Liang, and P. Xiao. Fabrication of Mn–Co Spinel Coatings on Crofer 22 APU Stainless Steel by Electrophoretic Deposition for Interconnect Applications in Solid Oxide Fuel Cells. *International Journal of Applied Ceramic Technology*, 11(2):332–341, March 2014.

[178] Z. Yang, G. Xia, S. P. Simner, and J. W. Stevenson. Thermal Growth and Performance of Manganese Cobaltite Spinel Protection Layers on Ferritic Stainless Steel SOFC Interconnects. *Journal of The Electrochemical Society*, 152(9):A1896–A1901, September 2005.

[179] L. V. Gambino, N. J. Magdefrau, and M. Aindow. Microstructural effects of the reduction step in reactive consolidation of manganese cobaltite coat-

ings on Crofer 22 APU. *Materials at High Temperatures*, 32(1–2):142–147, January 2015.

[180] N. J. Magdefrau, L. Chen, E. Y. Sun, and M. Aindow. The effect of $Mn_{1.5}Co_{1.5}O_4$ coatings on the development of near surface microstructure for Haynes 230 oxidized at 800 °C in air. *Surface and Coatings Technology*, 242:109–117, March 2014.

[181] R. Trebbels, T. Markus, and L. Singheiser. Investigation of Chromium Vaporization From Interconnector Steels With Spinel Coatings. *Journal of Fuel Cell Science and Technology*, 7(1):011013–011013, November 2009.

[182] X. Zhang and A. Zunger. Diagrammatic Separation of Different Crystal Structures of A_2BX_4 Compounds Without Energy Minimization: A Pseudopotential Orbital Radii Approach. *Advanced Functional Materials*, 20(12):1944–1952, June 2010.

[183] E. J. Verwey, P. W. Haayman, and F. C. Romeijn. Physical Properties and Cation Arrangement of Oxides with Spinel Structures II. Electronic Conductivity. *The Journal of Chemical Physics*, 15(4):181–187, April 1947.

[184] D. C. Johnston. Superconducting and normal state properties of $Li_{1+x}Ti_{2-x}O_4$ spinel compounds. I. Preparation, crystallography, superconducting properties, electrical resistivity, dielectric behavior, and magnetic susceptibility. *Journal of Low Temperature Physics*, 25(1-2):145–175, October 1976.

[185] H. Kawazoe and K. Ueda. Transparent Conducting Oxides Based on the Spinel Structure. *Journal of the American Ceramic Society*, 82(12):3330–3336, December 1999.

[186] J. B. Goodenough and A. L. Loeb. Theory of Ionic Ordering, Crystal Distortion, and Magnetic Exchange Due to Covalent Forces in Spinels. *Physical Review*, 98(2):391–408, April 1955.

[187] C. N. R. Rao and G. V. Subba Rao. Electrical conduction in metal oxides. *Physica Status Solidi (A)*, 1(4):597–652, April 1970.

[188] K. Momma and F. Izumi. *VESTA 3* for three-dimensional visualization of crystal, volumetric and morphology data. *Journal of Applied Crystallography*, 44(6):1272–1276, December 2011.

[189] R. J. Hill, J. R. Craig, and G. V. Gibbs. Systematics of the spinel structure type. *Physics and Chemistry of Minerals*, 4(4):317–339, August 1979.

[190] H. Bordeneuve, S. Guillemet-Fritsch, A. Rousset, S. Schuurman, and V. Poulain. Structure and electrical properties of single-phase cobalt manganese oxide spinels $Mn_{3-x}Co_xO_4$ sintered classically and by spark plasma sintering (SPS). *Journal of Solid State Chemistry*, 182(2):396–401, February 2009.

[191] S. Naka, M. Inagaki, and T. Tanaka. On the formation of solid solution in $Co_{3-x}Mn_xO_4$ system. *Journal of Materials Science*, 7(4):441–444, April 1972.

[192] T. Brylewski, W. Kucza, A. Adamczyk, A. Kruk, M. Stygar, M. Bobruk, and J. Dąbrowa. Microstructure and electrical properties of $Mn_{1+x}Co_{2-x}O_4$ ($0 \leq x \leq 1.5$) spinels synthesized using EDTA-gel processes. *Ceramics International*, 40(9):13873–13882, November 2014.

[193] E. Aukrust and A. Muan. Phase Relations in the System Cobalt Oxide–Manganese Oxide in Air. *Journal of the American Ceramic Society*, 46(10):511–511, 1963.

[194] T.F.W. Barth and E. Posnjak. Spinel structures with and without variate atom equipoints. *Zeitschrift fur Kristallographie*, 82(5/6):325–341, 1932.

[195] E. J. W. Verwey and E. L. Heilmann. Physical Properties and Cation Arrangement of Oxides with Spinel Structures I. Cation Arrangement in Spinels. *The Journal of Chemical Physics*, 15(4):174–180, April 1947.

[196] E. J. W. Verwey, F. de Boer, and J. H. van Santen. Cation Arrangement in Spinels. *The Journal of Chemical Physics*, 16(12):1091–1092, December 1948.

[197] F.C. Romeijn. Physical and crystallographical properties of some spinels. *Philips Research Reports*, 8(4):304–320, 1953.

[198] J. D. Dunitz and L. E. Orgel. Electronic properties of transition-metal oxides-II: Cation distribution amongst octahedral and tetrahedral sites. *Journal of Physics and Chemistry of Solids*, 3(3–4):318–323, 1957.

[199] D. S. McClure. The distribution of transition metal cations in spinels. *Journal of Physics and Chemistry of Solids*, 3(3–4):311–317, 1957.

[200] S. H. Wei and S. B. Zhang. First-principles study of cation distribution in eighteen closed-shell $A^{II}B^{III}{}_2O_4$ and $A^{IV}B^{II}{}_2O_4$ spinel oxides. *Physical Review B*, 63(4):045112, January 2001.

[201] V. Stevanović, M. d'Avezac, and A. Zunger. Simple Point-Ion Electrostatic Model Explains the Cation Distribution in Spinel Oxides. *Physical Review Letters*, 105(7):075501, August 2010.

[202] A. Navrotsky and O. J. Kleppa. The thermodynamics of cation distributions in simple spinels. *Journal of Inorganic and Nuclear Chemistry*, 29(11):2701–2714, November 1967.

[203] R. K. Datta and R. Rustum. Dependance on Temperature of the Distribution of Cations in Oxide spinels. *Nature*, 1961.

[204] N. Yamamoto, S. Higashi, S. Kawano, and N. Achiwa. Preparation of $MnCo_2O_4$ by a wet method and its metal ion distribution. *Journal of Materials Science Letters*, 2(9):525–526, September 1983.

[205] D. G. Wickham and J. B. Goodenough. Suggestion Concerning Magnetic Interactions in Spinels. *Physical Review*, 115(5):1156–1158, September 1959.

[206] I. Aoki. Tetragonal Distortion of the Oxide Spinels Containing Cobalt and Manganese. *Journal of the Physical Society of Japan*, 17(1):53–61, January 1962.

[207] B. Boucher, R. Buhl, R. Di Bella, and M. Perrin. Etude par des mesures de diffraction de neutrons et de magnétisme des propriétés cristallines et magnétiques de composés cubiques spinelles $Co_{3-x}Mn_xO_4(0.6 \leq x \leq 1.2)$. *Journal de Physique*, 31(1):113–119, 1970.

[208] E. Rios, J. L. Gautier, G. Poillerat, and P. Chartier. Mixed valency spinel oxides of transition metals and electrocatalysis: case of the $Mn_xCo_{3-x}O_4$ system. *Electrochimica Acta*, 44(8–9):1491–1497, December 1998.

[209] H. Bordeneuve, C. Tenailleau, S. Guillemet-Fritsch, R. Smith, E. Suard, and A. Rousset. Structural variations and cation distributions in $Mn_{3-x}Co_xO_4$ (0<x<3) dense ceramics using neutron diffraction data. *Solid State Sciences*, 12(3):379–386, March 2010.

[210] A. Purwanto, A. Fajar, H. Mugirahardjo, J. W. Fergus, and K. Wang. Cation distribution in spinel $(Mn, Co, Cr)_3O_4$ at room temperature. *Journal of Applied Crystallography*, 43(3):394–400, June 2010.

[211] A. K. M. Zakaria, F. Nesa, M. A. Saeed Khan, T. K. Datta, S. Aktar, S. I. Liba, S. Hossain, A. K. Das, I. Kamal, S. M. Yunus, and S. G. Eriksson. Cation distribution and crystallographic characterization of the spinel oxides $MgCr_xFe_{2-x}O_4$ by neutron diffraction. *Journal of Alloys and Compounds*, 633:115–119, June 2015.

[212] Y. Liu, J. W. Fergus, and C. D. Cruz. Electrical Properties, Cation Distributions, and Thermal Expansion of Manganese Cobalt Chromite Spinel Oxides. *Journal of the American Ceramic Society*, 96(6):1841–1846, June 2013.

[213] R. Subramanian, R. Dieckmann, G. Eriksson, and A. Pelton. Model calculations of phase stabilities of oxide solid solutions in the Co–Fe–Mn–O system at 1200 °C. *Journal of Physics and Chemistry of Solids*, 55(5):391–404, 1994.

[214] T. R. Paudel, A. Zakutayev, S. Lany, M. d'Avezac, and A. Zunger. Doping Rules and Doping Prototypes in A_2BO_4 Spinel Oxides. *Advanced Functional Materials*, 21(23):4493–4501, December 2011.

[215] K. Uusi-Esko, E.-L. Rautama, M. Laitinen, T. Sajavaara, and M. Karppinen. Control of Oxygen Nonstoichiometry and Magnetic Property of $MnCo_2O_4$ Thin Films Grown by Atomic Layer Deposition. *Chemistry of Materials*, 22(23):6297–6300, December 2010.

[216] G. V. Bazuev and A. V. Korolyov. Magnetic behavior of $MnCo_2O_{4+\delta}$ spinel obtained by thermal decomposition of binary oxalates. *Journal of Magnetism and Magnetic Materials*, 320(18):2262–2268, September 2008.

[217] O. I. Gyrdasova, G. V. Bazuev, I. G. Grigorov, and O. V. Koryakova. Preparation of $MnCo_2O_4$ whiskers and spheroids through thermal decomposition

of $Mn_{1/3}Co_{2/3}C_2O_4 \cdot 2H_2O$. *Inorganic Materials*, 42(10):1126–1132, October 2006.

[218] Y. Nissinen, T.and Kiros, M. Gasik, and M. Lampinen. Comparison of preparation routes of spinel catalyst for alkaline fuel cells. *Materials Research Bulletin*, 39(9):1195–1208, July 2004.

[219] Y. Shi, P. F. Ndione, L. Y. Lim, D. Sokaras, T.C. Weng, A. R. Nagaraja, A. G. Karydas, J. D. Perkins, T. O. Mason, D. S. Ginley, A. Zunger, and M.F. Toney. Self-Doping and Electrical Conductivity in Spinel Oxides: Experimental Validation of Doping Rules. *Chemistry of Materials*, 26(5):1867–1873, March 2014.

[220] A. Navrotsky. Thermodynamics of A_3O_4–B_3O_4 spinel solid solutions. *Journal of Inorganic and Nuclear Chemistry*, 31(1):59–72, January 1969.

[221] H. St C. O'Neill and A. Navrotsky. Simple spinels; crystallographic parameters, cation radii, lattice energies, and cation distribution. *American Mineralogist*, 68(1-2):181–194, February 1983.

[222] H. St C. O'Neill and A. Navrotsky. Cation distributions and thermodynamic properties of binary spinel solid solutions. *American Mineralogist*, 69(7-8):733–753, 1984.

[223] T Holstein. Studies of polaron motion: Part I. The molecular-crystal model. *Annals of Physics*, 8(3):325–342, November 1959.

[224] T. Holstein. Studies of polaron motion: Part II. The small polaron. *Annals of Physics*, 8(3):343–389, November 1959.

[225] N. Tsuda, K. Nasu, A. Fujimori, and K. Siratori. *Electronic Conduction in Oxides*, volume 94 of *Springer Series in Solid-State Sciences*. Springer Berlin Heidelberg, Berlin, Heidelberg, 2000.

[226] A. Rousset, C. Tenailleau, P. Dufour, H. Bordeneuve, I. Pasquet, S. Guillemet-Fritsch, V. Poulain, and S. Schuurman. Electrical Properties of $Mn_{3-x}Co_xO_4$ (0<x<3) Ceramics: An Interesting System for Negative Temperature Coefficient Thermistors. *International Journal of Applied Ceramic Technology*, 10(1):175–185, January 2013.

[227] W. A. Groen, C. Metzmacher, P. Huppertz, and S. Schuurman. Aging of NTC Ceramics in the System Mn-Ni-Fe-O. *Journal of Electroceramics*, 7(2):77–87, November 2001.

[228] Y. Liu, J. W. Fergus, K. Wang, and C. D. Cruz. Crystal Structure, Chemical Stabilities and Electrical Conductivity of Fe-Doped Manganese Cobalt Spinel Oxides for SOFC Interconnect Coatings. *Journal of The Electrochemical Society*, 160(11):F1316–F1321, January 2013.

[229] A. D. Sharma, J. Mukhopadhyay, and R. N. Basu. Synthesis and Characterization of Nanocrystalline $MnCo_2O_{4-\delta}$ Spinel for Protective Coating Application in SOFC. *ECS Transactions*, 35(1):2509–2517, April 2011.

[230] X Chen, P Hou, C Jacobson, S Visco, and L Dejonghe. Protective coating on stainless steel interconnect for SOFCs: oxidation kinetics and electrical properties. *Solid State Ionics*, 176(5-6):425–433, February 2005.

[231] T. Kiefer, M. Zahid, F. Tietz, D. Stöver, and H.R. Zerfass. Electrical conductivity and thermal expansion coefficientes of spinels in the series $MnCo_{2-x}Fe_xO_4$ for application as a protective layer in SOFC. *Proceedings of the 26th Risö International Symposium on Materials Science : Solid State Electrochemistry*, 2005.

[232] D. R. Ou, M. Cheng, and X. L. Wang. Development of low-temperature sintered Mn–Co spinel coatings on Fe–Cr ferritic alloys for solid oxide fuel cell interconnect applications. *Journal of Power Sources*, 236:200–206, August 2013.

[233] D. C. Carter and T. O. Mason. Electrical Properties and Site Distribution of Cations in $(Mn_yCo_{1-y})_{0.4}Fe_{2.6}O_4$. *Journal of the American Ceramic Society*, 71(4):213–218, April 1988.

[234] N. Sakai, T. Horita, Y. P. Xiong, K. Yamaji, H. Kishimoto, M. E. Brito, H. Yokokawa, and T. Maruyama. Structure and transport property of manganese–chromium–iron oxide as a main compound in oxide scales of alloy interconnects for SOFCs. *Solid State Ionics*, 176(7–8):681–686, February 2005.

[235] Z. Lu, J. Zhu, A. E. Payzant, and M. P. Paranthaman. Electrical Conductivity of the Manganese Chromite Spinel Solid Solution. *Journal of the American Ceramic Society*, 88(4):1050–1053, April 2005.

[236] J. Xiao, W. Zhang, C. Xiong, B. Chi, J. Pu, and L. Jian. Oxidation of $MnCu_{0.5}Co_{1.5}O_4$ spinel coated SUS430 alloy interconnect in anode and cathode atmospheres for intermediate temperature solid oxide fuel cell. *International Journal of Hydrogen Energy*, 40(4):1868–1876, January 2015.

[237] J. S. O. Evans. Negative thermal expansion materials. *Journal of the Chemical Society, Dalton Transactions*, (19):3317–3326, 1999.

[238] C. Y. Ho and R. E. Taylor. *Thermal Expansion of Solids*. ASM International, 1998.

[239] A. K. Tyagi and S. N. Achary. Diffraction and Thermal Expansion of Solids. In S. L. Chaplot and N. Mittal, R.and Choudhury, editors, *Thermodynamic Properties of Solids*, pages 197–267. Wiley-VCH Verlag GmbH & Co. KGaA, 2010.

[240] D. Marrocchelli, N. H. Perry, and S. R. Bishop. Understanding chemical expansion in perovskite-structured oxides. *Phys. Chem. Chem. Phys.*, 17(15):10028–10039, 2015.

[241] S.R. Bishop, D. Marrocchelli, C. Chatzichristodoulou, N.H. Perry, M.B. Mogensen, H.L. Tuller, and E.D. Wachsman. Chemical Expansion: Implications for Electrochemical Energy Storage and Conversion Devices. *Annual Review of Materials Research*, 44(1):205–239, July 2014.

[242] B Touzelin. High temperature X-ray diffraction in a controlled atmosphere of cobalt and nickel oxides. *Revue Internationale des Hautes Temperatures et des Refractaires*, 15(1):33–41, 1978.

[243] V. A. M. Brabers and A. D. D. Broemme. Low-spin-high-spin transition in the Co_3O_4 spinel. *Journal of Magnetism and Magnetic Materials*, 104–107, Part 1:405–406, February 1992.

[244] A. Podlesnyak, S. Streule, J. Mesot, M. Medarde, E. Pomjakushina, K. Conder, A. Tanaka, M. W. Haverkort, and D. I. Khomskii. Spin-State Transition in $LaCoO_3$: Direct Neutron Spectroscopic Evidence of Excited Magnetic States. *Physical Review Letters*, 97(24):247208, 2006.

[245] M. Y. Yoon, E. J. Lee, R. H. Song, and H. J. Hwang. Preparation and properties of a $MnCo_2O_4$ for ceramic interconnect of solid oxide fuel cell via glycine nitrate process. *Metals and Materials International*, 17(6):1039–1043, December 2011.

[246] Y. Xu, Z. Wen, S. Wang, and T. Wen. Cu doped Mn–Co spinel protective coating on ferritic stainless steels for SOFC interconnect applications. *Solid State Ionics*, 192(1):561–564, June 2011.

[247] G. G. Xia, Z. G. Yang, and J. Stevenson. Manganese-Cobalt Spinel Oxides as Surface Modifiers for Stainless Steel Interconnects of Solid Oxide Fuel Cells. *ECS Transactions*, 1(7):325–332, June 2006.

[248] U Pippardt, J Boer, Ch Bollert, A Hoffmann, M Heidenreich, R Kriegel, M Schulz, and A Simon. Performance and Stability of Mixed Conducting Composite Membranes Based on Substituted Ceria. *Journal of Ceramic Science and Technology*, 05(04):309–316, 2014.

[249] N. J. Kidner and Nextech Coatings. Protective Coatings for Metallic SOFC Components 13th Annual SECA Workshop, 2012.

[250] R. Sun. Diffusion of Cobalt and Chromium in Chromite Spinel. *The Journal of Chemical Physics*, 28(2):290–293, February 1958.

[251] F. H. Lu and R. Dieckmann. Point defects and cation tracer diffusion in $(Co_xMn_{1-x})_{3-\delta}O_4$ spinels. *Solid State Ionics*, 67(1–2):145–155, December 1993.

[252] F. H. Lu and R. Dieckmann. Point defects and cation tracer diffusion in $(Co,Fe,Mn)_{3-\delta}O_4$ spinels: I. Mixed spinels $(Co_xFe_{2y}Mn_y)_{3-\delta}O_4$. *Solid State Ionics*, 53–56, Part 1:290–302, July 1992.

[253] J. Töpfer, S. Aggarwal, and R. Dieckmann. Point defects and cation tracer diffusion in $(Cr_xFe_{1-x})_{3-\delta}O_4$ spinels. *Solid State Ionics*, 81(3–4):251–266, November 1995.

[254] Y. Liu, K. Wang, and J. W. Fergus. Effect of chromium doping on the crystal structure, electrical conductivity and thermal expansion of manganese cobalt spinel oxides. In *Advances in Solid Oxide Fuel Cells VII: Ceramic Engineering and Science Proceedings*. Bansal, Narottam P. and Singh, Prabhakar and Widjaja, Sujanto and Singh, Dileep, 2011.

[255] T. Horita, H. Kishimoto, K. Yamaji, Y. Xiong, M. E. Brito, H. Yokokawa, Y. Baba, K. Ogasawara, H. Kameda, Y. Matsuzaki, S. Yamashita, N. Yasuda, and T. Uehara. Diffusion of oxygen in the scales of Fe–Cr alloy interconnects and oxide coating layer for solid oxide fuel cells. *Solid State Ionics*, 179(38):2216–2221, November 2008.

[256] S. R. Akanda, M. E. Walter, N. J. Kidner, and M. M. Seabaugh. Mechanical characterization of oxide coating–interconnect interfaces for solid oxide fuel cells. *Journal of Power Sources*, 210:254–262, July 2012.

[257] L. Latu-Romain, Y. Madi, S. Mathieu, F. Robaut, J. P. Petit, and Y. Wouters. Advanced STEM/EDX investigation on an oxide scale thermally grown on a high-chromium iron–nickel alloy under very low oxygen partial pressure. *Corrosion Science*, 101:193–200, December 2015.

Appendices

Appendix A

Supplementary material for Manuscript I

Figure A1 shows X-ray diffraction patterns for spinel ceramics in air at 1100 °C (5h) + 800 °C (12 h). The results were used to determine the lattice parameters, as described in Manuscript I.

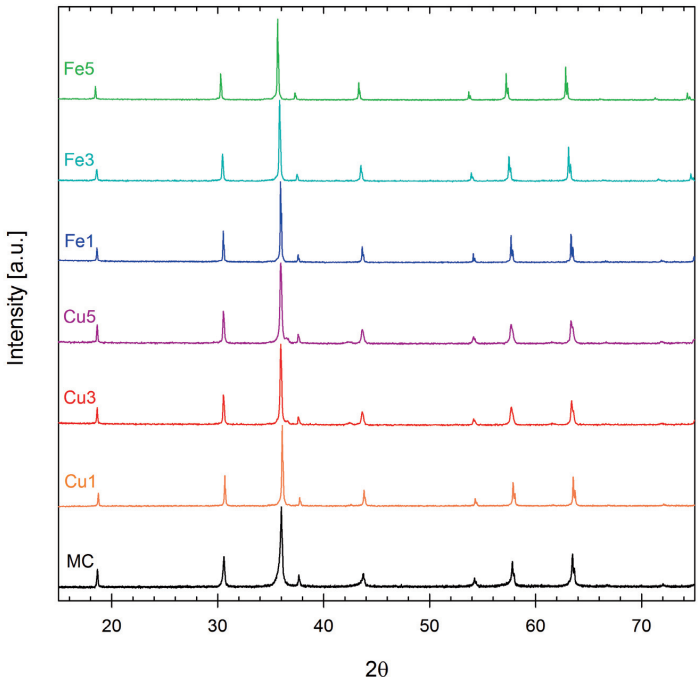

Figure A1. X-ray diffractograms of spinel ceramics sintered in air at 1100 °C (5h) + 800 °C (12 h).

In Manuscript I only the heating parts of the dilatometer measurements were shown. Figure A2 shows both the heating and cooling curve for the Fe1 composition, measured between room temperature and 1000 °C. A significant negative hysteresis is observed between the heating and cooling segments. Figure A2 also shows a new sample of the same material measured between room temperature and 800 °C. The hysteresis is seen to be considerably reduced, although not completely eliminated when the measurement is reversed at lower temperature. Based on this, the large

hysteresis when the measurement is reversed at 1000 °C was attributed to creep or the onset of Co-reduction in the materials.

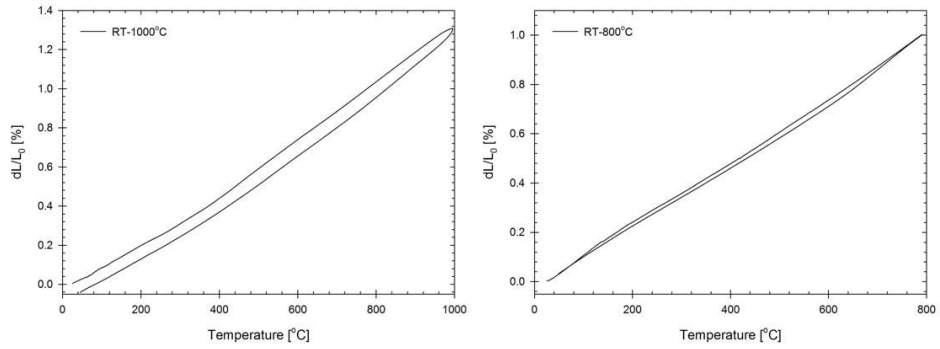

Figure A2. Heating and cooling curve for the thermal expansion data of the Fe1 material. Measurement reversed at 1000 °C (left) and 800 °C (right).

A hysteresis in the electrical conductivity of the $MnCo_2O_4$ material was observed between heating and cooling (Figure 6 in Manuscript I). A3 shows the electrical conductivity of this material measured continuously between room temperature and 500 °C with a heating and cooling rate of 3 °C/min. The hysteresis between heating and cooling is still observed. Figure A4 shows the electrical conductivity for two different samples of the Cu1 material. The sample with 60 % density displays hysteresis in electrical conductivity between heating and cooling. The sample with 84 % density does not display any hysteresis. The reasons for the hysteresis in electrical conductivity were discussed in Manuscript I.

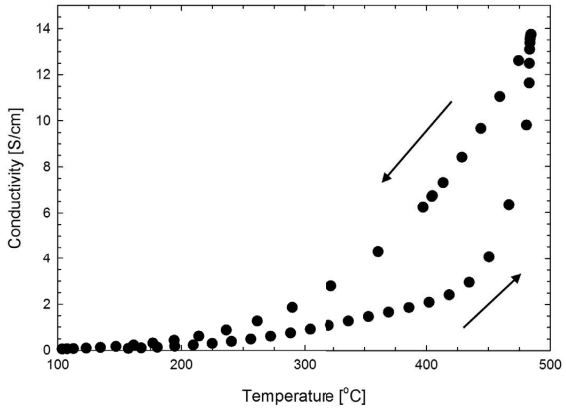

Figure A3. Electrical conductivity of $MnCo_2O_4$ measured during heating and cooling.

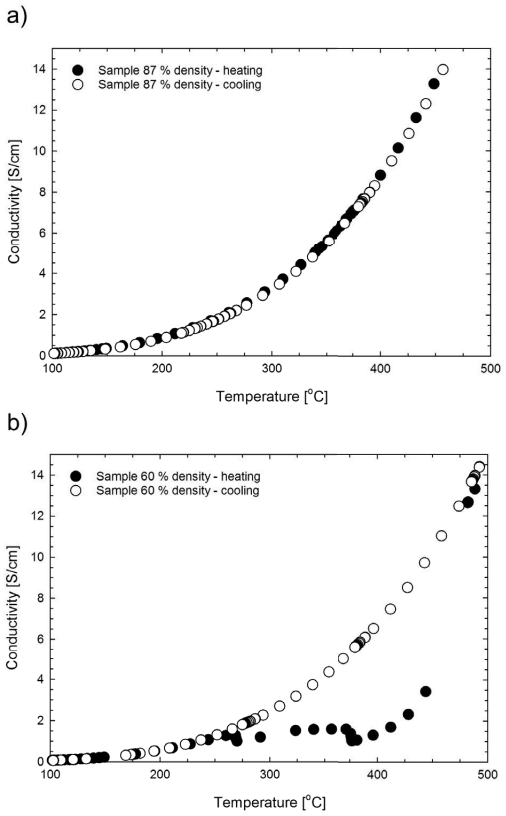

Figure A4. Electrical conductivity of Cu1 measured during heating and cooling in air . Results for two samples with different sample density, (a) 87 % and (b) 60 %. The results are excerpts from measurements between room temperature and 1000°C.

Thermogravimetric analysis (TGA) was performed using TG 439 Thermo-Microbalance from Netzsch, illustrated in Figure A5. The mass change of the sample is measured against a reference (Al_2O_3 powder) and in principle, this should eliminate any buoyancy effects. This means that a measurement with empty crucibles should result in no recordable mass change with change in temperature. In practice, this was not the case. Figure A6 shows the measurement with empty crucibles between room temperature and 800 °C, with heating and cooling rates of 10 K/min (first cycle) and 1 K/min (second cycle). All the results presented in Manuscript I were corrected against the background. Figure A6 also shows the measurement results of the $MnCo_2O_4$ powder before the background correction was made. It may be noticed that the mass change of the sample is significantly larger than the mass change in the background measurement.

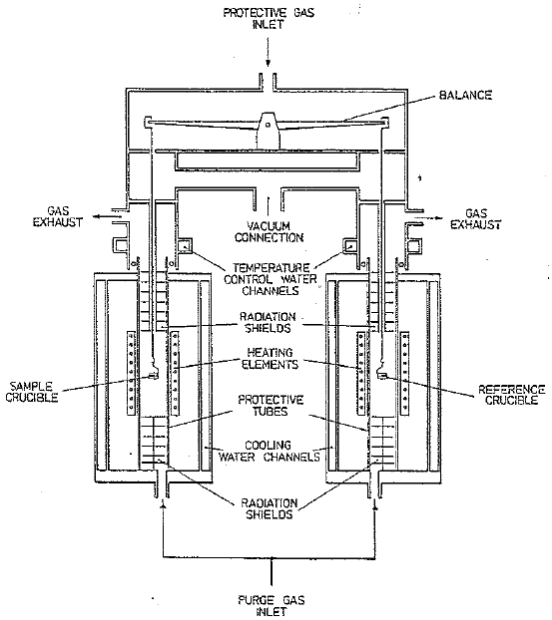

Figure A5. Schematic drawing of the TG 439 equipment by Netzsch. Figure from equipment manual.

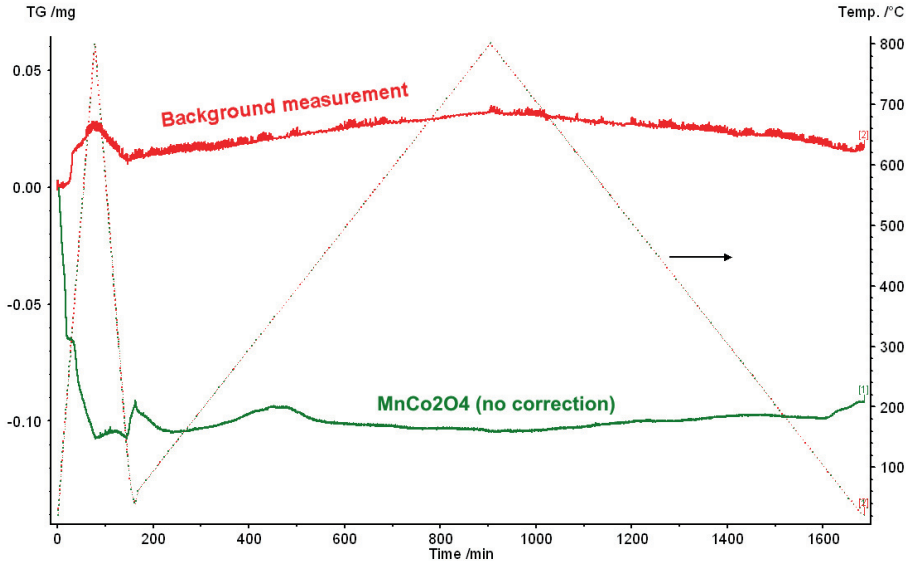

Figure A6. Background measurement for thermogravimetrical analysis made with empty alumina crucibles and original measurement data for $MnCo_2O_4$ before applying the background correction.

To improve readability of the TGA results, the inherent noise of the measurement was reduced by fitting the experimental data to a polynomial curve. This was performed using the negative exponential function in Sigmaplot 13.0. The polynomial degree was set to 1 or 2 based on visual evaluation of best fit to original data. Figure A7 shows an example of the fitting procedure for the $MnCo_2O_4$ material.

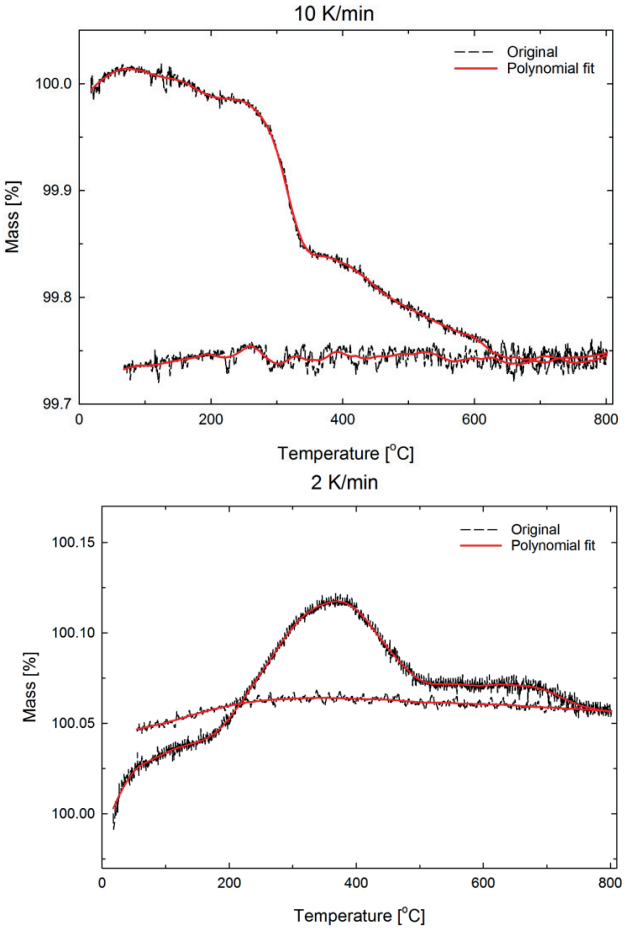

Figure A7. Polynomial fit of the experimental thermogravimetric analysis data of $MnCo_2O_4$.

Appendix B

Supplementary material for Manuscript II

Figure B1 shows SEM images of uncoated Crofer 22 APU after 1000 h and 2000 h oxidation at 800 °C in air. The alloy is seen to be deformed at the sample edges. This is probably an artifact of the laser cutting and sample polishing procedure. The thinned edges become depleted in Cr faster than the bulk, leading to localized break-away oxidation (formation of Fe-rich oxides). Localized break-away is believed to be (at least in part) responsible for the deviation from parabolic oxidation kinetics observed during oxidation of Crofer 22 APU at 800 °C (Manuscript II and V).

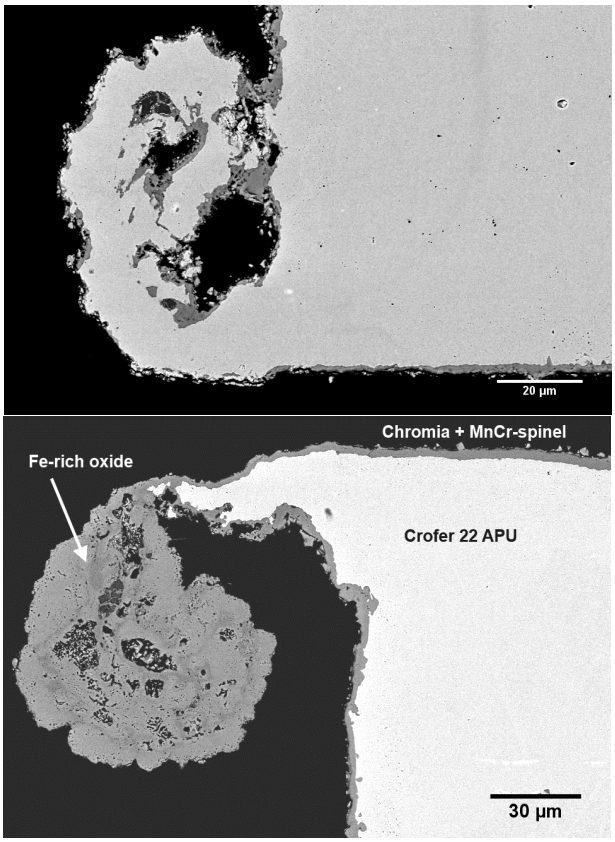

FIGURE B1. SEM backscatter electron images of Crofer 22 APU edge after 1000 h (top) and 2000 h (bottom) oxidation at 800 °C in air.

Figures B2-B4 show energy dispersive X-ray spectroscopy (EDX) maps of spinel coated Crofer 22 APU after 2000 h of oxidation at 900 °C in air. These maps were used to depict the extent of the reaction layer in Figure 8 in the main paper.

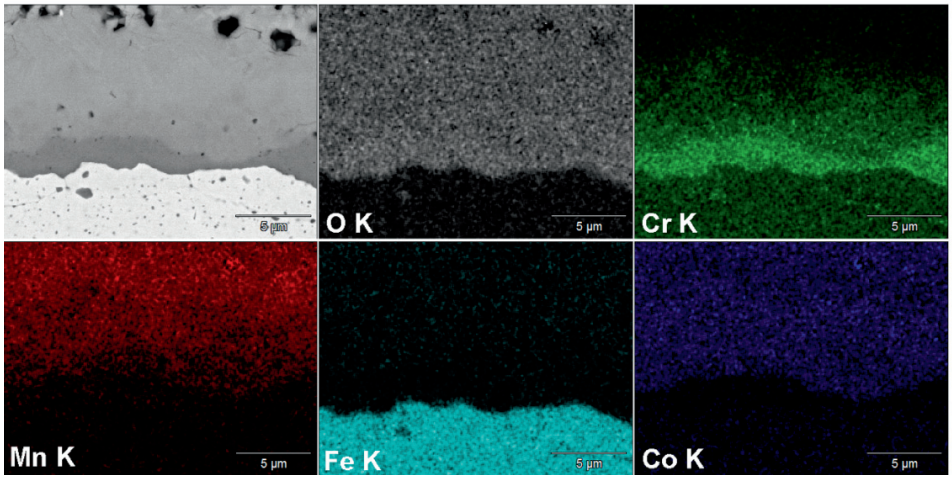

FIGURE B2. EDX-maps of MC coated Crofer 22 APU after 2000 h oxidation at 900C in air.

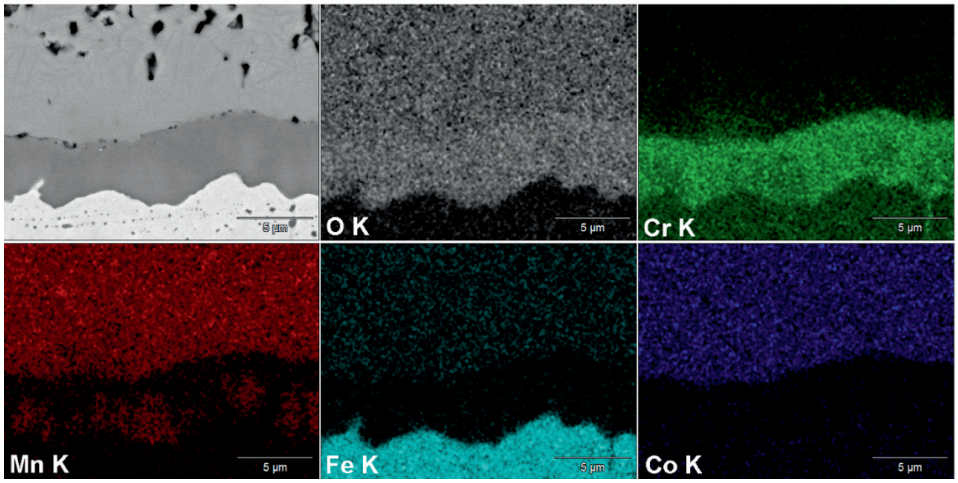

FIGURE B3. EDX-maps of MCFe coated Crofer 22 APU after 2000 h oxidation at 900C in air.

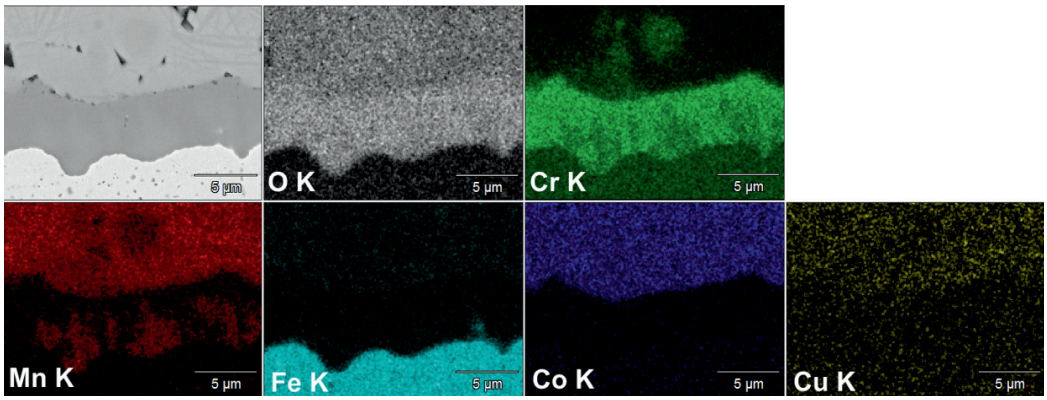

FIGURE B4. EDX-maps of MCCu coated Crofer 22 APU after 2000 h oxidation at 900C in air.

The area specific resistance (ASR) was measured on two samples of each coating material in the same stack. Since the experimental set-up allowed for measuring across the two surfaces on each sample individually (see Manuscript II for details), this gave totally four measurement results for each coating material. In the manuscript only one measurement for each surface, found to best represent the average behavior, was plotted. The ASR measured across all four surfaces is shown in Figures B5-7. The results shown in the main paper are for the MC(1)-up, MCFe(1)-up and MCCu(1)-up interfaces. The largest difference between two measurements of the same coating material is 4 $m\Omega cm^2$. Note that the degradation rate in the paper was calculated based on the average degradation rate of all the tested samples of each coating material.

Since the current is past from the top of the stack to the bottom, the effect of current may be evaluated by comparing the "up" and "down" samples of the different coating materials. I.e. on one side of the sample current is in the direction LSM → coating → oxide scale → alloy, while on the other side it flows in the opposite direction. From the results it is clear that the current direction does not have a significant effect on the ASR development.

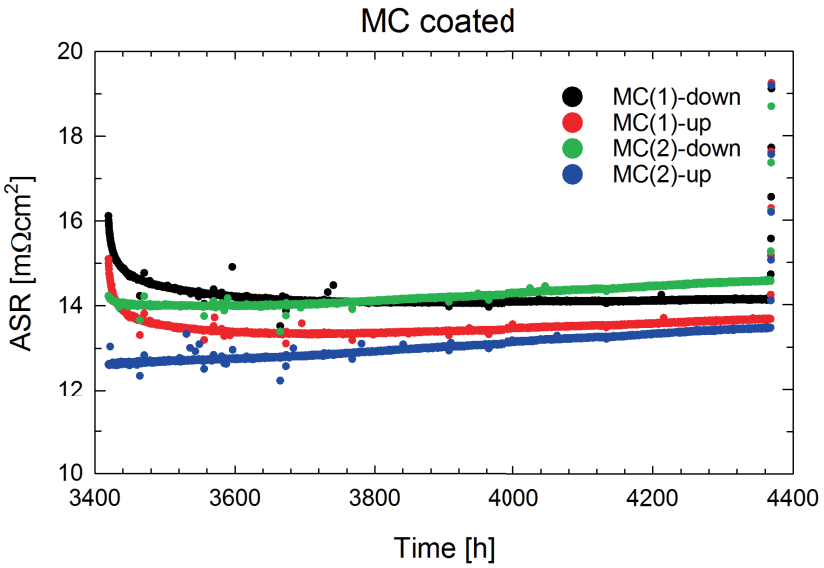

FIGURE B5. ASR measured across four individual surfaces of MC coated Crofer 22 APU in contact with LSM at 800C with applied current density of 0.5 A/cm^2. ´

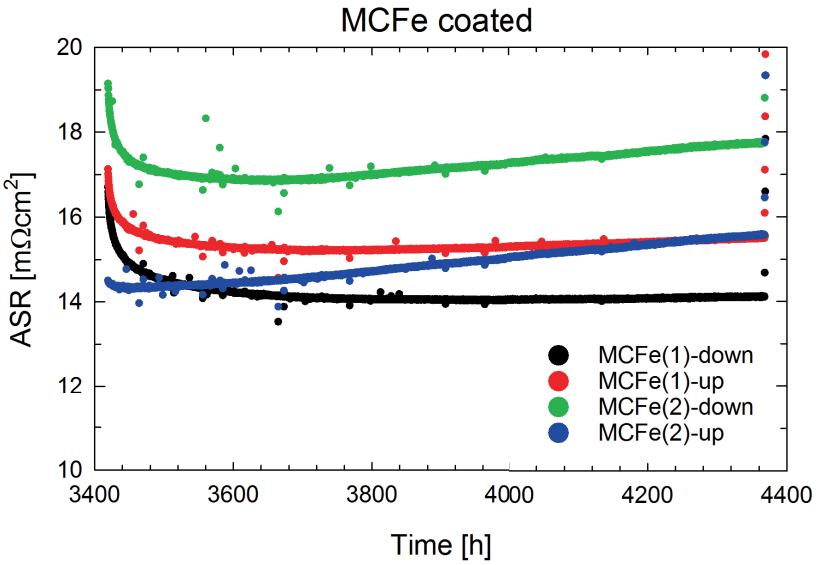

FIGURE B6. ASR measured across four individual surfaces of MCFe coated Crofer 22 APU in contact with LSM at 800C with applied current density of 0.5 A/cm^2.

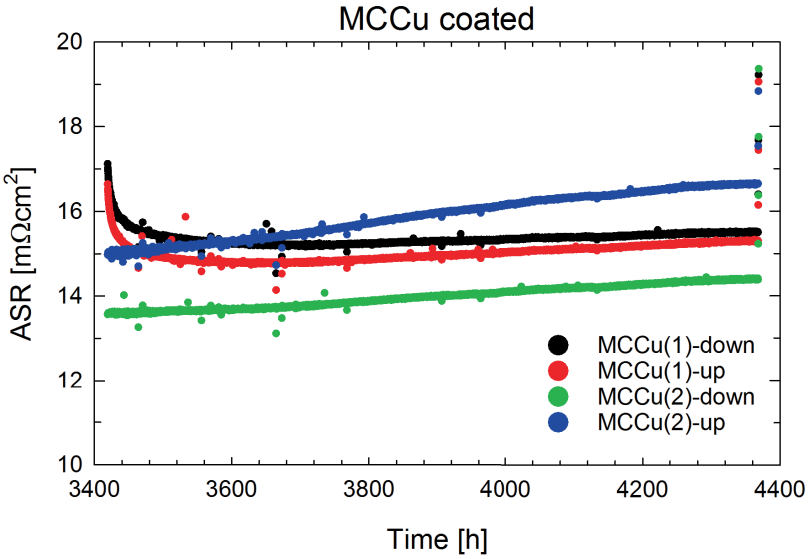

FIGURE B7. ASR measured across four individual surfaces of MCCu coated Crofer 22 APU in contact with LSM at 800C with applied current density of 0.5 A/cm^2.

Figure B8 shows the initial 4000 h of ASR measurement for one of the MCFe coated samples and the LSM reference plate. The first 2000 h of this measurement are at 800 °C. After an initial large drop (<100 h), the ASR of both LSM and MCFe coated Crofer 22 APU continue to decrease until ca. 1700 h. The decreasing ASR can be attributed to sintering of the LSM plate. This masks any ASR increase due to growth of the chromia scale on the spinel coated samples.

After 2000 h measurement, 30 thermal cycles between 100 °C and 800 °C were conducted before the temperature was returned to 800 °C. The ASR of the other samples in the stack was logged first after these thermal cycles (results presented in Figures B5-B7).

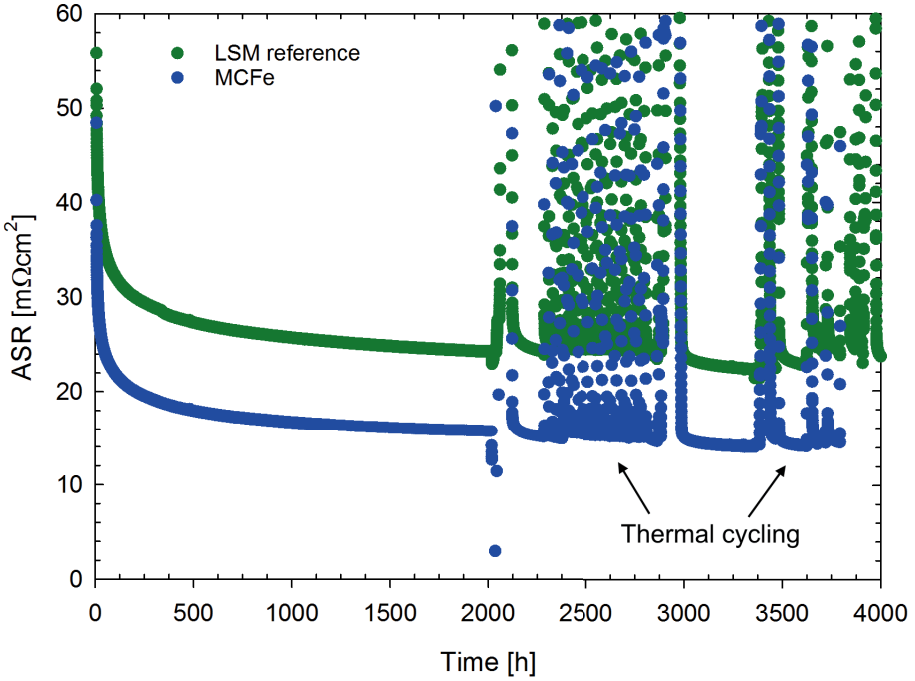

Figure B8. ASR measurement of MCFe(1)-down and LSM reference plate the first 4000 h.

SEM images and corresponding EDX maps of the MCCu and MCFe coated samples after ASR measurement are shown in Figure B9 and B10, respectively.

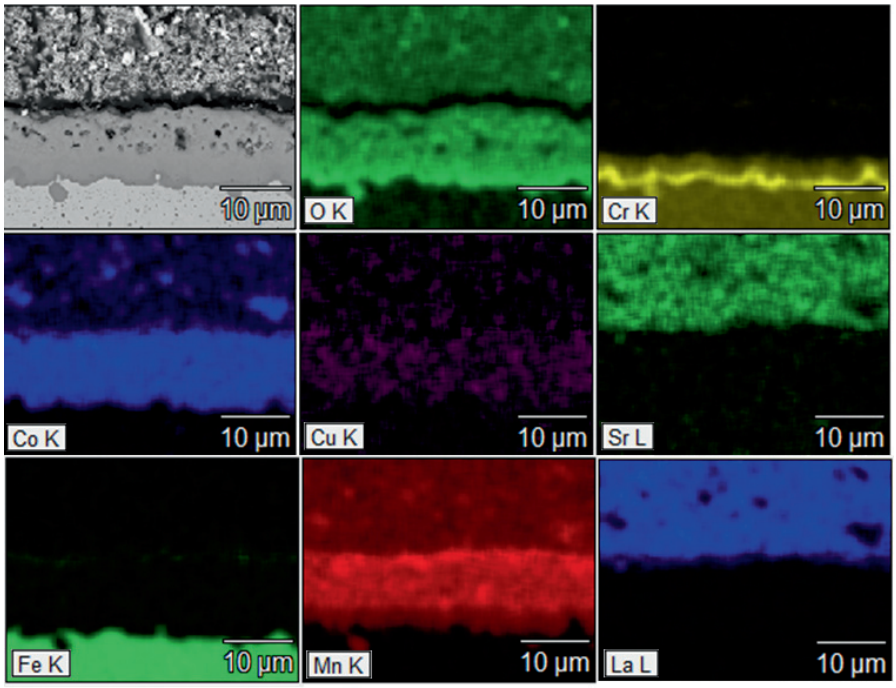

FIGURE B9. SEM image and corresponding EDX map of MCCu coated Crofer 22 APU and LSM contact plate after ASR measurement at 800°C for ca. 4300 h.

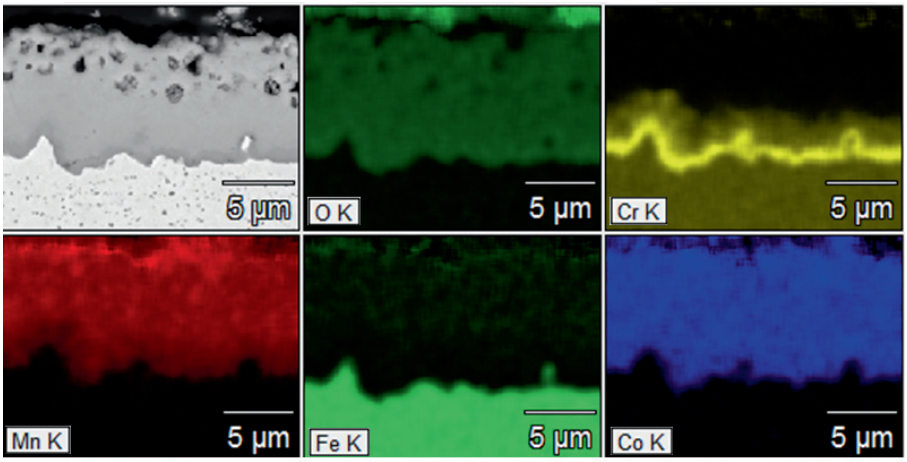

FIGURE B10. SEM image and corresponding EDX map of MCFe coated Crofer 22 APU after ASR measurement at 800°C for ca. 4300 h.

Appendix C

Supplementary material for Manuscript V

Polished coupons of Crofer 22 APU were oxidized in N_2-9%H_2-1%H_2O at 1100 °C for 5 h followed by in air at 800 °C for 5 h (R1100+O800). The oxide scale was subsequently removed by grinding and polishing. Figure C1 shows the mass change of these samples measured during oxidation at 800 °C in air. The results for the as-received sample are shown for comparison.

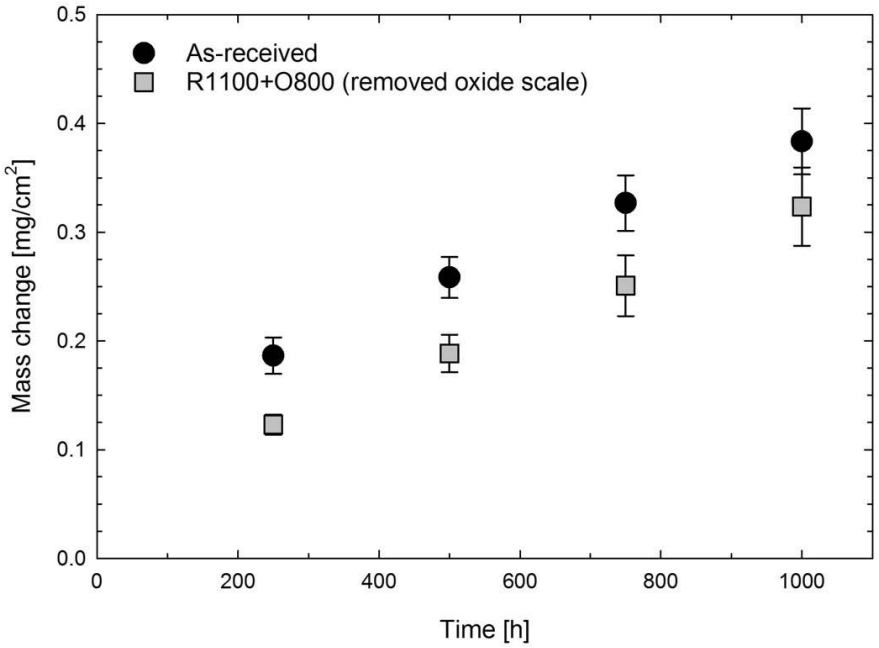

FIGURE C1. Mass change measured during oxidation at 800 °C in air. Average of three samples with error bars showing standard deviation.